DURBAN UNIVERSITY OF TECHNOLOGY
INYUVESI YASETHEKWINI YEZOBUCHWEPHESHE

OPTIMIZATION OF DISTRIBUTION STATIC COMPENSATOR FOR MITIGATION OF POWER QUALITY ISSUES IN GRID-TIED PHOTOVOLTAIC SYSTEMS

By
Abayomi Aduragba Adebiyi

A thesis submitted in fulfilment of the requirements for the award of Doctor of Engineering degree in Electrical Power Engineering

to the

Department of Electrical Power Engineering
Faculty of Engineering and the Built Environment at the
Durban University of Technology
Durban, South Africa

May 2021

DECLARATION

I, Abayomi Aduragba Adebiyi, declare that this thesis is the original representation of my work. It has not been submitted in part or totality for another degree in this or any other university, and I have appropriately referenced all text that I cited.

10 / 11 / 2021

Abayomi Aduragba Adebiyi — Date

Student number: 21556780

Approved for Final Submission by:

13 / 11 / 2021

Prof. Ian J. Lazarus — Date
Supervisor

13 / 11 / 2021

Prof. Akshay K. Saha — Date
Co-Supervisor

15 / 11 / 2021

Dr. Evans E. Ojo — Date
Co-Supervisor

DEDICATION

I dedicate this thesis to God Almighty, my Alpha and Omega, my Lord, and the Creator of my being. Also, to an extraordinary person, my wife, Mrs. Faith N. Adebiyi, for her unrelenting and faithful love, understanding, and support throughout my pursuit of this doctoral degree, which has made the completion of this thesis possible. I greatly value her contribution and sincerely appreciate her belief in my ability. I extend my dedication to my children, Goodnews Eniola and Great Akolade, for their patience all this while that I was far away from home since I began this pursuit. Likewise, my elder brother and mentor, Professor A.A. Adebiyi, for his kind words, support, and direction. To the memory of my father, Late Elder (Chief) A.A. Adebiyi, a man of prayer and faith, and my mother, Late Madam M.O. Adebiyi, I know that I have made you proud, daddy and mummy.

ACKNOWLEDGMENTS

I acknowledge the Almighty God for His abundant grace and mercy since I was conceived and throughout this doctoral degree study.

I acknowledge my main and co-supervisors', Professor I.J Lazarus, Professor A. K. Saha, and Dr. E.E. Ojo, for their supervision.

My gratitude goes to the Chair and Head, Department of Electrical Power Engineering, Professor I.E. Davidson, a worthy epitome of erudition, for his moral and academic support throughout this study.

I cannot forget the kind support of my elder brother, Professor A.A Adebiyi – you are a worthy role model that everyone who desires to go far should seek. I appreciate you greatly, sir, and your amiable wife, Professor M.O. Adebiyi.

To my darling wife, Mrs. Faith Nneka Adebiyi – a pillar of support par excellence whose prayers have lifted me to rise and keep running to achieve my set goals, whose sacrifice form the ladder on which I stand tall. Also, to my children, Goodnews Eniola Adebiyi and Great Akolade Adebiyi, who were denied my presence while this academic journey lasted. I appreciate your huge sacrifice. May God bless you all richly in Jesus' name. Amen.

I cannot forget Dr. AnuOluwapo Aluko, and Dr. Elutunji Buraimoh, for their support. My friend, Milan Joshi, for those lovely times we spent together in the laboratory.

I also wish to gratefully acknowledge the South Africa National Research Foundation (NRF) for the financial support extended to me.

ABSTRACT

The global energy demand is rising above the all-time average, and fossil fuel reserves, which power a large chunk of the existing power generation plants, are being depleted. Hence, Renewable Energy Technologies (RET) have become the alternative to meet demand and provide sustainable power. Solar photovoltaic (PV) energy, an essential aspect of RET, which generates emission-free power, is one of the world's emerging resources. Rooftop PV technology installation is advanced in residential and commercial applications due to government subsidies, lower investment costs, and feed-in tariffs.

The rapid penetration of PV systems into conventional distribution grids has created some power quality and power stability issues. Power quality (PQ) distortion is the most critical problem in distribution grids. The literature studied revealed that the several nonlinear loads and PV systems power electronic-based inverters that penetrate the grid and contribute to poor power quality issues, i.e., voltage rise, voltage dip, voltage unbalance, flicker, and harmonics. Also, the PV system maximum power point (MPP) controller's performance was investigated since the current-voltage (I-V) characteristic of PV panels is nonlinear and dependent on variables such as solar radiation and temperature. A comparative analysis conducted showed that the incremental conductance tracks the maximum power point better than the perturb and observe method for better power generation.

MATLAB/Simulink system model simulations were run for several case studies to analyze the maximum power point tracking (MPPT) algorithm's performance under varied solar irradiation. The results obtained suggested a course to the implementation of the proposed incremental conductance MPPT algorithm. Selected power quality problems in a grid-tied PV system were analyzed via simulations and enhanced with the application of conventional proportional-integral (PI) controlled D-STATCOM. Also, field measurement-based experiments were conducted to determine system performance in a typical grid-tied PV system. The real-life 110 kW grid-tied PV system installed at the Durban University of Technology (DUT), Steve Biko campus, was used for the fieldwork. Taken into consideration was the impact of solar radiation dynamic variation on the field study.

According to the results obtained, the 110 kW PV system's voltage quality data were within the limits of the local and internationally defined standards. The concept of D-STATCOM was implemented with an Enhanced Jaya (E-Jaya) optimization algorithm to mitigate specific power quality issues, such as voltage rise, voltage dip, voltage unbalance, and current harmonics. The precision with which the D-STATCOM reference compensation current is selected is vital to the device's performance. The synchronous reference frame theory of phase lock loop (PLL) for a three-phase system is described in this thesis. The objective was to keep the source current THD below 5% to comply with the recommended limits of the IEEE-519 Standard harmonic limits. The implemented novel E-Jaya control optimization algorithm-based D-STATCOM provided continuous and adequate voltage regulation and harmonic compensation to mitigate power quality issues in the grid-tied PV distribution system. Simulation comparative analysis results of the developed control method with Artificial Bee Colony (ABC) and Jaya optimization algorithm indicated that the developed novel E-Jaya optimization algorithm enhanced the grid-tied PV system's performance by providing superior voltage regulation and source current THD compensation significantly declined to 1.01% from 31.93%.

TABLE OF CONTENTS

LIST OF FIGURES

LIST OF TABLES

LIST OF ABBREVIATIONS

a-Si – Amorphous Silicon

c-Si – Crystalline Silicon

CdTe – Cadmium-Telluride

CIGS – Copper-Indium-Gallium-Diselenide

CVT – Constant Voltage Transformer

CPD – Custom Power Device

D-STATCOM – Distribution Static Synchronous Compensator

DR – Depletion Region

DER – Distributed Energy Resources

DSOs – Distribution system operators

DoE – Department of Energy

DUT – Durban University of Technology

DVR – Dynamic Voltage Restorer

EVS – Electric Voltage Stabilizer

GaAs – Gallium-Arsenide

GHG – Greenhouse Gas

GW – Gigawatts

IEA – International Energy Agency

IGBT – Insulated Gate Bipolar Transistor

IRP – Integrated Resource Plan

kW – Kilowatts

LPF – Low-pass Phase Filter

mc-Si – Multi-crystalline

MW – Megawatts

MoJaya – Modified Jaya

MPP – Maximum Power Point

MPPT – Maximum Power Point Tracker

PC – Personal Computer

PCC – Point of Common Coupling

PECVD – Plasma-Enhanced Chemical Vapour Deposition

PI – Proportion-Integral

PQ – Power Quality

PSO – Particle Swarm Optimization

p.u – Per Unit

PV – Photovoltaic

QNR – Quasi-neutral Region

REN – Renewable

RES – Renewable Energy Sources

RMS – Root Mean Square

RPPs – Renewable Power Plants

SAREGC – South African Renewable Energy Grid Code

sc-Si – Single-crystalline

SRF – Synchronous Reference Frame

STATCOM – Static Synchronous Compensator

SVC – Static Var Compensator

THD – Total Harmonic Distortion

TW – Terawatts

µc-Si – Microcrystalline Silicon

VRT – Voltage Ride-Through

VSD – Variable Speed Drive

VSI – Voltage Source Inverter

VSC – Voltage Source Converter

VUF – Voltage Unbalance Factor

CHAPTER ONE

1.1 Introduction

The global economy evolves as the world's population increases, causing energy consumption to rise quicker than ever, especially in emerging economies. Global power usage increased in the year 2018 by 2.9 percent [1]. Research has shown that there will be a 45 percent increase in demand for electricity by 2035 [2]. The current energy supply is generated primarily from nonrenewable fuel sources, i.e., natural gas, coal, and crude oil. But, these nonrenewable energy sources cannot meet the increasing call for cleaner energy.

Moreover, using nonrenewable fuel sources in electricity generation causes ecological issues such as greenhouse gas (GHG) emissions, which are toxic to the atmosphere leading to global warming. The significantly rising demand for electricity and increasing electricity prices have posed a global concern causing many countries across the Globe to push for the implementation of renewable energy sources (RES) to guarantee a safe, sustainable, ecologically friendly, and affordable power supply. Figure 1.1 presents the global growth trend of RES, which stood at 2,378 gigawatts (GW) in 2019. These resources facilitate innovative economic possibilities and provide individuals without electricity access to clean and affordable energy. It is projected that RES such as solar photovoltaic energy, wind energy, biomass energy, geothermal energy, and hydropower will supply a significant proportion of potential global electricity demand in the near future [1]. Renewable energy generation capacity had its highest annual rise in 2018, with approximately 160 GW installed globally, increasing by nearly 9 percent over 2017 [3]. The RES took the lead globally, with over 55 percent of recently installed electrical power capacity in 2019 being RES, which marked an all-time high. The International Renewable Energy Agency (IRENA) latest data indicate that solar PV, wind, and other green technologies now supply about two-quarter of the world's electricity [4], as depicted in figure 1.2. For the newly installed power plants, more RES plant capacity was provided than the total for fossil fuels and nuclear-based power plants [1].

Due to the sustainability of renewable energy-based Distributed Energy Resources (DER), the number of DER has been increasing in recent decades. In South Africa, according to the Department of Energy (DoE) 's 2019 report, the total power generation capacity from all sources stood at 51,309 megawatts (MW). Approximately 91.2 percent (46,776 MW) was generated from thermal power plants, while RES made 8.8 percent (4,533 MW) of the total electric power capacity. The updated Integrated Resource Plan (IRP) released in August 2018 estimates that 19,400 MW of renewable energy capacity will be added to the current power generation capacity by 2030 [5].

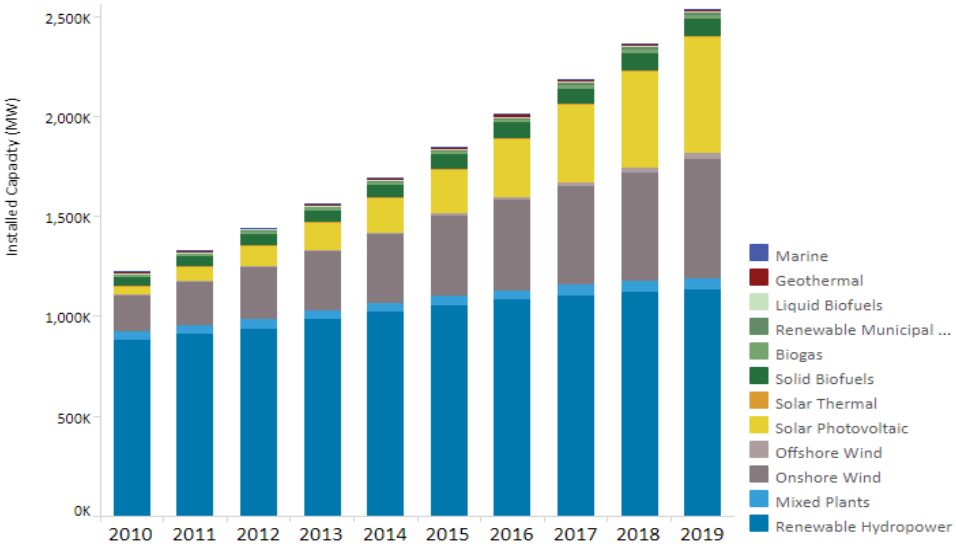

Figure 1. 1 Global installed renewable energy capacity trends [4]

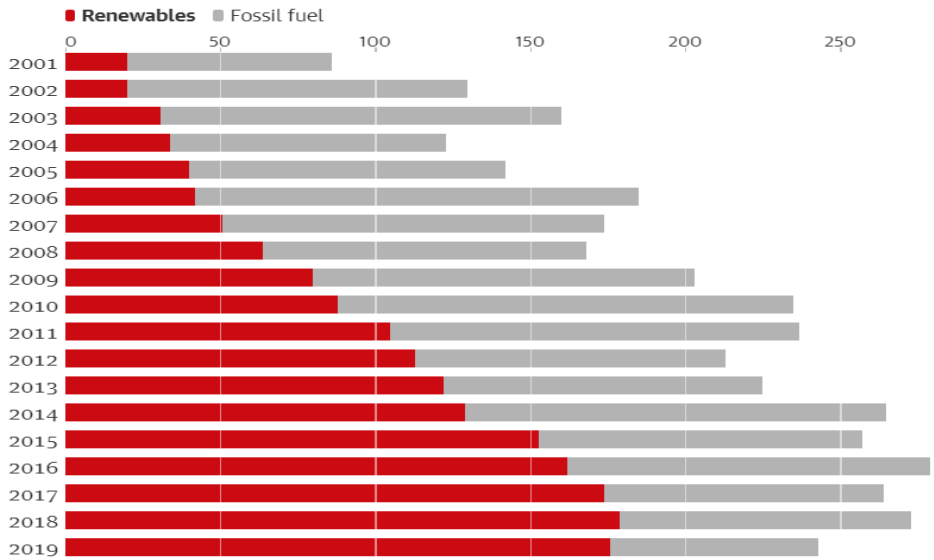

Figure 1. 2 New capacity installed each year (gigawatts) [4]

Globally, the PV system has successfully penetrated the medium and low-voltage grid; therefore, its impact on grid power distribution needs to be investigated to develop a method for its smooth integration into the grid. A detailed review of the pressing concerns that affect the distribution system resulting from a grid-tied PV system is presented in this thesis. The impact of significant power quality (PQ) concerns crucial to the power distribution system's stability, and reliability like voltage rise, voltage dip, voltage unbalance, voltage flicker, and harmonics were also methodically studied. High-level PV penetration in the low-voltage distribution grid leads to injecting substantial active power into the feeder, causing voltage rise, among other PQ issues [6-9]. A custom power device (CPD) based on reactive power compensation was developed to mitigate these problems. The distribution static compensator (D-STATCOM), a CPD, was implemented with different optimization algorithms for power quality issues compensation in a grid-tied PV system. A comparative analysis of the results obtained was conducted to validate the effectiveness of the developed optimization method.

1.2 Thesis Motivation

The data released by the International Energy Agency (IEA) in 2019 reveal that 600 million people do not have access to electricity in Africa [10] even though the earth receives approximately 86,000 terawatts (TW) in solar energy from the sun annually [11]. If this energy were effectively harnessed and converted for use, it would sustain the global energy demand. Due to the availability of high-level solar irradiation in sub-Sahara Africa, PV systems could play a crucial role in the region's energy crisis. Power consumers would engage in power generation and probably integrate their PV systems into the grid, particularly the low voltage distribution system. This thesis was motivated by the need to minimize the impact of the grid-tied PV system on power quality in the distribution system power quality and to optimize the grid performance for better power quality.

The steadily increasing PV system penetration into the South African grid has prompted the adoption of a national standard, the South African Renewable Power Plants (RPPs) Grid Code [12], which sets out PQ standards for

renewable energy sources (RES) generators. The grid code regulates power quality issues like voltage rise, voltage dip, voltage flicker, voltage unbalance, harmonic currents, and voltage harmonics. However, it became evident that there were compliance issues after the first round RPPs were installed [13, 14]. This study sought to implement a novel mitigation strategy for voltage distortion and harmonics on grid-tied PV systems.

1.3 Statement of the Problem

The PV system's increased penetration in the low voltage distribution grid has raised concerns about reactive power management for grid power quality. The IEEE 1159, IEEE 1159.2, IEEE P1564, and IEEE 519 standards [15] call for a study to control the integration of this renewable energy source due to their associated power electronic-based converters that tend to introduce harmonics into the grid. This study utilized optimized D-STATCOM to mitigate power quality issues by developing an innovative method using a soft computing approach to enhance the power quality of a grid-tied PV system for voltage stability and harmonics distortion mitigation.

1.4 Research Objectives

This research aims to study and analyze different power quality concerns caused by the integration of PV systems into the distribution network and to develop a novel optimization algorithm to mitigate them. The following are the research objectives intended to enable the integration of high-level PV systems into the distribution system.

1. Model and simulation in MATLAB/Simulink, a PV MPPT control algorithm to maximize the grid-tied PV system energy yield.

2. To investigate voltage quality performance in a real-life grid-tied PV system using field measurements from an experimental study conducted at the Durban University of Technology (DUT) 110-kW grid-tied PV system.

3. To implement a distribution static compensator (D-STATCOM) device to mitigate voltage dip impact and source current total harmonic distortion on a grid-tied PV system.

4. To propose, implement and validate a novel control optimization algorithm, Enhance Jaya (E-Jaya) optimization algorithm, for D-STATCOM to mitigate power quality issues in a grid-tied PV system.

1.5 Concept of this research

PV system, one of the leading renewable energy sources, generates environmentally friendly power. However, the power fluctuates due to the variation of solar irradiation and ambient temperature levels caused by moving clouds. If the PV system grid penetration increases, the problem can aggravate the grid power quality [16, 17]. Therefore, it is necessary to implement an efficient maximum power point tracking (MPPT) algorithm for maximum power delivery at all times, regardless of the loads and weather conditions. The MPPT regulates the PV system DC-DC converter's duty cycle to keep the system operating at the maximum power point (MPP) [18, 19]. There are quite a few MPPT algorithms in the existing literature. This research has implemented the incremental conductance (InCond) MPPT algorithm after a comparative analysis with the Perturb and Observe (P & O) MPPT algorithm indicated the former's better performance.

The introduction of power electronic-based PV inverters and loads on the grid generates harmonics, which causes voltage distortion in the distribution system [20]. Thus, the IEEE 13 bus test system, an unbalanced distribution system, was modeled and simulated in MATLAB/Simulink software to analyze the severity of a grid-tied PV system on the network PQ. Also, typical grid-tied PV systems experimental-based data were measured with the Elspec PQ analyzer and analyzed to investigate the impact of the PV system on the grid at the Point of Common Coupling. The 110 kW grid-tied PV system at the Durban University of Technology (DUT), Steve Biko campus, was utilized to evaluate different operating scenarios.

Distribution Static Synchronous Compensator (D-STATCOM), a custom power device, was designed in this study to optimize the performance of a distribution grid-tied PV system. This custom power device provides voltage regulation, harmonic mitigation, and dynamic reactive power compensation for the grid. A swarm-based intelligence algorithm and metaheuristics optimization algorithm (the Artificial Bee Colony (ABC), Jaya optimization, Enhanced Jaya (E-Jaya) optimization algorithms) was implemented for the D-STATCOM. These control techniques were implemented and compared in mitigating the power quality issues in an unbalanced distribution system with a grid-tied PV, using the IEEE 13 bus test system as a case study.

1.6 Research Methodology

This research reviewed the relevant extant literature on state-of-the-art PV technologies, related IEEE standards on modeling power systems and studied the PV inverter model to address the research objectives. This literature consists of mathematical modelling using MATLAB/Simulink. Two MPPT algorithms to track and maximize a distribution grid-tied PV system's energy yield were implemented and compared. The performance of a typical 110 kW grid-tied PV system was studied for power quality issues with field measurements obtained at the Durban University of Technology PV power plant. A systematic analysis of D-STATCOM implementation, control algorithms, and reference current control methods was studied and improved to compensate for reactive power and mitigate harmonics distortion on the distribution grid.

1.7 Research Contribution

This study should contribute a novel metaheuristics optimization approach of controlling D-STATCOM to mitigate the power quality issues on a distribution grid by proposing and implementing an Enhanced Jaya (E-Jaya) optimization algorithm optimized D-STATCOM PI-controller. The developed method independently optimizes the parameter of the current controllers of D-STATCOM to improve the power quality of the grid. This approach maintains the distribution system voltage profile at a constant magnitude. Also, it enhances voltage by compensating for reactive power during voltage dip and voltage unbalance

events on the grid. The developed E-Jaya algorithm optimized D-STATCOM achieved the following:

a) Reduce the voltage dip along the grid bus to the allowable limit of 5% of the nominal voltage value;
b) Mitigate current and voltage total harmonic distortions for optimal performance of the grid-tied PV system.
c) Provide robust support to the performance of the D-STACOM at load variation.

1.8 Thesis Outline

This thesis consists of six chapters, chapters one to six. Chapter one provides the general introduction to the study which includes the research motivation, the research concept, the methodology, research contribution, and the list of publications that the study generated. The chapter also discusses the global growth of photovoltaic technologies. Chapter two focuses on reviewing extant literature on power quality impacts of PV systems penetrated distribution grid. The chapter introduces the PV cell technology in their different generation and the four different configurations of the grid-tied PV inverter. The South Africa renewable energy grid code is reviewed alongside other international regulatory standards and current practices based on power quality requirements. Different methodologies reported for power quality issues compensation were examined to identify research gaps for this study.

Chapter three presents a detailed background theory for this research model and describes the tool used in the study to simulate the PV system's dynamic characteristics. Following that is the detailed mathematical modelling of the PV array, DC-DC converter, the MPPT algorithms, and inverter control implementation in MATLAB/Simulink. Finally, presented is the IEEE 13 bus test system model, an unbalanced distribution system for the case study, and different load models required to analyze voltage quality issues and provide appropriate harmonic analysis on an unbalanced distribution grid.

In chapter four, voltage quality concern in grid-tied PV systems is investigated and analyzed through simulation of typical system scenarios and field

measurement of a 110 kW grid-tied PV system under natural operating conditions at the Durban University of Technology, Steve Biko campus PV site. An ELSPEC power quality analyzer was connected at the point of common coupling (PCC) to measure the experimental data. This chapter addresses different power quality problems, such as voltage rise, voltage dip, voltage unbalance, and voltage flicker.

Chapter five presents the application and control of a shunt Flexible AC Transmission Systems (FACTS) device. The Distribution Static Synchronous Compensator (D-STATCOM), a custom power device (CPD). Three different control optimization methods were implemented and compared in MATLAB/Simulink for optimal control of the D-STATCOM to mitigate power quality issues in the distribution system. The comparative analysis studies the Artificial Bee Colony (ABC) optimization algorithm, Jaya optimization, and the developed novel Enhanced Jaya optimization (E-Jaya) algorithms. The designed and implemented algorithms control the current controller structure of the D-STATCOM. Based on the simulation results obtained, the developed E-Jaya provides robust compensation for reactive power and harmonic better than the ABC and Jaya optimization algorithms during grid disturbances. Chapter six presents the conclusion and recommendations drawn from the study and suggests further research areas that could be explored.

1.9 List of Publications

Journal

- ✓ A.A. Adebiyi, I. Lazarus, A.K Saha, and E.E Ojo, *"Performance Analysis of Grid-tied Photovoltaic System under Varying Weather Condition and Load,"* International Journal of Electrical and Computer Engineering 11(1), 2020, pp. 82–95.
- ✓ A.A. Adebiyi, I. Lazarus, A.K Saha, and E.E Ojo, *"An Experimental Analysis of the Impact of a Grid-tied Photovoltaic System on Harmonic Distortion."* Springer Nature, 2021.

Conference

- ✓ A.A. Adebiyi, I. Lazarus, A.K Saha, and E.E Ojo: *"Performance Analysis of PV Panels connected in various orientation under different climatic conditions,"* in Proceedings of the South Africa Solar Energy Conference (SASEC 2018), Durban, South Africa, 2018, pp. 48-53, ISBN: 978-0-7972-1765-2.
- ✓ A.A. Adebiyi, I. Lazarus, A.K Saha, and E.E Ojo: *"Investigation to Determine the Impacts of SPV Penetration on an Unbalanced Distribution Grid,"* in *Proceedings of IEEE PES/IAS PowerAfrica conference*, pp. 116-120. IEEE, 2019.
- ✓ A.A. Adebiyi, I. Lazarus, A.K Saha, and E.E Ojo: *High PV Penetration Impact on an Unbalanced Distribution Network"* in *Proceedings of IEEE PES/IAS PowerAfrica conference*, pp. 706-710. IEEE, 2019.
- ✓ A.A. Adebiyi, I. Lazarus, A.K Saha, and E.E Ojo: *"Impacts of a grid-tied photovoltaic system on distribution network power quality,"* in Proceedings of the 4th Interdisciplinary Research and Innovation Conference, Durban, South Africa, 2019.
- ✓ A.A. Adebiyi, I. Lazarus, A.K Saha, and E.E Ojo: *"An experimental analysis of the Impact of a grid-tied photovoltaic system on harmonic distortion,"* in Proceedings of the International Conference on Power Electronics and Renewable Energy System, India, 2021.

CHAPTER TWO

LITERATURE REVIEW

2.1 Introduction

This chapter presents a review of the extant literature on the need to investigate the impacts of integrating high-level PV systems on the distribution grid. This review aims to identify critical research gaps and ascertain potential methods and solutions for the proposed research objectives. The historical background of the PV cell technology and the three different PV technology generations are reviewed, and the different types of PV system inverters configurations that were studied are described. Relevant research on power quality (PQ) issues such as voltage rise, voltage dip, voltage unbalance, voltage flickers, and harmonics on distribution grids are discussed in this chapter. A grid connection code for renewable power plants, the South African Renewable Energy Grid Code (SAREGC) [21], was introduced by the National Energy Regulator of South Africa (NERSA) to regulate grid-tied renewable energy generation. With the release of this code, electricity utilities in municipalities such as eThekwini (Durban) municipality have embraced this development to facilitate the implementation of renewable energy source (RES) technologies within the city [22]. Both the local grid code and the globally defined IEC and Cigré regulations, standards, and established best practices were reviewed. These regulations provide requirements and guidelines for the PQ criteria at the Point of Common Coupling (PCC) (primarily flicker data, harmonic data, and voltage unbalance data) and provide specific specifications for appropriate PQ. The conventional method of distribution system performance enhancement and the application of custom power devices for mitigating PQ issues were also studied. The chapter ends by identifying research gaps this thesis seek to address as a contribution to the broader body of knowledge.

2.2 Photovoltaic Cell Technology

The PV cell uses a physical process that converts solar incident light into electrical power by an optic-electromagnetic effect termed the PV effect. The concept of the PV effect refers to the production of current and voltage in a material when exposed to solar incident light. This phenomenon is both chemical

and physical. Edmond Becquerel discovered it in 1839 when he first found that when subjected to light, certain materials generate current. In 1877, two Cambridge University researchers, Richard Day and William Adams released the first PV effect study [23]. Charles Fritt, an American inventor, developed the first solar cells in 1883 made from selenium wafers, which have less than 1% efficiency [24]. Chapin, Fuller, and Pearson created the first silicon PV cell at Bell Laboratory with a p-n junction as the first PV cell to convert sufficient solar energy from the sun into electric power to run electrical equipment daily. Bell Telephone Laboratories manufactured a 4% efficient silicon solar PV cell and subsequently reached an efficiency of 11%. Today, it is possible to achieve an efficiency of 20% to 46% for PV cells [25-28].

PV cell is produced basically with semiconducting materials that can absorb much solar incident light spectrum [29]. It has a p-n junction designed in a diode-like semiconductor structure, as shown in figure 2.1. When sunlight, photons, penetrates the PV cell, it provides sufficient energy to release some electrons from the n-type silicon to the p-type silicon. The potential difference between the cell's positive and negative layers operates on the electrons to generate a voltage that can be used to push current through a circuit [30].

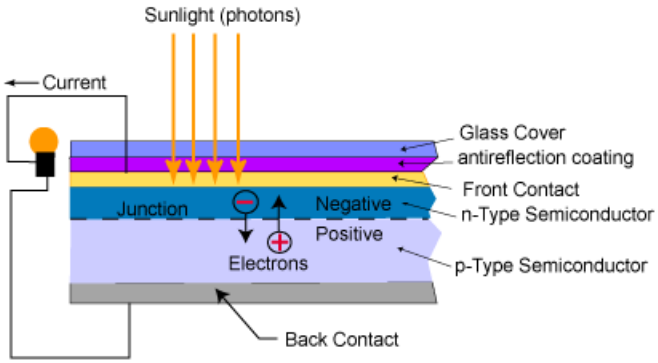

Figure 2. 1 Crystalline PV cell cross-section schematic

Today, a range of PV cell technologies is available on the market, using different material types. Much research has focused on PV cell material types, accounting for nearly 50 percent of the module cost. The three generations of PV cell technologies are reviewed in the next section.

2.2.1 First Generation

Wafer-based crystalline silicon (c-Si) technology, either single-crystalline (sc-Si) or multi-crystalline (mc-Si) technology, is the first PV cell generation invention. Single-crystalline cells are more effective than multi-crystalline cells, but they are more expensive to produce. Silicon (Si) and Gallium-Arsenide (GaAs) dominated this generation and are generally still used today as they have been validated to be technologically effective. They have achieved a significant market share, especially in remote off-grid and grid-tied PV systems installations lately. However, from the onset, there were several inherent limitations to this first-generation technology.

Silicon wafers are quite brittle, and the manufacturing process is complex, resulting in high costs [31]. However, crystalline silicon-based solar cells have a wide spectral absorption spectrum and high carrier mobility. Mono-crystalline silicon solar cells' efficiency is currently peaking at around 28 percent, while poly-crystalline cells are about 20% [32]. The external quantum efficiency of the three different types of silicon-based cells is shown in figure 2.2. The most significant difference has been in the short-wavelength region (i.e. $\lambda \leq 500$ nm), where the luminescent back-shifter needs to absorb efficiently.

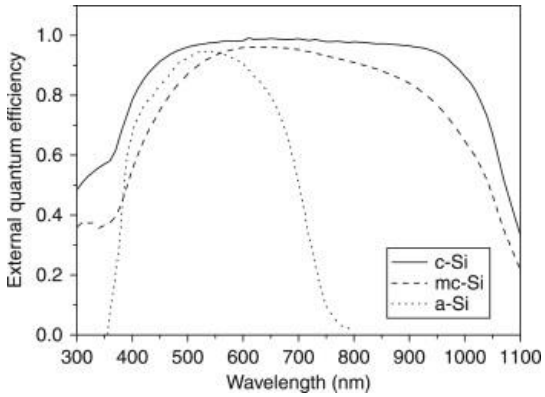

Figure 2. 2 Quantum efficiency of C-Si, mc-Si, and a-Si based solar cells [32]

2.2.2 Second Generation

Due to the high production costs of first-generation solar cells, second-generation solar cells, known as thin-film technologies, were developed. Thin-film PV solar cell technology dominates the second generation solar PV cells, and it is classified into three categories: a) Cadmium-Telluride (CdTe); b) amorphous (a-Si) and microcrystalline silicon (µc-Si); and c) Copper-Indium-Gallium-Diselenide (CIGS). This technology entails depositing a thin layer of photoactive substrate (non-crystalline silicon) using the plasma-enhanced chemical vapour deposition (PECVD) process onto a low-cost

substrate material. The thin-film PV cells are less susceptible to breaking and are not prone to most of the other manufacturing glitches common to the crystalline solar PV cells; however, their efficiency is sizably lower [33].

2.2.3 Third Generation

The third-generation solar PV cell technologies still use the second-generation method of thin-film deposition to achieve high-efficiency PV panels. The concept is to reduce peak power costs under set Standard Test Condition (STC) by implementing into the design of the cells intermediate band [34], multi-junction [35], and hot carrier [36] to make the PV cell structure formidable by preventing voltage drop. Almost all of these theoretical high-efficiency third-generation concepts are still in the proof-of-concept stage, except for the efficient multi-junction-based panels. The III-V multi-junction concentrator cells with a record 44 percent efficiency are already available commercially [37]. The possible efficiency and cost of all three solar PV cell generation are presented in figure 2.3 below.

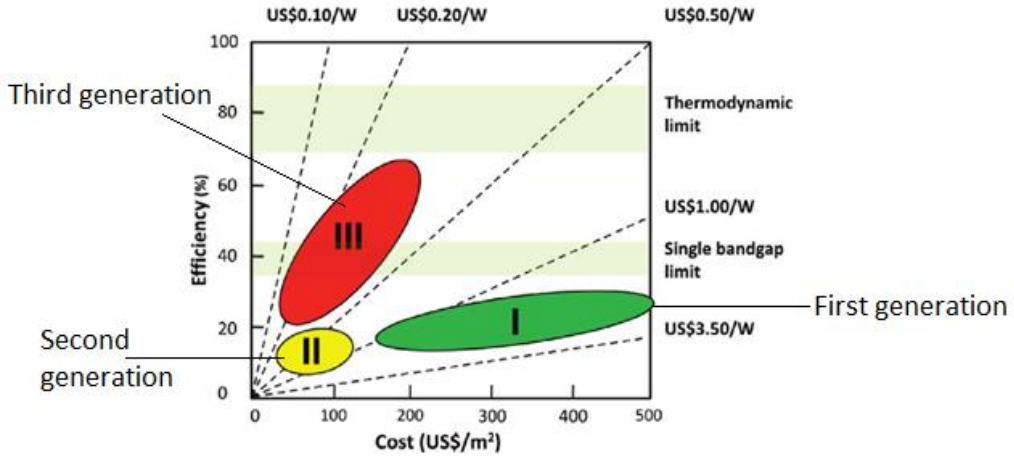

Figure 2. 3 Efficiency and cost of PV technologies generations [23]

2.3 Topology of solar photovoltaic systems

Solar PV systems are classified into two categories: a) off-grid (standalone); and b) grid-tied systems, as presented in figure 2.4, based on their functionality and operational requirements.

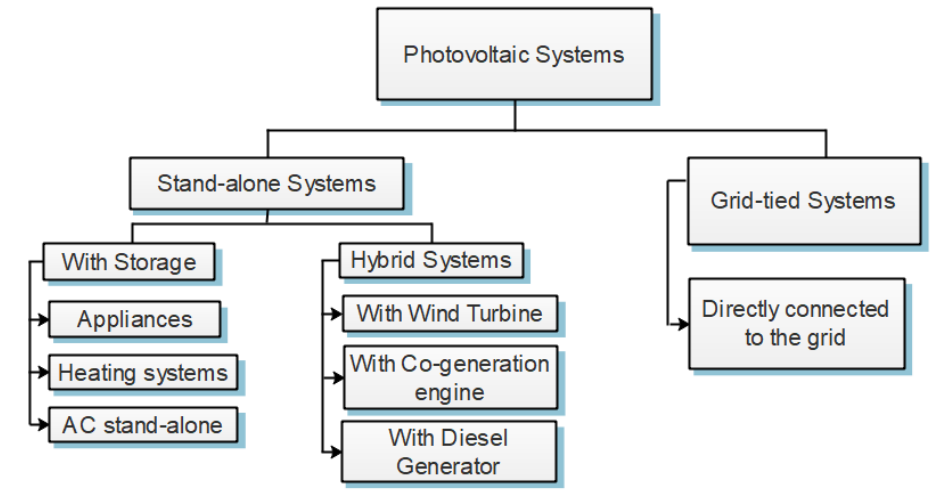

Figure 2. 4 PV technology category

2.3.1 Off-grid (Standalone) System

An off-grid PV system typically supplies power to isolated areas where there is no utility power. This system is suitable for cottages and remote home locations where grid connections are not available or for individuals who desire greater energy independence. For backup purposes, the off-grid system is usually connected to a fossil-fuelled generator, with an array of PV panels strung together; the DC output flows to the inverter via a controller, as presented in figure 2.5. The PV array DC output power is regulated by the controller to the batteries, and the inverter converts it to AC power, which is used by loads like lightings and appliances. The generator is used for powering the loads and charging the batteries during times of no sunlight. Likewise, a wind turbine may be connected to the system; this configuration is called a hybrid system when wind turbines and solar power systems are integrated.

Figure 2. 5 Illustration of an off-grid PV system

2.3.2 Grid-tied PV System

As presented in figure 2.6, grid-tied PV systems are generally installed to improve the voltage profile and enhance the distribution system's performance. The PV systems provide power at the distribution system's load side, reducing feeder active power loading, thus enhancing voltage profile. The DC/AC inverter is an integral part of the system; it converts PV array DC output power to grid AC power. A high-quality sinusoidal current waveform is fed into the grid and is synchronized to the grid voltage. This section discusses the different inverter configurations: centralized inverter [38, 39], string inverter [38], multi-string inverter [40, 41], and module integrated inverter [42, 43].

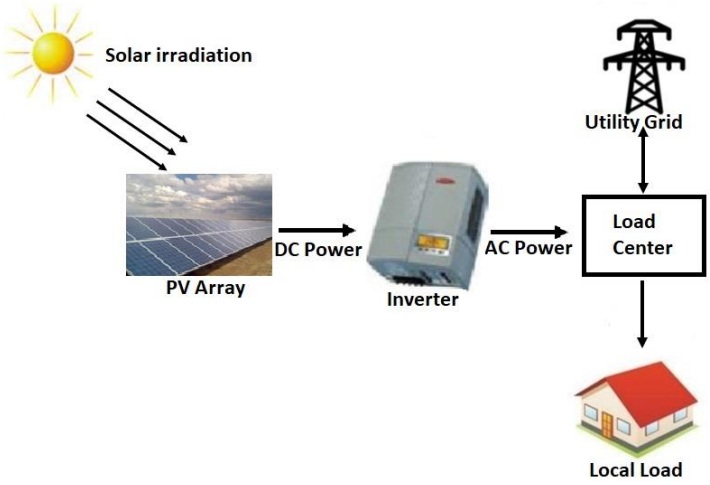

Figure 2. 6 Grid-tied PV system

2.3.2.1 Centralized Inverter

As illustrated in figure 2.7, this inverter topology is generally used for large PV systems with a high power output of up to several megawatts. In a centralized inverter topology, a single inverter is connected to the PV array. The main advantage of the centralized topology is its low cost and the ease of maintenance of the inverter as opposed to other inverter configurations. However, this topology has low reliability as the inverter's failure causes the PV system not to operate. Moreover, there is significant power loss in the mismatch cases between the PV panels and partial shading due to one MPPT controller for tracking the maximum power point [44].

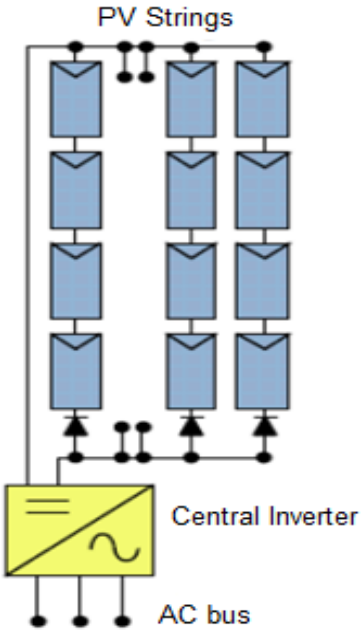

Figure 2. 7 Grid-tied PV system centralized inverter topology [45]

2.3.2.2 String Inverter

As shown in figure 2.8, the string inverter is a simpler version of the centralized inverter. Here an inverter is attached to every single string of PV panels [46, 47]. This configuration was developed to improve on the disadvantages of central inverters.

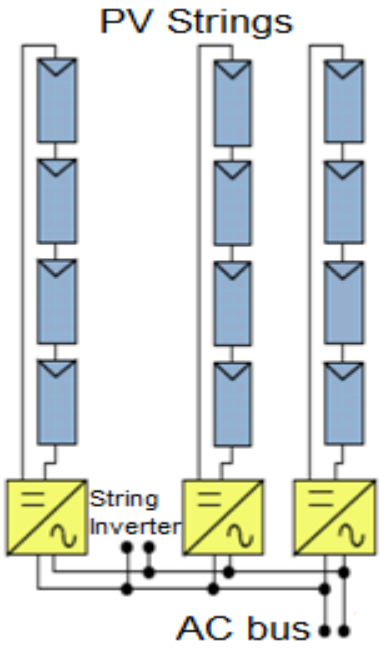

Figure 2. 8 Grid-tied PV system string inverter topology [45]

In this topology, unlike the case with centralized inverters, the PV strings are linked to different inverters; therefore, this topology configuration keeps the

voltage level before the inverter is boosted. String diodes are avoided in this inverter configuration since each string has its inverter, reducing system mismatch losses. The system's reliability is also improved as this configuration allows an individual maximum power point tracker (MPPT) for each string, and the overall efficiency increases compared to the centralized inverter topology. This type of PV system inverter was installed for this research fieldwork experiment.

2.3.2.3 Multi-String Inverter

In the multi-string inverter topology, each string is connected to a DC-DC converter to track the maximum power point (MPP) and boost the array voltage, as presented in figure 2.9. All the DC-DC converters are connected to a single inverter through a DC bus. This topology combines the advantages of centralized and string topologies. It increases the power output due to separate MPP tracking while using a central inverter, which reduces cost [46].

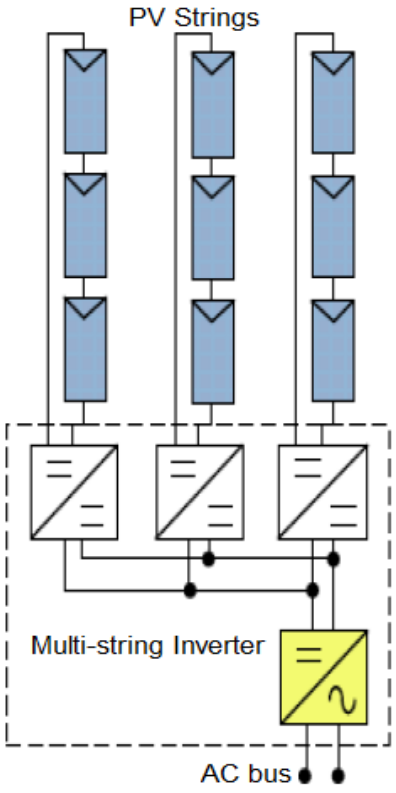

Figure 2. 9 Grid-tied PV system multi-string inverter topology [45]

2.3.2.4 Module Integrated Inverter

Module integrated inverter topology [48, 49] is the most recent PV inverter configuration. Each PV string is connected to the grid via an inverter, as shown in figure 2.10. In this configuration, the mismatch losses between the PV panels are eliminated. It has many advantages, such as reduced power losses due to partial shading and better monitoring for maintenance during string failure.

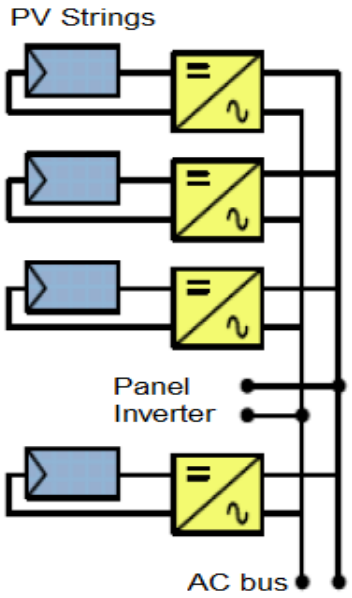

Figure 2. 10 Grid-tied PV system module integrated inverter topology [45]

2.4 Impact of grid-tied PV system penetration

The impact of high-level penetration of PV systems is quite significant, and accurate modelling is required to identify all potential adverse effects of high-level integration of PV systems, as stated in the International Energy Agency's (IEA) 2019 Annual Report [50]. In the integration of PV systems on existing distribution grids, critical issues concerning the network's technical performance need to be determined. The basic power quality parameters required to demonstrate grid code compliance in South Africa are voltage control, voltage unbalance, voltage flicker, and harmonics (current and voltage harmonics) [13, 21]. Distribution grid collapse can be caused by voltage instability [51]. Thus, power system experts and researchers are fascinated by voltage control in modern power systems as system security, stability, and reliability depend on the grid voltage stability [52]. It is, therefore, essential to study and solve voltage issues caused by high-level penetration of the grid-tied PV system.

Research has shown that distribution grid-tied PV systems introduce intense variability into the grid at the point of common coupling (PCC) due to the system's intermittent generation nature [53-55]. Studies have been carried out in recent years to unveil the impacts of unregulated PV system penetration on the low voltage distribution grid's power quality. As noted in the International Energy Agency (IEA) 2018 annual report [56], there are three primary concerns regarding the high-level PV system's penetration on the distribution grid. The first is the voltage rise when the PV system's energy is higher than the load demand; the voltage rises above the voltage limit recommended by local and international standards. The second issue is the need for reactive power compensation to support the PV's increasing penetration into the power system. PV inverters are supposed to operate at unity power factor (PF) to maximize active power generation. However, the inverter, a power electronics device, and other utility customers' inductive loads, use up reactive power. The grid, therefore, supplies most of the reactive power causing the distribution transformer to operate at a reduced power factor value. The third major issue is the islanding operation of PV systems during the loss of power supply after a fault occurs [57].

High-level PV penetration has gained traction globally, and different studies provide essential sources of knowledge. Lately, the primary research focus in modelling PV systems has focused on steady-state models that are simpler to use during load flow studies. In [58, 59], the model presented could simulate PV systems' steady-state operation when parameters for the meteorological, PV, and power grid are provided. When juxtaposed to the actual measurements of the PV system, this model's simulation error indicated relatively low deviations at noontime and permissible error in the afternoon hours. The model is built on the principle of instant power balance and can be applied easily to a significant number of topologies. Still, it cannot perform transient analysis and harmonic studies.

The impact of weather patterns on voltage quality was examined in [60-62]; the research shows that under intermittent weather conditions, PV systems affect the distribution grid's voltage quality, particularly with high-level solar radiation and low load demand situations. Evaluation of PV system islanding operation was investigated with a PV system field data in [63] and experimental data with

computer simulation in [64]; these studies show that voltage rise is gradual in dispersed grid-tied PV systems compared to clumped PV systems.

Performance models capable of predicting the active power produced by the PV system using the temperature, solar irradiation, system efficiency, and measured performance co-efficient were studied in [65-67]. These models can not be used in transient studies because they do not consider the PV inverter dynamics [68]. Nonetheless, they were used in a distribution grid with different PV integration levels to define the steady-state voltage levels [69-71]. Also, PV systems' steady-state behaviour was characterized by recurrent neural networks in [72] and compared to the conventional component-based PV system model [72] referred to in [65].

2.5 Power Quality Concept of Grid-tied PV System

Power quality is a collection of electrical properties that enables a system or equipment to operate as designed without any critical performance failure. It measures the system's operation based on the nominal operating voltage, current, and frequency limits [73]. The IEC standard alternatively defines power quality as a "*set of parameters that describe the properties of the power delivered to the load in normal operating conditions in terms of continuity of supply and characteristics of voltage (waveform, magnitude, and frequency)* [74]. Utility operations, consumer load types, and equipment designs, among other factors, influence power quality issues. Two variables, namely "*continuity*" of supply and "*quality*" of voltage, characterize the quality of electrical power supplied as set out in IEEE Standard 1100 [75]. The use of power electronic devices in the power system is increasing, and these devices inject harmonic current into the system, causing some power quality challenges. These include voltage rise, voltage unbalance, voltage fluctuations/flickers, interruptions, voltage dip, harmonic distortions, and variations in frequency [76, 77].

2.5.1 Voltage Rise

The voltage rise is characterized by IEEE 1159 as the increase of the RMS voltage level from 1.1 p.u - 1.8 p.u of the nominal voltage, at the power frequency duration of half period to one minute [78]. It is described as a condition of short-term voltage variability and is one of the categories of power quality issues.

Voltage rise is the inverse of voltage dip. Voltage rise could be caused by sudden switching off of large load or variation in reactive power compensation, such as switching to a capacitor bank—inadequate capacity for system voltage control or regulation resulting in voltage rise as presented in figure 2.11. Usually, voltage rise causes damage to lightings, electronic loads, electric motors and often causes equipment shutdowns.

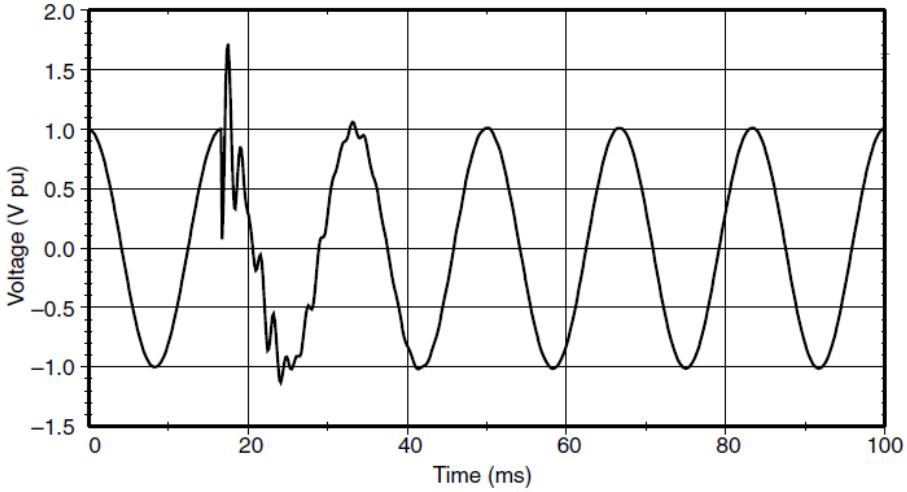

Figure 2. 11 Typical voltage rise waveform [79]

Conventionally, distribution systems are designed as unidirectional power flow systems with a single power source. During steady-state operation, current flows across line impedance and into the loads, resulting in a voltage drop along the feeder line. Different voltage regulatory devices such as on-load tap changer transformers (OLTC), phase voltage regulators, capacitors bank [80] are used to compensate for voltages on the distribution system; these are designed with the consideration of the primary substation. The regulators' purpose is to control the output voltage and improve the feeder voltage. But due to the penetration of PV systems, the grid is becoming a bi-directional power-flow system. Large-scale penetration of PV systems into the existing distribution system makes the local voltage levels rise significantly due to reverse power flow that is a severe technical concern. Notably, in [80, 81], it was concluded that the power injected from the PV system in the case of high-level PV generation at low load conditions harms the feeder. Usually, PV inverters are designed to produce only active power without regulating voltage; consequently, there is a significant problem in regulating voltage as a result of the negative coordination of the unidirectional regulating devices and the PV systems [82, 83]. Thus the number of unwanted

operations of the regulating equipment tends to increase due to shadowing caused by cloud movement in the case of short-term voltage variation, therefore, reducing the lifespan of the equipment. In [84], the droop-based inverter reactive power compensation (RPC) algorithm and active power curtailment (APC) methods were used to regulate the local voltage at the inverter. The study was based on low load and high-level PV system integration scenarios where the distribution system overvoltage condition arises due to reverse power flow. Consequently, active power curtailment yielded enhanced voltage control. In [70, 85, 86], voltage rise impacts have been studied on an unbalanced distribution system with PV integration about phase loading, bus layout, and unbalanced bus impedance.

2.5.2 Voltage Fluctuations

IEEE defines voltage fluctuations as a series of unsystematic voltage variations whose amplitude falls within regular voltage limits, as presented in figure 2.12. The variations' typical frequencies are below 25 Hz and range from 0.1 to 7 percent of the nominal voltage [87]. Therefore, the most critical consequence of this power quality issue is the variation in the intensity of light of different lighting sources, usually called flicker. Flicker is the experience of visual instability brought about by a lighting intensity fluctuation over time. Voltage flicker and voltage fluctuation are linked as they affect voltage fluctuation on light intensity due to the rapid variation of power demand by large loads. The unstable nature and limited predictability of solar irradiation are notable concerns that could cause voltage fluctuation with PV systems generation [88, 89]. Listed in the existing literature are various methods of measuring voltage fluctuation; according to the [90] [91], the most significant are the short-term (P_{ST}) and long-term (P_{LT}) flicker severity index and maximum and the minimum phase RMS voltage values.

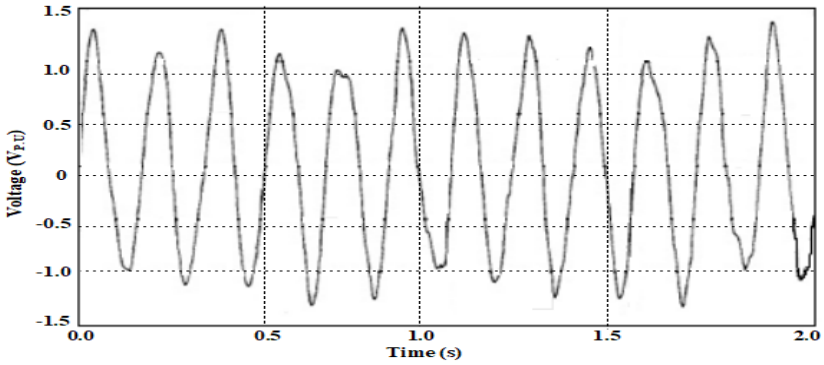

Figure 2. 12 Instantaneous voltage rise [79]

VAr control method for voltage fluctuation mitigation was studied in [92]. The applied VAr control function method to mitigate the voltage fluctuation issue was embedded in a PV inverter utilizing Particle Swarm Optimization (PSO) to search for the optimum control function parameters and analyze simulation results on a modified 24-bus low voltage test system. The study in [93, 94] investigated the impacts of voltage fluctuation due to PV generation variation in an unbalanced distribution system. A constant variation in PV power output was considered to represent the cloud movement effect scenario. The rapid solar radiation variations caused by cloud movement led to voltage distortions at the point of common coupling [69, 95]. Voltage fluctuation minimization and reactive power compensation with static synchronous compensator (STATCOM) were developed and implemented in [96] with a two-level voltage source inverter (VSI). The STATCOM was integrated into the grid synchronization control system and the control system of the DC-link capacitor voltage regulator. Even though STATCOM provided dynamic reactive power compensation and responded to the feeder voltage fluctuations, the DC-link voltage indicated a significant voltage drop before it settled at the reference voltage, which suggests the need for a better control method. The challenge of voltage fluctuations is a crucial constraint in a distribution network with a high penetration level of PV systems. The rapid ramp on distribution systems caused by PV power generation increases the number of undesired operations of the system voltage regulating equipment. Therefore, it is essential to investigate the impact of voltage fluctuation on distribution system power quality.

2.5.3 Voltage Dip

Voltage dip is regarded as one of the critical power quality problems in the distribution system. It is also called voltage sag and has its magnitude expressed as per unit (p.u) or percentage (%) of the nominal voltage. Voltage dip in the electrical system is the sudden decrease in voltage between 10% to 90% of the nominal voltage at a point caused by a short circuit or overload current followed by a voltage recovery after a short period, from half a cycle to one minute [97, 98]. This definition implies that voltage dip is a multidimensional electromagnetic disturbance whose magnitude and duration could be defined. The IEEE classifies voltage sag into three categories based on the dip's duration, as presented in Table 2.1. Voltage dip within 0.5 seconds and 30 cycles is categorized as an instantaneous dip. Voltage sag of 30 cycles to 3 seconds is classified as momentary, while temporary voltage sag duration is within 3 seconds to 60 seconds. The voltage magnitude in these categories is usually between 10% and 90% of the nominal voltage [99].

Table 2.1 IEEE Voltage sag categorization [99]

Category	**Voltage sag duration**	**Voltage sag magnitude**
Instantaneous	0.5 seconds – 30 cycles	10% – 90%
Momentary	30 cycles – 3 seconds	10% – 90%
Temporary	3 seconds – 60 seconds	10% – 90%

Voltage dip magnitude is the residual voltage value. The voltage dip duration is when the RMS voltage remains below the level of allowed voltage variation, as illustrated in figure 2.13. Figure 2.14 shows a typical voltage dip caused by a single-line-to-ground (SLG) fault.

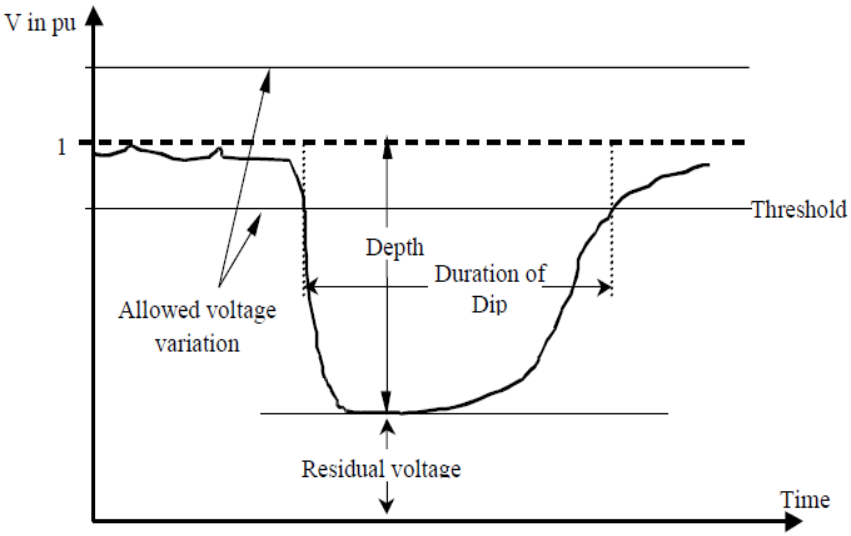

Figure 2. 13 Voltage dip and its fundamental characterization [79]

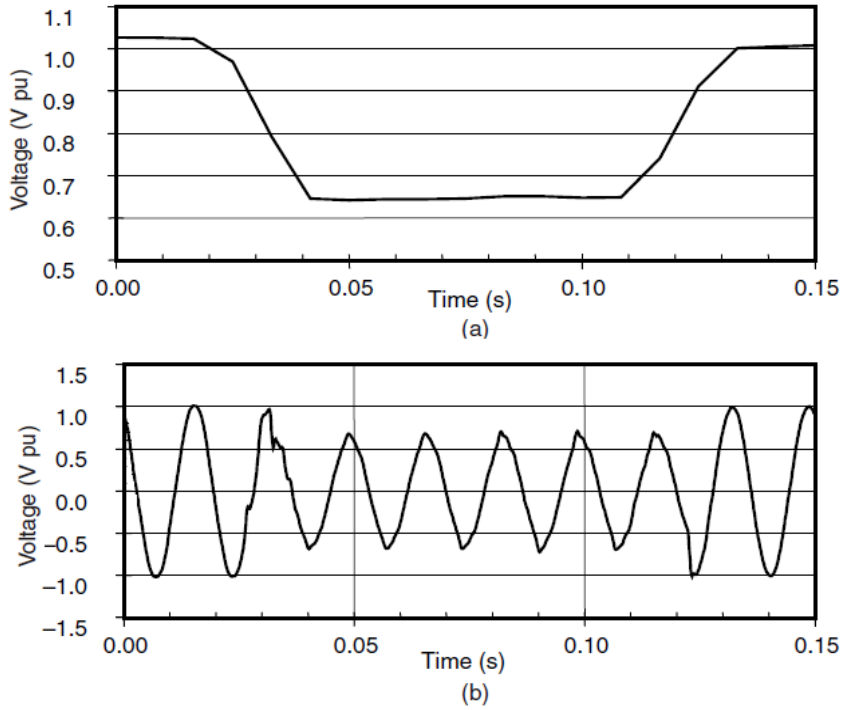

Figure 2. 14 Voltage dip caused by a fault. (a) RMS waveform for voltage dip event. (b) Voltage dip waveform [79]

Voltage dip is triggered by symmetrical and unsymmetrical three-phase faults on responsive loads that trip the breaker causing loss of supply [100]. Faults in the distribution grid isolate the PV systems from the grid [101], so, in heavily loaded phases, it causes unbalanced voltage dips. Voltage dip mitigation methods in literature have been categorized into active and passive methods. The active techniques reduce the sensitivity of the equipment and the number of faults causing the voltage dips. Several active methods for voltage dip mitigation have

been implemented, such as having underground cables instead of overhead lines; reducing the duration of faults; increasing equipment protection, using covered conductors instead of bare overhead lines; and changing the power system layout [102]. The passive methods, on the other hand, compensate for the voltage dip during the disturbance [99] by installing devices such as automatic voltage stabilizers, like constant voltage transformers (CVT), electronic step controllers, electric voltage stabilizers (EVS) [99]. Also installed custom power devices, such as Dynamic Voltage Restorer (DVR), Static Var Compensator (SVC), or a distribution static synchronous compensator (D-STATCOM), can be used to improve the fault ride-through capability of the grid [103]**.** A new D-STATCOM control technique was implemented in [104, 105], with compensation current control that integrated a proportion-integral (PI) controller with a repetitive controller to mitigate voltage dip, but with calculation complexity that deserves further study.

2.5.4 Harmonic Distortions

"Power system harmonics are defined as sinusoidal voltages and currents at frequencies that are integer multiples of the main generated (or fundamental) frequency. They constitute the major distorting components of the main voltage and load current waveforms" [106]. It implies that for a 50-Hz system, the second and third-order harmonic frequencies are 100-Hz and 150-Hz. Harmonics interfere with either the system's fundamental voltage or current, forming a non-sinusoidal wave, thereby creating waveform distortion of the power quality. The non-sinusoidal wave summarizes many sine waves with varying phase angles and magnitude; its multiple frequencies are multiples of the system frequency. The problems of harmonic distortions are rampant in distribution systems, originating from nonlinear loads, transformers, and power electronic converters on the power system. Mathematically, the harmonics components are fundamental frequency and multiple harmonic frequencies that cause overheating of dispersed nonlinear loads, conductors and equipment, malfunctioning of circuit breakers, and pulsation of torque in motors [107]. The total harmonic distortion (THD) index in figure 2.15 illustrates the overall harmonic distortion.

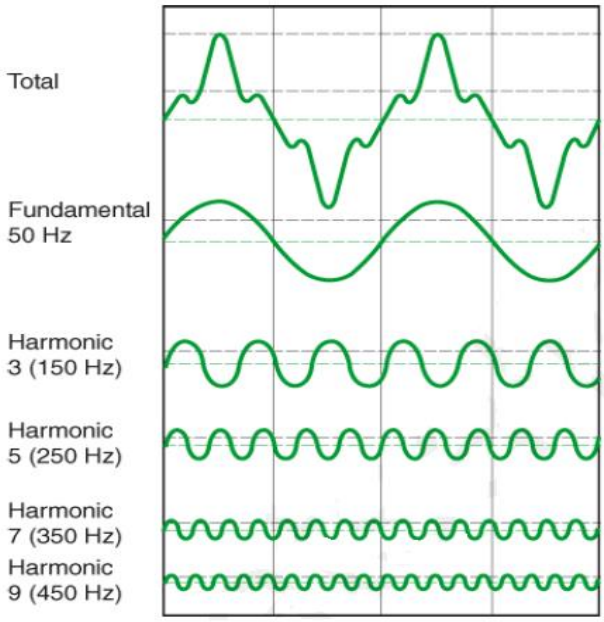

Figure 2. 15 Harmonic distortion and its components

2.5.5 Harmonic issues related to PV System

PV systems generally consist of solar panels, DC-DC boost converter, maximum power point tracking (MPPT) controller, DC-AC inverter, and LC filter grid interface [108, 109]. With the rapid developments in PV technology, a wide range of PV inverters using various control methods is commercially available on the market. The generation of harmonics from these inverters will be divergent, depending on the type of control strategy and size of the PV systems. To maintain the grid's power quality, the harmonics that are injected into the grid must follow the required specifications [110] [111]. Due to the impact of the frequent change in weather coupled with the influence of cloud movement on PV arrays, the generation of solar power becomes variable. Therefore, when the solar radiation becomes low, the PV inverter switches at high frequency, causing it to inject a distorted current into the grid [112]. A PV inverter that has a lower switching frequency also produces harmonic emissions. The consequent harmonics predictably impact the grid power quality. The generated harmonics are categorized as low-frequency, high-frequency, and inter-harmonics distortion, which are vital to ensure grid power quality [113]. Many transformerless grid-tied PV inverters have a rapid power switch with a switching range of about 5-kHz to 150-kHz. These PV inverters generate high-frequency switching signals that lead to high-frequency leakage currents that flow between the ground and the PV array [114, 115]. High-frequency harmonics cause

distortion of the grid current and issues of electromagnetic nosiness, which significantly deteriorates the grid power quality [116]. A design methodology for an LCL filter to dampen the high-frequency switching variable is implemented in [117] to minimize the permissible harmonic current emission injected into the grid. But to avoid the degradation of the grid power quality by high-frequency harmonic resonance [118], the harmonics attenuation needs to be appropriately designed. Hence to reduce the adverse effect of voltage and current harmonics distortion on power transfer efficiency and power losses, evaluating the harmonics current generated by grid-tied PV inverters for different operating conditions [112, 119].

2.6 Methods developed for enhancing grid power quality

Different methods have been developed and investigated in several research studies to optimize distribution grid power quality at the utility and end-user sides [120]. These methods could be categorized into series, parallel, and series-parallel connected line and load conditioning devices [121-123]. Different custom power devices (CPD) have been implemented in the extant literature for enhancing grid power quality issues. CPD could be connected to the line in series or parallel to the load via a voltage source converter with a pulse width modulator (PWM). The concept of CPD is based on a power electronic device designed to mitigate power quality issues caused by high-level PV system penetration on the grid's source side or load side. This section explores the literature on the main CPD, such as dynamic voltage restorer (DVR), Unified Power Quality Conditioner (UPQC), and D-STATCOM [120, 124].

2.6.1 Dynamic Voltage Restorer

Dynamic Voltage Restorer (DVR), a series-connected CPD, mitigates distribution grid voltage disturbances [125]. The device is a controllable voltage source that is connected between the load (V_L) and the point of coupling (V_S) of the system [126]. The device injects appropriate voltage and regulates load voltage magnitude in any event of voltage disturbance. Similarly, it controls the grid's active and reactive power exchange, correct power factor, and mitigates

harmonics distortions [127]. The device consists of a voltage source converter, a voltage injecting transformer, a passive filter (PF) that filters harmonic components out of the inverter switching signal to obtain a sinusoidal waveform, and an energy storage unit, as presented in figure 2.16.

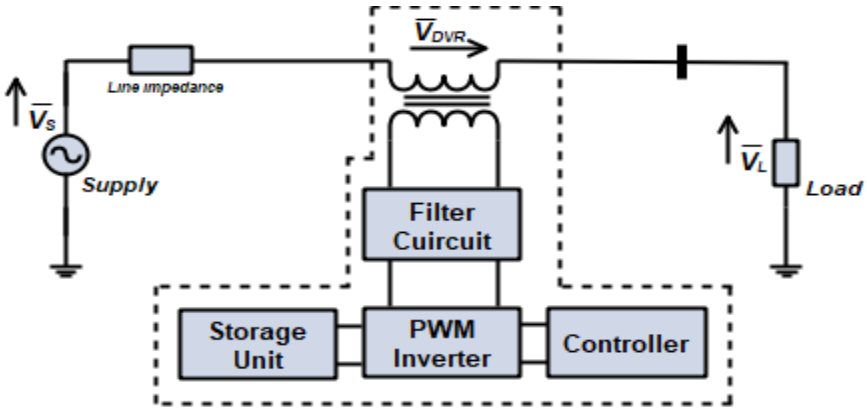

Figure 2. 16 The DVR design configuration

In [128], a DVR equipped with an enhanced control scheme to mitigate the residual fault currents on a distribution grid was proposed and implemented in PSCAD. The device was used to inject regulated three-phase voltage in series with the grid source voltage to improve voltage reliability following a voltage dip event by modifying the phase angle and voltage profile. During balanced and unbalanced conditions, the DVR provided a fault current interruption (FCI) function and compensated voltage dip [128]. A new approach in variable selection was developed in [129] to improve a PV system-based DVR control performance to mitigate power quality issues. Different scenarios were modelled in MATLAB/Simulink to compare the conventionally-tuned controller with a fuzzy logic controller (FLC)-based DVR. It is reported that the FLC tuned controller approach showed superior performance over the conventional method. A DVR multilevel transistor clamped H-bridge inverter scheme was implemented with a five-level repetitive controller to compensate voltage dip simultaneously with a voltage unbalance and harmonics in [130, 131]. The device inverter topology was observed to reduce the device complexity and cost and had a fast response in mitigating the voltage quality issues mentioned above. A dynamic voltage restorer digital State-Feedback (SF) controller was developed in [132] to enhance grid power quality. The robustness of the system was verified under changing system parameters. The controller design was compared with a cascade controller and proportional integral differential (PID) controller to show

the developed controller's ability to damp voltage quality issues under varying load conditions of linear and nonlinear loads. The cascade and PID controllers demonstrated accurate performance; but, the State-Feedback controller-based DVR was able to dampen the PQ issues properly. DVR application for harmonic distortion mitigation was reported in [133]. The issue of voltage unbalances, voltage rise, and voltage dip caused by fault current at the distribution grid downstream was mitigated by a two-pulse voltage source converter-based DVR in [134]. The application of DVR is the simplest technique to compensate for the voltage quality issues, but for long-term disturbance compensation, it requires a large energy storage unit [135]. An energy-optimization control system was proposed in [135] to improve the dc-link energy unit's performance by optimizing the dc-link energy supply or reducing the injected voltage amplitude.

2.6.2 Unified Power Quality Compensation

Unified Power Quality Compensation (UPQC), as shown in figure 2.17, is the combination of a shunt and series active power filters linked back-to-back on the DC bus via a DC-link capacitor [136]. The series UPQC side mitigates disturbances like voltage rise, voltage dip, voltage flicker, voltage unbalance, and harmonics on the supply side. Simultaneously, the shunt active power filter acts on the customer's current quality issues such as load harmonic, currents, and poor power factor. The device mitigates current harmonic distortion on the grid, provides load VAR requirement that maintains grid current and voltage in phase, and regulates at the rated value the load voltage in the event of voltage dip [137].

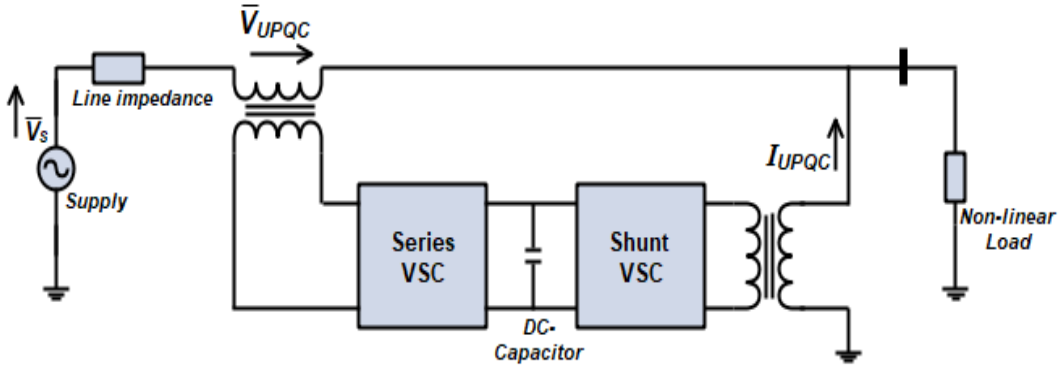

Figure 2. 17 The UPQC design configuration

2.6.3 Distribution Static Compensator

The Distribution Static Compensator (D-STATCOM) is a FACTS device that is shunt-connected at a specific feeder in a distribution network for current harmonics compensation, voltage stability, and reactive power compensation. It is a three-phase voltage source converter (VSC). The D-STATCOM consists of an inverter with a DC-link capacitor and on the AC-side, a transformer that links to the grid, an active power filter to filter the high-frequency components injected by the VSC-based Insulated Gate Bipolar Transistor (IGBT) [120, 124] [138], as shown in figure 2.18. It could be strategically controlled to compensate for the different power quality issues on a distribution network. The D-STATCOM primarily injects reactive power into the distribution grid, being a shunt-connected device [139]. Active and reactive power could be exchanged between the D-STATCOM and the distribution grid by controlling the VSC output voltage magnitude and phase angle [140]. D-STATCOM improves transient stability and damps power oscillation during a post-fault event; it could also reduce the impact of voltage flicker [141].

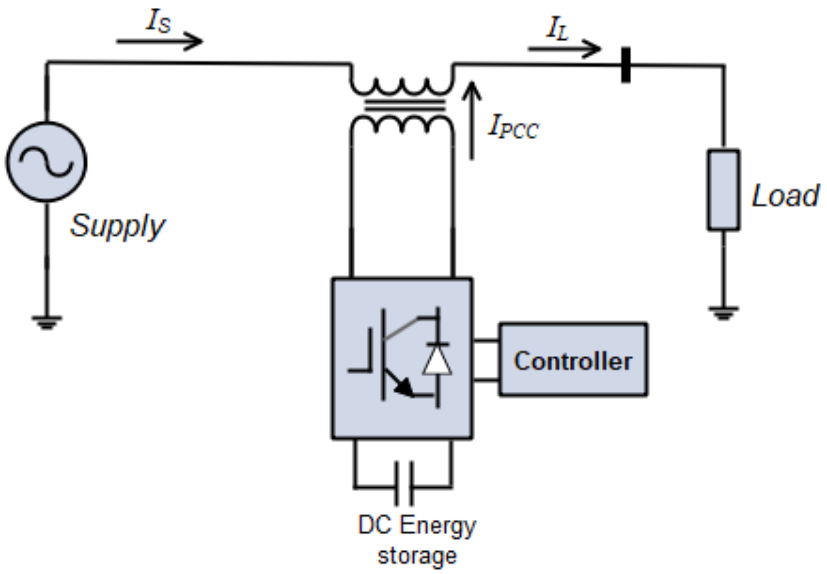

Figure 2. 18 A D-STATCOM schematic diagram

D-STATCOM has several advantages when compared to other shunt-connected FACTS devices, e.g., Static Var Compensator (SVC) [142, 143]:

- **V-I and V-Q characteristics:** The D-STATCOM provides better voltage support than Static Var Compensator (SVC), another shunt device during massive system disturbance when the voltage dips beyond the

compensator's linear operating range. D-STATCOM provides better dynamic reactive power compensation flexibility and a more comprehensive operating voltage range than a standard SVC [144]. Even at low system voltage levels, D-STATCOM could operate over its maximum output current range. Its maximum inductive or capacitive output current is not dependent on the AC system voltage. The maximum reactive power it generates or absorbs changes linearly with the AC system voltage. The ability to provide maximal compensating current at low system voltage allows the D-STATCOM to offer dynamic compensation in several applications [141]. The device operates by sensing the distribution line voltage if the voltage is above the reference voltage (V_{Ref}); D-STATCOM operates in an inductive mode. If lower, it works in the capacitive mode [145] to stabilize it, as shown in 2.19.

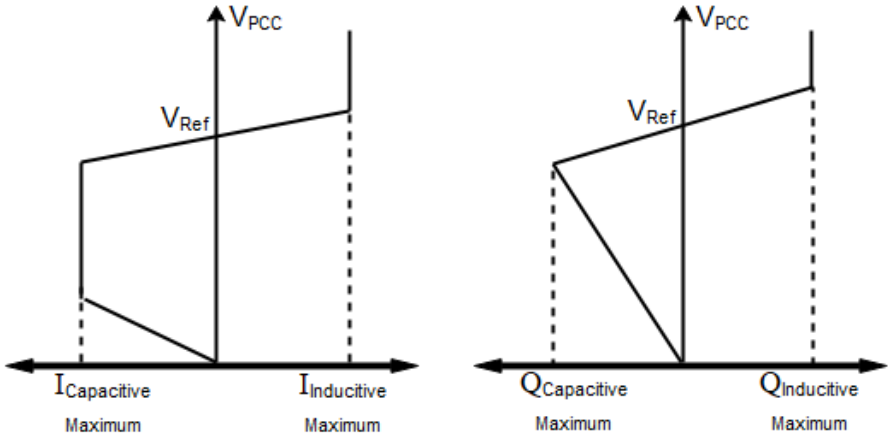

Figure 2. 19 A D-STATCOM V-I and V-Q characteristics

- **Response time:** D-STATCOM provides fast voltage support during a fault event. With its voltage source converter technology, it updates its control within a half-cycle to return the line voltage to its nominal value within a few milliseconds' response time to prevent power interruptions to the load [146].
- **Transient stability:** The issue of transient stability in today's extremely loaded power system is critical for its safe operation. The D-STATCOM's capacity to keep maximum capacitive current at low line voltage efficiently

enhances transient stability. Power is improved when D-STATCOM provides shunt compensation [141].

- **Actual size:** D-STATCOM, with its VSC technology for reactive power injection and absorption, does not have a big reactor and capacitor banks that are used in the traditional shunt compensator; thus, the device size is reduced considerably [141].

Different studies have been conducted on the application of D-STATCOM in literature. A review of the literature reveals that to determine the appropriate location to install the device, the voltage stability index of each bus of the distribution system is to be identified, and the device is connected to the bus with the highest voltage stability index value [147] [148]. A three-phase four-wire D-STATCOM was implemented in [149] for power quality improvement. The two-stage grid-tied PV system considered consisted of a DC-DC boost converter and a three-leg voltage source inverter with a star/delta transformer. The synchronous reference frame (SRF) theory was used to generate the reference current. The proposed system delivers reactive power compensation, and it reduces current harmonic distortion. It was noted from the source current spectral analysis that the total harmonic distortion (THD) was reduced; nevertheless, it did not meet the IEEE 519 standard of above five percent after compensation.

A three-phase grid-connected PV-DSTATCOM was proposed in [150] system using a leaky least mean fourth (LLMF) control algorithm. The control algorithm was implemented to extract from the load currents fundamental components to compensate harmonics, realize rapid response at changing conditions, and maintain system stability. The proposed system was modelled and simulated with MATLAB/Simulink toolbox, and an experimental prototype system was developed to verify the algorithm performance. The PV-DSTATCOM LLMF control algorithm was able to regulate the terminal voltage at PCC, achieve load balancing, and mitigate harmonic distortion. Adaptive neuro-fuzzy inference system least-mean-square (ANFIS-LMS)-based control algorithm for typical operation of a three-phase D-STATCOM was proposed in [151] to mitigate current-related power quality issues. The control algorithm based on ANFIS-LMS was implemented to calculate the reference supply current, which extracts

fundamental active and reactive power components from a non-sinusoidal load current. The proposed D-STATCOM control algorithm was verified experimentally with a shunt compensator laboratory prototype to provide voltage regulation, power factor correction, and harmonics distortion compensation. The performance of the D-STATCOM with ANFIS-LMS-based control algorithm during steady-state and dynamic load conditions improved on the fixed-step LMS (FS-LMS), and variable-step LMS (VS-LMS) reported in the existing literature. The authors in [152] proposed a forward gradient learning method, the real-time recurrent learning (RTRL) control algorithm, to control a distribution static compensator (D-STATCOM). This algorithm reduces the instantaneous squared difference between the actual and calculated value at any given moment for the period of the process. The implemented D-STATCOM based on the RTRL control algorithm mitigated power quality issues like current harmonics, compensated for reactive power on the grid, and improved power factor.

A dual tree-complex wavelet transform-based control algorithm for a D-STATCOM to mitigate power quality (PQ) issues such as total harmonic distortion and phase load current unbalance in a distribution grid was developed in [153]. The algorithm split the three-phase current harmonic into different levels to extract the line frequency component to estimate the reference active power component. The D-STATCOM VSC reference current was generated by the derivative of the sensed currents from the estimated reference components. The D-STATCOM control algorithm was simulated for different load conditions. The grid current under the varying load conditions was found to have total harmonic distortion (THD) less than five percent, which is acceptable according to the IEEE-519 requirements. A multilayer Artificial Neural Networks (ANN) with Levenberg-Marquardt Backpropagation (LMBP) algorithm-based D-STATCOM was developed in [154] to mitigate voltage rise, voltage dip, and total harmonic distortion among the power quality issues caused by nonlinear loads on the grid. The (ANN-LMBP) D-STATCOM optimization algorithm was tested on the IEEE 13-bus test system. The results obtained were compared with a PI-controlled D-STATCOM; the artificial intelligent-controlled D-STATCOM provided better power quality compensation. The authors in [155] considered the optimal placement of D-STATCOM intelligently on the distribution grid by proposing the

Modified Shuffled Frog Leaping Algorithm (MSFLA). The optimization of the designed MSFLA approach implemented on an IEEE 33 bus test system was juxtaposed with the results obtained from a similar system controlled with a genetic algorithm. The simulation results showed the efficacy of the optimization approach for locating D-STATCOM for power quality issues compensation. A comparison study of PI-controlled and fuzzy logic-controlled DSTATCOM to improve the power quality and the frequency control of a distribution grid has been implemented in [156] using the SimPowerSystem toolbox. The D-STATCOM controllers' performance was evaluated under varying load conditions and during system voltage dip. The results showed that the FLC-controlled D-STATCOM delivered a better dynamic response to the system and thus enhanced the power quality and stability of the power distribution network. A three-phase D-STATCOM was designed and implemented in [157] for a grid with distorted supply voltage with an interior point optimization-based control algorithm. The proposed algorithm was used to calculate the optimal value of load susceptance and conductance to minimize the reactive power supply and maintain a predefined harmonic current distortion and total harmonic distortion (THD) limit according to international standard. This optimization method is based on the computations of its matrices that make it efficient during load variation. The proposed control method mitigated different power quality problems by providing reactive power compensation, load balancing, THD reduction, and power factor correction under linear and nonlinear loads.

A comparative study of two custom power devices, namely, Dynamic Voltage Restorer (DVR) and Distributed Static Compensator (D-STATCOM), is presented in [158]. These systems were implemented for different voltage quality concerns posed by random PV installations on a low voltage distribution grid. The shunt compensator, D-STATCOM, improved power quality on the distribution grid by compensating active and reactive power. The DVR, a series compensator, mitigated voltage fluctuations and boosted load voltage to its peak. The study found that D-STATCOM was far more capable of reducing voltage unbalance, and it enhanced voltage profile efficiently. Specific compensating features of the D-STATCOM operations on voltage rise and dip under grid disruptions were discussed in [159-161]. The D-STATCOM also

provides dynamic reactive power and harmonic compensation. A new configuration was proposed in [162] using an improved dq0 controller method to mitigate voltage unbalance, flickers during one-line to ground fault, and three-phase fault.

Jaya, a novel metaheuristic optimization method, was proposed in [163] to optimize the parameters of a PV-fed D-STATCOM proportional and integral (PI) controller and its filter parameters. The performance of this optimization tool lessens the drawbacks of other optimization algorithms with its reduced computational work to achieve global optima. To analyze the performance of this novel Jaya optimized D-STATCOM, a comparative analysis was done with a D-STATCOM optimized with Teaching Learning Based Optimization (TLBO) and Grenade Explosion Method (GEM). The D-STATCOM optimized by Jaya had a faster convergence from the results obtained than those optimized by TLBO and GEM. Also, the proposed system performance did maintain stability during load variation. Therefore, to no small extent, the Jaya-based D-STATCOM was suitable to support the grid to mitigate power quality issues. Several D-STATCOM control techniques have been presented in existing literature [144, 164-169] for the three-phase inverter topologies to compensate for reactive power and generate compensation currents to regulate voltage. All of these techniques are designed for balanced, sinusoidal, and steady-state conditions.

Nonetheless, such control techniques are inadequate in the case of an unbalanced system with nonlinear unbalanced loads. Therefore, a suitable control method should be put in place to improve the quality of power in an unbalanced system as a cost-effective solution for both PV system users and the distribution system operators (DSO). From the literature review on the application of custom power devices to mitigate power quality issues on a utility grid, this author decided to implement Artificial Bee Colony (ABC) optimization algorithm-based D-STATCOM. Jaya and Enhanced Jaya optimization algorithms a population-based meta-heuristic optimization algorithm-based D-STATCOM. The algorithm-specific and nonparametric technique builds on previous heuristic optimization methods. The proposed E-Jaya algorithm-based

D-STATCOM is run in a comparative analysis study with ABC and Jaya algorithm to validate the E-Jaya optimized grid-tied PV system's performance.

2.7 Regulatory Standards Overview

This section presents an overview of the standards regulating power quality requirements for a grid-tied PV system. Power quality study is a research area that is drawing the attention of various researchers. It encompasses any irregular current or voltage conditions that could cause economic or operational risk to grid users [73]. The modifications caused by the rapid integration of power electronic devices in the distribution system make the analysis of power quality issues very relevant. Usually, when the power supply is strong enough to withstand disruption, the traditional way of transmitting electricity from the power plant to customers does not cause severe distribution system problems. Occasionally, depending on the distance from power generating stations and the nature of loads, very few customers can encounter a local area's power quality problem. According to a U.S. report, the economic costs of power quality issues ranged from around $119 to $188 billion annually [170, 171]. As projected in Europe, power quality problems contribute to an avoidable decline in industrial output with an annual economic effect of more than €150 billion [172]. With the energy sector liberalization, power quality has become a critical issue for the future power grid. Consequently, studies on power quality would play an essential role in improving modern utilities' overall performance [173].

2.7.1 Grid Codes

South Africa has a grid code that governs the integration of Renewable Power Plants (RPPs) to the electricity transmission or distribution network [12]. The South African Renewable Energy Grid Code (SAREGC) sets out basic minimum requirements for RPPs to penetrate the country's transmission and distribution networks. The code was designed to enable the country to cope with the proliferation of power generation by the Independent Power Producer (IPP) and to maintain the grid power quality with the stability of the grid standards. SAREGC has identified five different categories of RPPs, as presented in Table 2.2. The plants are categorized as per the size and voltage level of the RPP connection. The South African Renewable Energy Grid Code specifies that all RPPs compliance testing is to be performed at the Point of Common Coupling

(PCC) and not at the generator terminals as provided by some international codes [174, 175].

Table 2.2 South Africa renewable energy grid code categories [174]

Category	Minimum Size (kW)	Maximum Size (kW)	Connection Voltage
A1	0	13.8	LV connected
A2	13.8	100	LV connected
A3	100	1 000	LV connected
B	0	20 000	MV connected
C	>20 000		MV/HV connected

The code characterized power quality issues withn voltage and current quality that need to be evaluated against defined reference parameters on the transmission and distribution system are: voltage regulation, voltage, current harmonics, voltage flicker, and voltage unbalance. Likewise, it has voltage events like voltage dip, voltage rise, voltage transients, supply interruptions, and supply frequency [12].

2.7.2 Standards for Voltage Quality

Voltage magnitude distortion is a significant constriction in a high-level PV penetrated distribution system. According to the American standard ANSI C84.1-2006 [176], the ideal operational minimum and maximum voltage limit is 95 percent and 105 percent of the nominal voltage. When juxtaposed with South Africa's similar regulation NRS 048-2:2003 [177], it specified that the three-phase (400V) and single-phase (230V) voltage limits should not exceed ±5% tolerance. The steady-state voltage limits for the 11kV network at the consumer connection points should be within ±5 percent of nominal voltage. The capacity of renewable power plants to ride-through voltage disruption caused by faults on the grid is critical to maintaining grid stability. Voltage ride-through prevents loss of power generation during fault events on the grid. Therefore, the South Africa renewable energy grid code necessitates the design of RPP to ride-through voltage dip up to 0 pu at the PCC for a maximum period of 0.15 seconds [12]. Also, in the event of system disturbance, during voltage rise or dip, the SAREGC requires the grid to be able to withstand a sudden phase shift of up to 20^{o} at the PCC without reducing the PV output or disconnecting it. Besides, Table 2.3

presents the maximum disconnection period for Category A1 and A2 grid-tied PV systems.

Table 2. 3 SAREGC maximum disconnection period for RES of category A1 and A2 [12]

Voltage range (at the PCC)	Maximum trip time (Seconds)
V < 50%	0.2
50% ≤ V ≤ 85%	2
85% ≤ V ≤ 110%	Continuous operation
110% < V < 120%	2
120% ≤ V	0.16

Figure 2.20 illustrates the SAREGC Categories A1 and A2 voltage ride-through conditions to be fulfilled at the PCC.

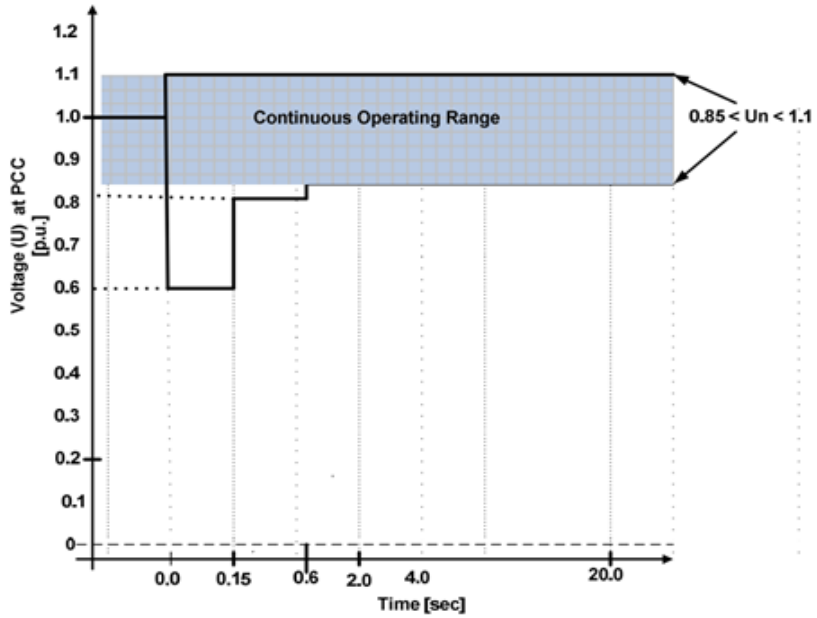

Figure 2.20 Voltage Ride Through conditions for the Category A1 and A2 [12]

This measurement for the fieldwork of this study recorded at the Durban University of Technology 110kW PV power plant falls within the SAREGC Category A3. For the categories A3, B, and C, the grid code requires the plants to be designed to ride-through voltage distortion without disconnecting from the grid when the voltage at the point of common coupling remains within the upper and lower limit curve (Area A, B, and D) illustrated in figure 2.21 [12].

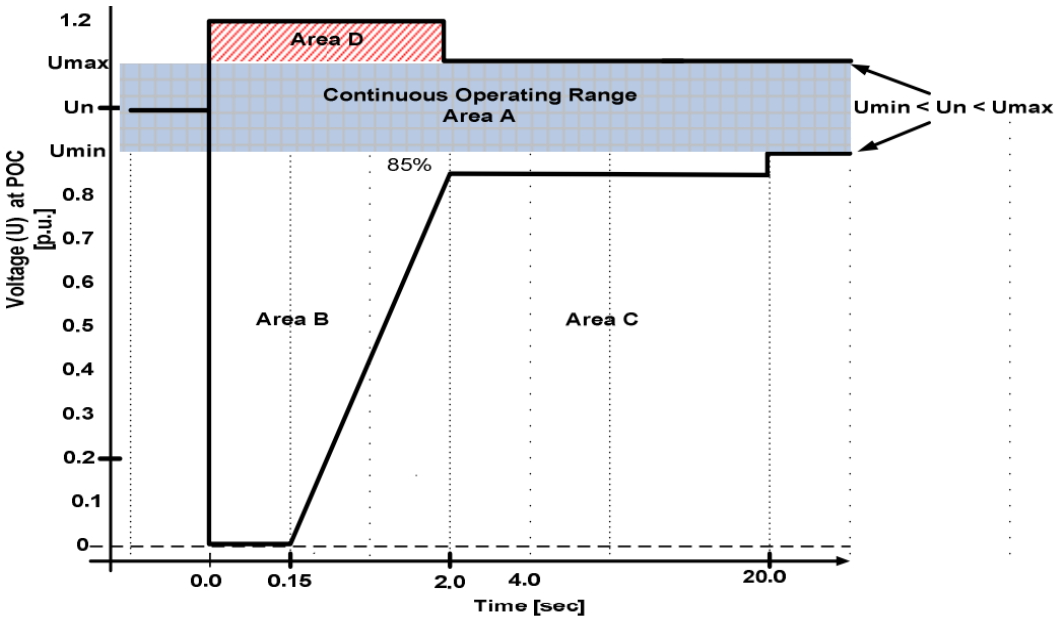

Figure 2.21 The RPPs Category A3, B, and C Voltage Ride-Through capacity [12]

Thus, the grid code requires the Category A3 RPPs to be optimized to ride-through grid voltage dip up to zero pu at the PCC at least for 0.15 seconds. It is also mandatory for Category C RPPs to ride through about 120 percent voltage rise for a minimum of 2 seconds at the PCC (see Table 2.3). If a series of sequential faults occur within Area B and advances into Area C, disconnection is permitted, as depicted in figure 2.21. The RPPs are to be able to ride-through voltage dip and voltage rise with the ability to absorb or inject reactive power, as presented in figure 2.22. Figure 2.22 illustrates the grid code requirements for reactive power control during a grid disturbance event. Area A (1.1pu ≤ V ≤ 0.9pu) is the continuous operation range at steady-state. For Area B (0.9pu ≤ V < 0.2pu), the renewable power plants remain connected to the grid. At the same time, the Category A3 PV power plants are to provide maximum voltage support by injecting a controlled level of reactive power into the grid to stabilize it and keep the RPPs connected to maintain power generation. While in Area E, where the voltage is less than 0.2pu at the PCC, PV power plants continue to inject reactive power within its design limits to help stabilize the grid voltage. Disconnection is only allowed after the requirement in figure 2.21 is met. The RPPs remain connected in Area D and provide maximum voltage support by absorbing reactive power from the grid to stabilize the voltage

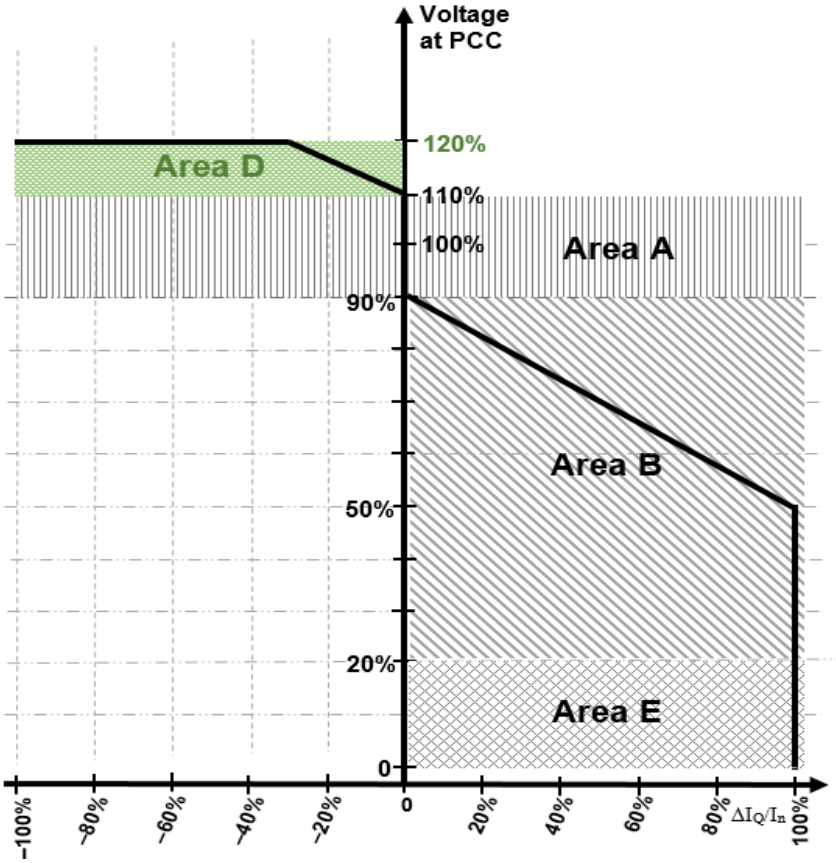

Figure 2.22 Reactive power support requirements during voltage dip or rise at the PCC [12]

The characterization of voltage unbalance (VU), and its formula is presented in [178]. Voltage unbalances in a three-phase system are expressed as a percentage in equation (2.1), an equation defined in the IEC 61000-4-30 standard [179], as the ratio of the magnitude of the negative sequence voltage component to the magnitude of the positive sequence voltage component. This occurs when the RMS voltage or phase angle values between three-phase are not equal.

$$\%VU = \frac{Magnitude\ \ of\ \ \ negative\ \ sequence\ \ voltage\ \ component}{Magnitude\ \ of\ \ \ positive\ \ sequence\ \ voltage\ \ component} x100\% \qquad (2.1)$$

$$\%VU = \frac{\max\left(\left|V_{avg} - V_a\right| \cdot \left|V_{avg} - V_b\right| \cdot \left|V_{avg} - V_c\right|\right)}{V_{avg}} x100$$

Where, $V_{avg} = \frac{(V_a + V_b + V_c)}{3}$

The major concern posed on the field is the difficulty of evaluating the sequence components when only the RMS meter is available; but, with equations (2.2), the voltage unbalance may be determined using only the phase-to-phase voltage RMS values without the angle [180].

$$\%VU = \sqrt{\frac{1-\sqrt{3-6\beta}}{1+\sqrt{3-6\beta}}}\, x100\% \tag{2.2}$$

Where, $\beta = \frac{U_{AB}^4 + U_{BC}^4 + U_{CA}^4}{\left(U_{AB}^4 + U_{BC}^4 + U^4\right)^2}$

2.7.3 Standards for Harmonic Distortion in Distribution System

The distribution grid has a lot of nonlinear loads that generate harmonics connected to it. Renewable energy sources power electronic converters, arc furnace systems, computers, transformer saturation, fluorescent lighting due to the rectifier circuit it utilizes, and variable speed drives (VSD) are just a few among these harmonic sources [181]. The IEEE Standard 519 defined harmonic as a sinusoidal component of a periodic wave having a frequency that is an integer multiple of the fundamental frequency [182]. Total harmonic distortion (THD) is a measure of the harmonic distortion present in a power system. It is defined as the ratio of the equivalent root mean square (RMS) voltage of all the harmonic frequencies (from the 2nd harmonic on) to the fundamental frequency RMS voltage.

Current and voltage harmonics in the power grid are issues of concern to researchers and grid operators alike due to their importance in analyzing power quality. Harmonics on the grid causes abnormal heating of machines and conductors, misfiring of adjustable speed drives, and pulsation of torque in electric motors. This section presents the harmonics regulations in literature and the fundamental indicators used to measure harmonics on the distribution grid.

Standard IEC 61800-3:2018 states the harmonics requirements for variable speed electrical power drive systems in a low voltage (230/400 Volt, 50 Hz) distribution grid. The set standard limits apply for equipment with rated current less than or equal to 16 Ampere, while standard IEC 61000-3-12:2018 applies to equipment with a rated current higher than 16 Ampere but less than 75

Ampere. If one or more variable speed drive systems (VSD) are used in a piece of equipment, the requirements refer to the entire equipment, not just the VSD itself. The harmonic currents and the equivalent total harmonic current are to be calculated for each order up to the 40th order. To achieve the standard calculations, the VSD is to be connected to the PCC with an initial voltage distortion of less than one percent and with a short circuit ratio of R_{SC} = 250 [183]. The IEEE Standard 1547.4-2011 [184] defines the integration criteria for distributed generation resources on the grid; the IEEE standard 519-2014 [185] concentrates on the permissible rates of harmonic distortion on the distribution system while providing a guide on the evaluation of harmonic limits on the grid, as depicted in figure 2.23. The limit for individual odd current harmonics as provided should not exceed 4 percent, up to 11th order, then 2 percent for up to 17th order, the limit for up to 23rd order should not exceed 1.5 percent and less than 0.6 percent for orders over 23rd to 35th. Also, in [185], it was indicated that the individual voltage harmonic should not exceed 5%, and all limits for the THD should not be greater than 8% to be evaluated with equations (2.3) and (2.4) with respect to the harmonic current and harmonic voltage.

$$THD_I = \frac{\sqrt{\sum_{h=2}^{\infty} I_{h\_rma}^2}}{I_{fund\_rms}} * 100\% \tag{2.3}$$

where: I_{h_rms} is the RMS current to the *hth* harmonics.

I_{fund_rms} is the RMS current of the fundamental frequency

For voltage harmonics calculation:

$$THD_V = \frac{\sqrt{\sum_{h=2}^{\infty} V_{h\_rms}^2}}{V_{fund\_rms}} * 100\% \tag{2.4}$$

where: *h* is an integer limited to 50

V_{h_rms} is the RMS voltage to the *hth* harmonics.

V_{fund_rms} is the RMS voltage of the fundamental frequency

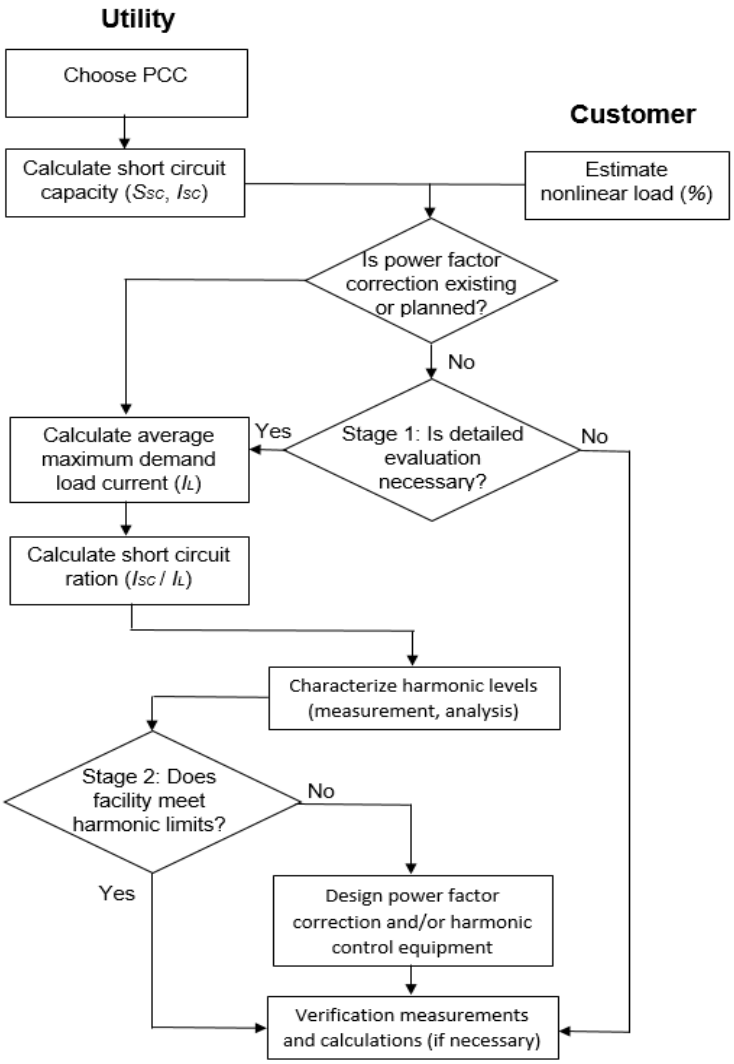

Figure 2. 23 Harmonic distortion evaluation flowchart [186]

Similarly, the South Africa standard, NRS 048-2:2003 [177], requires 8 percent of the grid's fundamental voltage as the limit for voltages harmonic and THD up to the 40th order as presented in Table 2.4.

Table 2 1 The compatibility degree for voltage harmonic [177]

Odd harmonics				**Even harmonics**	
Order h	*Magnitude (%)*	*Order H*	*Magnitude (%)*	*Order h*	*Magnitude (%)*
5	6	3	5	2	2
7	5	9	1.5	4	1
11	3.5	15	0.5	6	0.5
13	3	21	0.3	8	0.5
17≤h≤49	[2.27x(17/h)] – 0.27	21≤h≤45	0.2	10≤h≤50	[0.25x(10/h)] – 0.25

2.8 Summary

A clear overview of the problems associated with integrating PV systems on distribution systems has been reviewed in this chapter. Studies in extant literature have shown that power quality is a fundamental concern in distribution systems. It is deduced that voltage quality concerns like voltage unbalance, voltage dip/rise, voltage flicker, fluctuations, and harmonics are critical issues in LV grids caused by PV systems penetration coupled with nonlinear loads that excite resonance issues and influence system harmonics distortion. Consequently, it is crucial to analyze, model, and develop mitigation methods to minimize the impact of poor power quality on the distribution grids.

CHAPTER THREE

SYSTEM DESCRIPTION AND MODELLING

3.1 Introduction

It is crucial to create a detailed model of the PV system, the load, and the grid to investigate the impact of PV system penetration on the distribution system. The concept and detailed models of different grid-tied PV system components like MPPT algorithms, DC-DC converter, and DC-AC inverter control methods are presented in this chapter. The IEEE 13 bus test system and load modeling specifications appropriate for different power quality impact analyses in a typical scenario are discussed.

3.2. Grid-Tied PV System

The grid-tied PV system converts solar energy from solar irradiation to electricity causing significant modifications to the power system. The three categories of a PV system that integrates the grid are [187]:

- The centralized large-scale grid-tied PV system.
- The medium-scale grid-tied PV system.
- The small-scale grid-tied PV system.

The centralized large-scale grid-tied PV systems, generally 1 – 100 MW, are three-phase, connected in parallel to the grid through interfacing transformers. They are either integrated directly into the transmission system or through dedicated distribution sub-station feeders equipped with voltage and overcurrent protection schemes. The medium-scale PV systems' capacity ranges from 10 – 1000 kW, usually installed on commercial buildings. Larger units in hundreds of kW have a similar configuration to large-scale PV systems except for their transformer nominal ratings. The maximum capacity of small-scale PV systems is 10 kW, usually single-phase, integrated at the electricity consumer's residence. This category is most prevalent, as it does not require installing an interconnection transformer [8, 188]. Figure 3.1 shows a typical structure of a two-stage grid-tied PV system. It represents a generic residential rooftop PV system.

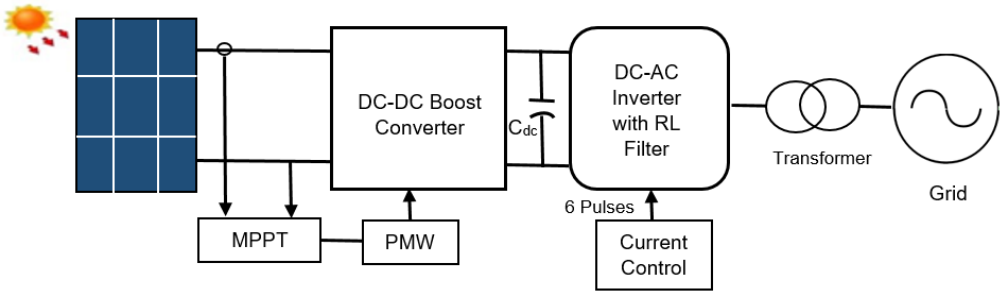

Figure 3. 1 Typical structure of a two-stage grid-tied PV system

As shown in figure 3.1, the grid-tied PV system DC-DC converter boosts the DC voltage of the PV array to an acceptable level at its output to obtain an optimal grid voltage level. The PV array current and voltage are fed into an MPPT controller, which calculates the MPP of the PV array at any point in time and optimizes the array's power output under all operating conditions; the MPPT

output controls the converter to operate the system at the MPP. The PV system penetrates the grid via a DC-AC inverter. The power electronic-based inverter controls the magnitude of the output voltage and the phase angle per the PCC reference voltage. It also controls the grid injected active and reactive power. The PV array's power output is not always constant because of the energy source variation; both solar irradiation and temperature are variable. The variation affects the DC-link voltage (V_{dc}) as the DC-link capacitor (C_{dc}) is not kept constant; it needs to discharge and charge to keep the grid-tied PV system power supply to the grid constant. However, a constant DC-link voltage must be maintained to minimize harmonics at the inverter output due to the inverter's IGBT switching by the sinusoidal PWM. Thus, a controller in a d-q synchronous frame is set up in a grid-tied PV system to regulate the DC-link voltage at an optimal level and control the PV system's injected active and reactive power to the grid.

3.3 Modelling PV Array

Generally, PV manufacturers include the electrical parameters of their PV panels like current at maximum power point (I_{mpp}), the voltage at maximum power point voltage (V_{mpp}), power at maximum power point (P_{max}), short circuit current (I_{sc}), and open-circuit voltage (V_{oc}). These parameters are typically measured under Standard Test Conditions (STCs) as depicted in figure 3.2, which assume a temperature of 25^{o}C for the panel, 1.5 air mass density, and solar irradiance of 1000 W/m^2. In addition, manufacturers also present these PV panels' current and voltage (I-V) characteristic curves. However, these parameters are insufficient because the PV panel operates in conditions different from the standard test conditions.

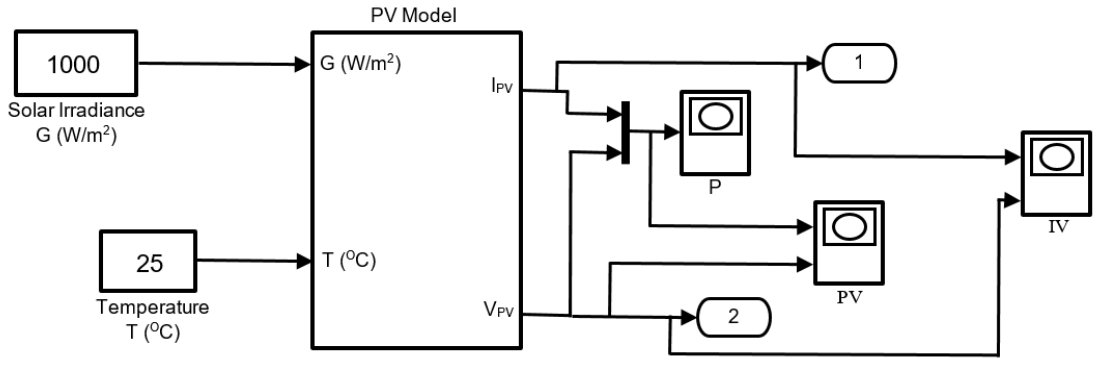

Figure 3. 2 Block diagram of the PV array model

When modelling solar PV sources, different diode models can be used to represent the solar cell, such as; single diode model [189-192], two diode model [189, 193, 194], and three diode model [195-197]. The single diode model is generally used because it provides a reasonable balance between simplicity and precision compared to the other models [189]. The two diodes model is modelled by adding a second diode parallel to the first one to reflect the effect of carrier recombination and usually setting the ideality factor to two. It also has greater accuracy that aligns with a more reliable projection of the PV system's performance. The three-diode model diodes are capable of clearly defining the various current components of the solar cells. The effect of grain boundaries and significant leakage current through the fringes is taken into consideration with it. The I-V and P-V characteristics of the PV cell are represented by nonlinear equations, which are complex to solve by conventional mathematical methods. The three different diode models are discussed in this chapter, and an accurate modeling approach was implemented for the PV array based on the two diode model.

3.3.1 Ideal Solar PV Cell

The solar cell, which is essentially a junction between P-N semiconductors, is the PV panel's major component. Figure 3.3 depicts an ideal solar PV cell characterized by a photocurrent (I_{pv}), which is generated in proportion to solar irradiation. It is the simplest PV model since no consideration is given to the impact of series and parallel resistance. The cell output current is defined by its *I–V* characteristics and expressed mathematically in equations (3.1) to (3.3).

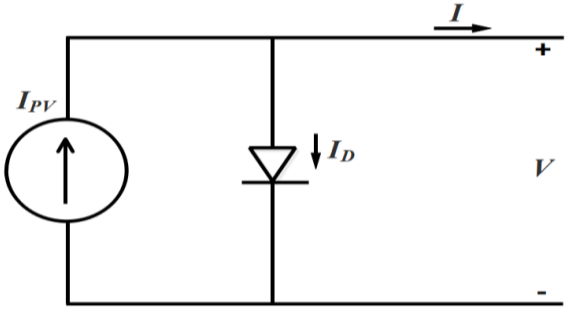

Figure 3. 3 Ideal solar PV cell configuration

$$I = I_{pv} - I_D \tag{3.1}$$

The Shockley equation derives an ideal solar PV cell:

$$I_D = I_0\left[\exp\left(\frac{qV}{akT}\right)-1\right] \tag{3.2}$$

$$I = I_{pv} - I_0\left[\exp\left(\frac{qV}{akT}\right)-1\right] \tag{3.3}$$

Equations (3.4) to (3.7) are applied to obtain the short-circuit current (I_{sc}), open-circuit voltage (V_{oc}), and the power curve of an ideal solar PV cell, as presented in figure 3.4.

$$I = I_{pv} - I_D - I_{sc} \tag{3.4}$$

$$I_{sc} = I_0\left[\exp\left(\frac{qV}{akT}\right)-1\right] \qquad \text{V=0} \tag{3.5}$$

$$V_{oc} = \frac{akT}{q} In\left[\frac{I_{pv}-1}{I_0}\right] \qquad \text{I= 0} \tag{3.6}$$

$$P = IV = \left(I_{pv} - I_0\left[\exp\left(\frac{qV}{akT}\right)-1\right]\right) \tag{3.7}$$

where:

I_{pv} = the photocurrent;

I_0 = the saturation current;

I_D =The shockley diode current

I_{sc} = the short-circuit current

V_{oc} = the open-circuit voltage

a = the diode ideality factor;

q = the electronic charge, 1.60217646 x 10^{-19} C;

k = the Boltzmann's constant,1.386503 x 10^{-23} J/K;

T = the ambient temperature, in Kelvin.

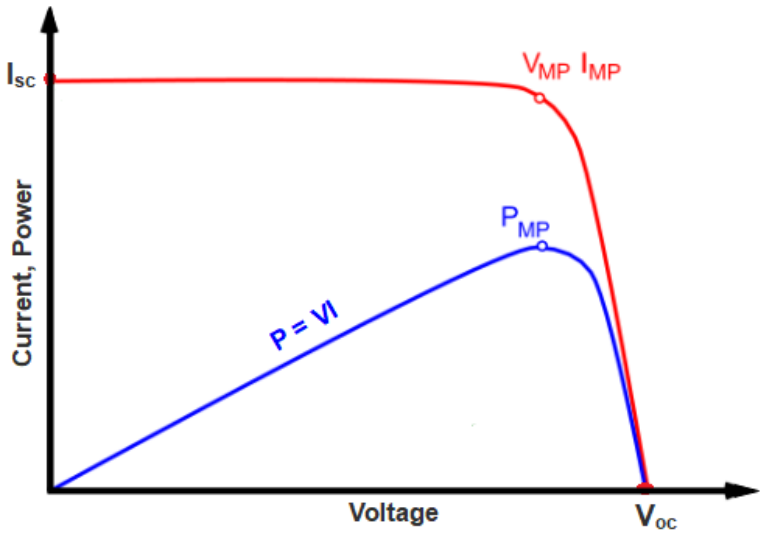

Figure 3. 4 I-V characteristic of an ideal solar PV cell

3.3.2 Single-Diode PV Cell Modeling Configuration

The ideal solar PV cell model is used only to illustrate the theory of cell modelling; usually, it is no use for simulating a working model. There are two types of single-diode PV cell model configuration, the series-resistance (R_s) and shunt-resistance (R_{sh}) single-diode model, as presented in Figures 3.5(a) and (b). These models consist of a current source parallel to a diode; the current source denotes the light-generated current, which varies proportionally with solar irradiation and temperature change. A series resistance (R_s) is integrated into the ideal PV cell model to denote the losses. The series resistance (R_s) mainly depends on the contact resistance. Likewise, a shunt resistance (R_{sh}) is connected in parallel to the diode primarily because of the p-n junction leakage current [198]. It is crucial to consider the losses due to the contact resistance and the current flow resistance in the PV cell material [199]. The relationship between the model four-parameter values (I_{pv}, I_0, R_s, and I) required for determination is expressed in equation (3.8) to (3.10).

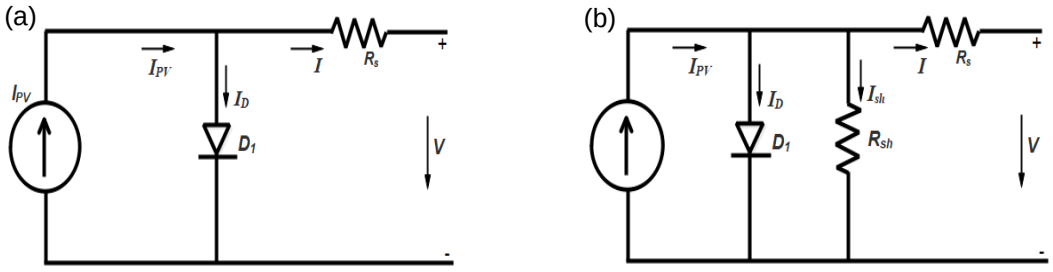

Figure 3. 5 Single diode Rs and Rsh PV cell model configuration

$$I_{pv} = \left(I_{sc} + K_I \Delta_T\right)\frac{G}{G_n} \tag{3.8}$$

Where: I_{sc} is the nominal current, K_I is the short-circuit temperature co-efficient, Δ_T change in temperature (in Kelvin), G is the actual solar irradiation per time, G_n is the nominal solar irradiation at STC.

Equation (3.9) express the reverse saturation current of a PV cell.

$$I_{rs} = \frac{I_{sc}}{\left[\exp\left(\frac{qV_{oc}}{N_s kTa}\right) - 1\right]} \tag{3.9}$$

Where: I_{sc} is the short-circuit current, q is the electron charge (1.6 x 10^{-19}C), V_{oc} is the open-circuit voltage, N_s is the number of series-connected cells. k is the Boltzmann's constant (1.3805 x 10^{-23}J/K), T is the operating temperature, a is the diode ideality factor.

The diode saturation current, I_0, is expressed in equation (3.10).

$$I_0 = \frac{I_{sc,n} + K_I \Delta_T}{\exp\left[\left(V_{oc,n} + K_V \Delta_T\right) \big/ N_s kTa\right] - 1} \tag{3.10}$$

Where $I_{sc,n,}$ and $V_{oc,n}$ is the nominal short-circuit current, and open-circuit voltage, respectively, and K_V is open circuit voltage temperature co-efficient.

$$I = I_{pv} - I_0\left[\exp\left(\frac{q\left(R_s I + V\right)}{N_s kTa}\right) - 1\right] - \frac{R_s I + V}{R_{sh}} \tag{3.11}$$

Where: I_{pv} and I_0 are the PV and diode saturation currents, $N_s kTa$ is the thermal voltage of the PV array with N_s cells connected in series, $R_{s,}$ and R_{sh} is the equivalent series and parallel resistance of the PV array, respectively [200].

3.3.3 Two Diode PV Cell Modeling Configuration

The two-diode solar PV cell model is the preferred choice in modeling and simulating the I - V and P - V characteristics of the PV array due to its superior accuracy at lower solar irradiation levels. Many analytical techniques have been suggested in the existing literature [201] to solve the two-diode model seven parameters, namely I_{PV}, I_{o1}, I_{o2}, R_p, R_s, a_1, and a_2. Still, it takes a long period to iterate them. Moreover, these techniques require additional coefficients that are

not available in the PV panel datasheet information. To make the two-diode model analytically realistic, as presented in figure 3.6, the model's seven unknown parameters, as stated in [202], are reduced to four. The parameter reduction is achieved by the assumption that $I_{o1} = I_{o2} = I_o$ and $(a_1 + a_2)/p = 1$. A simplified equation of the two-diode model based on this modification is obtained in equations (3.12) and (3.13).

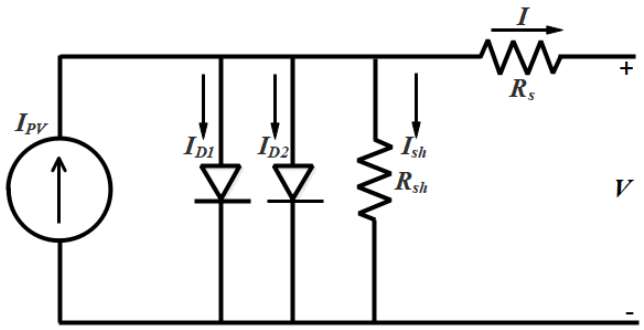

Figure 3. 6 Two diode PV cell model

$$I = I_{pv} - I_{D1} - I_{D2} - I_{sh} \tag{3.12}$$

$$I = I_{pv} - I_{o1}\left[\exp\left(\frac{q(R_s I + V)}{N_s kTa_1}\right) - 1\right] - I_{o2}\left[\exp\left(\frac{q(R_s I + V)}{N_s kTa_2}\right) - 1\right] - \frac{R_s I + V}{R_{sh}} \tag{3.13}$$

Where: I_{o1} is the saturation current for D_1,

I_{o2} is the saturation current for D_2,

a_1 *is the ideality factor for diode* D_1, *and*

a_2 *is the ideality factor for diode* D_2.

3.3.4 Three Diode PV Cell Modeling Configuration

Figure 3.7 presents the configuration of the three diode PV cell model. This model with three diodes has three currents: I_{D1}, I_{D2}, and I_{D3} [203]. The first diode provides the diode current (I_{D1}) as a result of diffusion and recombination in the quasi-neutral region (QNR) of the diode emitter. I_{D2} is the diode current due to recombination within the depletion region (DR). I_{D3} represents the diode leakage current and the defect region recombination. The semiconductor material is characterized by the series resistance (R_s), while the shunt resistance (R_{sh}) is the solar cell surface leakage current [204]. This PV cell model is more like the

two-diode model; the extra diode is added to minimize the effect of the defect region of the diode and its leakage current on the solar cell. Equation (3.14) to (3.15) presents the mathematical expression of the three-diode PV cell model's output current.

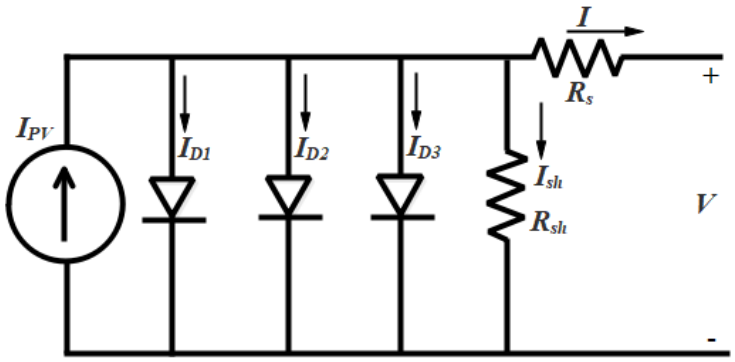

Figure 3. 7 Three diode PV cell model

$$I = I_{pv} - I_{D1} - I_{D2} - I_{D3} - I_{sh} \tag{3.14}$$

$$I = I_{pv} - I_{o1}\left[\exp\left(\frac{q(R_s I + V)}{N_s kTa_1}\right) - 1\right] - I_{o2}\left[\exp\left(\frac{q(R_s I + V)}{N_s kTa_2}\right) - 1\right] - I_{o3}\left[\exp\left(\frac{q(R_s I + V)}{N_s kTa_3}\right) - 1\right] - \frac{R_s I + V}{R_{sh}} \tag{3.15}$$

A PV panel consists of series-connected solar cells, and a PV array consists of PV panels connected in series and parallel. The single PV cell model could be sized up to represent a combination of several series (N_s) and parallel (N_p) panels, as shown in figure 3.8. It depicts a simple configuration of a PV array.

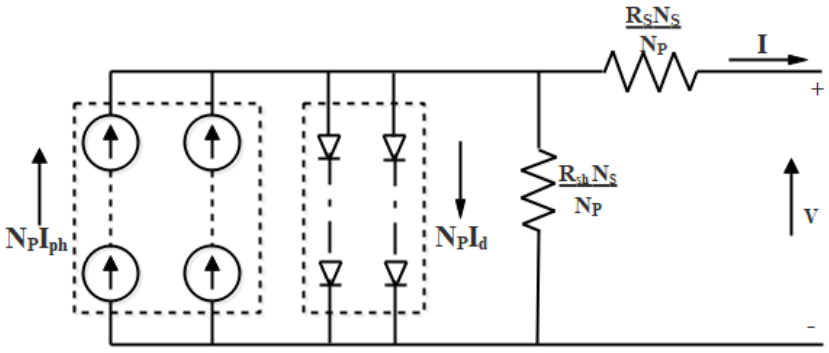

Figure 3. 8 PV array equivalent circuit

The relationship of the PV array current and its voltage characteristic is derived in equation (3.16). Notably, the power of the PV array output has a linear relationship with solar irradiation.

$$I = N_p I_{ph} - N_p I_d \left\{ \exp\left(\frac{\left[q\left(\frac{V}{N_s} + R_s I \right) \right]}{kTA} \right) - 1 \right\} - \left(\frac{\frac{N_p V}{N_s} + R_s I}{R_{sh}} \right) \tag{3.16}$$

Figures 3.9 to 3.13 depict the MATLAB/Simulink software model of the solar PV array used for simulation, based on equations (3.7) to (3.16), reflecting a typical system. A mathematical model of PV array, including essential components such as a diode, source current, series, and parallel resistors, are modeled.

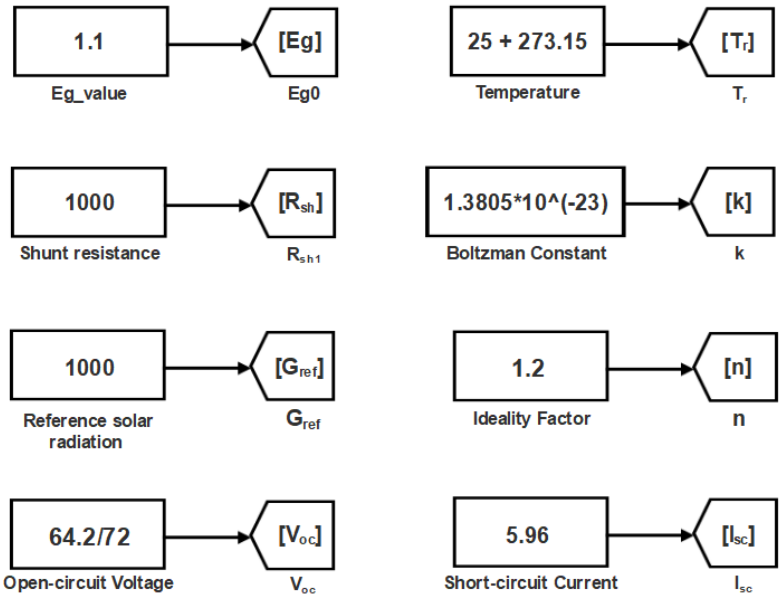

Figure 3. 9 Input parameters for PV array model simulation

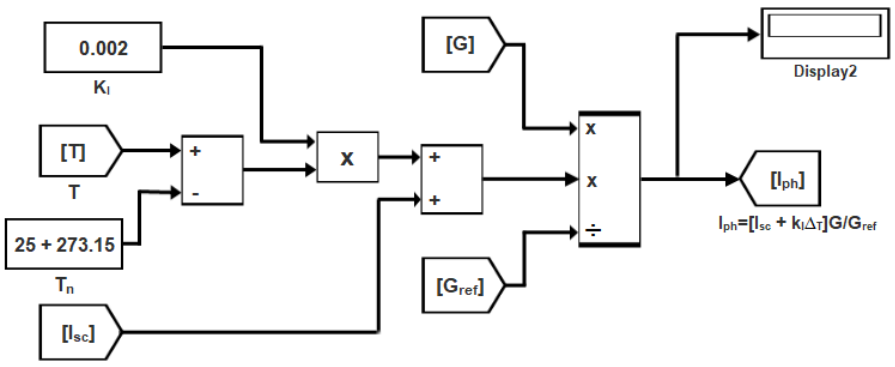

Figure 3. 10 PV array photocurrent model for equation 3.8

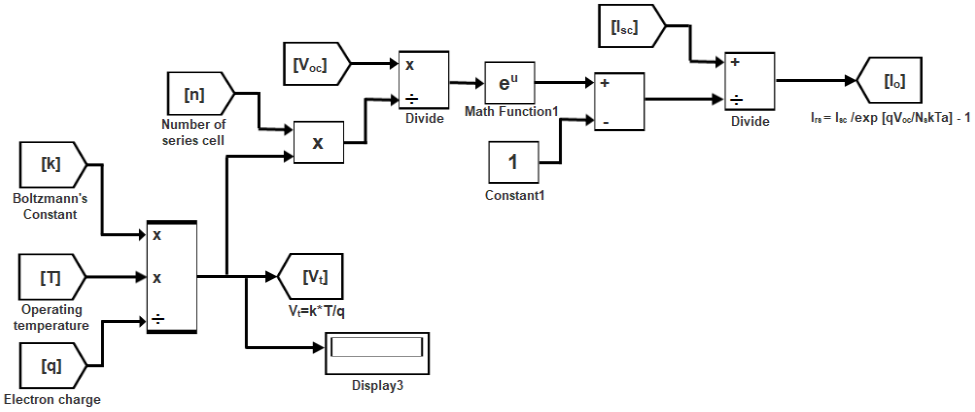

Figure 3. 11 Saturation reverse current model for equation 3.9

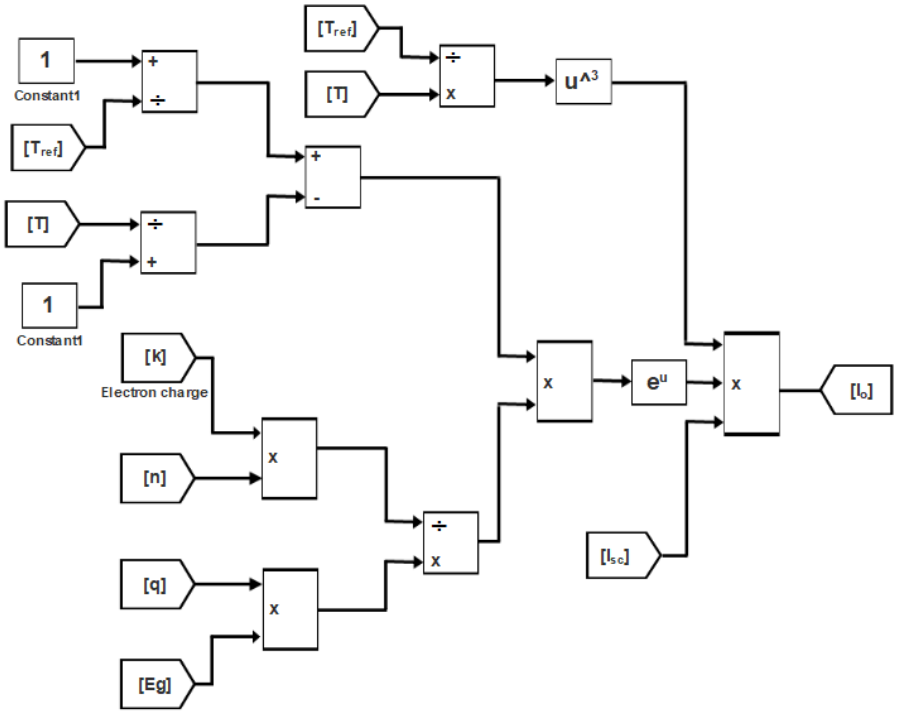

Figure 3. 12 Saturation reverse current model for equation 3.10

The mathematical expression in equation (3.16) was implemented in MATLAB/Simulink software to model a comprehensive PV array system. Figure 3.13 depicts the resultant *I* - *V* characteristics of a PV array at different solar irradiation levels from 1000W/m^2 to 250W/m^2. Similarly, in figure 3.14, the relationship between the array output power and open-circuit voltage under different levels of solar irradiation is presented. Table 3.1 provides the basic specification for each PV panel in the array.

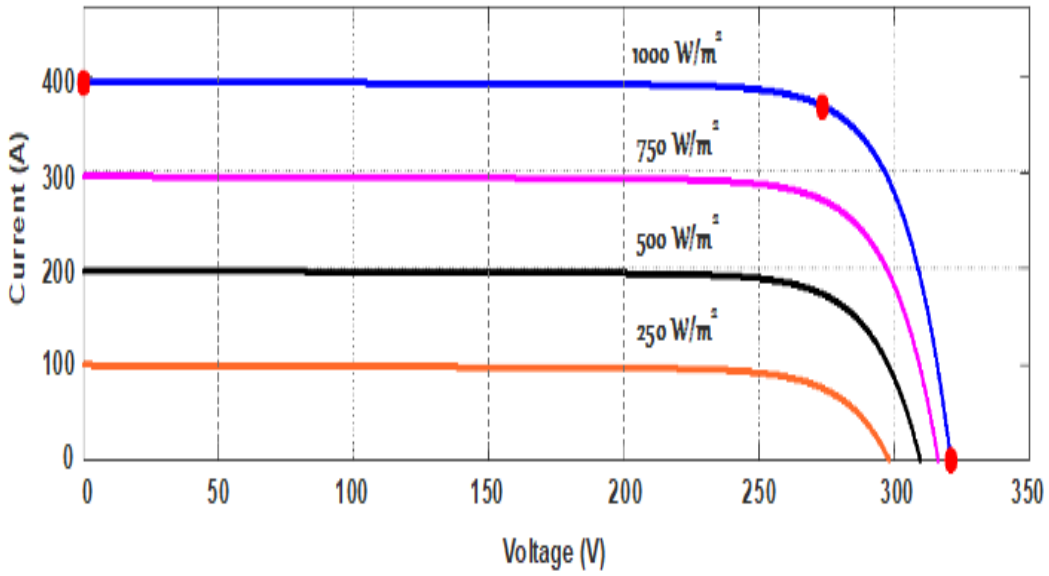

Figure 3. 13 Current-Voltage characteristics of PV array at different levels of solar irradiation

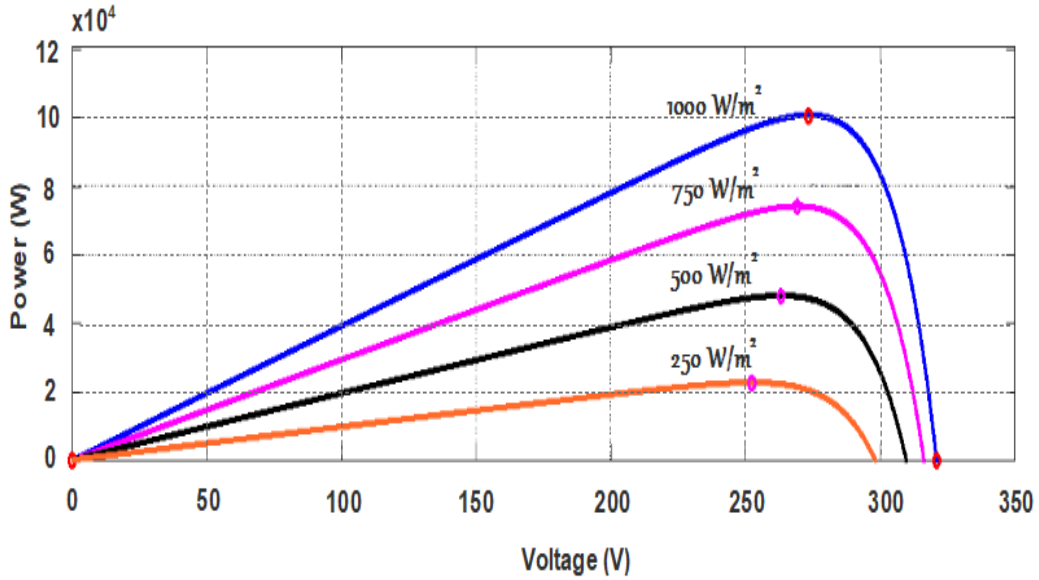

Figure 3. 14 Power-Voltage characteristics of PV array at different levels of solar irradiation

Table 3. 1 PV system specification

Description	Parameter
Module type	SunPower SPR-305-WHT
Voltage at Peak Power (V_{max})	54.7 V
Current at Peak Power (I_{max})	5.58 A
Short-Circuit Current (I_{SC})	5.96 A
Open Circuit Voltage (V_{OC})	64.2 V
Number of cell per module	96

Number of series module connect per string	6
Number of array per system	5
Maximum Power per array (P_{max})	100.6 kW
Peak Efficiency	18.7%
Power Tolerance	±5%

3.4 DC-DC Converters

In PV systems, DC-DC converters have broad applications, as buck-boost converters [205], buck converters [206], and boost converters [207, 208]. Achieving maximum power point (MPP) in the maximum power point tracking (MPPT) process is the DC-DC converter function, as it is the principal element in this regard. Without it, the MPP could not be achieved. In this study, to obtain the MPP of the system, a boost converter is used to adjust the PV array terminal voltage to a higher voltage required for the inverter. The boost converter consists of a capacitor, a diode, an IGBT switch, and an inductor. Figure 3.15 shows the DC-DC boost converter circuit diagram, and the converter mode of operation is presented in figure 3.16.

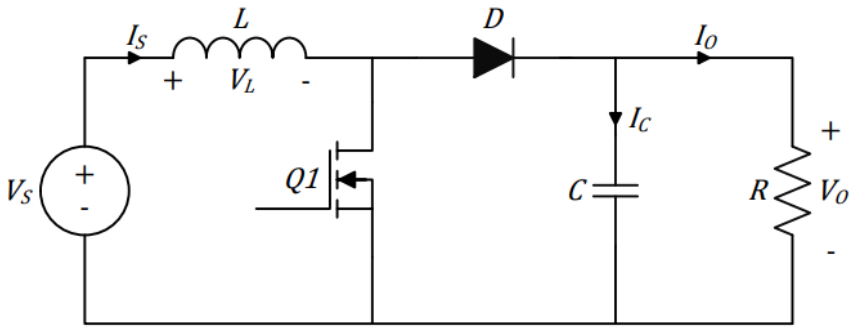

Figure 3. 15 The DC-DC boost converter circuit diagram

The operation of the boost converter is split into two cycles. The first cycle in figure 3.16 (a) starts when the switch (Q_1) turns on at t = T_{on}. Practically, no current flows in the other section of the circuit, as the diode and capacitor's combination has a higher impedance than the IGBT path. The rising input current

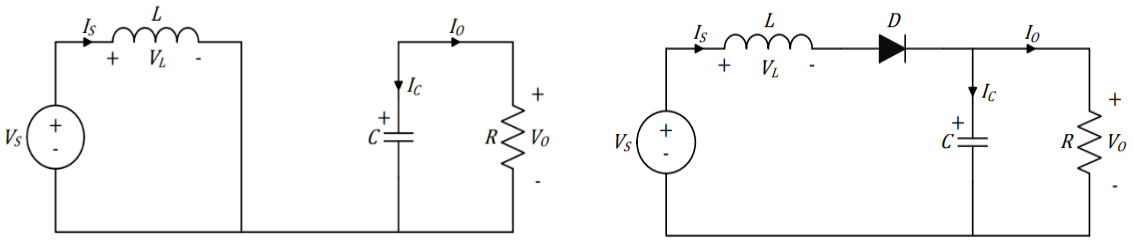

flows into the inductor (L). The energy is stored in the inductor when in this mode. Equations (3.17) and (3.18) are the voltage and current expressions across the inductor and capacitor.

(a). (b)

Figure 3. 16 The converter mode of operation (a) ON-Time (b) OFF-Time

$$V_L = V_S \tag{3.17}$$

$$I_C = \frac{-V_O}{R} \tag{3.18}$$

The current flowing through the inductor increases linearly during the ON-Time cycle. The steady-state analysis of the dc input parameters for the converter's voltage and current is expressed in equations (3.19) to (3.26).

$$V_L(t) = L\left(\frac{dI_L(t)}{dt}\right) \tag{3.19}$$

$$\left(\frac{dI_L(t)}{dt}\right) = \frac{V_L}{L} \Rightarrow \left(\frac{V_S}{L}\right) \tag{3.20}$$

$$I_L(T_{on}) - I_L(0) = \frac{1}{L}\int_0^{t_{on}} V_L(t)dt \Rightarrow \left(\frac{V_S}{L}\right) \tag{3.21}$$

Where $t_{on} = DT$

D = Duty cycle of the PWM

$$\Delta I_{L(on)} = \left(\frac{V_S}{L}\right)DT \tag{3.22}$$

The capacitor voltage is given by:

$$I_C(t) = C\left(\frac{dV_O(t)}{dt}\right) \tag{3.23}$$

$$\left(\frac{dV_O(t)}{dt}\right) = \frac{I_C}{C} \Rightarrow \left(\frac{-V_O}{R*C}\right) \tag{3.24}$$

$$V_C(T_{on}) - V_C(0) = \frac{1}{C}\int_0^{t_{on}} I_C(t)dt \Rightarrow \left(\frac{-V_O}{R*C}\right)t_{on} \tag{3.25}$$

Where $t_{on} = DT$,

D = Duty cycle of the PWM

$$\Delta V_{C(on)} = \left(\frac{I_O}{C}\right)DT \tag{3.26}$$

The second cycle starts by turning off the switch at t = T_{off}. The energy stored in the inductor causes its voltage to change polarity and sustain the current flow in the circuit; now, the output is connected to the inductor, as shown in figure 3.16 (b). The current flowing through the inductor and voltage across the capacitor is expressed in equations (3.27) to (3.36).

$$V_L = V_S - V_O \tag{3.27}$$

$$I_C = I_L \frac{-V_O}{R} \tag{3.28}$$

$$V_L(t) = L\left(\frac{dI_L(t)}{dt}\right) \tag{3.29}$$

$$\left(\frac{dI_L(t)}{dt}\right) = \frac{V_L}{L} \Rightarrow \left(\frac{V_S - V_O}{L}\right) \tag{3.30}$$

$$I_L(T) - I_L(0) = \frac{1}{L}\int_{t_{on}}^{t_{on}+t_{off}} V_L(t)dt \Rightarrow \left(\frac{V_S - V_O}{L}\right)t_{off} \tag{3.31}$$

Where $t_{off} = (1 - D)T$

D = Duty cycle of the PWM

$$\Delta I_{L(off)} = \left(\frac{V_S - V_O}{L}\right)(1 - D)T \tag{3.32}$$

The capacitor voltage is given as:

$$I_C(t) = C\left(\frac{dV_O(t)}{dt}\right) \tag{3.33}$$

$$\left(\frac{dV_O(t)}{dt}\right) = \frac{I_C}{C} \Rightarrow \left(\frac{I_L - \frac{V_O}{R}}{C}\right) \tag{3.34}$$

$$V_C(T_{off}) - V_C(0) = \frac{1}{C}\int_{t_{on}}^{t_{on}+t_{off}} I_C(t)dt \Rightarrow \left(\frac{I_L - \frac{V_O}{R}}{C}\right)t_{off} \tag{3.35}$$

Where $t_{off} = (1 - D)T$

$$\Delta V_{C(off)} = \left(\frac{I_L - I_O}{C}\right)(1-D)T \tag{3.36}$$

When the converter operates in a steady state, the inductor current's net change is zero under the inductor voltage waveform. The output voltage in terms of the input voltage and duty cycle of the boost converter can be obtained by applying the boost converter inductor volt-second balance equation for the output voltage as defined in equations (3.37) to (3.40).

$$\Delta I_{L(on)} + \Delta I_{L(off)} = 0 \tag{3.37}$$

$$\left(\frac{V_S}{L}\right)DT + \left(\frac{V_S - V_O}{L}\right)(1-D)T = 0 \tag{3.38}$$

$$\left(V_S\right)DT + V_S - V_O(1-D)T = 0 \tag{3.39}$$

$$V_O = \left(\frac{V_S}{1-D}\right) \tag{3.40}$$

Similarly, the capacitor voltage's net change is zero under the capacitor's current waveform when the converter operates in a steady-state. The output current equation in terms of input current and duty cycle for the boost converter can be obtained by applying the converter capacitor ampere-second balance equation for the output current as defined in equations (3.41) to (3.44).

$$\Delta V_{C(on)} + \Delta V_{C(off)} = 0 \tag{3.41}$$

$$\left(\frac{I_O}{C}\right)DT + \left(\frac{I_L - I_O}{C}\right)(1-D)T = 0 \tag{3.42}$$

$$\left(I_O\right)DT + \left(I_L - I_O\right)(1-D)T = 0 \tag{3.43}$$

$$I_L = \left(\frac{I_O}{1-D}\right) \tag{3.44}$$

The voltage and current output waveforms for the period of one cycle are shown in figure 3.17.

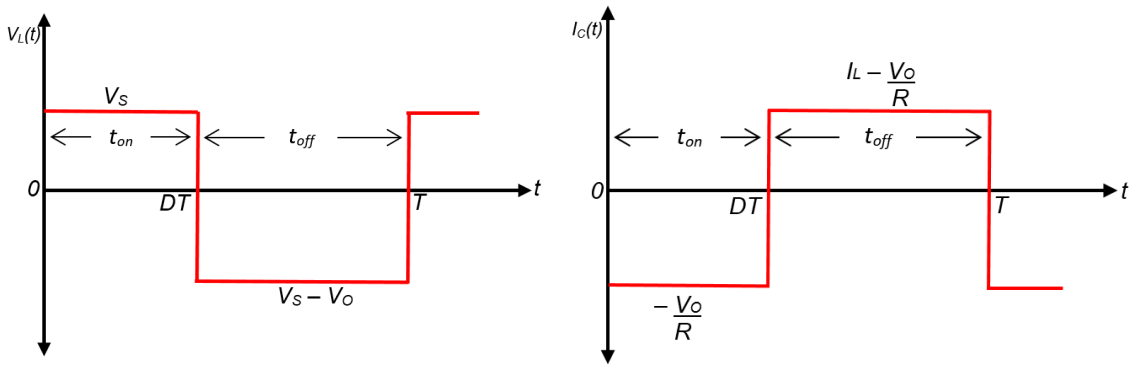

Figure 3. 17 Boost Converter inductor voltage and capacitor current waveforms

3.5 PV System Maximum Power Point Tracking Algorithms

Maximum Power Point Tracking algorithms are required to track PV systems' maximum power point since the PV array MPP varies with solar irradiation and temperature [209]. Consequently, extracting the maximum power from a solar PV array requires an MPPT control algorithm. Different methods of tracking the PV system MPP have been proposed in extant literature. These methods differ in many ways based on cost, complexity, convergence speed, ease of implementation, and tracking accuracy under varied weather conditions. In this research, the Perturb and Observe (P&O) and Incremental Conductance (InCond) algorithms were implemented and compared.

3.5.1 Perturb and Observe MPPT Algorithm

The Perturb and Observe algorithm works by perturbing the PV array terminal current or voltage and comparing the PV array's output power with its previous cycle to determine the increment or decrement to make to track the MPP. A result comparison with the prior calculation determines the shift direction to maintain the MPP. In this method, the implementation cost is lesser, and it is easier to implement without complexity. As depicted in figure 3.18, the voltage and current are measured, and the MPPT controller determines the reference voltage of the PV array. The difference between the V_{dc_ref} and V_{dc} serves as the Proportional-Integral (PI) regulator input, and the regulated voltage generates the converter's Pulse Width Modulation (PWM).

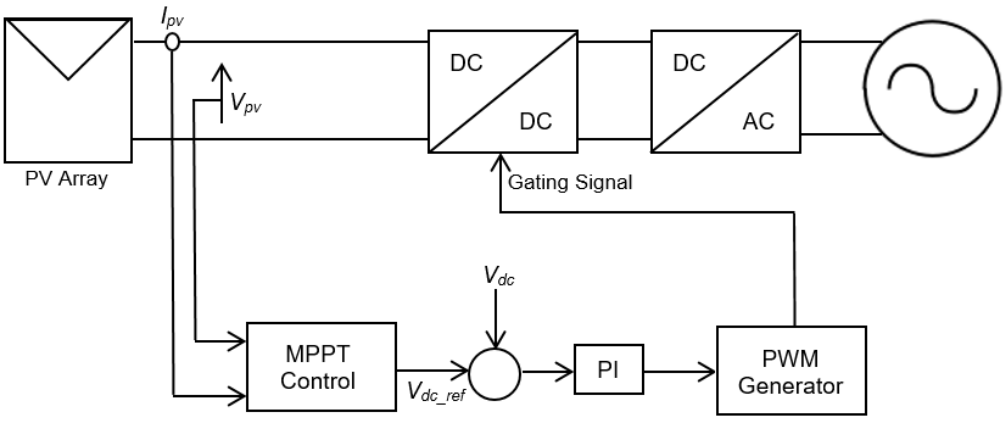

Figure 3. 18 PV system block diagrams with P & O MPPT control

Figure 3.19 presents the P & O MPPT algorithm's perturbation flow chart, and its MATLAB/Simulink model is shown in figure 3.20. The input parameter is the photovoltaic array voltage and current. The power is calculated from the two parameters, which determine the MPPT controller duty cycle value to ensure that the boost converter controls the input voltage within the limit.

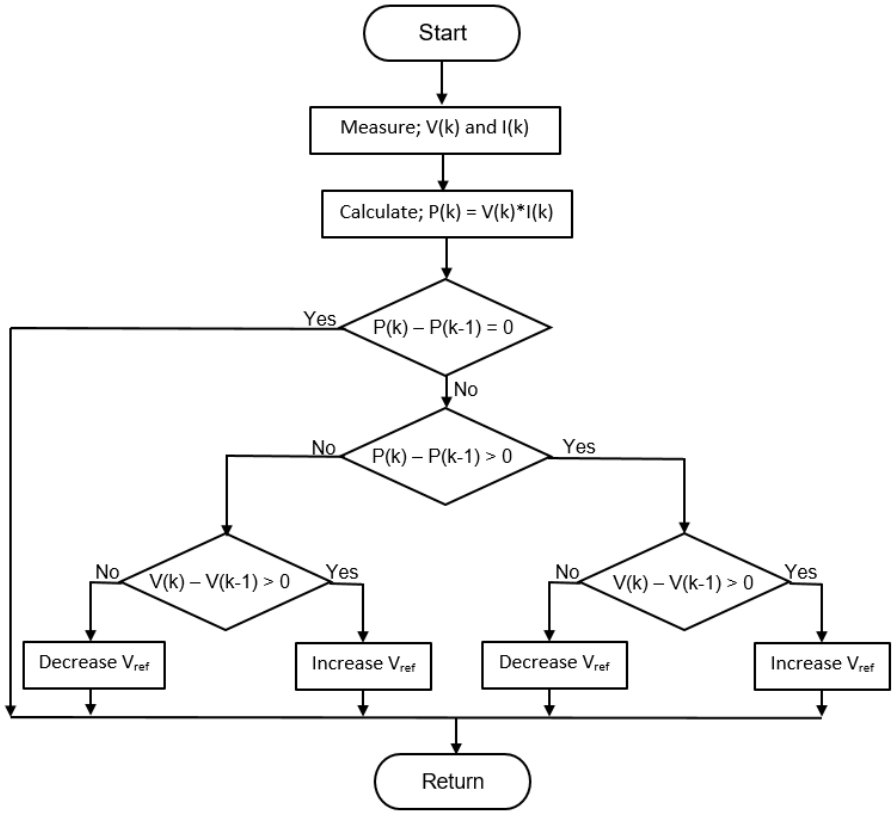

Figure 3. 19 P&O MPPT algorithm flowchart

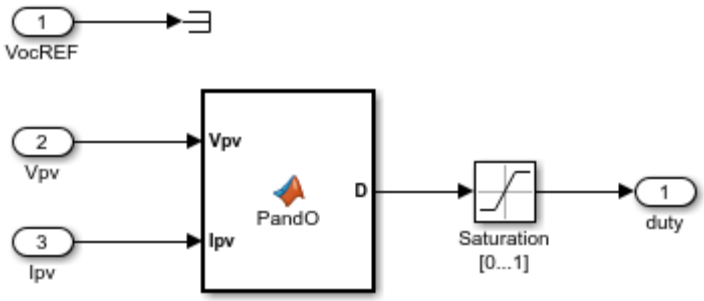

Figure 3. 20 P & O algorithm model in MATLAB/Simulink

3.5.2 Incremental Conductance MPPT Algorithm

The incremental conductance MPPT algorithm is designed to achieve MPP when the difference between the MPPT controller power against voltage is zero on the slope of the curve [210], as expressed in equations (3.45) to (3.50). The change in the PV power with a change in the voltage between two consecutive samples sampled within milliseconds is compared to determine the MPP voltage difference. The MPP is situated when the derivative of the instantaneous conductance is equal to zero.

$$\frac{\delta P}{\delta V} = \delta I * \frac{V}{\delta V} \tag{3.45}$$

$$\frac{\delta P}{\delta V} = \left(V * \frac{\delta I}{\delta V} \right) + 1 \tag{3.46}$$

$$\frac{\delta P}{\delta V} = -\frac{I}{V} \tag{3.47}$$

$$\frac{\delta P}{\delta V} > 0 \leftrightarrow \frac{\Delta I}{\Delta V} > -\frac{I}{V}, \text{ left of MPP} \tag{3.48}$$

$$\frac{\delta P}{\delta V} = 0 \leftrightarrow \frac{\Delta I}{\Delta V} = -\frac{I}{V}, \text{ at MPP} \tag{3.49}$$

$$\frac{\delta P}{\delta V} < 0 \leftrightarrow \frac{\Delta I}{\Delta V} < -\frac{I}{V}, \text{ right of MPP} \tag{3.50}$$

The equations above show the concept of the inputs of the InCond MPPT algorithm at the circuit sensor level. It indicates that in an attempt for the algorithm to track the MPP, it situates the MPP at a point by comparing the change in the instantaneous conductance (I/V) with the incremental conductance ($\Delta I/\Delta V$) till both are equal. Figure 3.21 depicts the flow chart of the

incremental conductance algorithm. The algorithm begins by measuring both the PV array data, the voltage, and the current value, and its derivative is computed; *k* and *k-1* are the present and previous time intervals. Depending on the chosen duty cycle, the process of updating the voltage and current of the PV array is attained intermittently; after that, they are compared with the previous input values. The next steps depend on the variability of the input values; the algorithm, therefore, estimates the change in voltage, current, and the difference between the instantaneous conductance compared to the incremental conductance to determine whether to increase or decrease the reference voltage (V_{ref}). The reference voltage helps keep the PV output at MPP until a change in current is detected, in which case the algorithm increases or decreases the V_{ref} to track the new MPP.

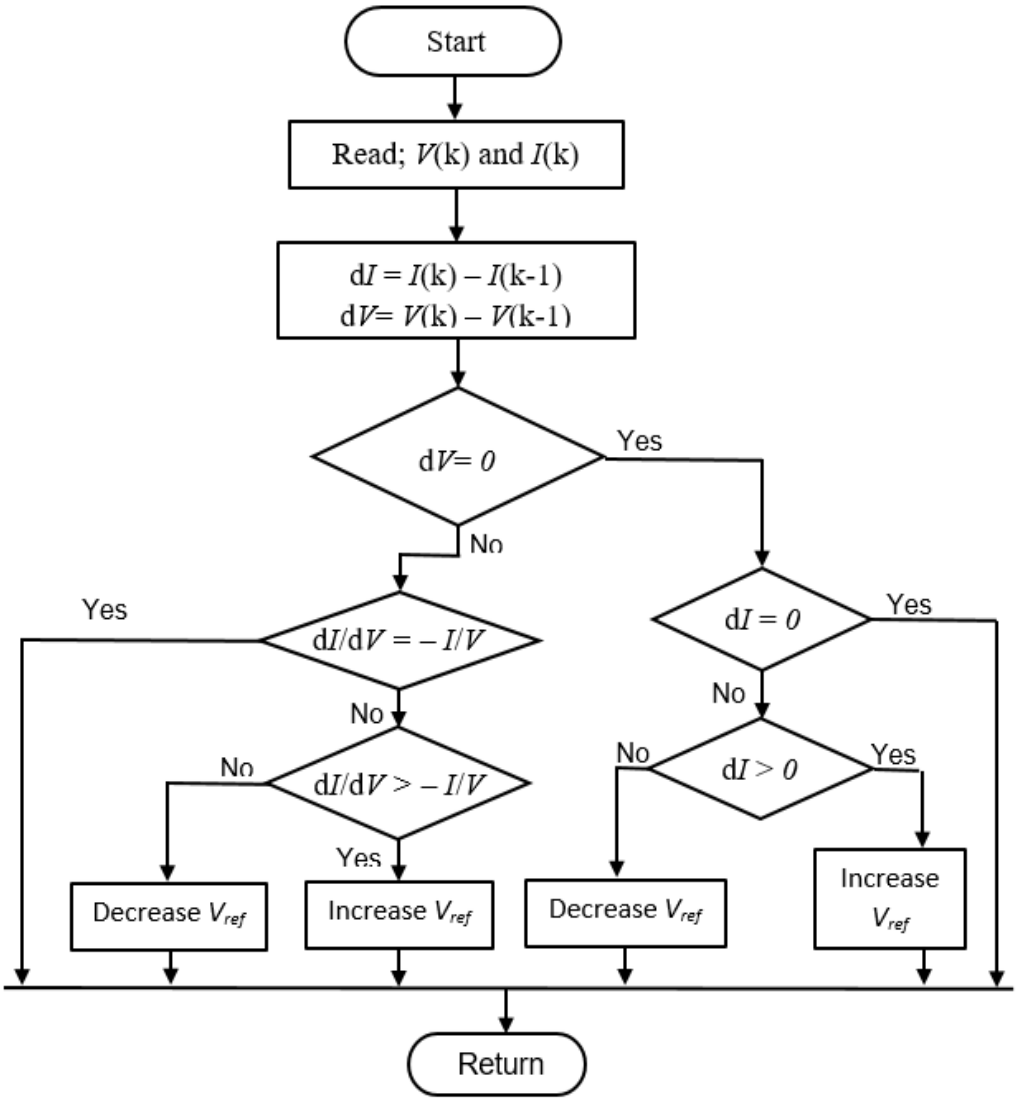

Figure 3. 21 InCond MPPT algorithm flowchart

Figure 3.22 presents the MATLAB/Simulink model simulation results showing the output curve of the P&O and InCond MPPT control algorithms implemented in this research. The InCond method was found to track the MPP accurately with lesser distortion after a comparative analysis of the two MPPT control algorithms' performance at the standard test condition (1000 W/m^2 and 25 ^{o}C).

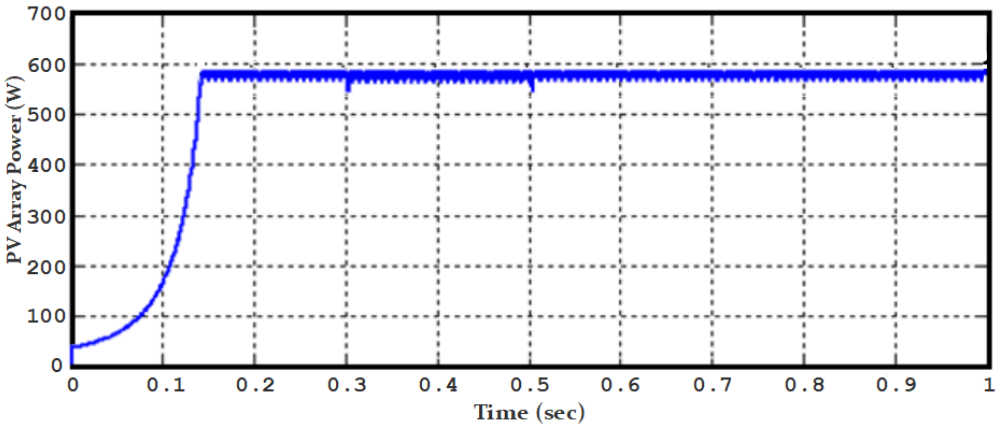

(a) P & O MPPT

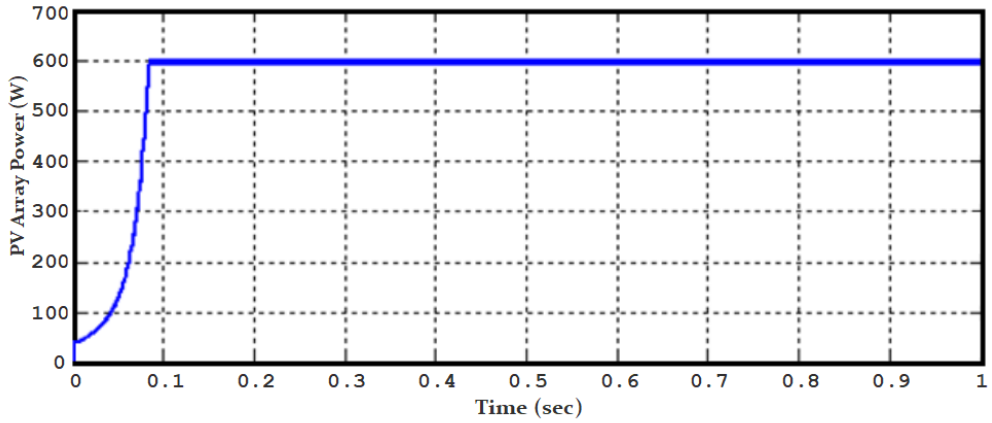

(b) InCond MPPT

Figure 3. 22 The performance of (a) P&O (b) InCond MPPT control algorithm

Further verification of the performance of the two MPPT control methods to effectively track the MPP is considered for varying solar irradiation and temperature. At 0.3 seconds, the irradiation changed from 500 W/m^2 to 1000 W/m^2 and the temperate from 10 ^{o}C to 25 ^{o}C at 0.5 seconds. The output power curves of the model simulation are presented in figure 3.23. The InCond algorithm method tracked the MPP faster and accurately with lesser distortion during solar irradiation variation operating conditions.

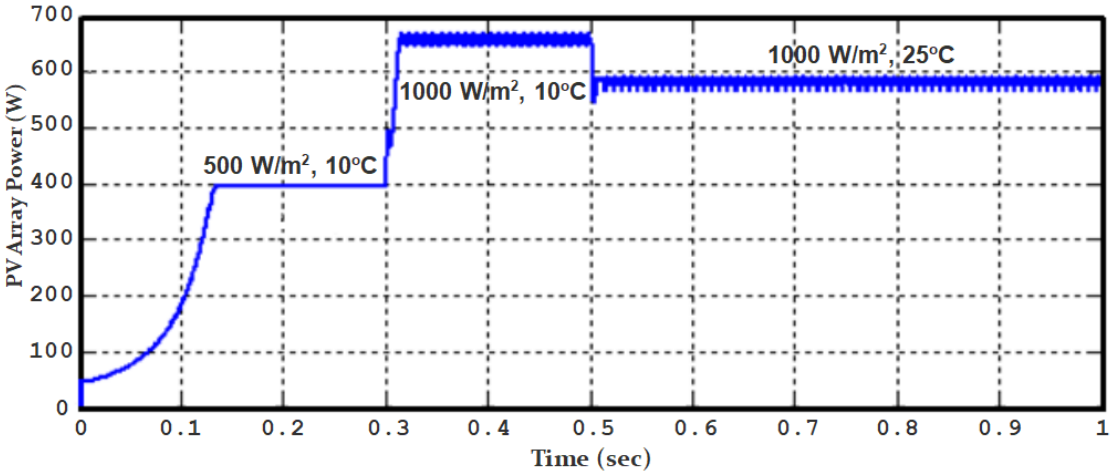

(a) P & O MPPT

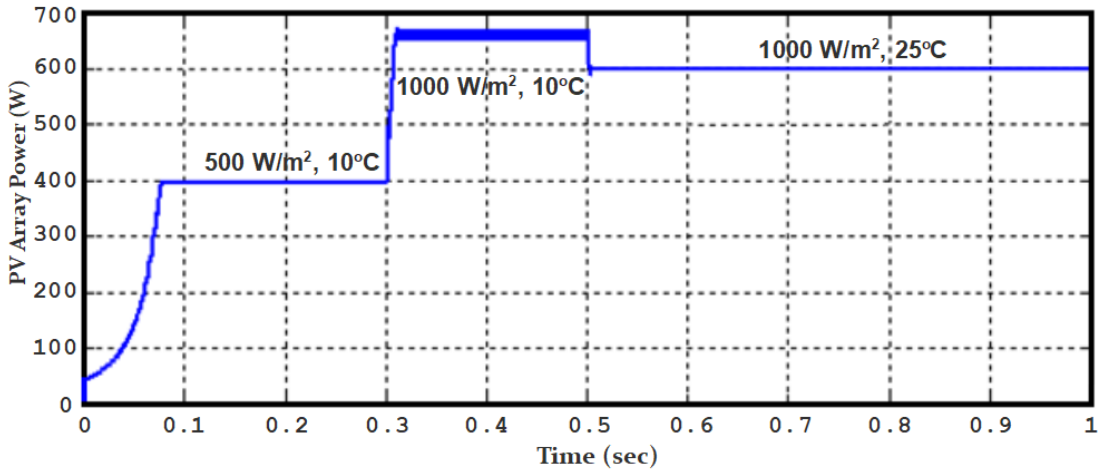

(b) InCond MPPT

Figure 3. 23 The two MPPT algorithm output power curves at different solar irradiation and temperature

3.6 PV Inverter (DC/AC) Types and Control Topology

The PV inverter is a power electronic device with semiconductor switches that operate as a voltage or current source (VSC or CSI) with different control and switching topologies [211]. The device converts PV array DC voltage to AC voltage and integrates the PV system to the distribution grid. There are two types of inverter configurations; single-phase and three-phase switching configurations; their application depends on the PV system's capacity. The two different inverter configurations with their filter are presented in figure 3.24.

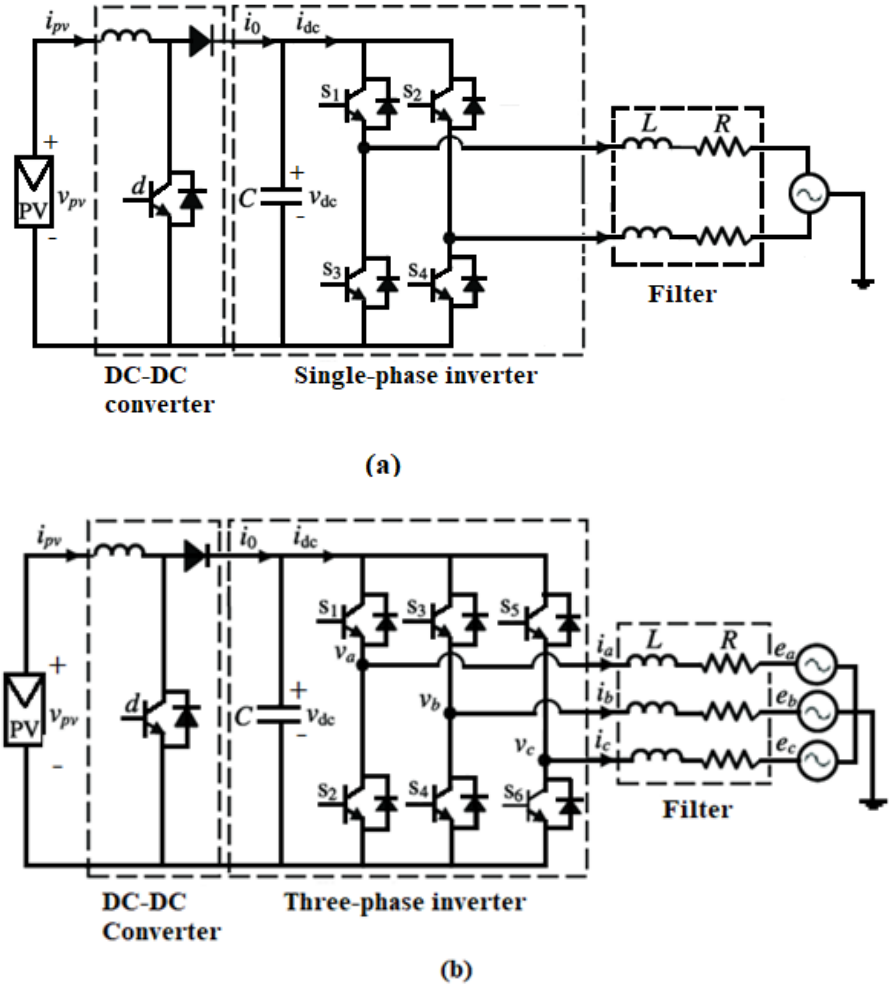

Figure 3. 24 PV inverter systems (a) Single-phase and (b) Three-phase

A two-level three-phase inverter was used in this research. It achieves high power ratings and allows high power applications, such as PV and wind power systems, to effectively interface with the grid [27]. A carrier-based pulse width modulation (PWM) switching technique for a three-phase PV system inverter was implemented for this research. A comparison of the reference signal with the triangular carrier waveform generated the inverter firing pulses. The grid voltage was considered the inverter reference signal to synchronize the PV system's voltage output magnitude and frequency.

The inverter consists of three branches of two series-connected IGBT switches, including their specific anti-parallel diodes, compensating for the impacts of the dead time between the switching on each phase, as shown in figure 3.24(b). Every branch generates a single-phase output signal (A, B, or C). The DC bus has a V_{dc} voltage as its input. In each phase, the three-phase output is generated

by properly sequencing the conductive periods and open switch times. At any given time, only one switch in each phase can operate to avoid short-circuiting of the DC bus; however, at the same time, both switches can remain open. Usually, current control techniques are implemented to control the three-phase PV inverter. For this research, the current-controlled voltage source inverter was utilized, as indicated in figure 3.25.

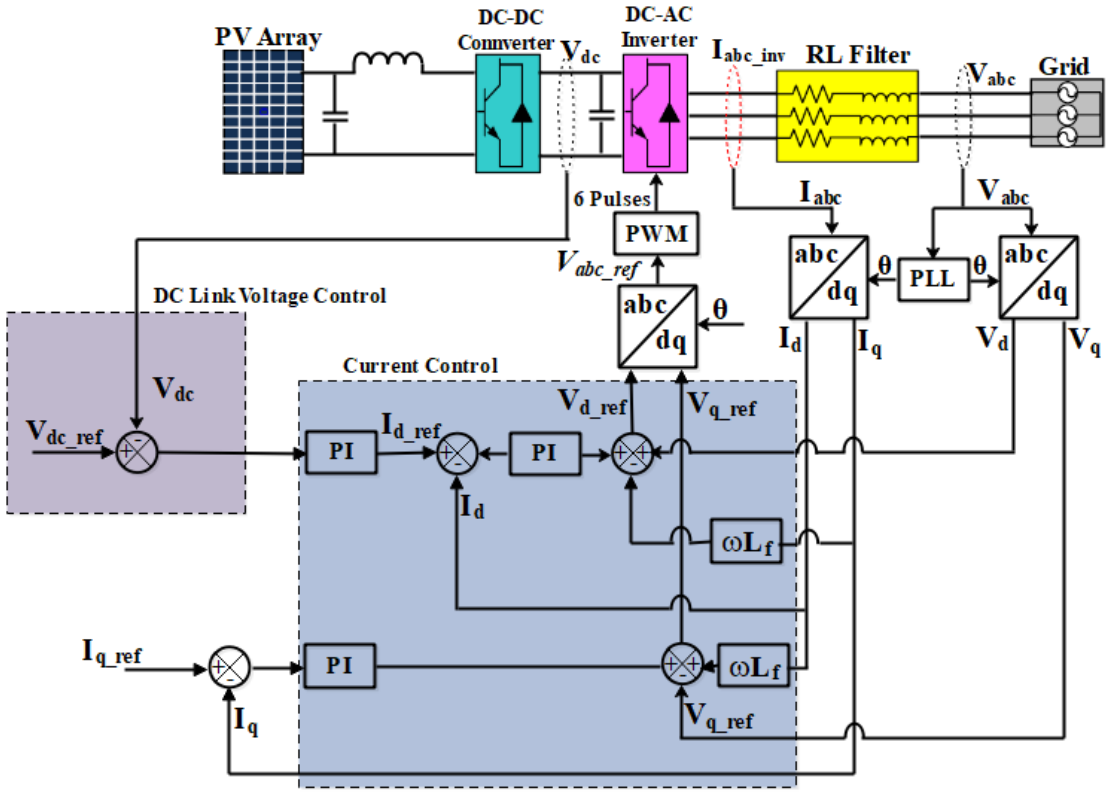

Figure 3. 25 The control scheme of the DC-AC inverter

The system consists of a DC link voltage controller that regulates the dc voltage across the capacitor to a constant value by controlling the active current injected into the inverter. If the PV output voltage is less than the DC link voltage reference, the controller reduces the active current to increase the DC voltage and the capacitor current; otherwise, it acts vice versa [212]. Equation (3.51) expresses the PI controller output used as the reference of the current controller.

$$I_{d-ref} = K_p\left(V_{dc\_ref} - V_{dc}\right) + K_i \int\left(V_{dc\_ref} - V_{dc}\right)dt + \frac{V_{pv}}{V_d} \tag{3.51}$$

Where: K_p and K_i are the proportional and integral gain of the PI controller.

Likewise, it includes a current loop with a recurring controller, which allows the current reference, I_{ref}, derived from the *d, q* current references (I_{d_ref}, and I_{q_ref}) using the *dq→abc* transformation to track the current injected into the grid. The phase-locked loop (PLL) decodes the grid phase voltage for synchronizing the reference frame through a PI controller required for generating V_{ref}, with the *d, q* current references determining the active power and reactive power exchanged with the grid. When the *d-q* current references are all equal to zero, the DC voltage generated and the grid voltage must be equal. That is, the inverter would be synchronized with the grid. At this point, the DC voltage and the grid voltages (V_a, V_b, and V_c) are feed-forward and applied through a low-pass phase filter (LPF) to the output of the recurring current controller to obtain the reference voltage, V_{ref}, as expressed in equation (3.52).

$$M_d = 0.5V_{dc}\left(2I_{dc\_ref} - 2I_d - LI_q + V_d\right)$$
$$M_q = 0.5V_{dc}\left(-2I_q - LI_d + V_q\right) \quad (3.52)$$

The q-axis component is set to zero for unity power factor operation to control the active and reactive power. With the inverse d-q transformation, the reference signals are then transformed into the stationary frame. These control signals are compared to the carrier's high-frequency signal, which generates the PV inverter firing pulses. Presented in figure 3.26 are the simulation output waveforms of the inverter current and grid phase voltage.

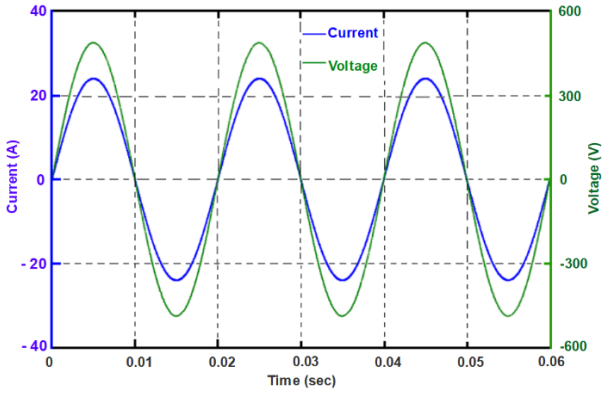

Figure 3. 26 Simulation output waveforms of inverter current and grid phase voltage

3.7 The Distribution Grid

The IEEE distribution test grid, 13 bus distribution system, was used as the test system in this research. The 13 bus distribution feeder has fascinating features

of an entire distribution system, with a nominal voltage of 4.16 kV, making it ideal for this research. The IEEE 13 bus radial test system is an unbalanced distribution network due to the three-phase, two-phase line configuration and the presence of single-phase loads that are not distributed evenly across the three-phase system. The total distributed load among consumers of industrial and residential energy is 4.054 MVA. The system also includes voltage regulators that are connected in wye at the substation. The voltage regulator keeps the lines during disturbance within allowable limits of the nominal voltage of the system. Modelled were the overhead and underground lines with their unbalanced line impedances with constant power (PQ), constant current (I), or constant impedance (Z) loads [213]. The test system's one-line diagram is depicted in figure 3.27.

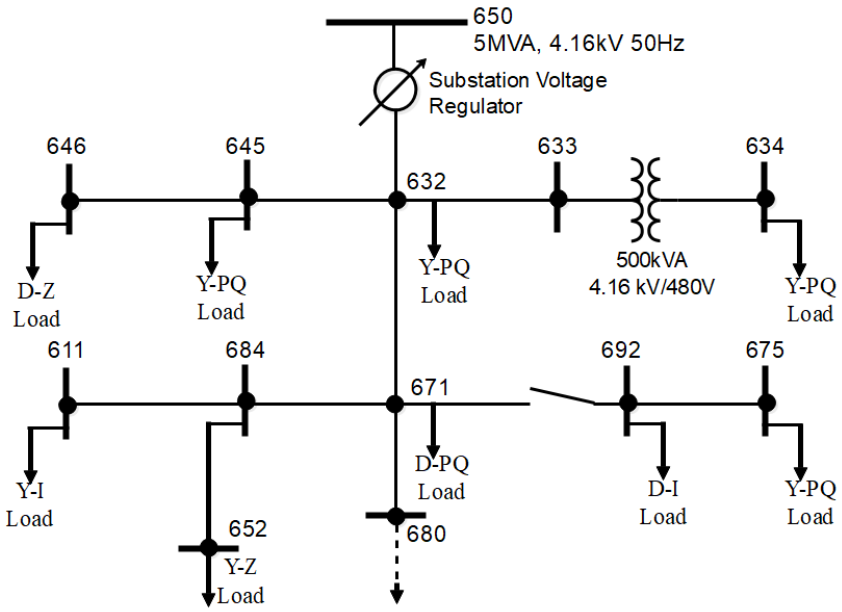

Figure 3. 27 One-line diagrams of the IEEE 13 bus test system

The Backward/Forward Sweep load flow technique, a three-phase load flow algorithm shown in figure 3.28, was implemented on the IEEE 13 bus distribution system in MATLAB/Simulink software to solve the system load profile. The load flow algorithm is based on three significant steps [214]. In the first step, the current injected at each bus, *"i"* is calculated with equation (3.53):

$$I_i^{(k)} = conj\left(\frac{P_{n-1} + jQ_{n-1}}{V_{n-1}^k}\right), \quad i = 1,2,...,n \tag{3.53}$$

Where P-Q is the power at the bus *"i"* and V^k is the voltage at the bus *"i"* solved from iteration *k.*

In the second step, the backward sweep, current $j_{i,\ i+1}$, is calculated starting from the last ordered branch from the bus "*i*" to "*i+1*" using equation 3.54.

$$J_{n-i}^{(k)} = -conj\left(\frac{P_{n-1} + jQ_{n-1}}{V_{n-1}^{k}}\right) + \sum_{r} J_{n-r}^{k}, \qquad r = 1,2,... \tag{3.54}$$

Where $\sum_{r} J_{n-r}^{k}$ is the current in branches coming from the bus, *"i."*

The forward sweep starts to calculate the bus voltages by applying equation (3.55) in the third step.

$$V_i^{(k)} = V_{i-1}^{(k)} - Z_i J_i^{(k)}, \qquad i = 1,2,...,n \tag{3.55}$$

Where Z_i is the branch *"i – 1, i."* series impedance.

These three steps are recurring until each bus voltage profile in the previous and present iteration is less than the threshold limit κ.

$$\max = \left(\left[V^{(k+1)}\right] - \left[V^{(k)}\right]\right) < \kappa \tag{3.56}$$

For simulation, the switch between buses 671 and 692 was closed. The solved voltage profile is discussed in chapter four.

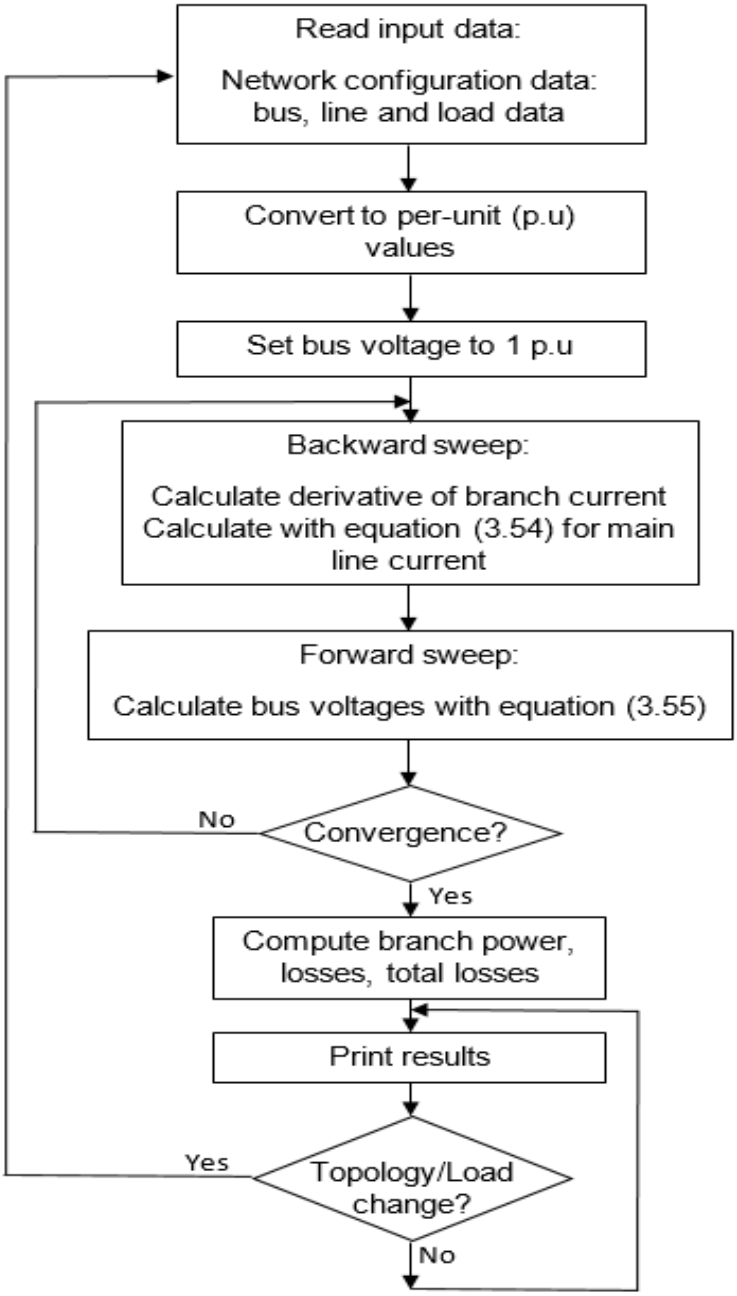

Figure 3. 28 Backward/Forward Sweep Load flow algorithm flowchart [215]

3.8 Load Modelling

Load modeling is the mathematical expression of the relationship between load bus power and voltage [216, 217]. There are two major categories of load modelling classified as static and dynamic load models. Many power quality analysis studies have used different load models, but the commonly used static load models are the exponential and polynomial (ZIP) load models [218]. Accurate modeling of distribution system loads is a process that involves a detailed study of the end-user load types, rating of their electrical appliances,

and equipment on the system. The consumption of residential and industrial load types such as lighting, cooking, heating, computers, and induction motors varies during the day, depending on consumer behaviour. Figure 3.29 depicts the typical load profile of industrial and residential consumers on the grid [219, 220]. The total load profile for residential and industrial uses could be calculated by aggregating their load profile. In this thesis, the ZIP representation of typical load was used to model the loads. The ZIP load model has three components: constant impedance (Z), constant current (I), and constant power (P), as expressed in equation 3.57. It is widely used for both dynamic and steady-state studies [216, 217].

$$P^{ZIP} = P_i\left[P^Z\left(\frac{V_{ph-N}}{V_0}\right)^2 + P^I\left(\frac{V_{ph-N}}{V_0}\right) + P^P\right]$$
$$Q^{ZIP} = Q_i\left[Q^Z\left(\frac{V_{ph-N}}{V_0}\right)^2 + Q^I\left(\frac{V_{ph-N}}{V_0}\right) + Q^P\right] \quad (3.57)$$

Where P_i, *and* Q_i, are the active and reactive power respectively at nominal voltage V_0 values. $V_{ph\text{-}N}$ is the phase to neutral voltage, P^z, P^I, P^P, and Q^z, Q^I, Q^P, are the ZIP load active and reactive power components for constant impedance, constant current, and constant power.

The constant impedance component represents purely resistive loads like an incandescent light, laptop charger. While the constant current component in the equation represents loads such as induction motor, and the constant power component refers to power supplies.

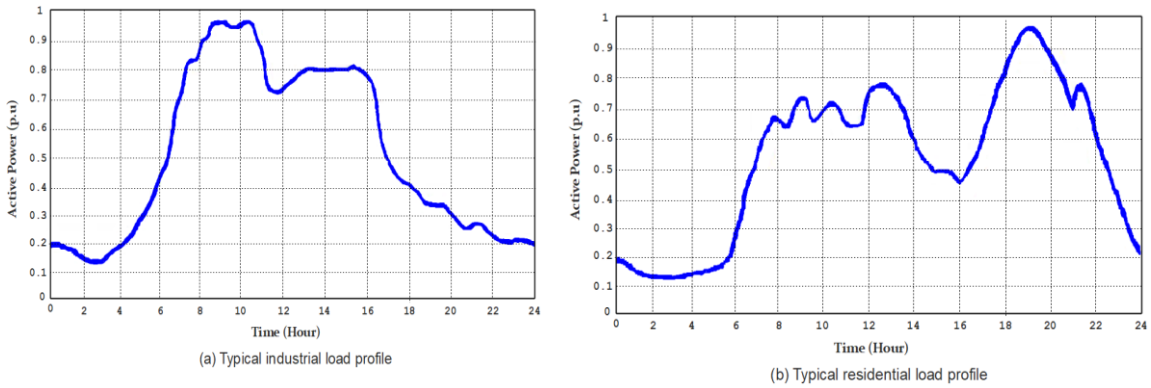

Figure 3. 29 Typical industrial and residential load profile

3.9 D-STATCOM for Power Quality Enhancement

This section discusses applying a distribution static compensator (D-STATCOM) for power quality enhancement, the operating principles, and the significance of the device multi-level voltage source converter (VSC) for voltage regulation, reactive power compensation, and the method of improving power quality. Today, the increasing penetration of PV system generation on the distribution grid brings critical power quality issues, necessitating implementing different control methods to mitigate them. The D-STATCOM is one of the shunt-connected custom power devices (CPD) used in distribution systems. The D-STATCOM provides dynamic voltage support in response to system disturbances and balances the reactive power demand of loads at the point of common coupling (PCC). The D-STATCOM injects and absorbs variable reactive power continuously to maintain a constant voltage magnitude at the PCC, with the continuous reactive power supply. The major component of the D-STATCOM is the VSC, a power electronics-based technology.

This study designed a D-STATCOM control method based on a multi-level VSC topology. The control scheme was designed to compensate for voltage rise and voltage dip caused by balanced and unbalanced faults and to mitigate current harmonics through reactive-power injection. Reactive power injection eliminates fault currents, while the compensation for voltage unbalance is performed by controlling the grid current. The D-STATCOM control method has a regulated PI controller, which generates a reference current in phase with source voltage and compares the source current to the reference current to calculate the error [221]. The voltage source converter switching signal is developed from the error [222]. The D-STATCOM was operated in two designed control loops to (a) generate reference current for the inverter switching signal, and (b) control the dc bus voltage. This section explains the different control methods for reference current generation and dc bus voltage control. Three other PI controller optimization methods, were implemented to tune the D-STATCOM controller and a comparative analysis of the three control algorithms for the transient performance of the D-STATCOM was done with the conventional PI controller in MATLAB/Simulink.

3.9.1 D-STATCOM Operating Principles

In this section, D-STATCOM's operating principle is discussed in detail according to its application method. When two AC sources with the same frequency are linked together via a series inductance, the phase angle difference determines the active power flow. The difference in voltage magnitude between the sources determines the reactive power flow [221]. Thus, D-STATCOM controls reactive power flow by controlling the fundamental component of VSC output currents (i_d and i_q) at the PCC. A D-STATCOM device provides an efficient solution for compensating reactive power and improving grid voltage magnitude. The components of the device consist of an IGBT-based voltage source converter (VSC), a coupling transformer, a DC storage (DC-link), and a controller, as shown in figure 3.30. The D-STATCOM is connected to the grid via the coupling transformer at the PCC. It is controlled to absorb or inject reactive power into the grid regulating at the PCC the grid three-phase sinusoidal voltage to eliminate current harmonics, compensate reactive power, and control voltage [223].

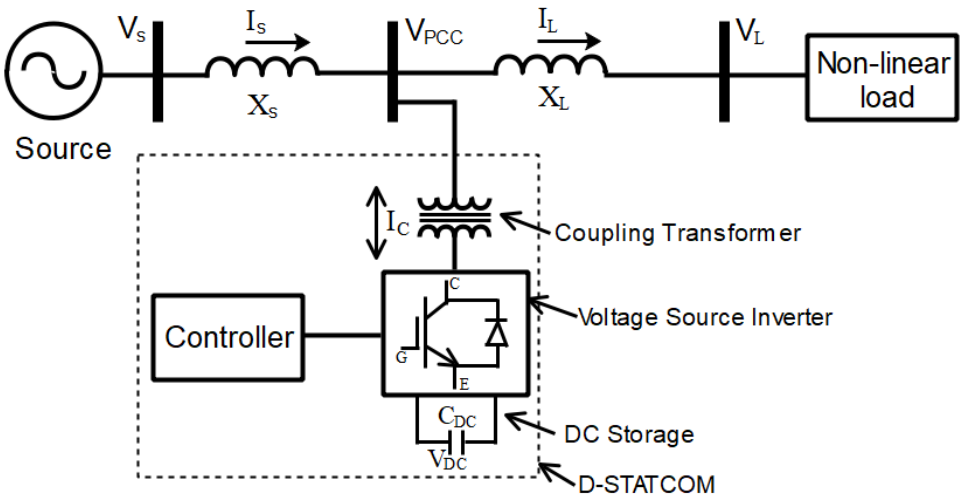

Figure 3. 30 D-STATCOM topology

Firstly, the equation for the concept of reactive power exchange is explained before the D-STATCOM operating principle is discussed. Two voltage sources V_S and V_R connected through impedance $Z = R + jX$ are connected, with current I_b flowing via the impedance, as shown in figure 3.31.

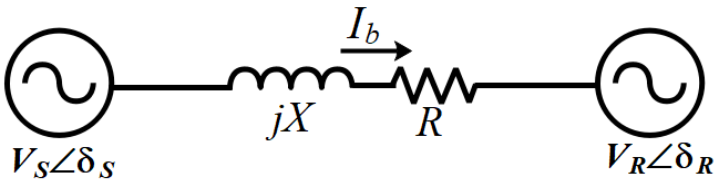

Figure 3. 31 Two voltage source line diagram

The angle difference between V_S and V_R when R is assumed to be zero since the ideal D-STATCOM is without power dissipation is δ as expressed in equation (3.58) to (3.60) [224].

$$\delta = \delta_s - \delta_R \tag{3.58}$$

The active and reactive power flow between the two voltage sources is expressed in equation (3.59).

$$P = \frac{V_s.V_R}{X}(\sin\delta)$$
$$Q = \frac{V_R}{X}(V_S\cos[\delta] - V_R) \tag{3.59}$$

If the sin δ becomes zero, the active and reactive power flow is expressed in equation (3.60).

$$P = 0$$
$$Q = \frac{V_R}{X}(V_S - V_R) \tag{3.60}$$

It is clear from equation (3.60) that if the angle difference between the two voltage sources becomes zero, only the reactive power flow depends on the difference between the two source voltage (V_S – V_R). Therefore, the reactive power exchange within the system occurs in two ways. If the voltage at V_S is higher than V_R, the reactive power flows to V_R from V_S; likewise, if the voltage at V_R is greater than the voltage at V_S, the reactive power flows from V_R to V_S. The same principle applies to the D-STATCOM operation. If the D-STATCOM in figure 3.31 operates in capacitive mode at the point that the device voltage (V_R) magnitude is higher than the grid voltage (V_S) [V_R>V_S], as shown in figure 3.32a, the D-STATCOM injects reactive power to the grid. It absorbs the grid's reactive power when operating in the inductive mode, when the grid voltage magnitude is higher than the D-STATCOM voltage magnitude (V_S>V_R), as shown in figure 3.32b. The reactive power is zero if V_R equals V_S [225].

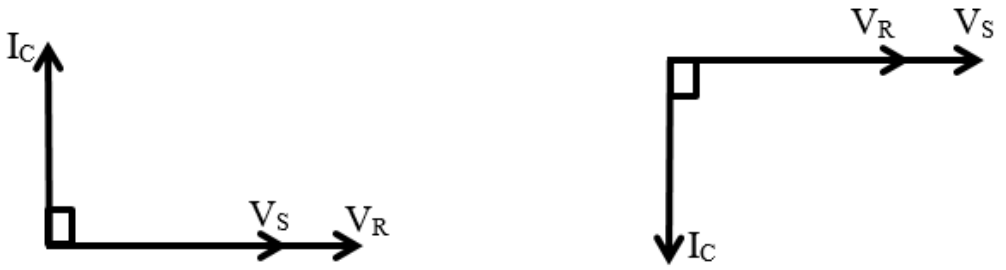

a. Capacitive mode b. Inductive mode

Figure 3. 32 D-STATCOM operational mode [225]

3.9.2 D-STATCOM Reference Current Controller

The voltage source converter (VSC) is the core of the D-STATCOM, which is operated through suitable control algorithms for various applications. In this study, the D-STATCOM was simulated in MATLAB/Simulink using the proportional-integral (PI) controlled SPWM to implement voltage regulation and harmonic elimination. The D-STATCOM performance depends on the control algorithm used to extract the reference current; to this end, the synchronous reference frame (SRF) control theory-based PWM was employed. The SRF control is based on the Clark transformation and Park transformation of the measured load currents in the *abc* reference frame into a synchronous rotating d-q frame via the *abc*-αβ and αβ-dq transformation utilizing phase angle information θ (ωt) of the grid voltage provided by the phase lock loop (PLL). It serves to estimate the grid phase voltage and frequency, then transforms the compensating current variables into *abc* frame from the *dq* frame fed into the current controller used to generate switching pulses for the inverter switches, as shown in figures 3.33 and 3.34 [226].

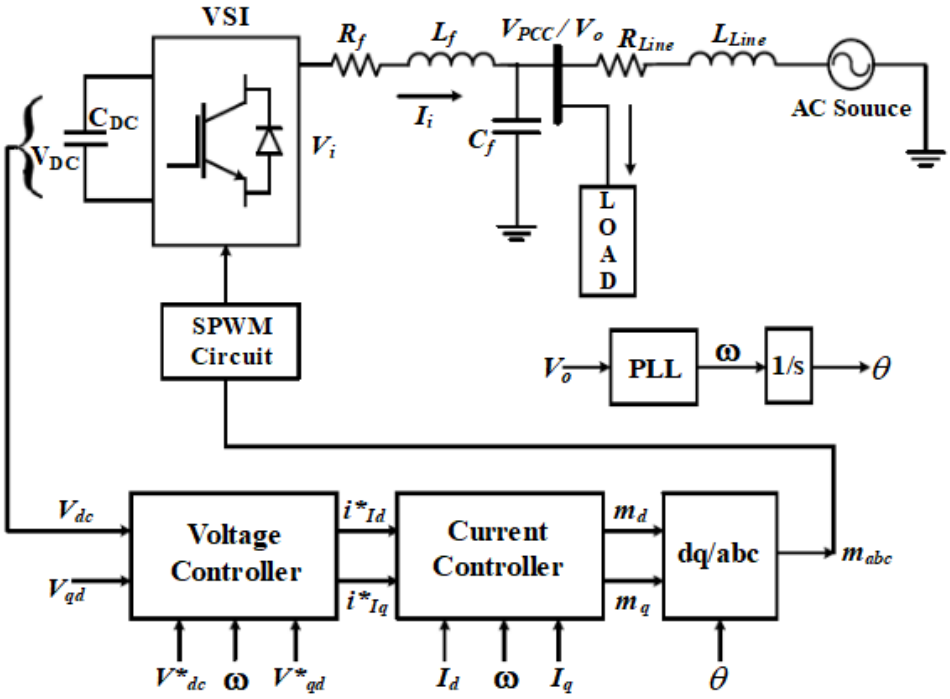

Figure 3. 33 Schematic views of D-STATCOM control connected to the source and load

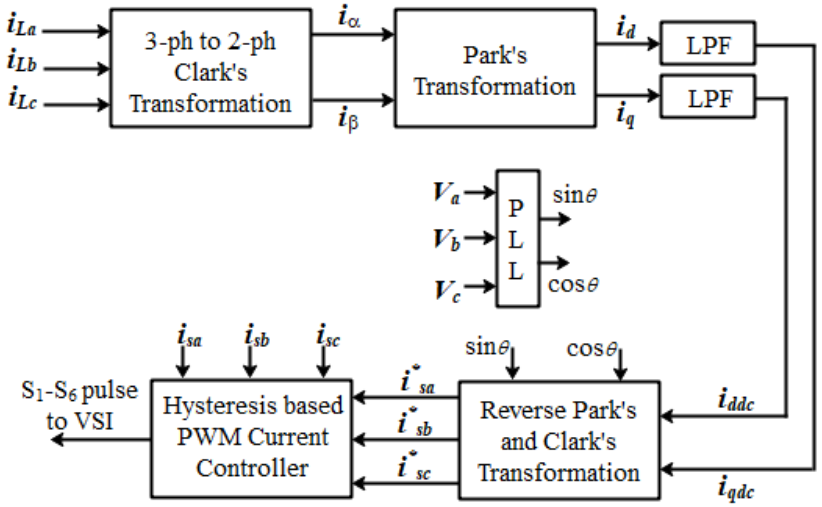

Figure 3. 34 Structure of SRF theory-based reference current generation

In this method, the source current variables (i_a, i_b, i_c) are detected carefully and then transformed from the three-phase stationary frame (a-b-c) into a two-phase stationary frame (α-β) as expressed in equation (3.61) [227].

$$\begin{bmatrix} i_d \\ i_q \\ i_0 \end{bmatrix} = \sqrt{\frac{2}{3}} \begin{bmatrix} 1 & -1/2 & -1/2 \\ 0 & \sqrt{3}/2 & -\sqrt{3}/2 \\ 1/2 & 1/2 & 1/2 \end{bmatrix} \cdot \begin{bmatrix} i_a \\ i_b \\ i_c \end{bmatrix} \quad (3.61)$$

The dc components i_d and i_q are generated by the SRF using low-pass filters (LPFs) for removal of current ripple from the components. Using reverse Park's Transformation, the extracted dc components i_{ddc} and i_{qdc} are transformed back into α-β frame, as expressed in equation (3.62) [226].

$$\begin{bmatrix} i_\alpha \\ i_\beta \end{bmatrix} = \begin{bmatrix} \cos\theta & \sin\theta \\ -\sin\theta & \cos\theta \end{bmatrix} \cdot \begin{bmatrix} i_{ddc} \\ i_{qdc} \end{bmatrix} \quad (3.62)$$

The PLL adjusts the generated phase angle to align the *d* axis of SRF with the grid current vector by regulating the *q* component of the grid current vector to zero based on the Park's Transformation of the three-phase grid current. The PI controller tuning by SRF was tested for different coefficients responsible for the PI controller's bandwidth. The step response of the PI controller tuned with varying coefficient values is presented in figure 3.35.

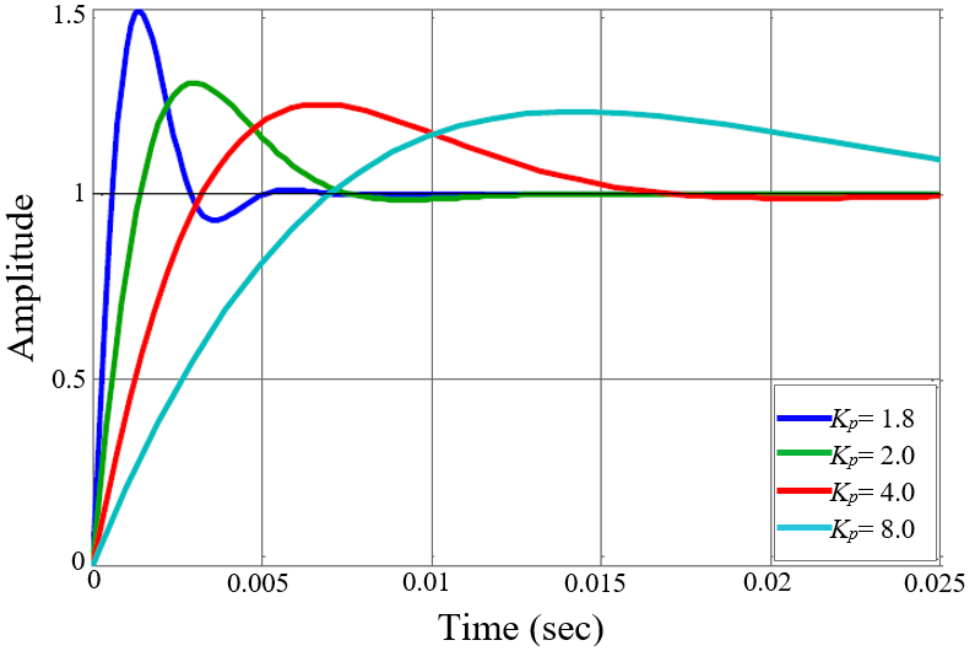

Figure 3. 35 PI controller step response for varying coefficient values

3.9.3 DC bus voltage control

The D-STATCOM dc bus consists of a capacitor charged from the power supply. The active filter injects or absorbs a quantity of active power into the dc capacitor during operation [226]. The active power control method is used to control the dc-bus voltage. The dc component in the direct-quadrature-zero coordinates corresponds to active power, according to the d-q theory. The required power is calculated with a dc-link voltage controller that compares the DC bus voltage (V_{dc}) to the corresponding value of reference voltage (V_{dc_ref}), which amplifies the error signal by a control gain 1.8. The dc bus voltage control is depicted in figure 3.36 [228].

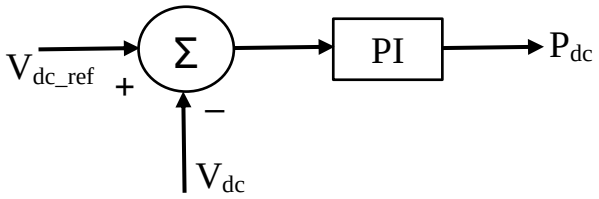

Figure 3. 36 PI controller for conventional DC bus voltage control

Sudden increase and decrease of loads on the grid significantly affect the dc bus voltage, resulting in a drop below or rise above the dc-link reference voltage. This study implemented the PI controller to keep the dc-link voltage equal to the reference voltage. The PI controller is one of the most commonly applied linear feedback controllers and was used here because of its simplicity, applicability, and ease of control. The controller is utilized to keep the DC link voltage at the reference value. The mathematical equation to calculate the power required by the capacitor is expressed in equation (3.63) [229].

$$P_{dc} = K_p\left(V_{dc\_ref} - V_{dc}\right) + K_i \int \left(V_{dc\_ref} - V_{dc}\right) \tag{3.63}$$

The equation shows the PI controller, which aligns the dc-link capacitor voltage to the reference value of the DC link voltage (V_{dc_ref}). The controller proportional gain (K_p) and Integral gain (K_i) values are 1.8 and 50 for the conventional PI controller.

3.10 Summary

The foregoing chapter presented a detailed theory of all the components of this research model. It explained the grid-tied PV system modelling of the PV array, the two-stage converter, and their control techniques, as implemented in MATLAB/Simulink software. The test system modelled is discussed with different load models required to evaluate voltage quality concerns and provide appropriate harmonic analysis on an unbalanced distribution grid. The research method discusses the principle and implementation of the D-STATCOM proposed to mitigate power quality issues on a grid-tied PV system. The conventional PI controller was designed for the D-STATCOM as a base case to operate in two designed control loops to generate reference current for the inverter switching signal and control the dc bus voltage.

CHAPTER FOUR

VOLTAGE QUALITY ANALYSIS

4.1 Introduction

The term voltage quality concern in the context of a distribution system refers to any glitch in the system due to voltage variations affecting the system's capability to feed the loads and withstand unexpected disruptions, such as system faults. These variations include harmonics distortion in current or voltage waveform, and frequency mismatch. This chapter presents an in-depth analysis of the voltage quality concerns caused by high-level penetration by the PV system on the distribution grid. In the subsequent sections, we discussed an assessment of voltage quality problems like voltage rise, voltage dip, and voltage unbalance concerns on a simulated unbalanced distribution grid with an integrated PV system using the IEEE 13 bus test system. A field investigation of a grid-tied PV system's performance was conducted on the typical 110kW grid-tied PV systems located at the Durban University of Technology's Steve Biko campus.

4.2 Evaluation of voltage quality concern in an unbalanced distribution system

This study investigated voltage quality utilizing the IEEE 13 bus test system in an unbalanced distribution grid, including residential and commercial loads that reflect the conventional distribution network. The defined detailed PV model described in chapter three of this thesis was implemented to depict a typical system for the grid-tied PV system. The voltage quality analysis in this study was conducted for two different scenarios to evaluate the impact of grid-tied PV system on an unbalanced distribution system. The first scenario undertook the evaluation of voltage rise, and voltage unbalance and the second scenario investigated the voltage dip caused by system fault conditions on a distribution grid-tied PV system.

4.2.1 Scenario one: Evaluation of voltage rise and voltage unbalance

Voltage unbalance is a condition in the power system where the voltage amplitudes or the phase angle between the magnitude are inconsistent. In this scenario, three different case studies were conducted to evaluate the PV system's integration on a single bus and simultaneous penetration on many

other grid buses to study the PV system's impact on voltage rise and unbalances. Firstly, a three-phase PV system penetrated the distribution network at bus 632, and distributed PV penetration was explored on bus 671 and 675 for the second case study with a total of 110 kW installed capacity. In the third case study, to evaluate the impact of voltage rise, and voltage unbalances problems, two other inverters were integrated on the grid to increase the capacity of the grid-tied PV penetration by 350 kW. The PV system's bus selection criteria were based on the load concentration and the grid's distance.

Since it is common to see random rooftop PV installation on a distribution grid, a PV system could have been installed by 70 percent of customers in a particular phase, while the remaining two phases have installed 40 percent and 10 percent PV penetration. In such a situation, though, even if the voltage unbalances of the distribution grid fall within the standard limits without the PV system, the same can not be guaranteed after the PV penetration. Therefore, the possible number of PV installations on such a grid must be investigated to maintain the voltage unbalance within the standard limit. Figure 4.1 presents the typical solar irradiation pattern used for this analysis with the PV array's resultant output power, which shows that the PV power is linearly proportional to the solar irradiation.

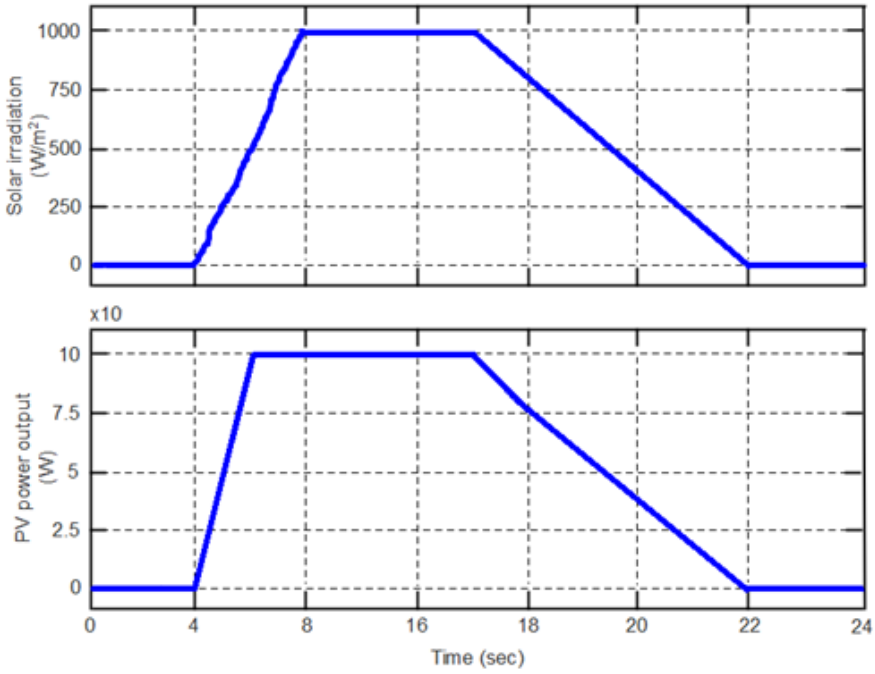

Figure 4.1 A typical solar irradiation pattern with corresponding PV power

Table 4. 1 Voltage profile for case study one

Bus No	Phase A voltage (p.u)			Phase B voltage (p.u)			Phase C voltage (p.u)		
	At 8 sec	At 20 sec	ΔV_A	At 8 sec	At 20 sec	ΔV_B	At 8 sec	At 20 sec	ΔV_C
632	1.0264	1.0195	0.0069	1.0418	1.0403	1.0015	1.0205	1.0161	0.0043
633	1.0233	1.0162	0.0072	1.0400	1.0384	0.0016	1.0179	1.0135	0.0044
634	0.9998	0.9925	0.0073	1.0218	1.0200	0.0018	0.9996	0.0046	0.0050
645	-	-	-	1.0328	1.0311	0.0017	1.0186	1.0142	0.0044
646	-	-	-	1.0312	1.0294	0.0018	1.0166	1.0121	0.0045
671	0.9958	0.9884	0.0074	**1.0530**	**1.0512**	0.0018	0.9816	0.9764	0.0052
675	0.9893	0.9818	0.0074	**1.0554**	**1.0536**	0.0018	0.9796	0.9744	0.0052
684	0.9939	0.9865	0.0074	-	-	-	0.9786	0.9729	0.0055
611	-	-	-	-	-	-	0.9796	0.9744	0.0052
652	0.9884	0.9809	0.0075	-	-	-	0.9777	0.9724	0.0053
692	0.9921	0.9851	0.0070	**1.0529**	**1.0510**	0.0019	0.9786	0.9734	0.0052

Table 4.1 has the corresponding simulation results of the 110 kW PV system at Bus 632, depicting the test system voltage profile for the first case study. Tables 4.2 and 4.3 likewise show the corresponding voltage magnitude result for the second and third case studies of the first scenario. As shown in figure 4.2, at time t = 8 seconds, the solar radiation is at the peak, 1000W/m^2, considered as daytime, and at time t = 20 seconds, considered as night-time, the irradiation stands at 450W/m^2. An increase in voltage profile is observed in phases B and C because of the PV system penetration on phase A. The magnitude of Phase A voltage increased by almost 0.7 percent at bus 632, and this trend occurs across the grid. In contrast, phase B voltage magnitudes on bus 692 at the end of the network reached higher values; however, the voltage differences (ΔV_B) were lower. It is observed that the voltage magnitude on buses 671, 675, and 692 rose to 1.0530 p.u, 1.0554 p.u, and 1.0529 p.u, respectively, which exceeded the 5 percent limit required by the IEC 61727 and SANS 959-2-4:2017 both international and national standard limits.

Table 4.2 presents the resultant voltage profile during the day and night times for the IEEE 13 bus test system with two distributed PV integrated on bus 671 and 675 for the second case study with a total of 110 kW installed capacity.

Table 4. 2 Voltage profile for case study two

Bus No	Phase A voltage (p.u)			Phase B voltage (p.u)			Phase C voltage (p.u)		
	At 8 sec	At 20 sec	ΔV_A	At 8 sec	At 20 sec	ΔV_B	At 8 sec	At 20 sec	ΔV_C
632	1.0267	1.0195	0.0071	1.0422	1.0403	0.0019	1.0220	1.0161	0.0059
633	1.0246	1.0162	0.0085	1.0416	1.0384	0.0032	1.0207	1.0135	0.0072
634	1.0093	0.9925	0.0168	1.0321	1.0200	0.0121	1.0102	0.9946	0.0155
645	-	-	-	1.0329	1.0311	0.0018	1.0199	1.0142	0.0057
646	-	-	-	1.0312	1.0294	0.0018	1.0178	1.0121	0.0057
671	0.9993	0.9884	0.0109	**1.0534**	**1.0512**	0.0022	0.9843	0.9764	0.0079
675	0.9929	0.9818	0.0111	**1.0566**	**1.0536**	0.0030	0.9841	0.9744	0.0097
684	0.9963	0.9865	0.0098	-	-	-	0.9830	0.9744	0.0086
611	-	-	-	-	-	-	0.9818	0.9724	0.0094
652	0.9922	0.9809	0.0113	-	-	-	-	-	-
692	0.9964	0.9846	0.0118	1.0198	1.0174	0.0024	0.9846	0.9753	0.0093

It is noted that based on the individual PV system, voltage support was provided for the grid downstream, as the voltage level rose significantly compared to the first case study. Remarkably, the voltage magnitudes of buses 675 and 671 on phase B were 1.0534 p.u and 1.0566 p.u, which were above the standard limits. The voltage differences due to reverse power flow also increased the grid upstream voltage magnitude compared to Table 4.1.

The same simulation approach was performed as in the previous case study, and the load flow results obtained are presented in Table 4.3. Two additional 200 kW and 150 kW PV systems penetrated the grid for the third case study at bus 671 and 675 to test the impact of high-level PV penetration on the distribution grid.

Table 4. 3 Voltage profile for case study three

Bus No	Phase A voltage (p.u)			Phase B voltage (p.u)			Phase C voltage (p.u)		
	At 8 sec	At 20 sec	ΔV_A	At 8 sec	At 20 sec	ΔV_B	At 8 sec	At 20 sec	ΔV_C
632	1.0317	1.0206	0.0111	1.0438	1.0414	0.0024	1.0241	1.0172	0.0069
633	1.0269	1.0127	0.0142	1.0434	1.0392	0.0042	1.0247	1.0144	0.0103
634	1.0123	0.9935	0.0188	1.0347	1.0221	0.0126	1.0088	0.9947	0.0141
645	-	-	-	1.0345	1.0322	0.0023	1.0223	1.0152	0.0071
646	-	-	-	1.0328	1.0303	0.0025	1.0204	1.0130	0.0074
671	1.0093	0.9895	**0.0198**	**1.0560**	1.0526	0.0034	0.9904	0.9774	0.0130
675	1.0048	0.9830	**0.0218**	**1.0601**	1.0538	0.0063	0.9885	0.9754	0.0131
684	1.0121	0.9875	**0.0246**	-	-	-	0.9871	0.9745	0.0126
611	-	-	-	-	-	-	0.9854	0.9731	0.0123
652	1.0048	0.9878	0.0170	-	-	-	-	-	-
692	0.9964	0.9801	0.0163	1.0198	1.0174	0.0024	0.9846	0.9743	0.0117

It was observed that a slight rise in the PV penetration greatly influences the voltage magnitudes. The voltage difference nearly doubled in phase A on bus 671 compared to the second case study. Likewise, at bus 675, the voltage profile shot to 1.06 p.u, far above the standards-specified limit. Voltage unbalance was also observed on the adjoining buses due to the increased PV penetration. The results obtained show that significant overvoltage occurs due to distributed PV penetration on the downstream of the distribution grid than at the upstream. Voltage variation observed on the grid was different for each phase due to the unbalanced loading of the three-phase distribution system, which increased the impact of voltage unbalance at the PCC as the PV system penetration increased. Figure 4.2 presents the voltage unbalance analysis calculated using the equation defined in the IEC 61000-4-30 standard [179], which uses phase to phase voltages to depict the high-level PV systems' impact on the distribution grid for the three case studies investigated.

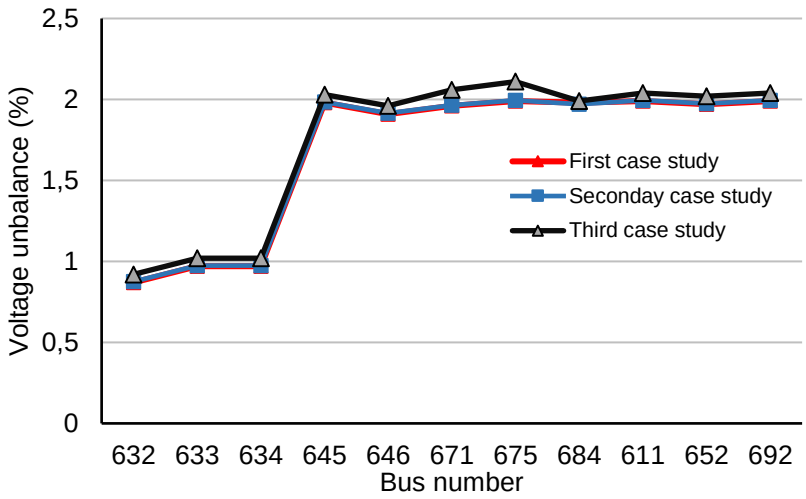

Figure 4.2 Analysis of voltage unbalance at different buses

The National Energy Regulator of South Africa (NERSA) grid code set a limit of 2% for voltage unbalance on the low voltage distribution grid [230]. It is observed in figure 4.3 that the voltage unbalances on the test system varied across the buses with higher percentages noticed at the downstream buses (671, 675, 680, and 692) because of variations in the demands on consumer loads in those buses. In all of the case studies, the voltage unbalance factor followed comparable trends. In the first case study, when the PV system penetrated the grid at bus 632 only, the voltage unbalance factor curve was found to have lower values than the case in the second and third study when the PV systems were distributed across the grid. Although the voltage unbalances were within the required limit stated in [179], for the first case study. The same was not the case for the second case study as the voltage unbalance (VU) was above the limit on bus 671. Likewise, in the third case study, voltage unbalance rose above the limit, notably on buses 671 and 675 to 2.06% and 2.11%, respectively, due to the integration of the dispersed PV systems at the network's downstream. The level of voltage unbalance caused should probably increase when the penetration level of grid-tied PV systems is increased. The result shows that dispersed random integration of PV systems can negatively impact voltage unbalance in the distribution system.

4.2.2 Scenario two: Voltage dip

Voltage dips occur far more often than a total power outage; they cause severe glitches and economic losses [231]. A voltage dip is, by definition, a reduction of the AC voltage, usually between 0.1 and 0.9 p.u at the power frequency, from a

half-cycle (10 ms) to a minute as defined in [232], the IEEE 1159 standard. Voltage dips are usually caused by faulty currents, which cause high voltage drop due to the various system impedances that act as a voltage divider. Voltage dips are not ompatible with sensitive loads such as computers, process controllers, programmable logic controllers (PLC), variable speed drives (VSD), and robotics. These equipment types do shut down whenever the voltage drops below the allowable voltage limit for a specific duration. The more profound and prolonged the dip, the more probable the load will underperform or trip off. These sensitive loads are generally not the bulk of the power demand, but they control many other plant processes. Thus the trip of any of these sensitive loads can cause the entire plant to shut down; hence mitigating these power quality issues is imperative.

The voltage dip caused by balanced and unbalanced faults is a significant power quality concern contributing to the stability problem in distribution systems. The earlier grid codes required the instant disconnection of grid-tied PV inverters during voltage dip events to prevent islanding on the grid [233]. The disconnection of PV inverters' during a voltage dip event has become undesirable with the increased PV system penetration into the distribution grid to prevent massive loss of the PV systems generated power, which could degrade the grid stability [233, 234]. The current grid code and standard requirement specify low voltage ride-through (LVRT) capacity for PV inverters to enable the inverter to stay connected to the grid over a limited period to help voltage recovery in such events [234]. Consequently, a 460 kW PV system is connected to the test system at bus 632, as performed in the third case study of scenario one. The objective of this case study is to show the impact of the PV system's performance on the grid voltage level variation; therefore, two types of system faults have been simulated. Single line to ground and three-phase to ground faults were simulated at 3.5 seconds for a period of 150 milliseconds with PV inverter penetration in an unbalanced distribution system in this section with and without D-STATCOM compensation.

4.2.2.1 Single Phase to Ground Fault

Single-phase to ground (SPG) fault is the most common fault event in a distribution system [235]. This section aims to study a PV inverter's performance

under an unstable condition with and without D-STATCOM compensation. The D-STATCOM was deployed as a parallel voltage dip mitigation device to enhance the simulated grid-tied PV system power quality since the D-STATCOM can balance and regulate the bus and load voltage by generating or absorbing the required reactive power at specific grid buses. Time-domain dynamic simulation of the grid-tied PV system model was implemented in MATLAB/Simulink with and without D-STATCOM compensation. The impacts of the SPG fault on the test system's performance were simulated with a fault resistance of 0.02 ohms. The unbalanced fault event occurred on Phase-A of bus 634, causing a 25 percent voltage dip to the nominal voltage while the two other phases remained undisturbed. Figure 4.3 presents the measured voltage dip at PCC during the event of the single-phase to ground fault.

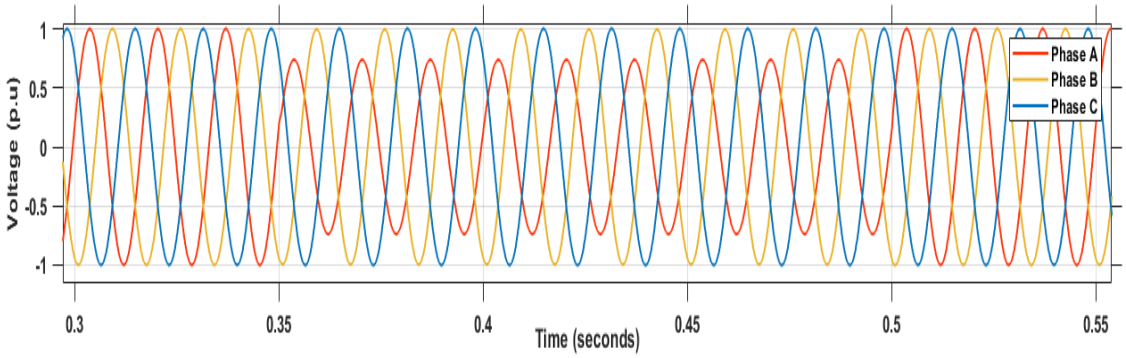

Figure 4.3 Measured three-phase voltage during SPG fault with PV Inverter

A one-second simulation fault was carried out, occurring from time t = 0.35 seconds to 0.5 seconds for 150 milliseconds. The grid response was distorted due to the voltage and current harmonics injected by the PV inverter. Figure 4.4 shows the transient period when the custom power device, the PI-controlled D-STATCOM mitigation method discussed in chapter three, was not connected to the test system. The load voltage dropped to 0.85 p.u, which is below the voltage regulation standard.

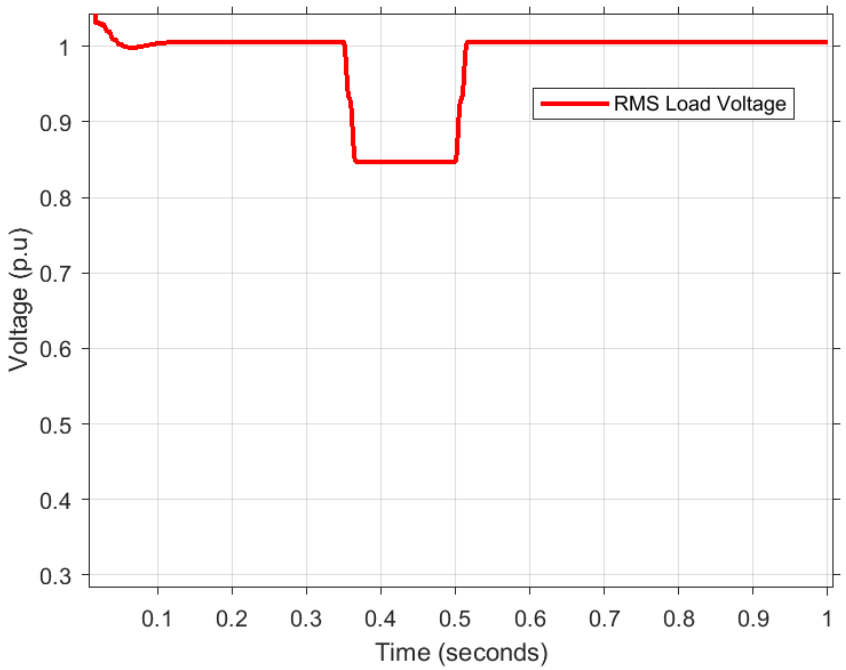

Figure 4.4 RMS load voltage at PCC without D-STATCOM

The same test system was simulated using the same scenario as above, but with a conventional PI-controlled D-STATCOM in operation. The total simulation period was 1000 milliseconds with the D-STATCOM. The device mitigated the voltage dip wholly, and the RMS voltage at the sensitive load was maintained at 100%, as shown in figure 4.5. The PI-controlled D-STATCOM compensated for voltage dip by injecting the required compensating reactive power components to maintain load voltage at the nominal voltage value, which mitigated the voltage dip and delivered a constant voltage at the load. Since the load bus is a voltage-sensitive feeder, it is paramount that the bus's voltage magnitude be maintained at 1 p.u. There was a significant improvement in the voltage recovery after compensation from the event of the voltage dip. The performance of the grid-tied PV system improved with the application of the conventional PI-controlled D-STATCOM.

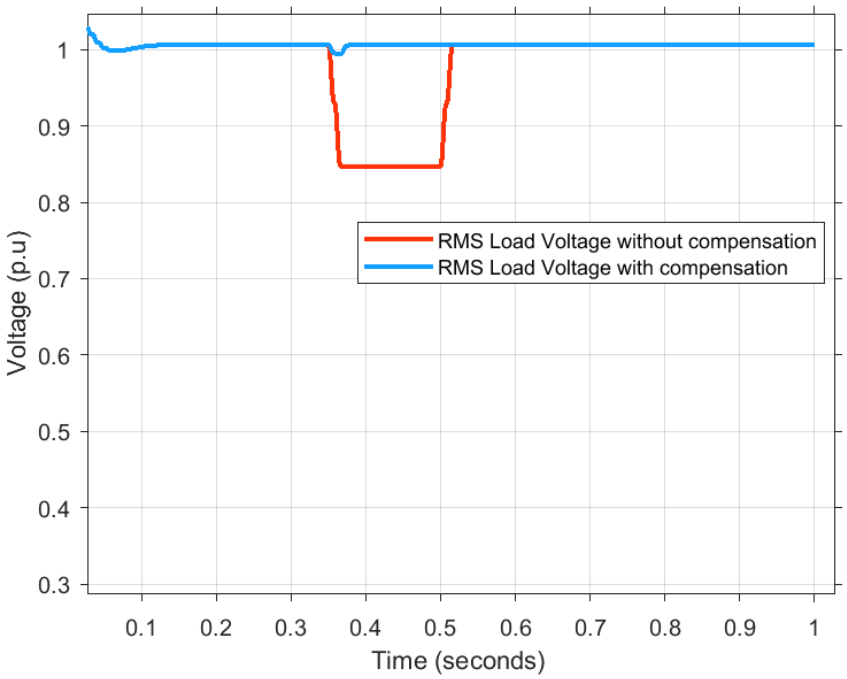

Figure 4.5 RMS voltage (phase A) at PCC with DSTATCOM

The simulation result for the grid-tied PV system's performance with the application of the D-STATCOM with the PI controller is presented in figure 4.6 and compared in terms of keeping the measured PCC voltage balanced. Unlike the waveform obtained in figure 4.3 for the uncompensated grid, figure 4.6 presents the RMS three-phase voltage waveform at the load after the PI-controller-based D-STATCOM compensated the voltage dip. The calculated unbalance current at bus 634 and the sensitive load was 1.14% and 0.15%, which was a significant drop compared to the uncompensated grid with 26.58% and 1.47%, respectively.

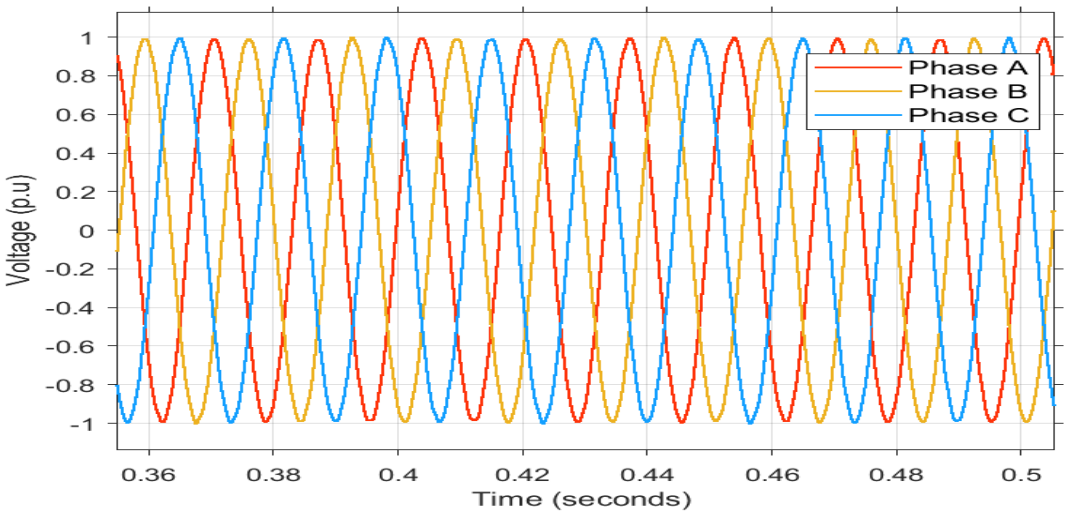

Figure 4.6 Three-phase voltage after D-STATCOM compensate

4.2.2.2 Voltage Harmonics Compensation during Single Phase to Ground Fault

Generally, harmonic distortion occurs during a single-phase fault due to the integration of power electronic devices and loads in the low-voltage distribution grid, resulting in an increase in total harmonic distortion (THD) in the current of the grid and subsequently in the grid voltage. To ensure safe grid operation and avoid deactivation of the grid by electric arc during a single-phase grid fault, the D-STATCOM was implemented to keep the RMS value of the fault current low, thereby reducing the voltage harmonics [236]. A passive filter was connected to the injection transformer at the inverter side to diminish the higher-order harmonics in this simulation. It is evident from the waveform of the sensitive load in figure 4.3 that the harmonics were minimized with a passive filter application. Figures 4.7 to 4.9 present the voltage total harmonic distortion (THD_V) spectrums injected into the grid, before, during, and with D-STATCOM compensation measured at the PCC during the single-phase to ground fault.

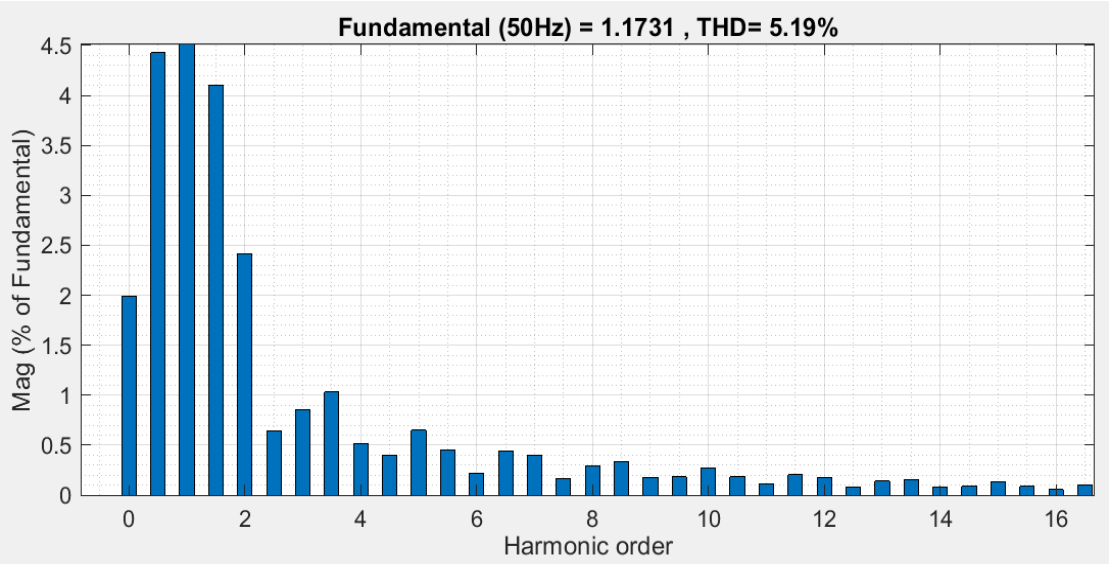

Figure 4.7 Harmonic spectrum before single-phase to ground fault

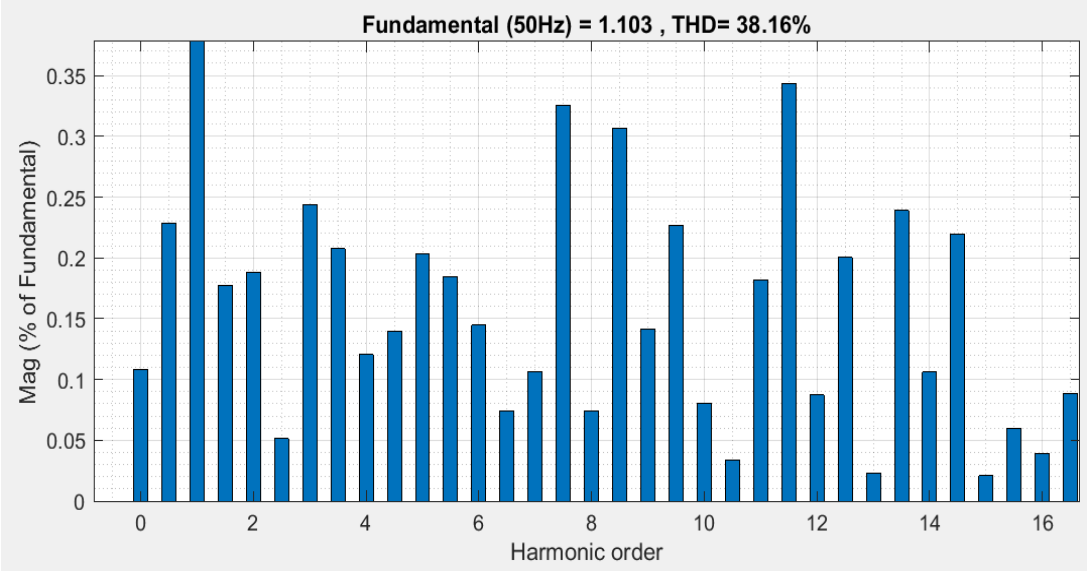

Figure 4.8 Harmonic spectrum during single-phase to ground fault

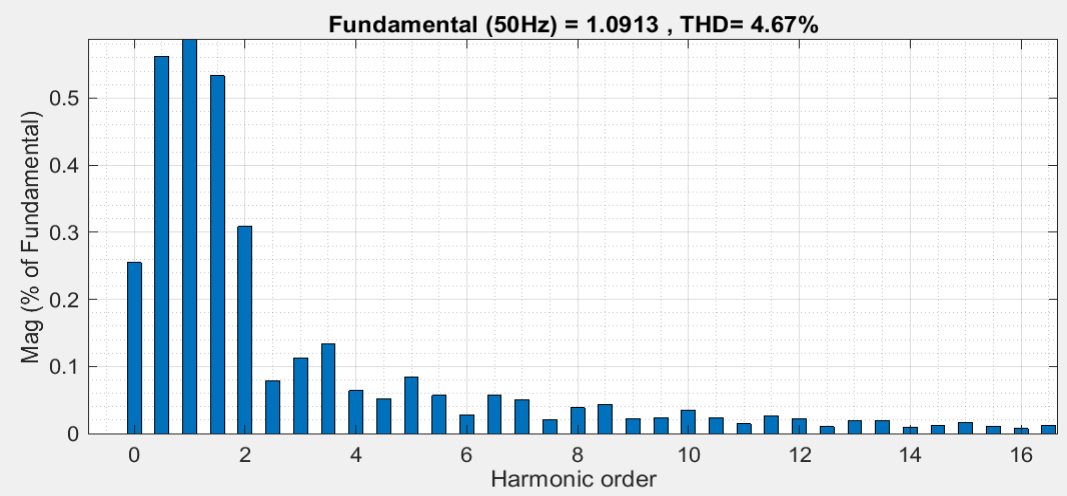

Figure 4.9 Harmonic spectrum with D-STATCOM compensation

It is observed that before the fault, there were no significant harmonics as the total harmonic deviation is 5.19%, which is within the required limit of 8% for voltage harmonics (THDv). During the fault, the measured THDv increased to 39.16%, above the required limit. Figure 4.10 shows the measured THDv at the PCC with D-STATCOM compensation. The FACTS device effectively mitigated the fault impact and improved the grid THDv to 4.67% as measured at the PCC.

4.2.2.3 Three-phase to Ground Fault (TPG)

The three-phase fault is the most unusual type of fault to occur on the distribution [235]. Still, It provides the most conservative fault results, which are most often used to calculate the selection of protective devices and electrical equipment

settings. Usually, a three-phase fault suggests to an electrical engineer the worst-case fault scenario value. For this section, a balanced three-phase to ground fault was simulated on bus 633. From the definition, the three-phase fault is defined as a symmetrical fault. Its significant feature is a huge fault current that brings the grid voltage magnitude to zero at the fault location [237]. This section aims to study a PV inverter's performance under an unstable condition with and without D-STATCOM compensation. The D-STATCOM was applied after the fault event to mitigate the voltage dip occurrence and enhance the simulated grid-tied PV system power quality. Time-domain dynamic simulation of the grid-tied PV system model was implemented in MATLAB/Simulink. with and without D-STATCOM compensation. A fault resistance of 10 ohms was simulated to evaluate the fault's impact on the test system performance. The balanced fault event occurred on all the phases of bus 633, causing more than an 80 percent voltage dip about the nominal voltage. Figure 4.10 presents the measured voltage dip at PCC during the event of the three-phase to ground fault.

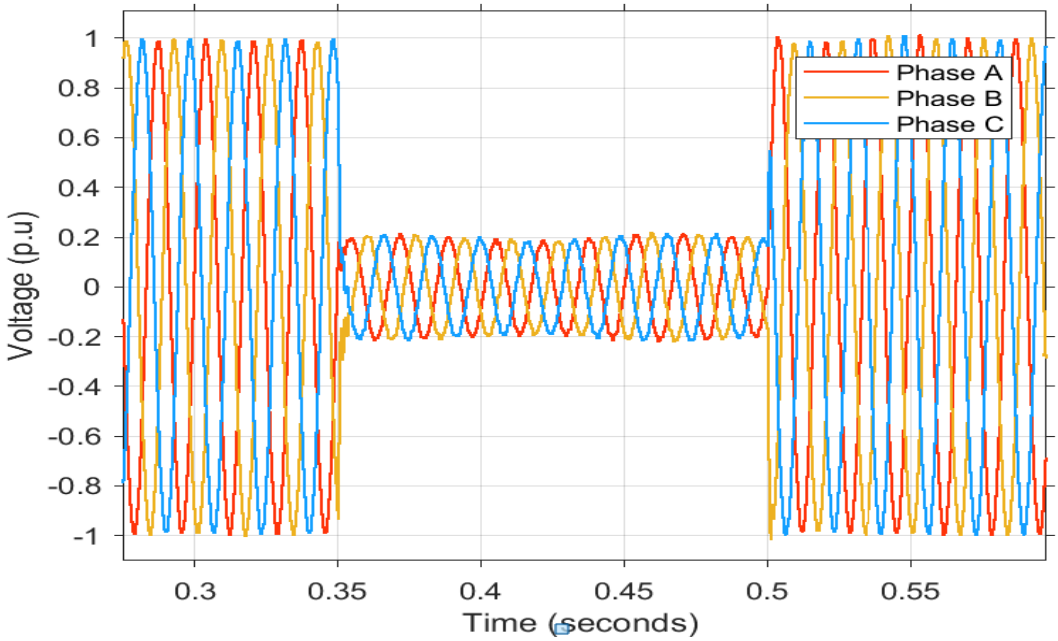

Figure 4.10 Measured three-phase voltage during TPG fault with PV Inverter

A one-second simulation period was considered, with the fault occurring from time t = 0.35 seconds to 0.5 seconds for 150 milliseconds. The grid response was distorted due to the voltage and current harmonics injected by the PV inverter. Figure 4.11 shows the transient period when the custom power device, the PI-controlled D-STATCOM mitigation method discussed in chapter three,

was not applied to any test system buses. The load voltage dropped to 0.15 p.u, which is below the voltage regulation standard.

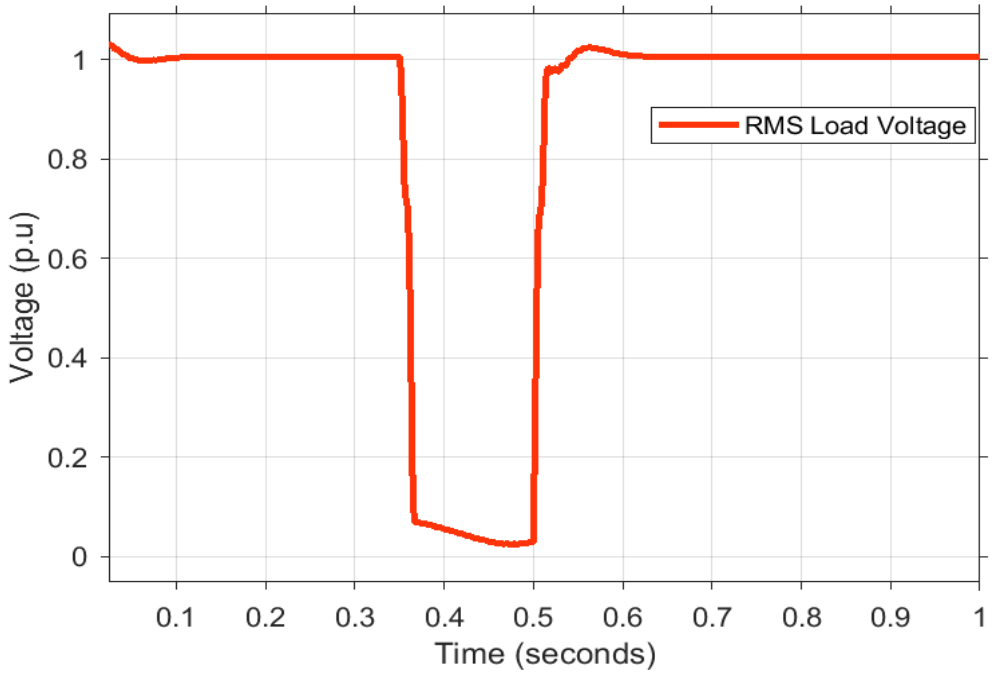

Figure 4.11 RMS voltage dip at PCC without DSTATCOM

The same test system was simulated using the same scenario as above, but with a conventional PI-controlled D-STATCOM in operation. The total simulation period was 1 second with the D-STATCOM. The device completely mitigated the voltage dip, and the RMS voltage at the sensitive load was returned to 1 p.u, as shown in figure 4.12. The PI-controlled D-STATCOM compensated for voltage dip by injecting the required compensating reactive power components to maintain load voltage at the nominal voltage value, which mitigated the voltage dip and delivered a constant voltage at the load. There was a significant improvement in the voltage recovery after compensation from the event of the voltage dip. The performance of the grid-tied PV system improved with the application of the conventional PI-controlled D-STATCOM.

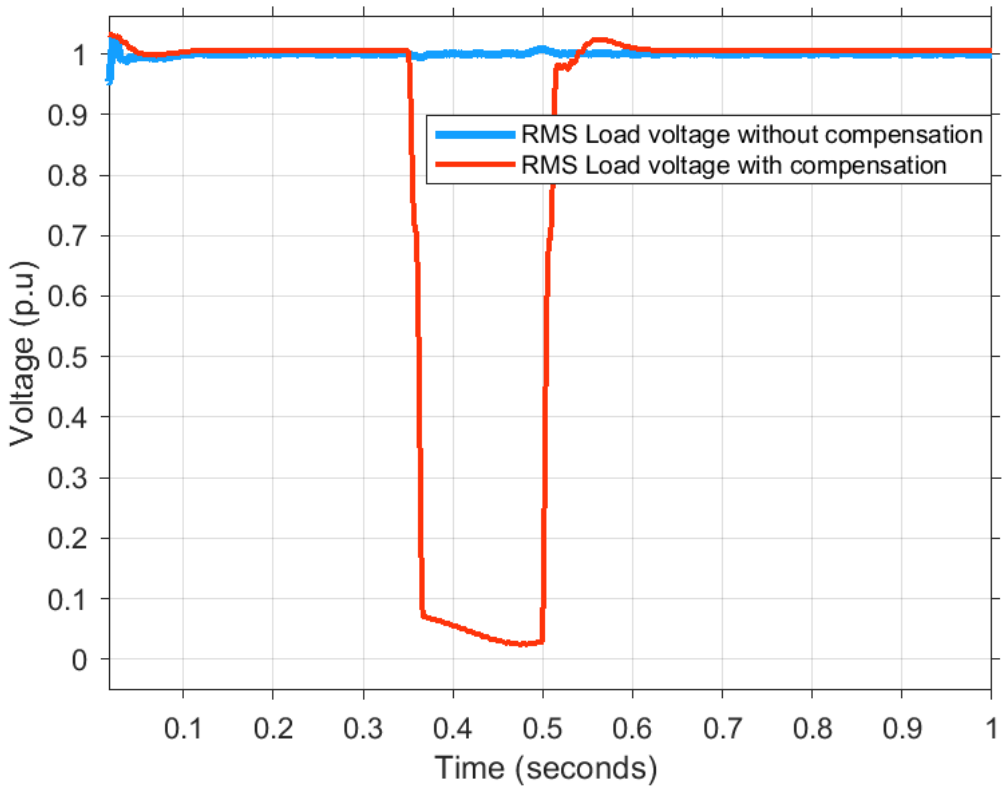

Figure 4.12 RMS voltage at PCC with DSTATCOM

The simulation result for the grid-tied PV system's performance with the application of the PI-controlled D-STATCOM is presented in figure 4.12 and compared in terms of keeping the measured PCC voltage balanced. Unlike the waveform obtained in figure 4.10 for the uncompensated grid, figure 4.13 presents the RMS three-phase voltage waveform at the load after the PI-controller-based D-STATCOM compensated the voltage dip. The calculated current unbalances at bus 633, and the sensitive load were 1.26% and 0.59%, which significantly dropped compared to the uncompensated grid with 31.71% and 1.83%.

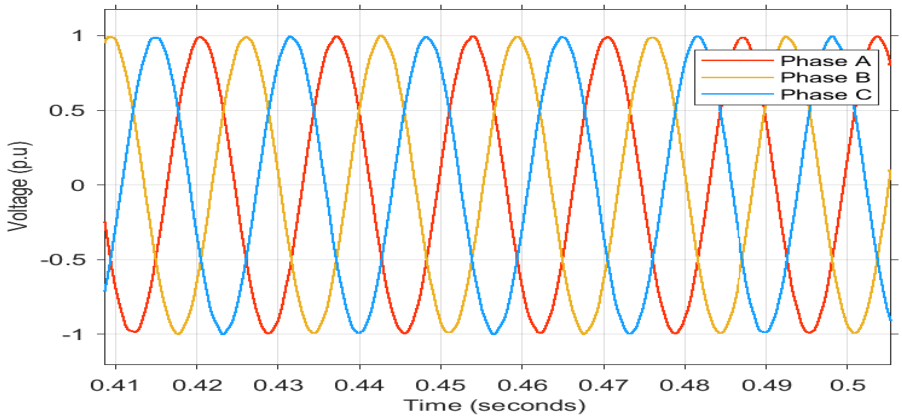

Figure 4.13 Three-phase voltage after D-STATCOM compensate TPF

4.2.2.4 Voltage Harmonics Compensation during Three Phase Fault

Generally, harmonic distortion occurs during a single-phase fault due to the integration of power electronics devices and loads in the low-voltage distribution grid, resulting in an increase in total harmonic distortion (THD) in the grid current subsequently in the grid voltage. To ensure safe grid operation and avoid deactivation of the grid by electric arc during a single-phase grid fault, the D-STATCOM was implemented to keep the RMS value of the fault current low, thereby reducing the voltage harmonics [236]. A passive filter was connected at the inverter side to the injection transformer to diminish the higher-order harmonics in this simulation. It is evident from the waveform of the sensitive load in figure 4.3 that the harmonics were minimized with a passive filter application. Figures 4.14 to 4.16 present the voltage total harmonic distortion (THD_V) spectrums injected into the grid, before, during, and with D-STATCOM compensation measured at the PCC during the three-phase to ground fault.

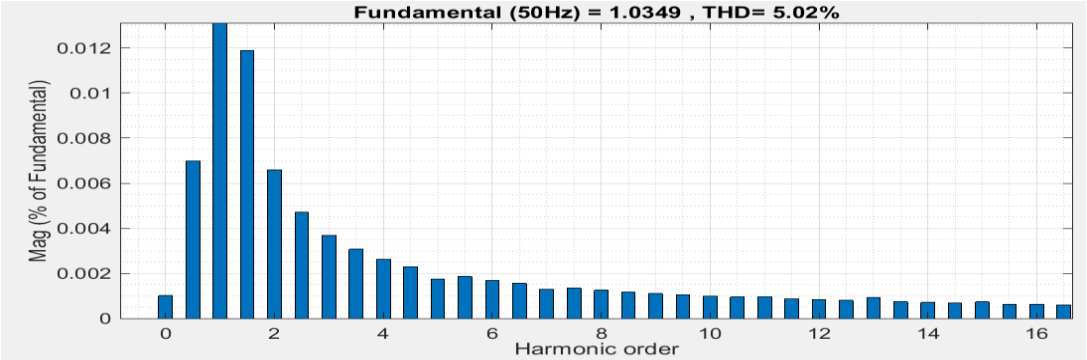

Figure 4.14 Harmonic spectrum before three-phase to ground fault

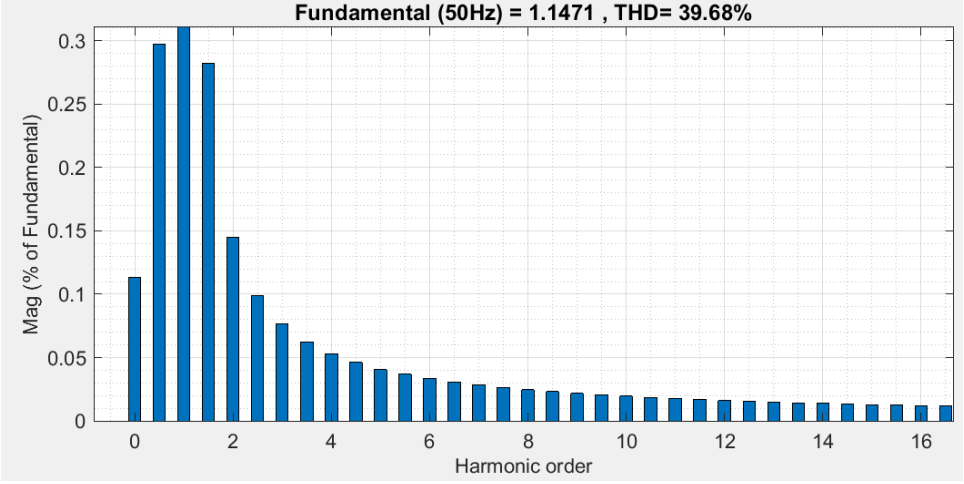

Figure 4.15 Harmonic spectrum during three-phase to ground fault

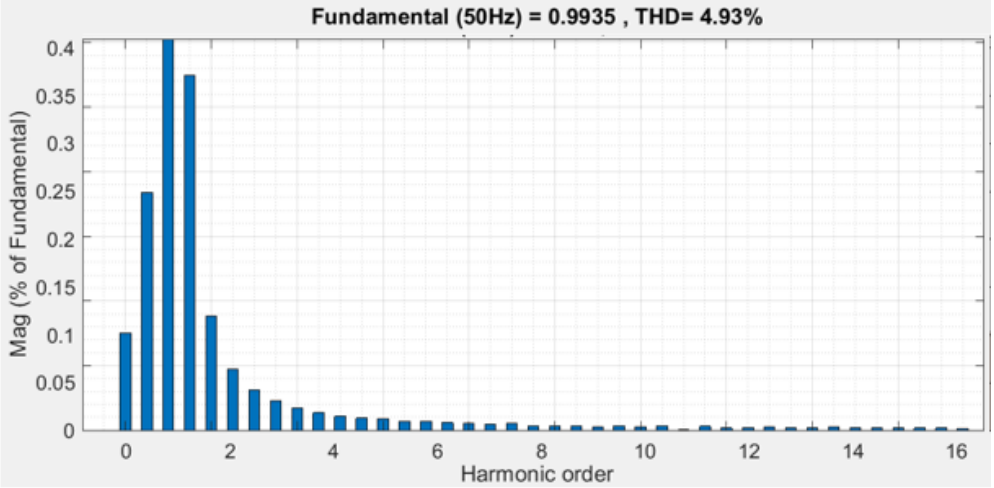

Figure 4.16 Harmonic spectrum with D-STATCOM compensation

It is observed from the simulation results that the PI-controlled D-STATCOM effectively mitigated the voltage dip in both study cases. It also reduced the voltage total harmonic distortion on the system with an LCL passive filter to validate the principle of applying the D-STATCOM for voltage regulation.

4.3 Field Investigation of Voltage Quality

This section discusses the field measurements conducted on the 110-kW grid-tied PV system located at the Steve Biko campus of the Durban University of Technology (DUT) to investigate the performance and impact of a PV system on voltage quality in a typical distribution system.

4.3.1. Overview of the Field Grid-tied PV System for Power Quality Analysis

The Energy Technology Station of the Durban University of Technology at the Steve Biko campus (-29.8579 N; 31.0276 E) has installed a 110-kW grid-tied PV system mounted on the campus library rooftop at a fixed tilted angle of 30^{o}. The system has 328 poly-crystalline silicon (330 and 340 Watt) PV panels connected in series into eleven strings to four different DC-AC inverters. There are SOLYS2 sun trackers and a pyranometer, as shown in figure 4.17(a). The installed pyranometer sensor has a high precision rate of 1 W/m^2 resolution and converts the global horizontal solar irradiation (GHI) it receives to an electrical signal that can be measured.

Figure 4.17 (a) Installed meteorological station (b) Installed PV array

The installation has four different three-phase inverters rated 27.6 kW. Each is equipped with a maximum power point tracking (MPPT) controller; the PV array terminates on these inverters' input ports, with the output connected directly to the grid. Figure 4.19 shows the grid-tied PV system DC-AC inverters. Tables 4.1 and 4.2 present the electrical characteristics of the PV panels and the inverters' specifications.


Figure 4.18 The three-phase inverter

Table 4. 4 Characteristics of the PV panels

(ARTsolar 330-72)	
Description	***Value***
Maximum Power (P_{max})	330 W
Maximum voltage at Peak Power (V_{max})	37.4 V
Maximum Current at Peak Power (I_{max})	8.83 A
Open circuit voltage (V_{oc})	46.1 V
Short-Circuit Current (I_{SC})	9.3 A
(ARTsolar 340-72)	
Maximum Power (P_{max})	340 W
Maximum voltage at Peak Power (V_{max})	37.8 V
Maximum Current at Peak Power (I_{max})	9.0 A
Open circuit voltage (V_{oc})	46.3 V
Short-Circuit Current (I_{SC})	9.41 A

Table 4. 5 Three-phase Solar Edge Inverter SE-27.6K

Output	
Rated AC power output	27 600 VA
Maximum power output	27 600 VA
Nominal output voltage: Line to Line/Line to Neutral	400/230 V_{ac}
Maximum output current (per phase)	40 A
Frequency	50 ± 5 Hz
Three-phase grid support	WYE with neutral
Input	
Maximum DC power (STC)	37 250 W
Maximum input voltage	900 V_{dc}
Nominal DC input voltage	750 V_{dc}
Maximum input current	40 A_{dc}
Transformerless	Yes

The low voltage distribution grid-tied PV system's power quality data was measured with an ELSPEC Power Quality Analyzer. This PQ measurement device meets the IEC 61000-4-30 Class A specifications requirement of

intelligently functional power quality measuring equipment. The PQ analyzer was connected to the PCC as required by the grid code at the 22/11kV substation power board as shown in figure 4.19; it logged data such as voltage, current, power, flicker, frequency, and harmonics parameters. The PV array power output was captured from the inverter, and the solar irradiation data were recorded from the radiometric station. The data collected were extracted to a personal computer (PC) for further analysis.

Figure 4.19 Set-up of the field data measurement at PCC

The DUT 110 kW grid-tied PV system power quality data were recorded in August 2020 at the PCC for performance analysis, and three scenarios were considered in this analysis:

- No power production.
- A 25%, 50%, 75%, and 100% PV power production on a sunny day.
- The grid-tied PV system performance on a cloudy day.

The monthly average GHI and the ambient temperature for the study period is presented in figure 4.20. It represents the Durban city annual radiometric data pattern, showing the monthly average solar irradiation dropping during the winter and increasing during the summer season. The maximum daily solar irradiation per month ranged from the lowest value of 110 kWh/m^2 in June to 190 kWh/m^2 in January. The highest monthly average temperatures of 26^{o}C, 25^{o}C, and 24^{o}C were recorded in January, February, and March, respectively, while the lowest monthly average temperatures were recorded in June and July, respectively, as 15^{o}C and 16^{o}C.

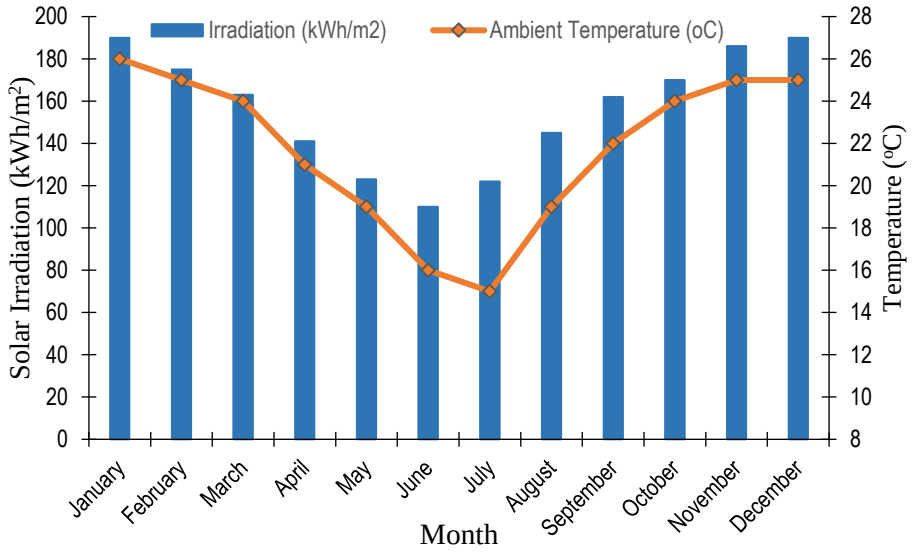

Figure 4.20 Monthly average global horizontal solar irradiation and temperature

Figure 4.21 depicts the solar irradiation pattern on a sunny day, while figure 4.22 presents the irradiation curve on a cloudy day when the PV array received less solar irradiation. The GHI peaked at around 980 W/m^2 on a sunny day with high solar irradiation intensity while it declined and remained unstable throughout the days with less solar irradiation.

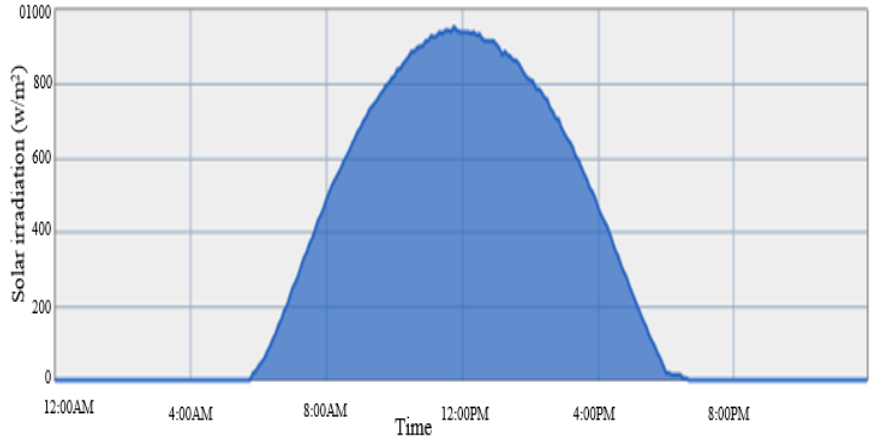

Figure 4.21 Solar irradiation plot on a sunny

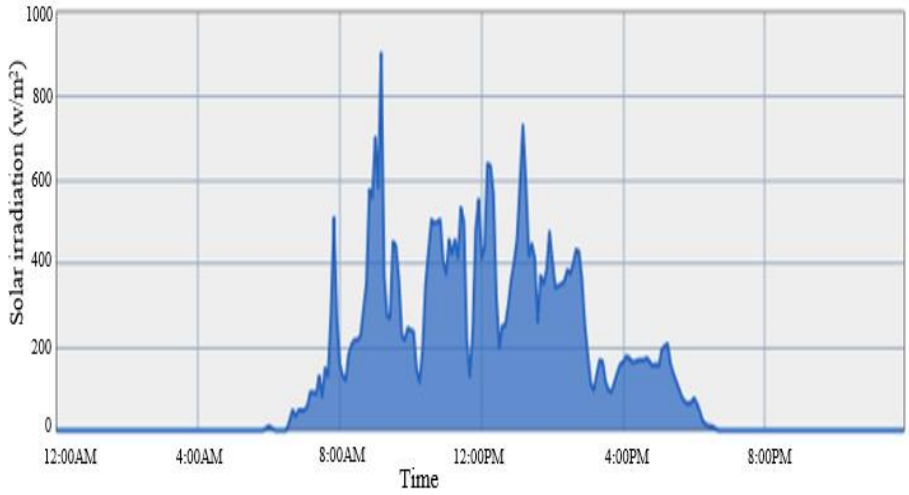

Figure 4.22 Solar irradiation plot on a cloudy day

4.3.2 Characterization of the Grid-tied PV Output Power

It is crucial to analyze the recorded data for the PV system power production, as this impacts all other measured parameters. In this section, PV output power from the three sunniest and three cloudiest days' is analyzed and compared. Figures 4.23 and 4.24 show the active and reactive power plots on sunny days (August 11, 12, and 15, 2020) and cloudy days (August 16 – 18, 2020), representing the period when the arrays had stable and varied solar irradiation during this study. The active power characterized the high solar irradiation, with a peak above 80 kW per phase. During load shedding, reverse power flow (-3,738 kW) was measured at the point that the generated power could not be fed into the grid, which caused the reactive power to drop to -31,35 kVAr.

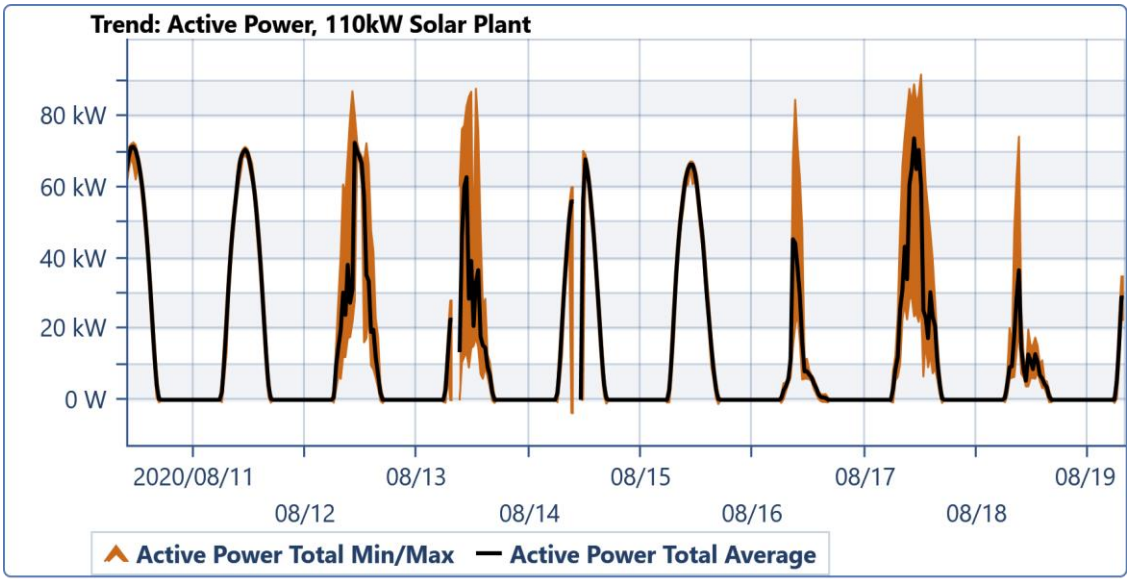

Figure 4.23 The 110 kW grid-tied PV system active power output on a sunny and cloudy day

Table 4. 6 The active power production

Component	Parameter	Minimum	Maximum	Average
110 kW solar plant	Total active power	-3.74 kW	91.96 kW	12,85 kW

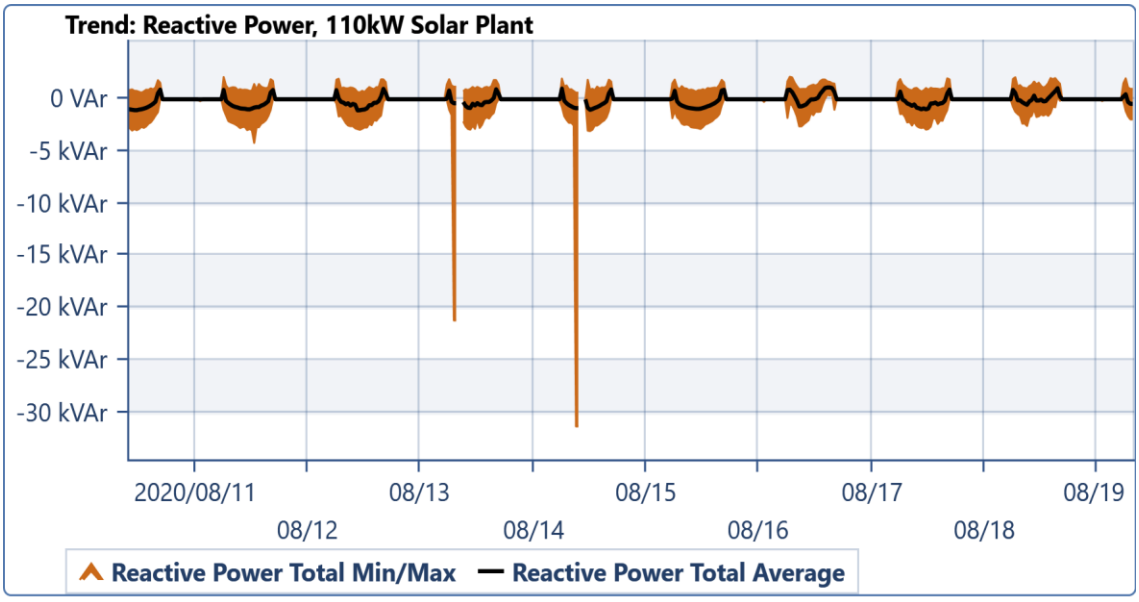

Figure 4.24 The 110 kW grid-tied PV system reactive power on a sunny and cloudy day

Table 4. 7 The reactive power production

Component	Parameter	Minimum	Maximum	Average
110 kW solar plant	Total reactive power	-31.35 kVAr	2.15 kVAr	-105.96 VAr

Figures 4.25 and 4.26 present the daily active and reactive power plot on a sunny day (August 11, 2020). Figure 4.25 demonstrates the linear relationship between

the solar irradiation and PV output power as the power output recorded a peak power of 71.52 kW, which is much higher than that obtained for the cloudy days.

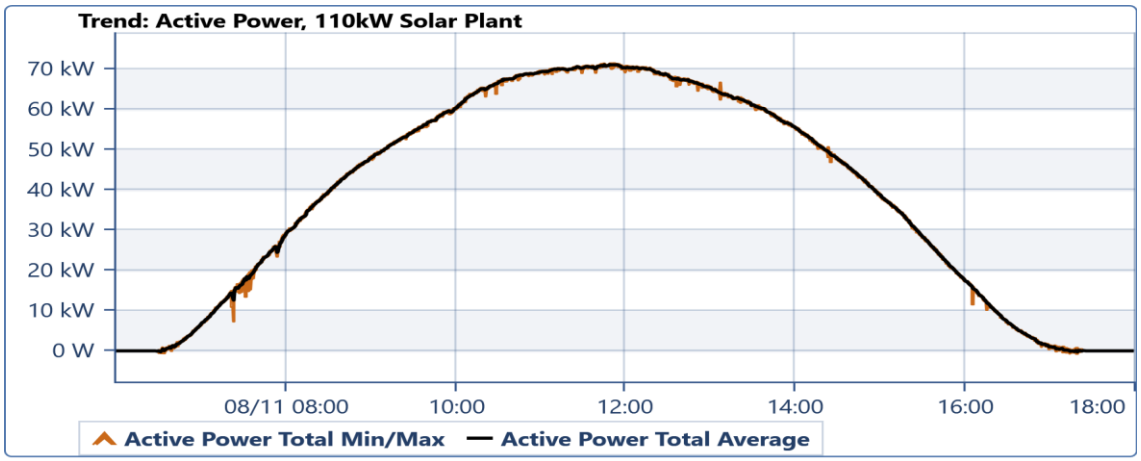

Figure 4.25 The grid-tied PV system active power output on a sunny day

Table 4. 8 The daily active power production

Component	Parameter	Minimum	Maximum	Average
110 kW solar plant	Total active power	-792.68 W	71.52 kW	38.44 kW

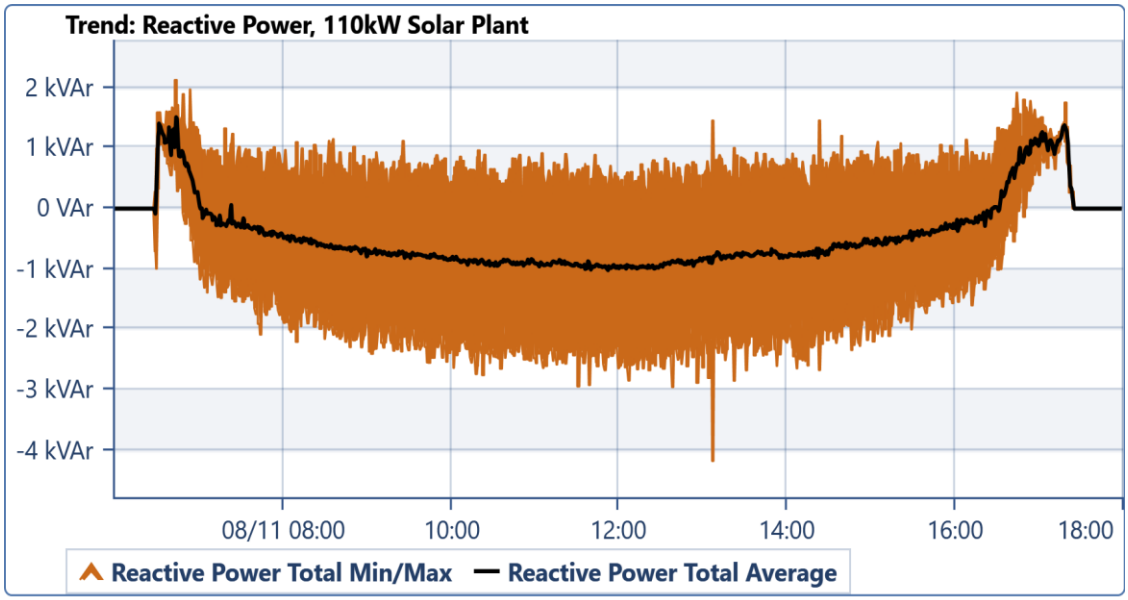

Figure 4.26 The grid-tied PV system reactive power output on a sunny day

Table 4. 9 The active power production

Component	Parameter	Minimum	Maximum	Average
110 kW solar plant	Total reactive power	-31,35 kVAr	2,151 kVAr	-105,959 VAr

4.3.3 Voltage Performance of the 110k W PV System

Voltage quality due to reverse power flow has become one of the major concerns of power utilities as PV system penetration in the distribution system increases. The grid voltages are sometimes distorted due to the intermittent nature of solar irradiation and temperature coupled with the potential external disturbances, which primarily influence the PV system's performance causing voltage dips and rises that skew the voltage waveform and harmonic values. Figures 4.27 and 4.28 depict the measured voltage magnitudes at the upstream and downstream of the distribution system on selected PV system operating days. The measured RMS phase to ground voltage level in the grid upstream rose to 1.06 p.u above the limit, as presented in figure 4.27. However, the least system voltage level obtained in figure 4.28 was 0.98 p.u on phase A which was within the allowable limit, with respect to the PV power injection at the peak of solar irradiation as it had installed an On-Load Tap Changer transformer, which regulates the voltage magnitudes. It is the more reason the upstream bus exhibit higher voltage levels compared to downstream bus voltages.

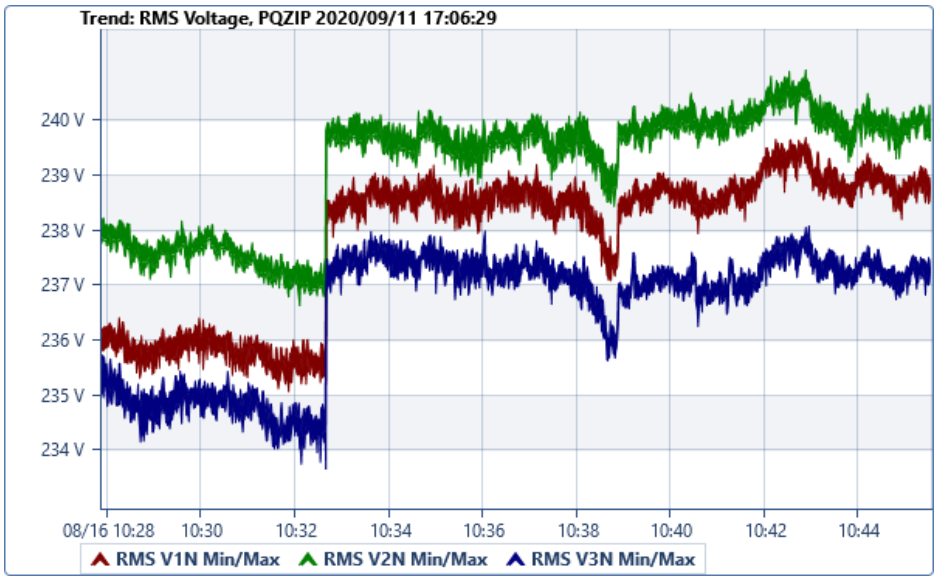

Figure 4.27 Voltage profile at the upstream of the distribution system

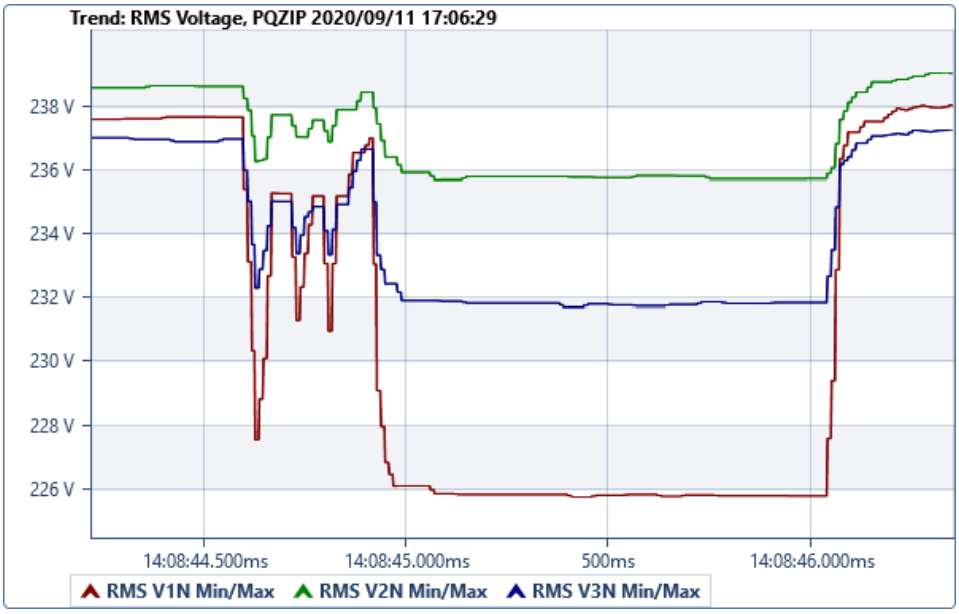

Figure 4.28 Voltage profile at the downstream of the distribution system

A brief transient current surge occurred on the grid, as depicted in figure 4.28, which exceeded the rated maximum output current (per phase). It was followed by a short period of marginally higher current than the rated current, which lasted only 0.1 seconds for the fault events.

The university load pattern is comparable to a commercial consumer load pattern, as depicted in Figure 3.29, with peak load demand between 7 am and 6 pm. It is observed from Figure 4.29 that the voltage levels during the low-load period (night-time), when there is no solar irradiation, range between 0.99 - 1.05 p.u, which is within limits.

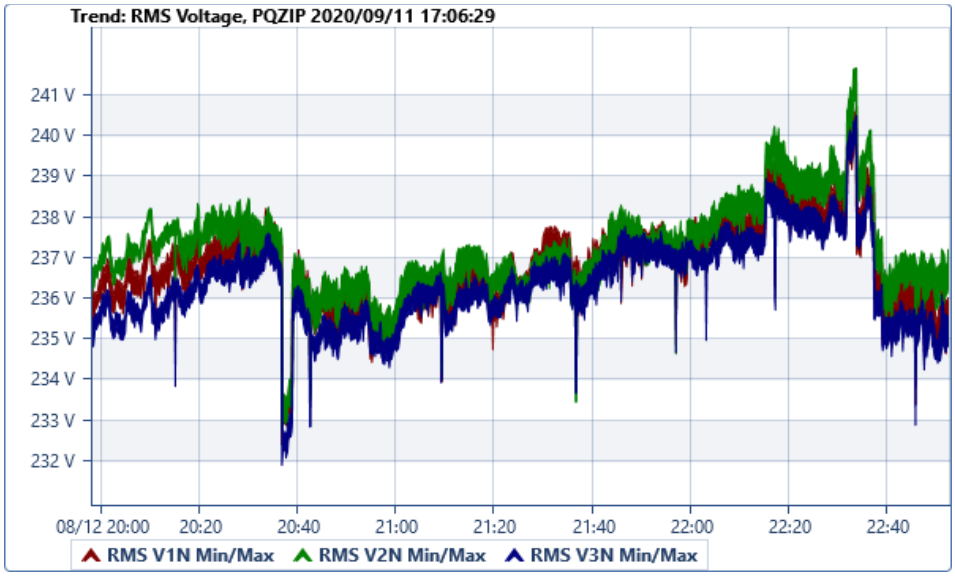

Figure 4.29 Voltages during the low-load period

Voltage total harmonic distortion (THD_V) and current total demand distortion (TDD_i) were used for this study analysis to get a better insight since the current THD was misleading during low loading/solar irradiation when some harmonics approach the fundamental current. The current TDD provided a more realistic representation of harmonics during low load demand/solar irradiation conditions.

4.3.3.1 Scenario 1: No Power Production

When there was no solar irradiation available during nighttime, the PV array did not produce energy. Therefore, there was no current flow during night time sample; this section presents the different grid performance analysis results obtained during the no solar production period. The following performance values were measured:

- The average voltage regulation varied between 234V_{LN} and 241V_{LN}.
- The voltage THD varied between 1.89% and 3.47%.
- Voltage harmonic spectrum showed that the:
  - 3rd order voltage harmonic was up to 0.58%
  - 5th order voltage harmonic was up to 2.54%
  - 7th order voltage harmonic was up to 0.67%
  - 11th order voltage harmonic was up to 0.29%
  - 13th order voltage harmonic was up to 0.08%

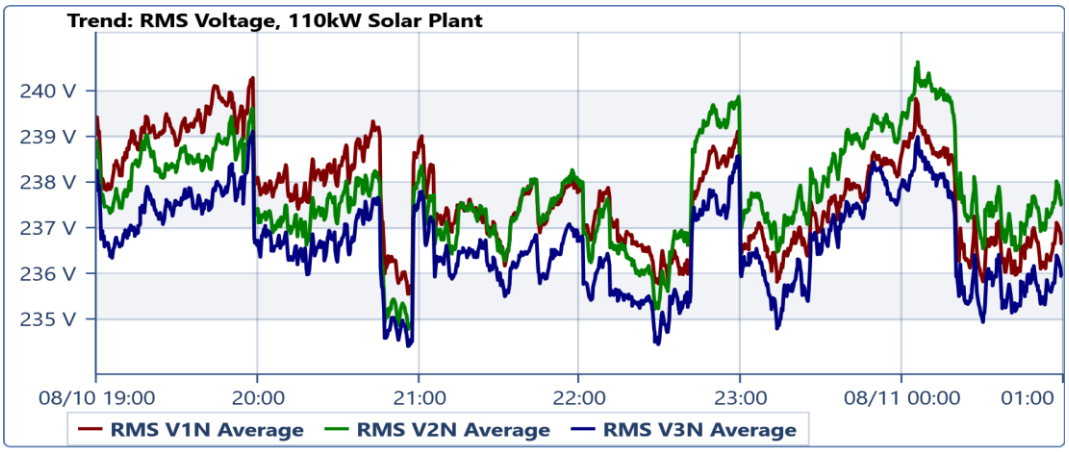

Figure 4.30 RMS three-phase average voltage during no energy production

Table 4. 10 Summary of the three-phase average voltage during no energy production

Component	Parameter	Minimum	Maximum	Average
110 kW solar plant	RMS V_1N	233.79 V	240.78 V	237.73 V
110 kW solar plant	RMS V_2N	233.53 V	241.02 V	237.76 V
110 kW solar plant	RMS V_3N	232.91 V	239.57 V	236.64 V

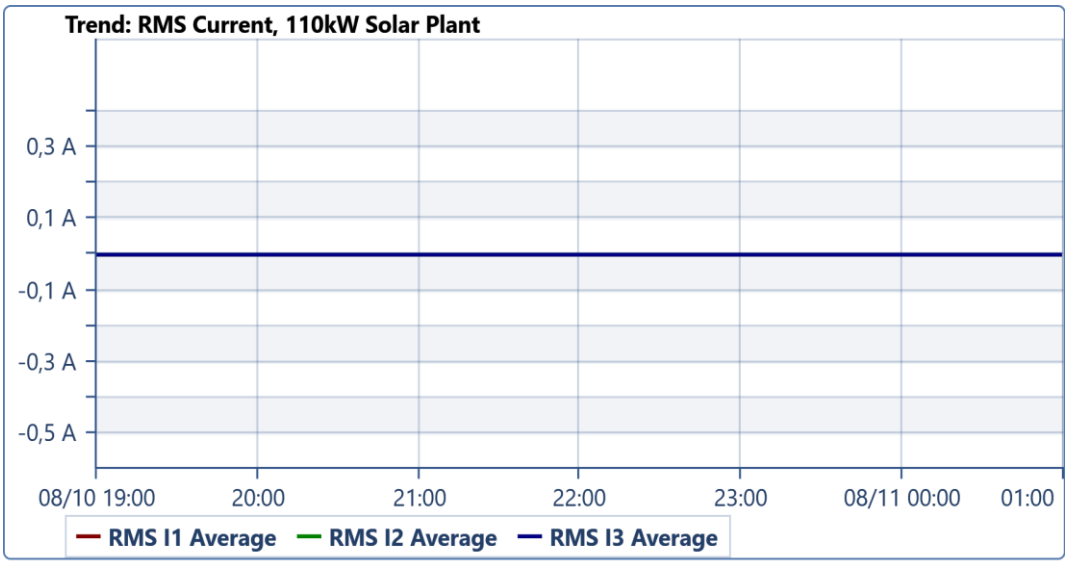

Figure 4.31 Measured RMS three-phase current during no energy production

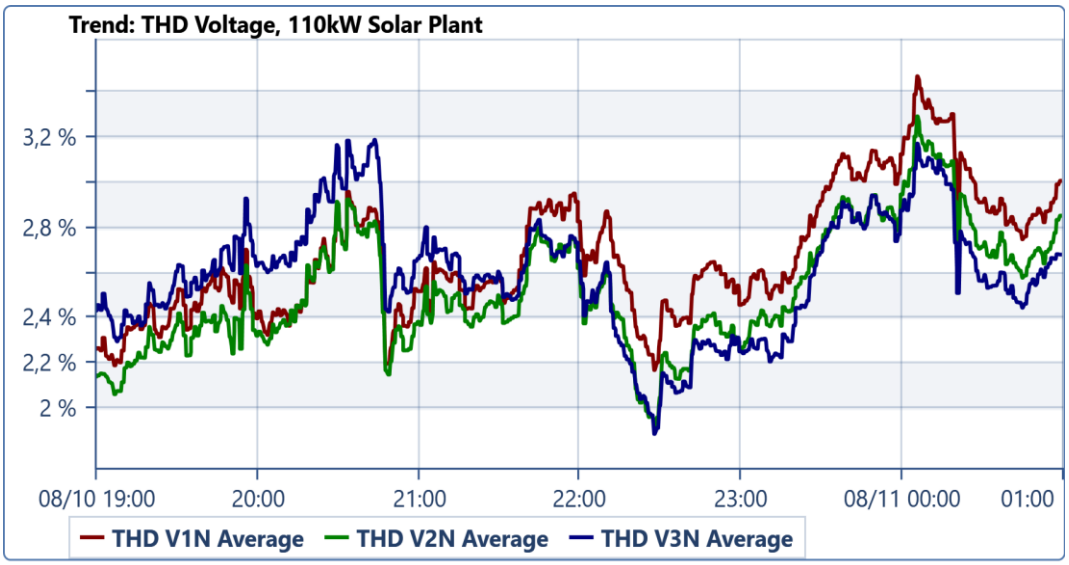

Figure 4.32 Measured three-phase voltage THD during no energy production

Table 4. 11 The three-phase voltage THD during no energy production

Component	Parameter	Minimum	Maximum	Average
110 kW solar plant	THD V_1N	1.91%	4.83%	3.27%
110 kW solar plant	THD V_2N	1.89%	5.26.%	3.53%
110 kW solar plant	THD V_3N	1.84%	3.47%	2.61%

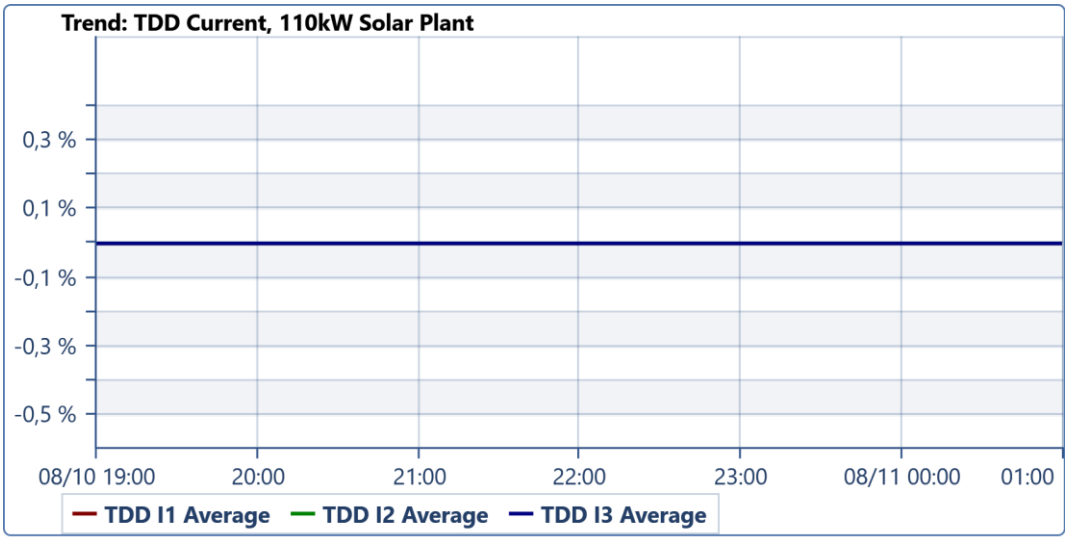

Figure 4.33 Measured three-phase current TDD during no energy production

Table 4. 12 The three-phase voltage THD during no energy production

Component	Parameter	Minimum	Maximum	Average
110 kW solar plant	TDD I_1N	0%	0%	0%
110 kW solar plant	TDD I_2N	0%	0%	0%
110 kW solar plant	TDD I_3N	0%	0%	0%

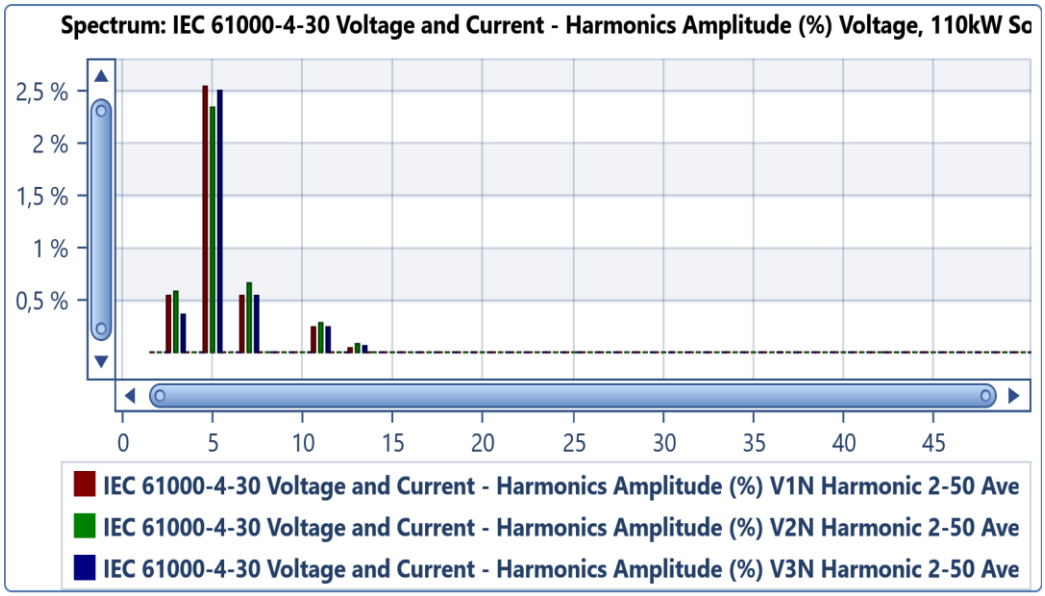

Figure 4.34 Measured voltage harmonics spectrum during no energy production

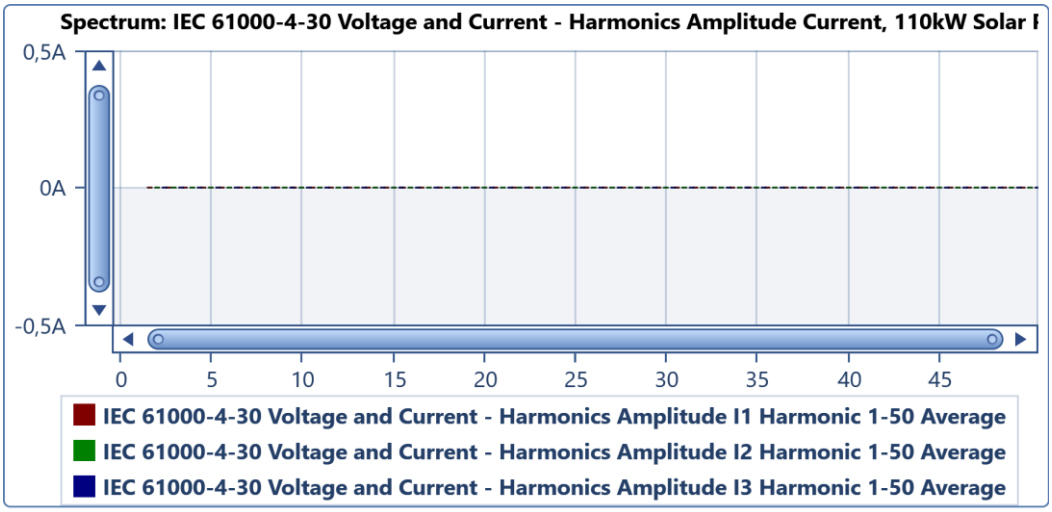

Figure 4.35 Measured current harmonics TDD spectrum during no energy production

4.3.3.2 Scenario 2: PV power production on a sunny day

This section considered the grid-tied PV system 100% solar production. During 100% production, the following values were measured:

- Voltage THD varies between 1.51% and 1.87%
- The TDD current up to 1.54%
- Voltage harmonic spectrum show:
  - 3rd of up to 0.55%
  - 5th of up to 1.6%
  - 7th of up to 0.59%
  - 11th of up to 0.24%
  - 13th of up to 0.13%
- Current harmonic spectrum show (production average):
  - 5th of up to 1.72A

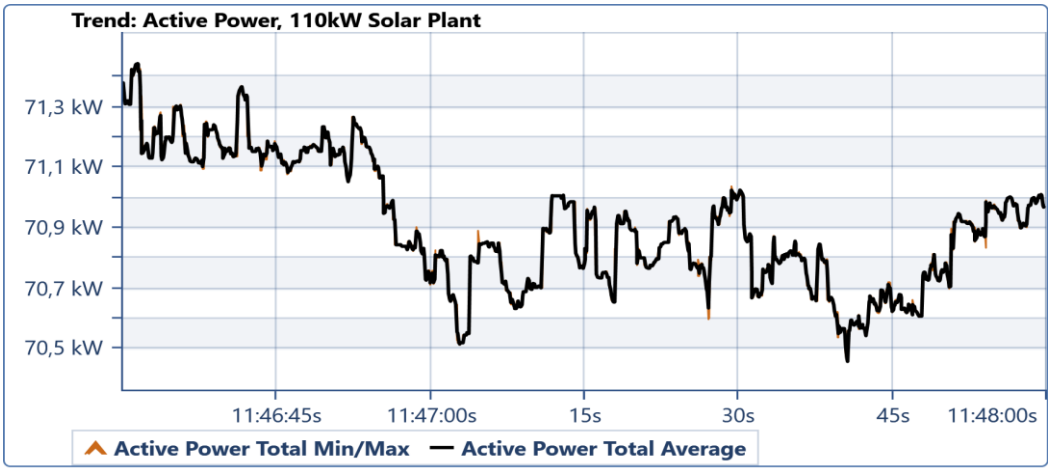

Figure 4. 36 Measured active power generated at 100% solar production on a sunny day

Table 4. 13 Measured active power generated at 100% solar production

Component	Parameter	Minimum	Maximum	Average
110 kW solar plant	Active Power Total	70.46 kW	71.45 kW	70.91 kW

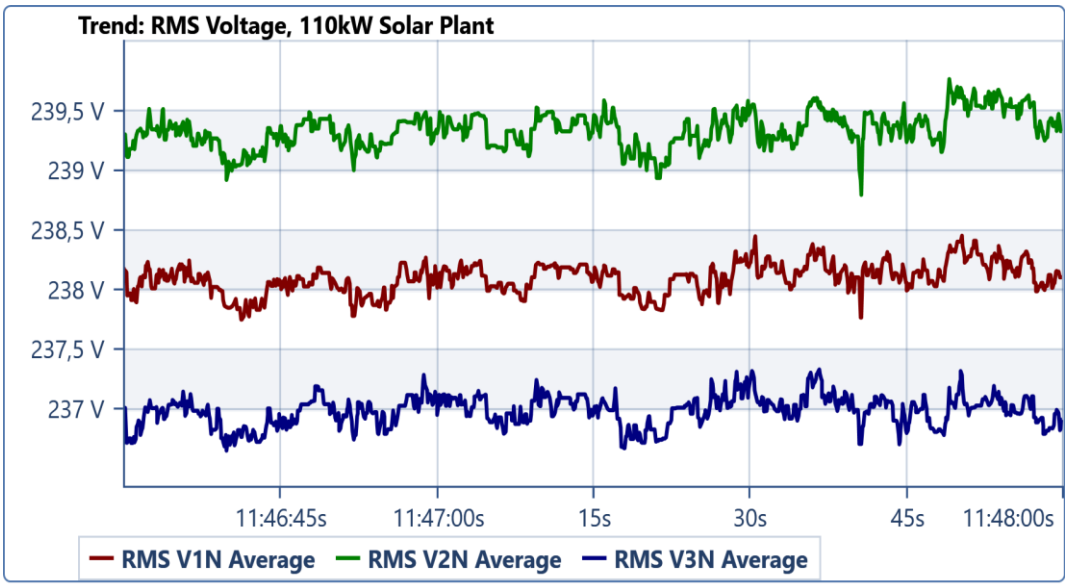

Figure 4.37 RMS three-phase voltage during 100% solar production on a sunny day

Table 4.14 Measured RMS three-phase voltage at 100% solar production

Component	Parameter	Minimum	Maximum	Average
110 kW solar plant	RMS V_1N	237.76 V	238.49 V	238.12 V
110 kW solar plant	RMS V_2N	238.80 V	241.67 V	239.34 V
110 kW solar plant	RMS V_3N	236.65 V	237.34 V	236.99 V

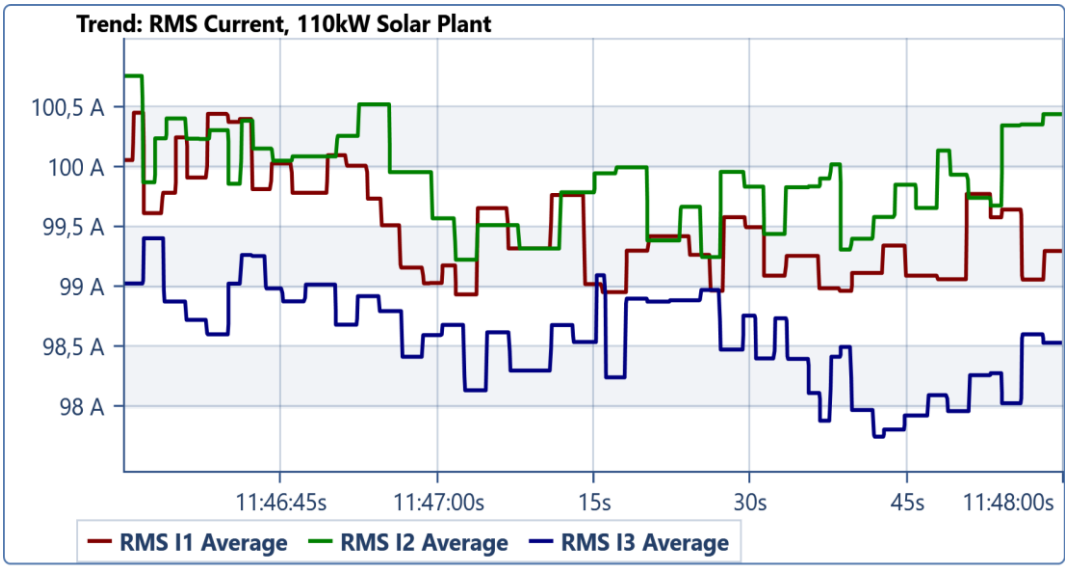

Figure 4.38 RMS three-phase current during 100% solar production on a sunny day

Table 4.15 Measured RMS three-phase current at 100% solar production

Component	Parameter	Minimum	Maximum	Average
110 kW solar plant	RMS I_1	98.94 A	100.46 A	99.51 A
110 kW solar plant	RMS I_2	99.23 A	100.77 A	99.89 A
110 kW solar plant	RMS I_3	97.76 A	99.41 A	98.58 A

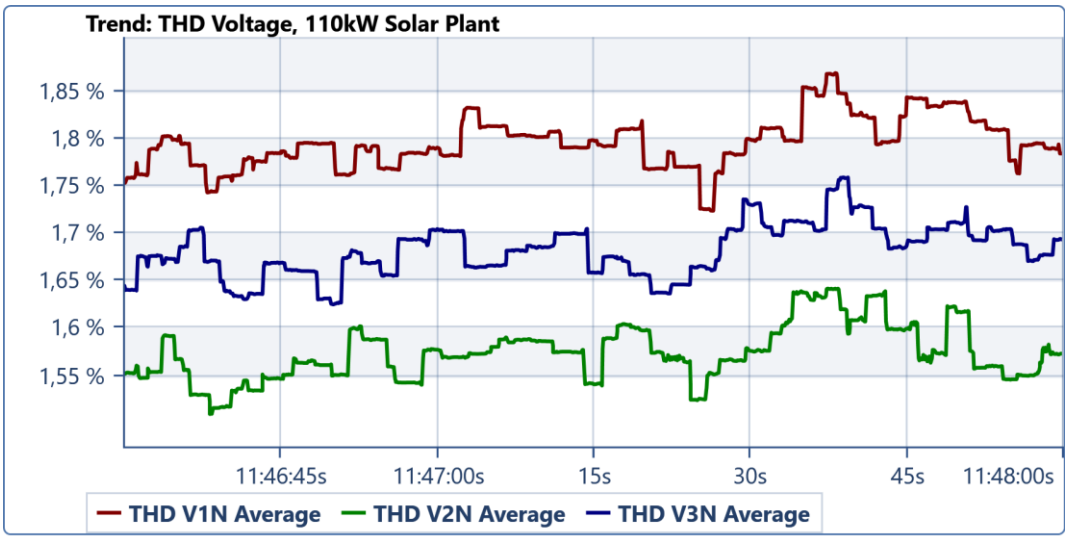

Figure 4.39 Measured voltage THD during 100% solar production on a sunny day

Table 4.16 The three-phase voltage THD during 100% solar production on a sunny day

Component	Parameter	Minimum	Maximum	Average
110 kW solar plant	THD V_1N	1.72 %	1.87 %	1.81 %
110 kW solar plant	THD V_2N	1.51 %	1.64 %	1.57 %
110 kW solar plant	THD V_3N	1.63 %	1.76 %	1.68 %

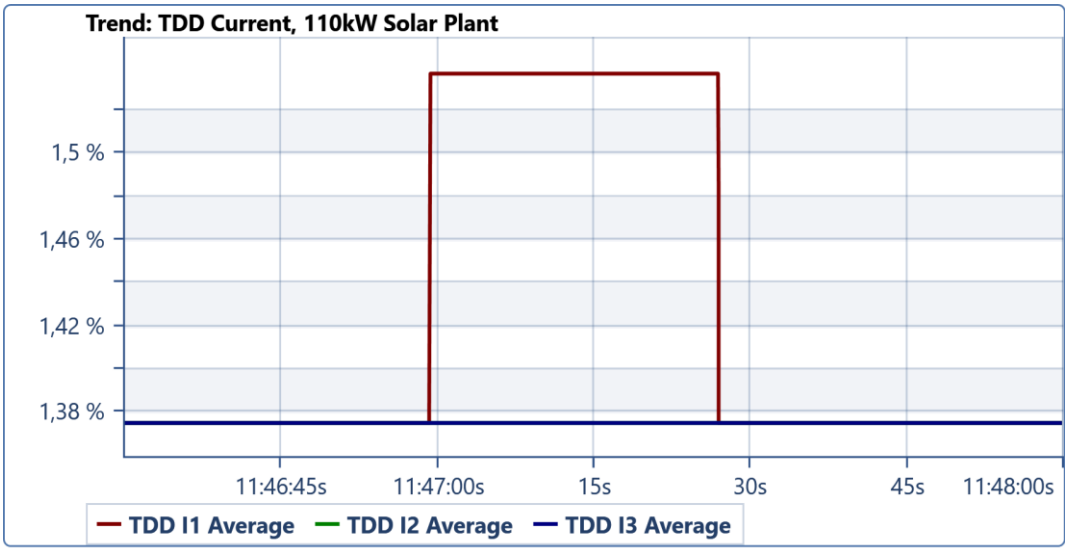

Figure 4.40 Measured current TDD during 100% solar production on a sunny day

Table 4. 17 Summary of the current TDD during 100% solar production on a sunny day

Component	Parameter	Minimum	Maximum	Average
110 kW solar plant	TDD I_1	1.38 %	1.54 %	1.43 %
110 kW solar plant	TDD I_2	1.38 %	1.38 %	1.38 %
110 kW solar plant	TDD I_3	1.38 %	1.38 %	1.38 %

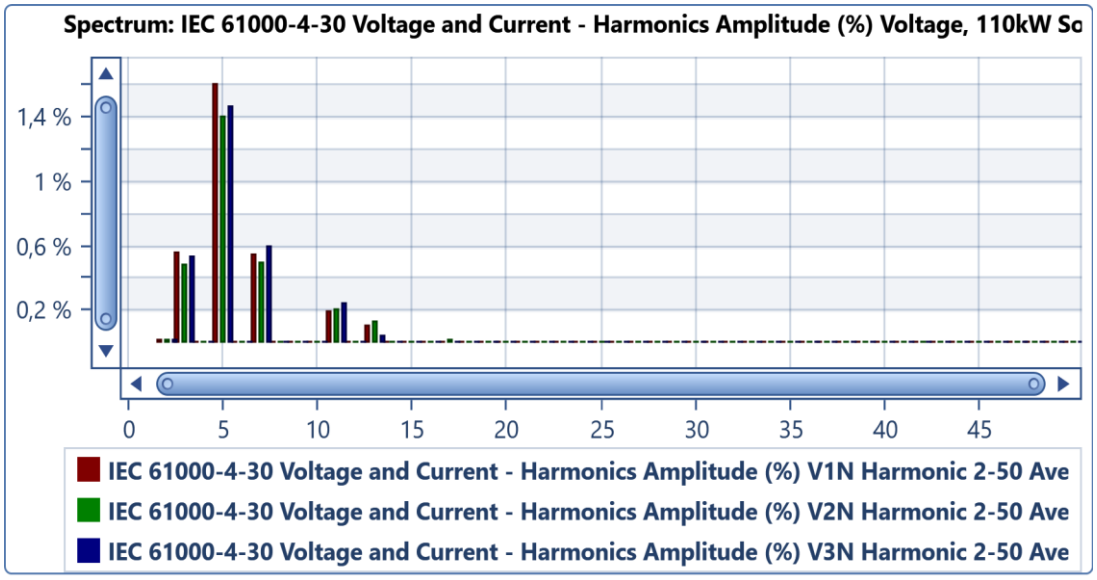

Figure 4.41 Voltage harmonic spectrum during 100% solar production on a sunny day

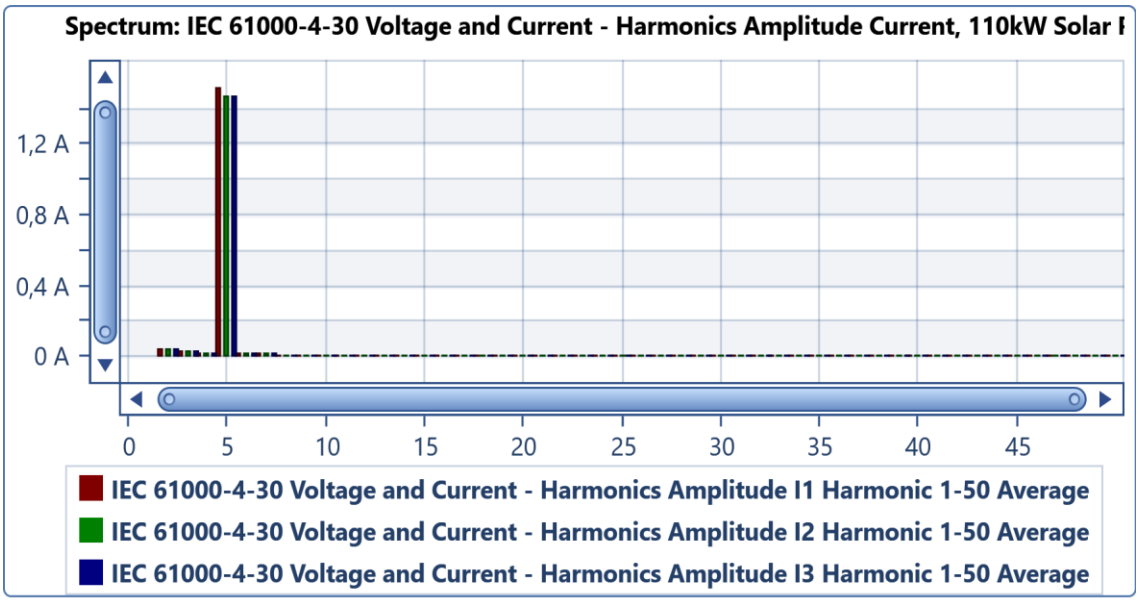

Figure 4.42 Current harmonic spectrum during 100% solar production on a sunny day

The 5th order current harmonic is measured as the highest, which is a concern to power quality experts as most harmonic-related problems on the distribution grid are traceable to this specific order of current harmonics, causing distortion

of the voltage waveform, transformer overheating, and blown shunt capacitor fuses, which necessitate the application of a custom power device, such as D-STATCOM to mitigate and keep the grid-tied PV system within the required power quality limits.

4.3.3.3 Scenario 3: PV Power Production on a Cloudy Day

A grid-tied PV system's performance under cloudy conditions has a relatively complex grid power quality behaviour. Performance comparison of the variations' impact due to low solar irradiation levels is analyzed in this section—the data for the analysis were collected on August 15, 2020. The figures below depict the results obtained, indicating that the current and voltage waveforms contain only odd-order harmonics. The most significant harmonics were the 3rd to 11th harmonic order, while the others were not significant. The following values were measured:

- Voltage THD varies between 1.01% and 2.29%
- The TDD current up to 3.36%
- Voltage harmonic spectrum show:
  - 3rd of up to 0.54 %
  - 5th of up to 1.59 %
  - 7th of up to 0.58 %
  - 11th of up to 0.2 %
  - 13th of up to 0.11 %
- Current harmonic spectrum show (production average):
  - 5th of up to 1.56 A
  - 7th of up to 0.82 A

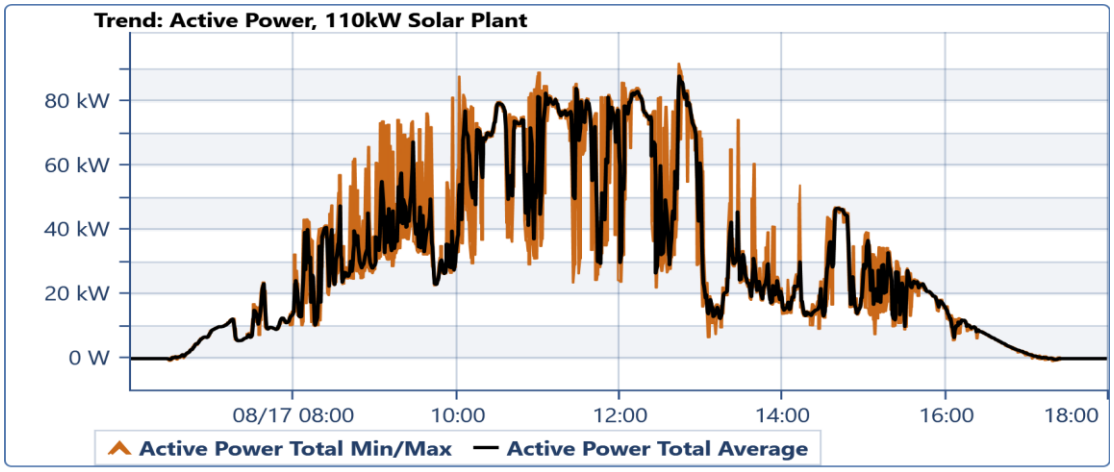

Figure 4. 43 Measured active power generated on a cloudy day

Table 4. 18 Measured active power generated on a cloudy day

Component	Parameter	Minimum	Maximum	Average
110 kW solar plant	Active Power Total	– 873.16 kW	91.96 kW	26.63 kW

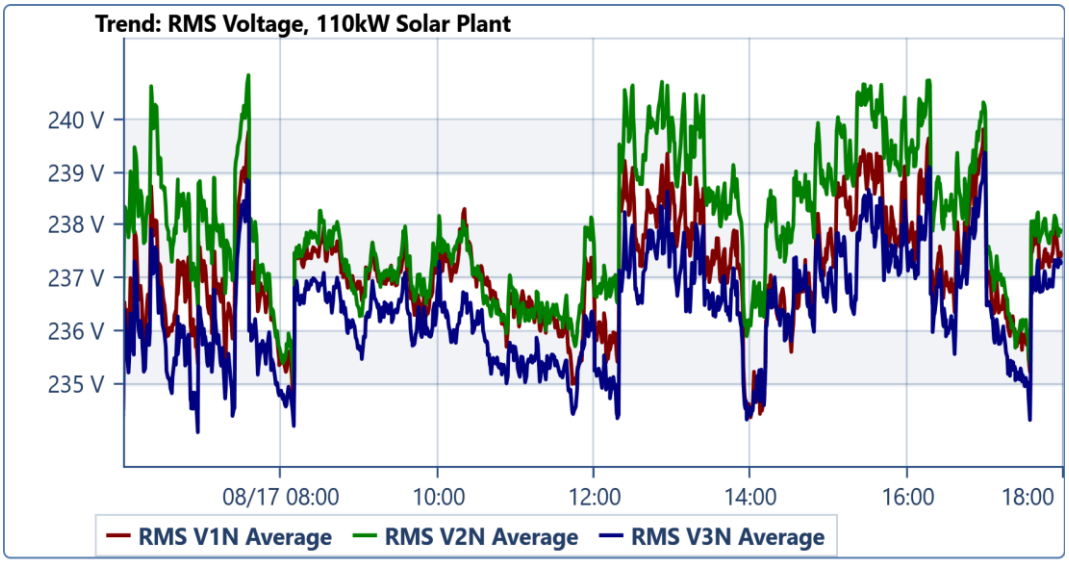

Figure 4. 44 RMS three-phase voltage during on a cloudy day

Table 4. 19 Measured RMS three-phase voltage on a cloudy day

Component	Parameter	Minimum	Maximum	Average
110 kW solar plant	RMS V_1N	231.91 V	241.21 V	237.12 V
110 kW solar plant	RMS V_2N	223.45 V	241.62 V	237.97 V
110 kW solar plant	RMS V_3N	223.59 V	240.58 V	236.38 V

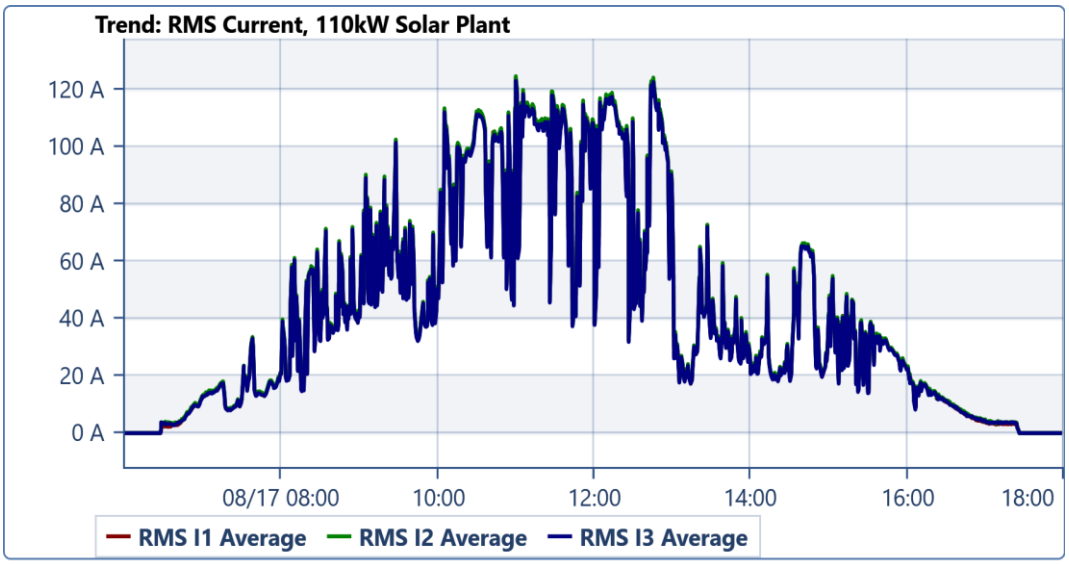

Figure 4.45 RMS phase to neutral on a cloudy day

Table 4. 20 Measured RMS three-phase current on a cloudy day

Component	Parameter	Minimum	Maximum	Average
110 kW solar plant	RMS I_1	2.59 A	128.95 A	42.07 A
110 kW solar plant	RMS I_2	0.52 A	128.89 A	42.41 A
110 kW solar plant	RMS I_3	0 A	127.45 A	41.65 A

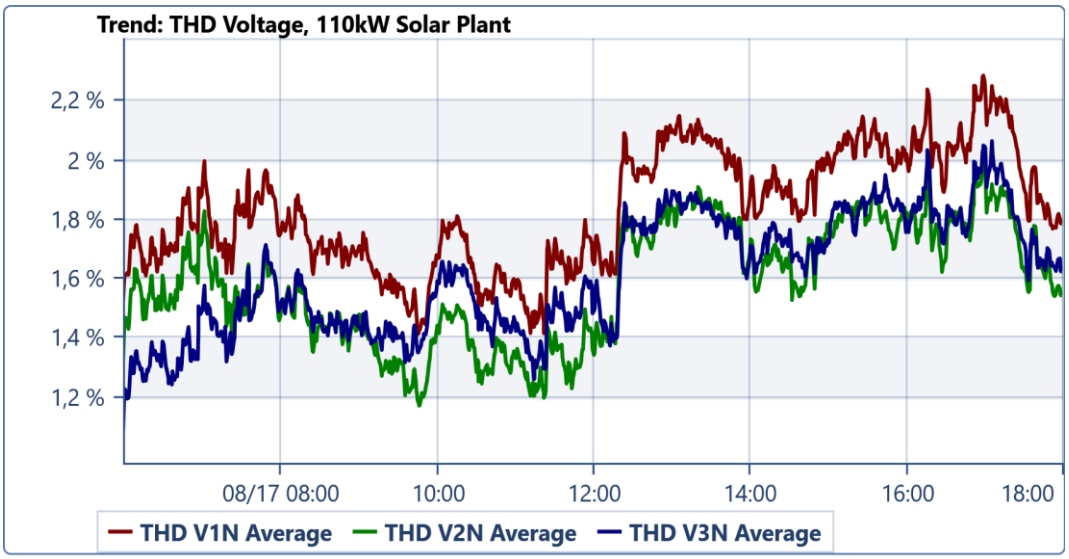

Figure 4. 46 Measured voltage THD on a cloudy day

Table 4. 21 The three-phase voltage THD on a cloudy day

Component	Parameter	Minimum	Maximum	Average
110 kW solar plant	THD V_1N	1.31 %	2.29 %	1.84 %
110 kW solar plant	THD V_2N	1.1 %	2.01 %	1.59 %
110 kW solar plant	THD V_3N	1.01 %	2.07 %	1.61 %

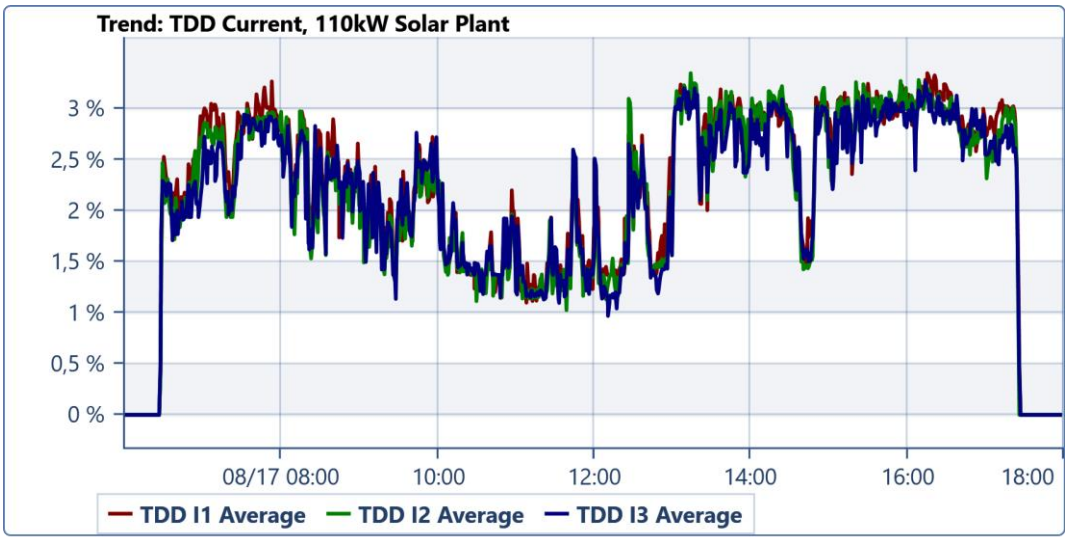

Figure 4.47 Measured current TDD on a cloudy day

Table 4.22 Summary of the current TDD on a cloudy day

Component	Parameter	Minimum	Maximum	Average
110 kW solar plant	TDD I_1	0 %	3.36 %	2.18 %
110 kW solar plant	TDD I_2	0 %	3.28 %	2.12 %
110 kW solar plant	TDD I_3	0 %	3.36 %	2.09 %

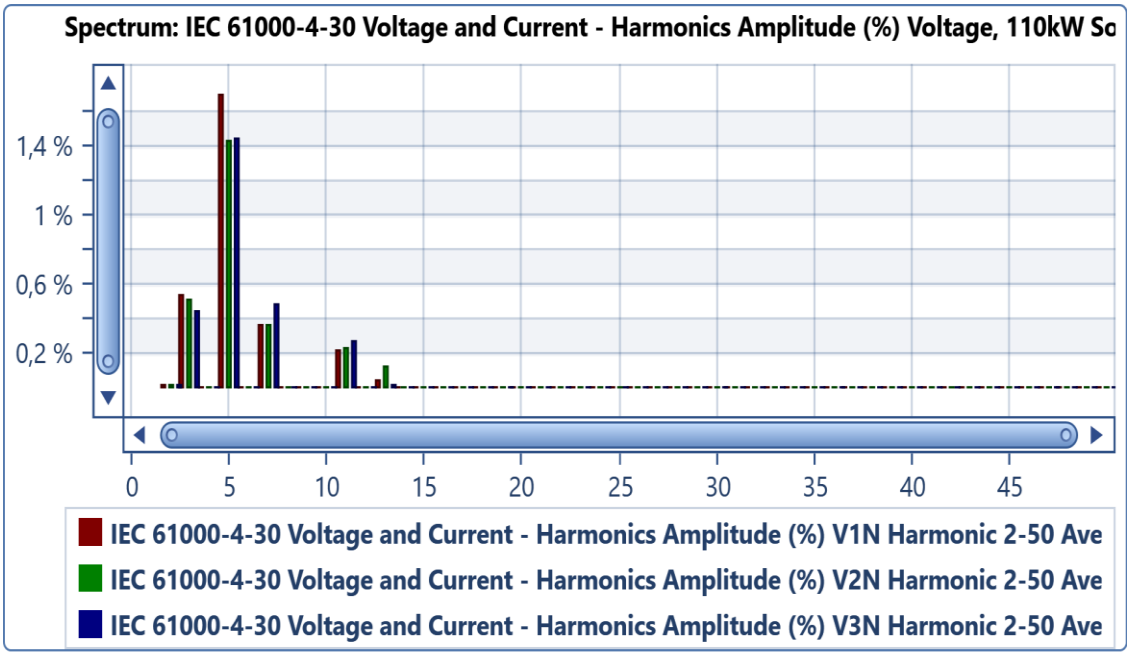

Figure 4.48 Voltage harmonic spectrum on a sunny day

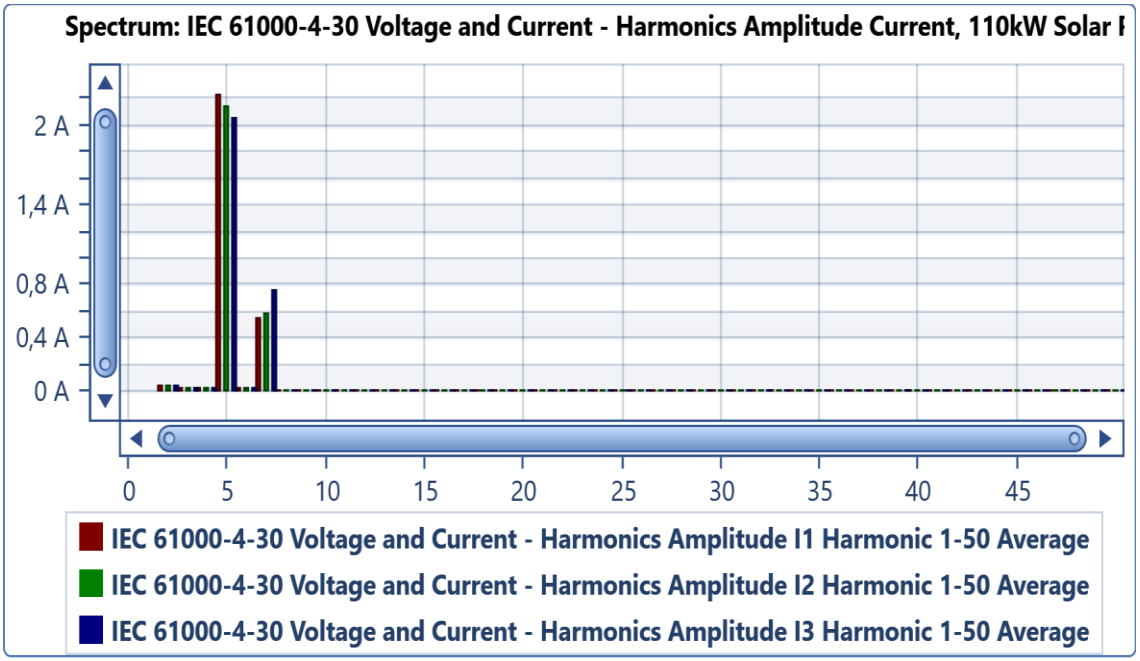

Figure 4.49 Current harmonic spectrum on a sunny day

The harmonic distortion generated by PV systems on the grid as measured at the PCC on a sunny and cloudy day was analyzed to determine the contribution of PV inverters to the distortion of the distribution system power quality. Total Harmonic Distortion (THD), a valuable method for determining a grid voltage or current harmonics content, was observed in this analysis. While current harmonics can lead to increased losses and failure of the grid protection scheme, voltage harmonics have the most significant potential to interrupt the operation of grid-connected loads and appliances. To this end, the South Africa renewable energy grid code set a limit of 8% for the voltage THD up to the 40th harmonic. The interface requirement of the IEC standard 61727 on grid-tied PV systems requires a limit of 5% for the current THD up to the 50th harmonic. The analysis shows that the voltage and current total harmonic distortion on the DUT 110 kW grid-tied system are within the regulated limits on sunny and cloudy days. However, the harmonic values increased slightly during 100% solar production and on cloudy day scenarios. Typically, the voltage rise level hinges on the grid-tied PV system capacity and location for the voltage rise analysis. The university's Steve Biko campus had lower daytime load demand than the PV plant's capacity during this experiment. Hence, the utility controls the voltage with a transformer that regulates the voltages in a range of 0.97 p.u – 1.05 p.u.

Consequently, to analyze the impact of the PV penetration on the grid, the ELSPEC PQ analyzer recorded the RMS voltage verse time for different operating days and the output power verse time for sunny and cloudy days. It was observed that the PV power curve was expansive during sunny days compared to cloudy days. The corresponding measured RMS voltage showed that the voltage variation trend had followed the PV power injection curve. The voltages were between 0.96 p.u and 0.99 p.u during the early morning and evening hours, which was within limits defined by the grid code. The voltage profiles fluctuated between 0.97 p.u and 1.026 p.u during the daytime, relatively to the PV power injected into the grid but were lower than the standard limit of 1.05 p.u.

4.3.4 Voltage Unbalance

Voltage unbalances in a power system is a three-phase voltage variation in which the voltage magnitudes or the phase angle differences between them are

not equal. It is primarily due to unequal loads or unbalanced phase impedance on distribution lines. The IEEE recommended practice for monitoring electric power quality recommends a maximum limit of 2% for voltage unbalance on a three-phase grid [238]. When it increases beyond the limit, it creates a problem for the loads. The voltage unbalance analysis of the DUT's 110 kW grid-tied PV system is presented in this section. The data on which the study is based were collected with the ELSPEC PQ meter. Figure 4.50 depicts the measured voltage unbalance against time, showing the minimum and maximum variation and its degree of severity on the grid-tied PV system. The three-phase negative sequence unbalances maintained the standard limits under steady-state operation until it peaked at 3.75% during a Stage 2 load-shedding (sudden cut of power by utility), which has a similar impact to a grid fault. The result indicates that the voltage unbalances exceeded the required limit of 2% on two different Stage 2 load shedding occasions during this study. Figure 4.51 presents the voltage unbalance curve for the period under consideration; it indicates that the unbalanced variation was well within the international and local standards and codes' requirements with a maximum negative sequence unbalance of 0.89% during steady-state operation.

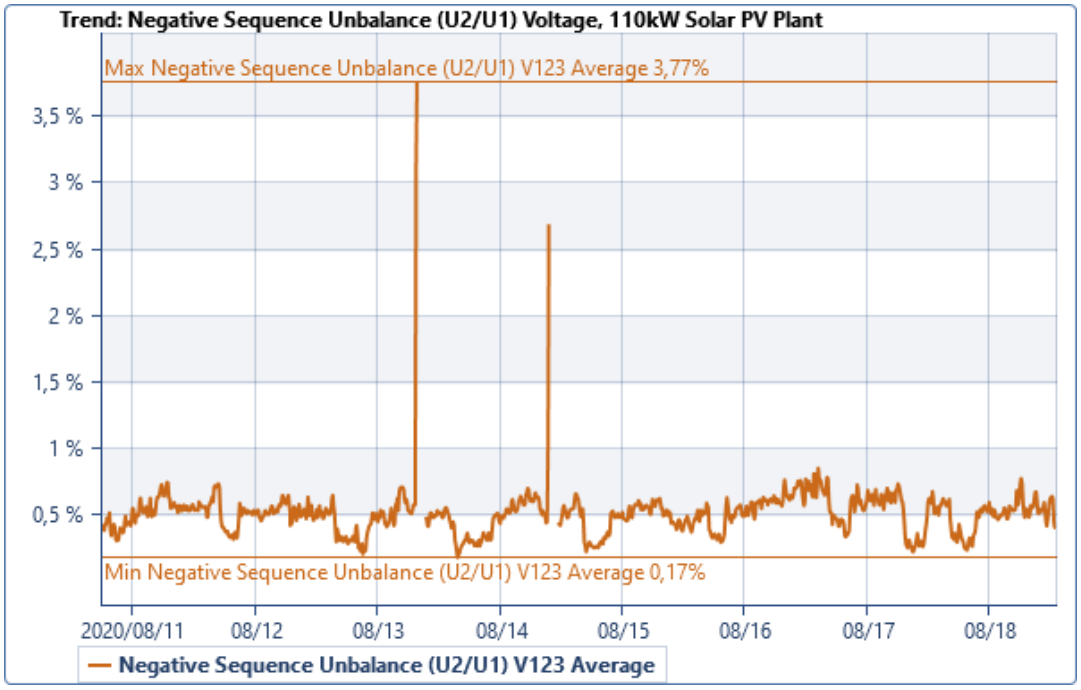

Figure 4.50 Impact of load shedding on voltage unbalance (%) recorded at the PCC

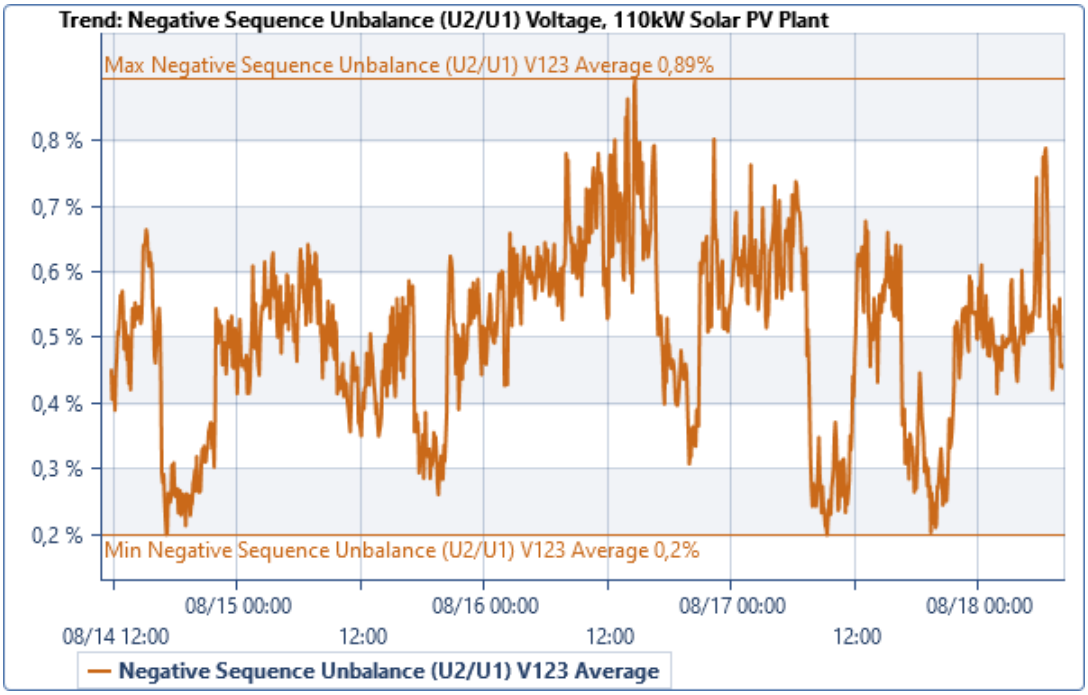

Figure6 4.51 Three-phase average voltage unbalance (%) during steady-state operation

4.3.5 Voltage Flicker Evaluation

Voltage flickering in a grid-tied PV system caused by power fluctuation due to load variation or shadow effect was evaluated on the DUT's 110 kW grid-tied PV system. The grid voltage fluctuated in response to the fast-changing loads, causing the lighting system to flicker in response to such variations. This study investigates the PV system's performance against international standards and the regulatory grid code, which defines voltage flicker limits. Two main parameters are regulated in the grid codes: Short Term Flicker Perceptibility (P_{ST}), usually measured over a few minutes, and the Long Term Flicker Perceptibility (P_{LT}) that is generally measured over 2 hours [239]. In the case of a grid-tied PV system, both parameters have limit values. The P_{ST} should not exceed 1.0 p.u, while P_{LT} should be maintained below 0.46 p.u at the PCC. A digital PQ analyzer was connected at the PCC to measure the short-term and long-term flicker severity data, extracted to a computer for analysis. Figures 4.52 and 4.53 present the results of the short-term (P_{st}) and long-term (P_{lt}) flicker severity measured for the selected days as per IEEE 1453-2004 standard.

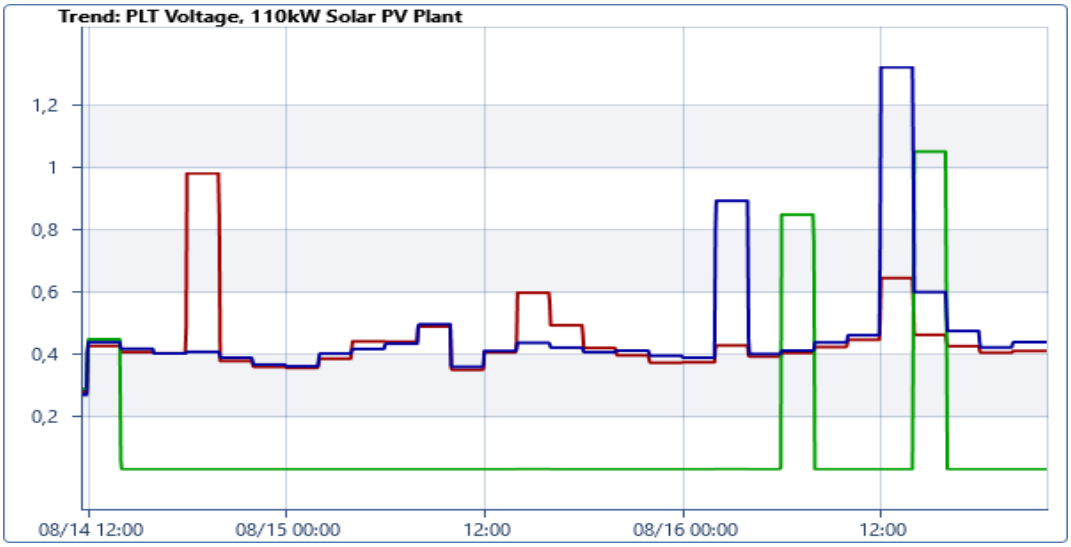

Figure 4.52 Measured short-term flicker perceptibility (PST)

The flicker values increased during the PV system operating time on a cloudy day (16th August 2020) due to rapid voltage fluctuations. The figure shows that the flicker value on phase A peaked at 0.98 p.u; however, the flicker value for phases B and C showed significant voltage variation in the system peak at 1.03 p.u and 1.25 p.u, respectively beyond the standard limit. Thus, the voltage flicker values obtained for phases B and C violated the limit due to changing load and the critical operating conditions on a cloudy day. Nonetheless, the measured long-term (Plt) flicker values are well within the grid code limit of 0.5 p.u. It was also observed that when the PV ceased to inject power to the grid, the measured P_{ST} and P_{LT} had values lower than 0.4 p.u.

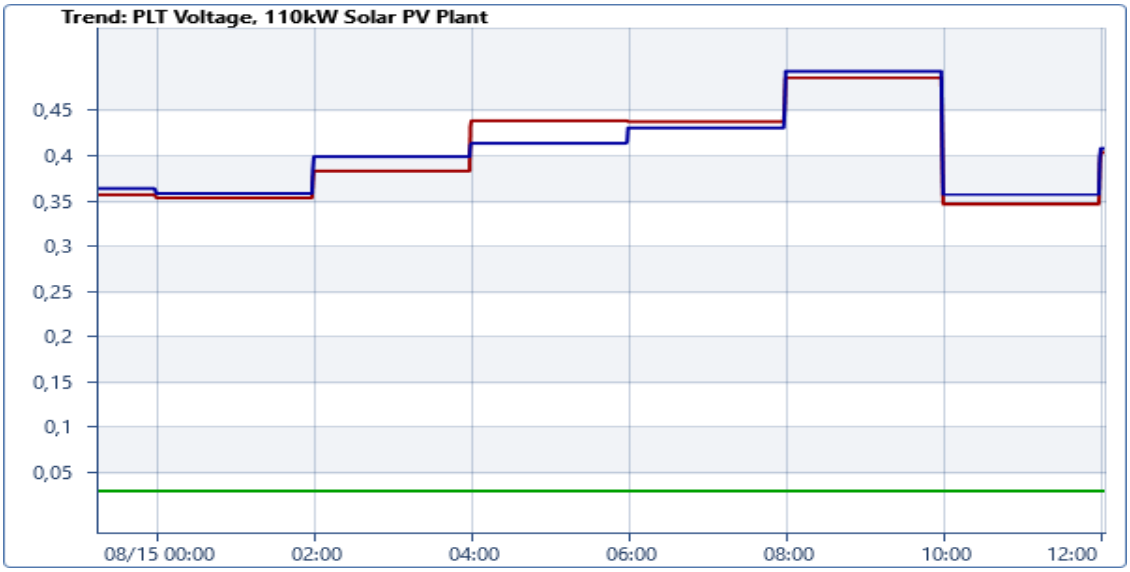

Figure 4.53 Measured long-term (Plt) voltage flicker

4.4 Summary

Voltage rise, voltage dip, harmonics, voltage unbalance, voltage flicker, among the power quality issues, have been investigated in this chapter using the MATLAB/Simulink model of the IEEE 13 bus test system. Likewise, PQ experimental field data measured at the PCC of the 110 kW grid-tied PV system under real operating conditions on the Durban University of Technology's Steve Biko campus have been presented and analyzed in two study cases. Voltage rise and dip were investigated in three different scenarios for the first study case. These involved integrating a single 110 kW grid-tied PV system that penetrates the upstream distribution system (at the beginning of the feeder). Also investigated was the penetration of dispersed multiple PV systems at different locations near the loads. It is observed from the results that the voltage rise impact of the dispersed grid integrated PV systems in the second and third scenarios was substantially higher than the lumped grid-tied PV system in the first scenario. With increased PV penetration in the third scenario, this impact became significantly higher. Fault analysis was performed in the second case study to analyze the voltage dip impact of the PV system on the IEEE 13 bus test system with three different types of fault. The results obtained indicated that the grid-tied PV system's performance improves during the fault conditions by applying the conventional PI-controlled D-STATCOM.

Also, the performance of a typical grid-tied PV system penetration on the grid voltage quality due to fluctuations in solar radiation was analyzed. The field investigation was carried out by installing a power quality meter on the 110 kW grid-tied PV systems located at the DUT Steve Biko campus to evaluate different power quality issues within the network. Data were collected at the inverter output level, the high voltage and low voltage side of the distribution system to evaluate the voltage flicker level on the network. This study analyzed voltage flicker impact on the grid-tied PV system on different operational days on the system voltage level. The results indicate that the system voltage magnitudes rise proportionately with the power PV system injected into the grid. Voltage quality issues from the results obtained were negligible and within the prescribed limits.

CHAPTER FIVE

Grid-tied PV System Optimization

5.1 Introduction

In general, the distribution static compensator (D-STATCOM) comprises of an inverter, dc-link capacitor, and a passive AC interface filter. The control structures of the D-STATCOM, based on the different current components control, are of two main types, namely: the synchronous reference frame (SRF) techniques (*dq* techniques) and the instantaneous active power theory (*pq* theory) [240]. The dq techniques generally work in the dq0 synchronous reference frame and use a low-pass filter to distinguish the load currents' fundamental and harmonic components. The use of a D-STATCOM was proposed and implemented on a low voltage distribution system to enhance the power quality performance of a grid-tied PV system [241, 242]. The D-STATCOM dc-link voltage must be kept at its optimum value for continuous and efficient mitigation of power quality issues. The grid voltage and a proportional-integral (PI) controller are usually used to achieve this optimum value.

A conventionally designed D-STATCOM *PI* controller suffers slow system convergence. In the literature, different research studies have resolved this issue by adopting nature-inspired evolutionary optimization algorithms for D-STATCOM. These algorithms, such as the Firefly optimization algorithm, Bacteria Forging Optimization (BFO), are algorithm-specific parameter control methods [243, 244]. Since their specific control parameters influence the performance of these optimization algorithms', they could not obtain suitable results under varying operating conditions due to the inappropriate selection of control parameters such as swarming and elimination in BFO when the system becomes more complicated. There is a considerable research gap in innovating an optimized D-STATCOM that performs independently of algorithm-specific control parameters to provide dynamic reactive power support to the grid for voltage regulation, harmonic and reactive power compensation at the point of common coupling (PCC). The D-STATCOM controller was modeled in the MATLAB/Simulink simulation environment. The D-STATCOM current controller gains were tuned and optimized using the meta-heuristic optimization method –

the novel Enhanced Jaya (E-Jaya) optimization algorithm. The comparative analysis of the optimization algorithm's superior performance for different load conditions is presented and discussed in this chapter by comparing the Artificial Bee Colony (ABC) evolutionary optimization algorithms with the Jaya optimization algorithm and, on the other hand, the proposed E-Jaya optimization method a meta-heuristic optimization technique.

5.2 D-STATCOM Control

A well-defined and robust control method is vital for the D-STATCOM model to mitigate power quality issues and then attain a stable system. The SRF method is generally used in the three-phase systems, where instantaneous phase angle θ is used to synchronize the three-phase Phase-Locked-Loop (PLL) rotating reference frame to the grid voltage vector. The PLL synchronizes the D-STATCOM signals with the PCC voltage by comparing the measured DC link voltage with a fixed reference voltage. The error between the reference DC voltage and the measured DC link voltage of the D-STATCOM is fed into a PI controller. The output of the PI controller gives the reference voltage V_{dref} in d-axis. The D-STATCOM currents (i_a, i_b, i_c) are converted to equivalent direct and quadrature (i_d, i_q) component current axes by utilizing *abc* to *dq0* transformation. In order to maintain the reactive power drawn from the grid at zero, the inverter's output currents are controlled so that the D-STATCOM VSC supplies the required reactive power for the load. Therefore for a unity power factor at the source end, the load's reactive power sets the reference for inverter control, which sets i_q reference as i_{qload}. The reactive current supplied by the inverter i_q is compared with the reference value i_{qref} to obtain the reactive current error for full compensation. This error signal is passed through a PI controller to obtain the reference voltage signal V_{qref}. The voltages V_{dref} and V_{qref} are fed into the *dq0-abc* transformation block, which generates reference voltages Vi_a, Vi_b, Vi_c to the pulse width modulation (PWM) signal generator of the multi-level inverter. These signals are compared with a level-shifted triangular carrier wave to obtain PWM signals for the switches employed in each of the inverter phases. The PI controller is utilized to reduce fluctuations and improve grid stability. However, the PI controller parameters require tuning to obtain the preferred performance. In manual tuning, PI controllers' values are adjusted based on the system

response; therefore, an efficient tuning method is required to obtain the best performance. Though a linear PI controller is suitable for controlling a nominal system, changing system parameters requirements are beyond a simple PI controller. The application of different manual tuning methods has been studied in the literature. However, most of these methods suffer a significant downside due to the PI controller's manual tuning. Therefore, non-specific control parameter optimization algorithms have become an attractive solution for optimization problems. In this study, meta-heuristics control optimization algorithms were been implemented to tune D-STATCOM PI controllers to enhance a distribution grid-tied PV system's power quality performance. Figure 5.1 depicts this research work concept where K_p and K_i denote the proportional and integral gains, respectively. The PI controller's input is the error of the actual variable of interest from the reference value. The PI controller gains are tuned using meta-heuristics optimization methods for optimal performance [245].

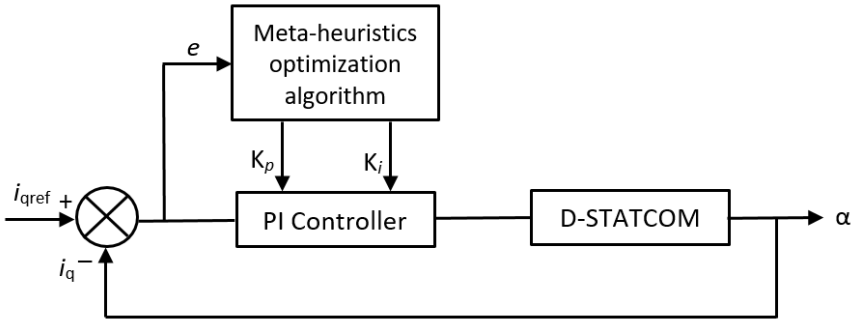

Figure 5.1 PI controller with meta-heuristic optimization methods

5.3 Optimisation Techniques for Grid-tied PV System

Optimization is the process of finding a solution to a problem in order to maximize or minimize a set of objective functions within a domain containing acceptable values of a variable while some constraints are satisfied [246]. Different optimization techniques exist in the literature for solving power system issues. These optimization methods are categorized into conventional optimization techniques and metaheuristics-based techniques [247]. The conventional optimization techniques use the linear programming approach. This method could only be used when the objective function and constraints are linear, as it cannot solve a nonlinear model. This method has been utilized for different power system issues, such as system operation and optimal power flow [247,

248]. Although the conventional optimization methods had performed well in many instances, they have certain limitations related to their inherent search mechanism. The conventional optimization techniques generally depend on the type of objective and constraint function and the type of variables used in the problem modelling. Their efficiency depends on the number of variables, constraints used, and the solution space size. The solutions obtained from the conventional optimization method depend mainly on selected initial conditions. They do not provide a generic solution that can be used to solve problems where different variables, constraints, and objective functions are used. Therefore, there is a need for effective and efficient optimization techniques for power system issues such as power quality. To tune the D-STATCOM PI controller for grid voltage regulation to suitably respond to sudden grid distortion due to faults and load variation. Due to the limitations of the conventional optimization methods, nature-inspired metaheuristic optimization techniques, such as Artificial Bee Colony, Jaya, and the novel Enhanced Jaya optimization algorithm that is non-parameter controlled techniques, have been implemented to tune D-STATCOM current controller gain for optimal performance of a grid-tied PV inverter. The nature-inspired optimization techniques solve the nonlinear models and are more robust than the conventional controller methods.

5.4 Objective Function Formulation

A carefully selected objective function leads to better performance of the system and meets the control design expectations. An objective function is an essential part of any optimization algorithm. It is a crucial aspect because it encapsulates the problem the optimization algorithm is trying to solve. The objective of applying the D-STATCOM on the grid-tied PV system is to minimize the voltage deviation by tracking the current controllers' error input to zero steady-state. The compensating capacity of D-STATCOM hinges on both the dc-link voltage and passive ac interface filter. If the dc-link voltage is not maintained at its reference value or the PI controller gain values are not appropriately tuned, the D-STATCOM possibly will not compensate for the power quality issues or will operate at lower efficiency. The PI controller regulates the dc-link voltage by providing twofold compensation; the Proportional (P) phase offers rapid response, while the Integral (I) phase ensures zero steady-state error.

However, an innovative optimization algorithm for D-STATCOM power quality compensation is desirable as the conventional PI controller has been criticized as a parameter-dependent method. As a result, this study implemented a non-parameter-dependent optimization algorithm to tune the PI controller gains (K_p and K_i) for improved D-STATCOM compensation capacity. The Integral Square Error (ISE) performance index 'J,' expressed in Equation (5.1), was utilized as the optimization objective function.

$$J = ISE = \int_0^{Ts} e_d^2 + e_q^2 \tag{5.1}$$

$$Error(e_r) = \left(i_d - i_{dref}\right)^2 + \left(i_q - i_{qref}\right)^2$$

A minimizing cost function was selected for better compensation and to reduce the input error. The optimization's objective was to track the best values for the parameters that were to be optimized so that the error input of the D-STATCOM current controllers could be maintained at zero steady-state. The maximum sensitivity function that measures the robustness of a PI controller tuning algorithm, defined by equation (5.2), was performed [245].

$$M_S = \max\left|S(j\omega)\right| \tag{5.2}$$

where: M_S is the maximum sensitivity function, max|S(jω)| is the impact of feedback on the output.

The value of M_S ranges from 1.1 to 2 and provides reasonable robustness of the closed-loop when max|S(jω)| < 1, the disturbances are mitigated and amplified when max|S(jω)| > 1. The robustness of the closed-loop increases with the decrease in M_S [245].

5.5 Artificial Bee Colony (ABC) Optimization Algorithm

The Artificial Bee Colony (ABC) optimization algorithm implemented in [249] is a recent swarm intelligence-based algorithm. ABC optimization algorithm is a nature-inspired high-speed and population-based stochastic search algorithm based on honey bees' intelligent behaviour, known for their intelligence and ability to perform complex tasks such as collecting food and building nests with a high degree of precision [245, 249]. It employs population size, maximum cycle

number, and a limit, which are the three control parameters [250]. It is designed to simulate the foraging behaviour of a honeybee colony.

Two main concepts describe swarm intelligence, namely self-organization and labour division [245, 251]. The self-organizing behaviour represents the complex collective behavior that arises from the interaction between the agents showing a simple self-directed behaviour. The labour division mechanism assigns specific tasks to the agents performing simultaneous activities, which results in a more efficient and time-saving performance. There are three bee colony categories in the ABC algorithm: the employed bees, onlookers, and scout bees. The employed bees go to the source of the food they have already visited, while the onlookers and scout bees look for other food sources. There is only one employed bee for every food source; that is, the number of employed bees is proportional to the number of food sources.

In contrast, the onlooker bees wait at the dance area to get information about the discovered food sources provided by employed bees. If a food source's position does not improve within several attempts known as limits, then the employed bees become scout bees by randomly searching for a new food source. In this manner, the exploitation process is performed by employed and onlooker bees while the scout bees explore for new solutions. The details of the different ABC stages are described in the following section.

5.5.1 Initialization

The ABC algorithm has three key parameters: the number of food sources known as population, the limit that is the number of tries after which a food source is to be dropped, and the criteria for termination, known as the maximum number of cycles. Random initialization of food sources' locations is performed using Equation (5.3) [245, 252].

$$x_{ij} = x_{\max j} + rand[0.1](x_{\max j} - x_{\min j}); i = 1,...,SN,\ j = 1,...,D \qquad (5.3)$$

Where: x_{ij} denote the i^{th} employed bee on j^{th} dimension, rand[0,1] is a function that randomly generates an evenly distributed number in the range [0,1], *i* is the number of food sources of the bee colony, D is the dimension of the problem,

while $x_{max\,j}$ and x_{minj} indicate the search upper and lower limits to minimize the objective function.

5.5.2 Employed Bee

The employed bees search for new food sources having more nectar within the neighbourhood of the food source in their memory. They find and evaluate the new food source profitability (fitness). The new food sources with higher fitness value take over the existing ones. The position of i^{th} candidate in j^{th} dimension is updated during this phase as defined by equation (5.4) [245, 252].

$$v_{ij} = x_{ij} + \phi\left(x_{ij} - x_{kj}\right) \tag{5.4}$$

Where: v_{ij} is the new solution or a food source, ϕ is a random value indicating the acceleration coefficients ranging in the between [– 1,1], and X_{kj} is a randomly selected food source. The fitness value of the solution, fit_i, is calculated using equation (5.5) to minimize the objective function.

$$fit_i = \left\langle \begin{array}{ll} \dfrac{1}{1+f_i}, & if \quad f_i \geq 0 \\ 1+abs\left(f_i\right), & if \quad f_i < 0 \end{array} \right\rangle \tag{5.5}$$

Where: f_i is the objective function of solution x_{ij}. A selection is made between the original and new food sources to choose the better one by keeping the fitness value according.

5.5.3 Onlooker Bee

The employed bees share information about food sources with the onlooker bees, and the onlooker bees probabilistically choose their food sources depending on this information. The selection probability for onlooker bee food source is calculated using equation (5.6)

$$p_i = \frac{fit_i}{\sum_{j=1}^{SN} fit_j} \tag{5.6}$$

After a food source for an onlooker bee is probabilistically calculated, a neighbourhood source is determined using Equation (5.4), and its fitness value is computed. As in the employed bees phase, a greedy selection is applied between v_{ij} and x_{ij}. Therefore, more onlookers are recruited to richer sources, and positive feedback behaviour appears.

5.5.4 Scout Bee Phase

Suppose a food source does not yield better results within the limit L, where L = 0.7 x (Number of optimization parameters) x (colony size). In that case, this food source is abandoned, and the bee associated with it becomes a scout bee. Therefore, a new source of food is randomly generated according to Equation (5.3). Figure 5.2 shows the flowchart of the ABC algorithm, which illustrates the process of a PI controller optimization. According to the ABC algorithm, the population size, maximum cycle number, and limit are initialized. Then, the fitness value is calculated, and the best food source is defined. The algorithm stops when the stopping criterion is met. The optimal solution is chosen according to the latest h_{best}. The ABC parameters and their values used in our study are provided in Table 5.1.

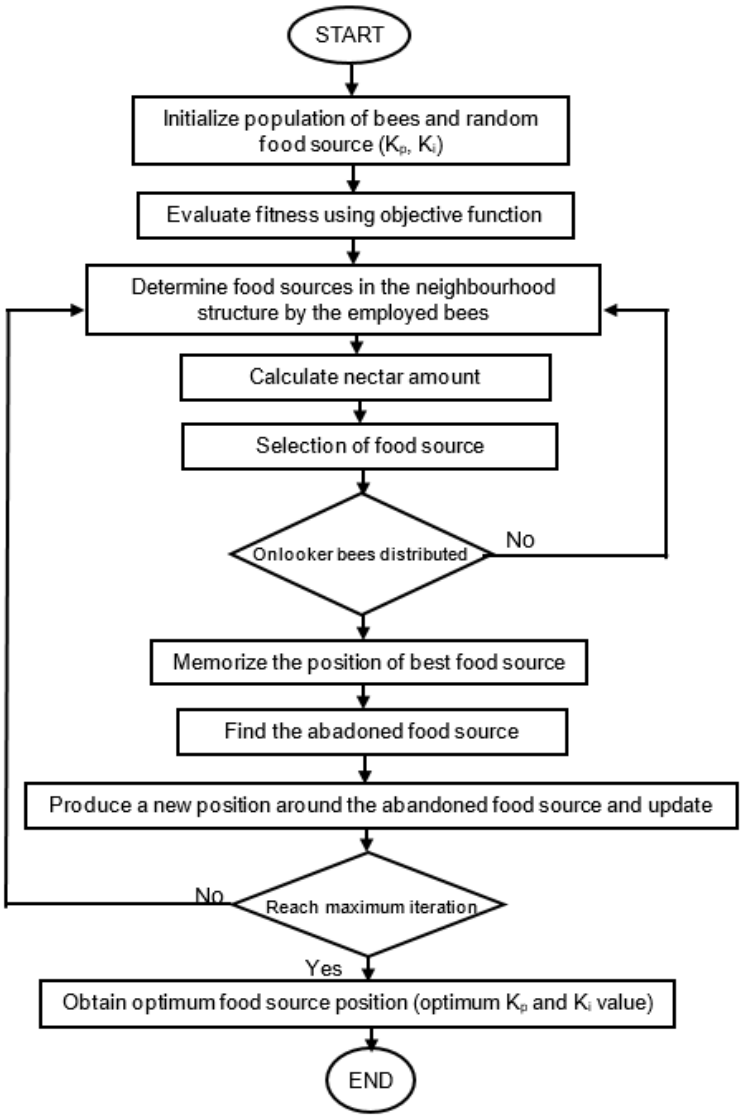

Figure 5.2 The ABC optimization algorithm flowchart [249]

Table 5. 1 ABC Parameter

Parameter	Value
Colony size	100
Number of iteration	100
Abandonment Limit	120
Acceleration co-efficient	1

5.6 Jaya Optimization Algorithm

Rao in [253] developed the Jaya optimization algorithm, which is a relatively new algorithm. The algorithm's concept is predicated on the postulation that an optimization problem's solution should advance toward the best option while avoiding the worst option. The algorithm continually attempts to find the optimum value by moving toward the best solution option while avoiding the worst solution. Figure 5.3 depicts the flowchart of the Jaya algorithm.

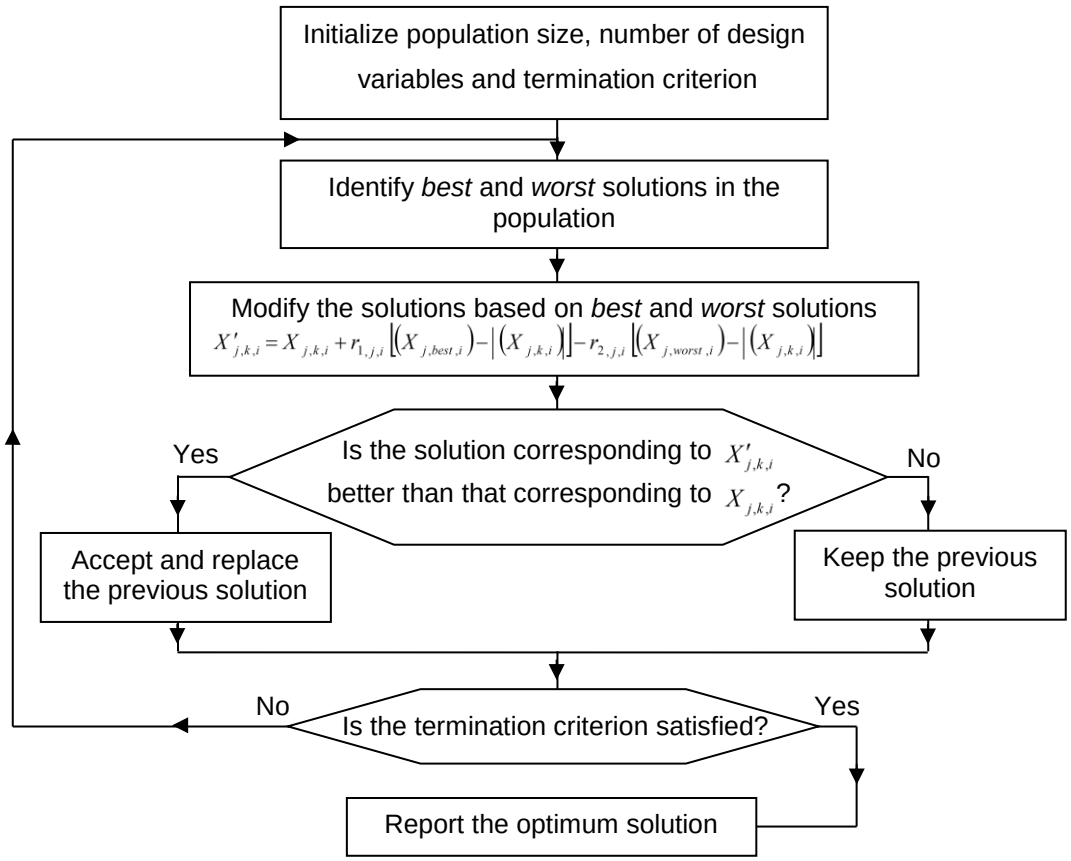

Figure 5.3 Jaya Optimization algorithm flowchart [253].

Jaya is much easier to use since only the typical control variables like the population size and the maximum number of generations with the number of

design variables are required. It does not need any algorithm-specific parameters, which require extensive PI controller tuning before actual optimization, and it converges faster to the best cost function value to achieve the optimum solution.

5.6.1 Implementation of Jaya Optimization Algorithm

This section outlines the step-by-step approach that was used to implement the Jaya algorithm.

Step 1: Is the definition of the objective function f(x) to be maximized or minimized. An initial population of Q solutions (Q = 1, 2, 3, … *n*) is created using random sampling from the design variable. Each i^{th} solution of the population is a vector containing the design variable *D* (d = 1, 2, 3, … *m*), the number of iteration (i.e., *i* = 1, 2, 3 … *k*), and the design variable upper and lower limits $\left(x_j^u \ and \ x_j^l\right)$ bound. Equation (5.7) is used to generate the upper and lower limits, while the number of iteration serves as the termination criterion where the best solution is obtained.

$$x_{j,i} = x_{j,i}^l + rand \times \left(x_{j,i}^u - x_{j,i}^l\right) \ i = 1,\ 2,\ 3...n \ ; \ \ j = 1,\ 2,\ 3...m \tag{5.7}$$

Where $x_j^u \ and \ x_j^l$ are the upper and lower limits of the design variable, respectively; *rand* is a random variable [0,1] uniformly distributed, *i* is the population size, and *j* is the design variable number.

Step 2: Based on the population size and number of design variables, generate a random population. The population size indicates the number of candidate solutions.

Step 3: Determine which candidates achieve the best and worst f(x) values. The candidate with the lowest f(x) is considered the best, and the candidate with the highest f(x) is regarded as the worst since the objective function is a minimizing function.

Step 4: Consider r_1 and r_2 for random variables in the range of *0* to *1*, the design variables values are updated as follows:

$$x'_{j,k,i} = x_{j,k,i} + r_{1,j,i}\left(X_{j,best,i} - \left|X_{j,k,i}\right|\right) - \ r_{2,j,i}\left(X_{j,worst,i} - \left|X_{j,k,i}\right|\right) \tag{5.8}$$

Where: $x'_{j,k,i}$ is the updated value of $x_{j,k,i}$, the $x_{j,k,i}$ is the value of the design variable (j^{th}) for the population candidate solution (k^{th}) during the (i^{th}) iteration, $X_{j,best,i}$ is the value of the j^{th} variable for the best candidate, $X_{j,worst,i}$ is the value of the j^{th} variable for the worst solution.

The $r_{1,j,i}\left(X_{j,best,i} - \left|X_{j,k,i}\right|\right)$ part of the Equation (5.8) relates to the algorithm's characteristics to advance toward the best solution, while the $r_{2,j,i}\left(X_{j,worst,i} - \left|X_{j,k,i}\right|\right)$ part implies the algorithm's propensity to avoid the worst solution.

Step 5: The corresponding objective function is computed and compared to the previous values after the new design variables' values are obtained. The lowest of each is considered the data to input into the next iteration. The objective function and design variables' values are updated after each i^{th} iteration based on their suitability.

Step 6: The best and worst solutions are selected from the updated f(x) values for the next iteration. The respective candidates are considered the best and worst solution. The design variables are updated according to steps 4 and 5 after selecting the new random variable values.

Step 7: Repeat steps 4, 5, and 6 until the termination conditions are met.

5.7 Enhance Jaya Optimization Algorithm

The Enhanced Jaya (E-Jaya) optimization algorithm is the improved version of the Jaya algorithm used to tune D-STATCOM PI controller gains innovatively since the Jaya algorithm attempts to find the optimum value by moving toward the best solution option only. The enhanced Jaya algorithm achieves fast analysis and optimization to the optimal solution by incorporating a mutation operator into the Jaya algorithm for better convergence [254]. Two modifications were introduced to the E-Jaya algorithm. First, variables in the E-Jaya population were divided into better and worse groups based on their fitness. The mean of the better and the worse groups' mean was used as the updated Equation's input. As a result, the E-Jaya finds the optimum solution value by moving towards the better group's mean and avoiding the worst group's mean. Second, a novel modification method of separating the two groups was developed to provide non-algorithm-specific parameters in E-Jaya [254].

5.7.1 Two-Cluster Modification of Enhance Jaya Optimization Algorithm

The E-Jaya builds on all the accepted variable values in the Jaya optimization algorithm based on Equation (5.8). The population variables were distributed into two clusters after being hierarchically ordered in ascending order from best to worst solutions based on each objective function's *f(x)* fitness. i_b elements are found in the better cluster C_b, while i_w elements are located in the worst cluster C_w. The following equations are satisfied by i_b and i_w.

$$i_b + i_w = i \tag{5.8}$$

Where: *i* is the population size.

The mean of the better cluster $X_{j,m_{better},i}$ and the worse cluster mean $X_{j,m_{worse},i}$ are calculated with Equations (5.9) and (5.10).

$$X_{j,m_{better},i} = \frac{\sum_{i=1}^{i_b} X_{j,k,i}}{i_b} \tag{5.9}$$

$$X_{j,m_{worse},i} = \frac{\sum_{i=1}^{i_w} X_{j,k,i}}{i_w} \tag{5.10}$$

The E-Jaya optimization algorithm's two clusters are to be updated using Equation (5.11).

$$x'_{j,k,i} = x_{j,k,i} + r_{1,j,i}\left(X_{j,m_{better},i} - \left|X_{j,k,i}\right|\right) - r_{2,j,i}\left(X_{j,m_{worse},i} - \left|X_{j,k,i}\right|\right) \tag{5.11}$$

The step-by-step approach to implementation of the E-Jaya algorithm two-cluster modification is outlined below. These steps are substituted for Jaya algorithm steps 3 to 6 to obtain the complete E-Jaya algorithm, as depicted in figure 5.3.

Step 1: Assess the population variable fitness

Step 2: Rank the fitness of the solutions in ascending order from best to worst solutions based on the objective function's *f(x)*

Step 3: Select i_b and i_w based on Equation (5.8)

Step 4: Compute $X_{j,m_{better},i}$ and $X_{j,m_{worse},i}$ based on Equation (5.9) and (5.10)

Step 5: Compute $x'_{j,k,i}$ based on Equation (5.11)

Step 6: If $x'_{j,k,i} < x_{j,k,i}$ then stop, the condition is met

Step 7: Return the minimum fitness $x'_{j,k,i}$ and corresponding $x_{j,k,i}$ solution

5.7.2 E-Jaya Algorithm Two-Cluster Dynamic Separation Approach

Since the Jaya algorithm does not require selecting any algorithm-specific control parameters, it is essential for the E-Jaya algorithm parameter C_b to be evolutionary, thereby maintaining the non-algorithm-specific parameters attribute.

The mean of the better cluster (m_b) is calculated using Equation (5.12) as follows:

$$m_b = \frac{i_b}{i} \tag{5.12}$$

Where m_b is a random variable [0 < m_b <1] uniformly distributed.

The separation of the modified two-cluster algorithm is calculated provided the values of m_b parameter are determined following the step below:

Step 1: For m_b, generate random numbers between [0 and 1]

Step 2: Calculate i_b based on Equation (5.12)

5.8 Results and Discussion

Dynamic performance analysis of a grid-tied PV system with D-STATCOM for power quality enhancement has been performed with regard to voltage unbalance and total harmonic distortion with a comparative analysis of the three different optimization algorithms in this section. The operation of D-STATCOM for power quality enhancement requires evolutionary tuning of its proportional-integral (PI) controller gains over the dc bus voltage. In chapter four, the PI controller gains K_p and K_i were determined based on a fixed-gain D-STATCOM (conventional). Since the PI controller gains provide dynamic responses as loading conditions change noticeably over time, which may cause grid voltage distortion and harmonics, it is paramount to tune the controller gains optimally during a significant grid load change. The ABC, Jaya, and E-Jaya optimization algorithms were implemented to self-tune the D-STATCOM PI controller gains, K_p, and K_i with ABC, Jaya, and E-Jaya optimization algorithms.

5.8.1 The Algorithms Convergence Comparison

In general, an optimization algorithm's efficiency is determined by how quickly it converges to the best solution. Figure 5.4 presents the dynamic response and

stability comparison of the three different optimization algorithms implemented for this study to select the D-STATCOM PI controller's optimal gain.

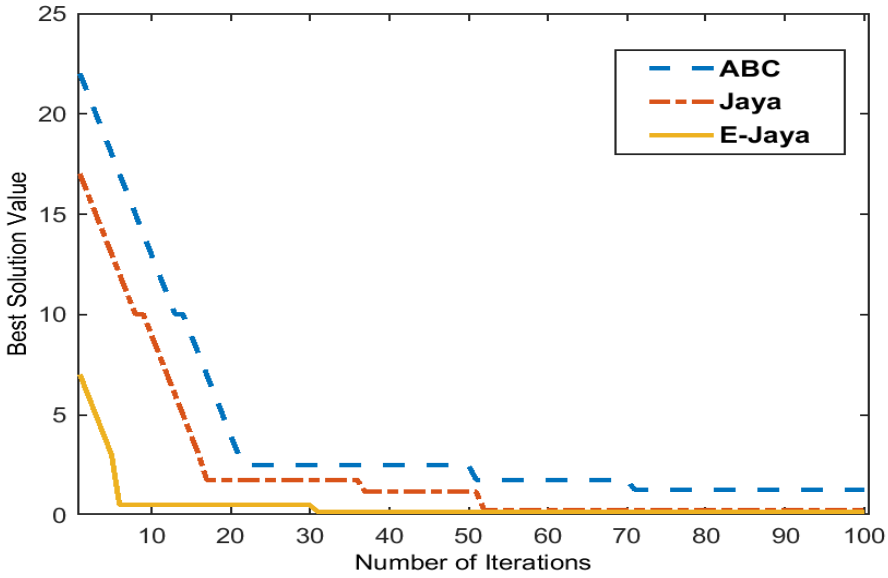

Figure 5.4 The optimization algorithms convergence plot

The developed E-Jaya optimization algorithm achieves the best solution with a suitable convergence rate and solution efficiency than the other two (Artificial Bee Colony (ABC) and Jaya optimized systems, as shown in figure 5.5. The E-Jaya and Jaya algorithms achieve the optimum solution at the 30th and 54th iterations, respectively. While the ABC optimization algorithm-based D-STATCOM could not converge to the best cost solution until the 100th iteration. The developed E-Jaya algorithm successfully converged faster and obtained the minimum value, demonstrating its effectiveness. The Enhanced Jaya optimization method's convergence quality is compared to that of ABC, and Jaya algorithms optimized PI gains, and the results are presented in Table 5.2.

Table 5. 2 The optimization algorithms optimized parameter solutions

Optimization Algorithm	K_p	K_i
Artificial Bee Colony	2.9479	303.75
Jaya	1.8238	107.84
Enhanced Jaya	0.8018	50

The conventional PI-controller-based tuning approach has a drawback of the trial-and-error process to determine the PI controller gains, which takes a long time to converge. Whenever the system responds to nonlinearities such as load

changes, steady-state shifts, or external disturbances, it becomes unstable. Table 5.3 provides the D-STATCOM comparative transient performance with and without the metaheuristic algorithm tuned PI controller.

Table 5. 3 Transient performance D-STATCOM with and without the optimized PI controller

Optimization Algorithm	**Rise Time (s)**	**Peak Time (s)**	**Maximum Peak (%)**	**Settling Time (s)**
Conventional PI	9.0969×10^{-9}	0.4364	1.6483	8.5829
Artificial Bee Colony	8.7743×10^{-9}	0.0090	1.8136	1.0463
Jaya	7.1982×10^{-4}	0.0042	0.8309	1.0003
Enhanced Jaya	6.7769×10^{-9}	0.0037	0.3887	0.7155

The results show that the E-Jaya algorithm tuned the D-STATCOM PI controller better with a minimum value of rising time, peak time, maximum peak, and settling time compared to the conventional PI controller, ABC, and Jaya optimization algorithm. The reference of the i_d, i_q in per unit validating the gain values' performance is presented in Figures 5.5 and 5.6. The conventional PI controller's response and that of the three optimization algorithm-based PI controllers at optimal gain value are compared. Comparative analysis from the figures indicates that the E-Jaya algorithm optimized and tracked the current error to zero faster and more efficiently than the conventional PI controller, ABC, and Jaya algorithm optimized PI controller.

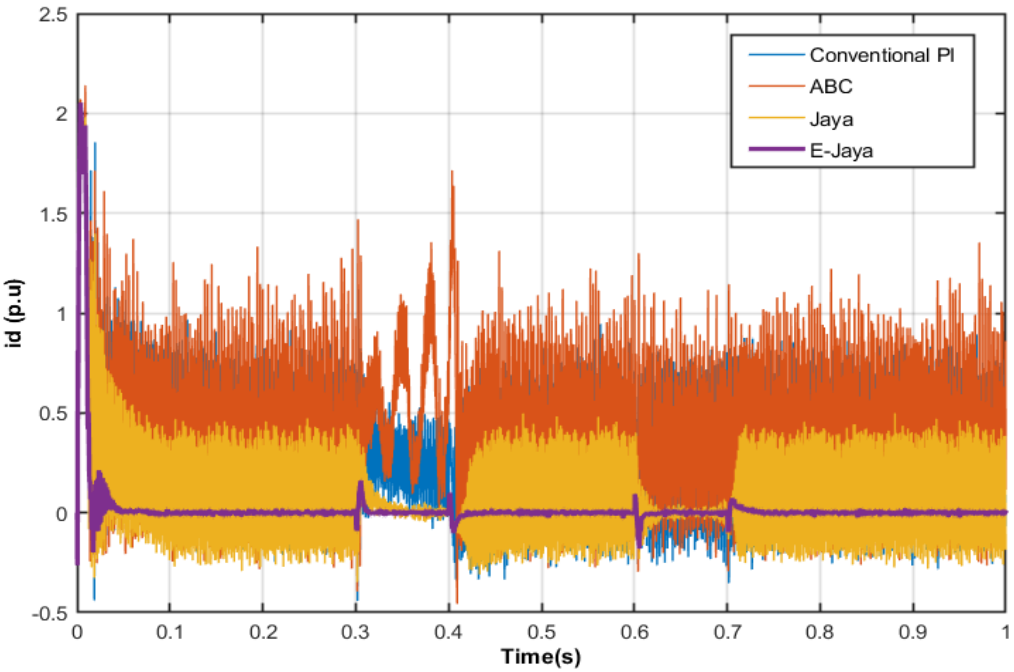

Figure 5.5 d-axis current control

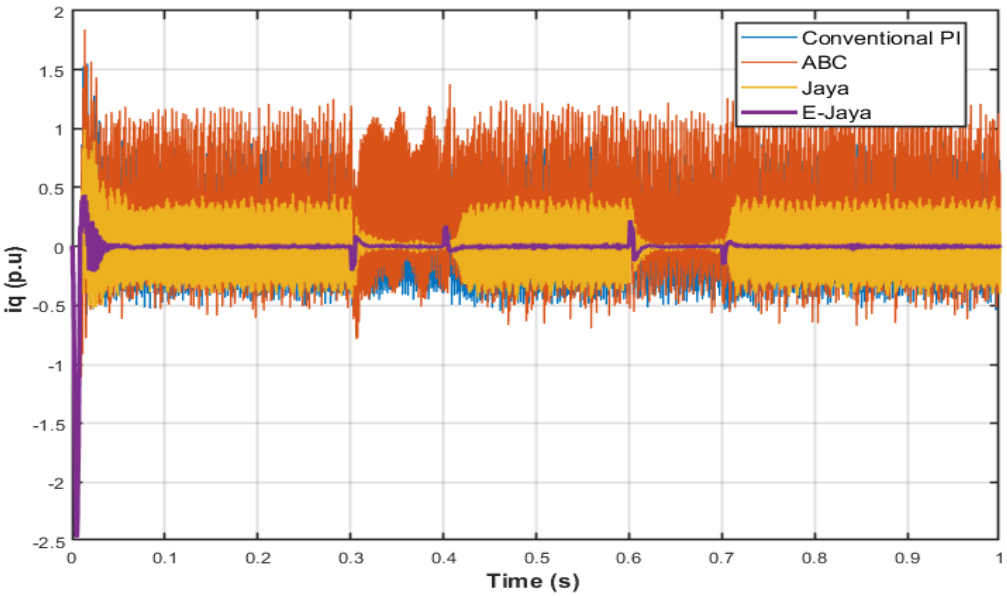

Figure 5.6 q-axis current control

5.8.2 Performance Analysis under Balanced Grid Voltage

This section presents the analysis of the grid-tied PV system's performance with and without optimized D-STATCOM operated under a balanced and ideal grid voltage. Before the D-STATCOM became operational, the grid current was non-sinusoidal and distorted with harmonics, as shown in figure 5.7 (b).

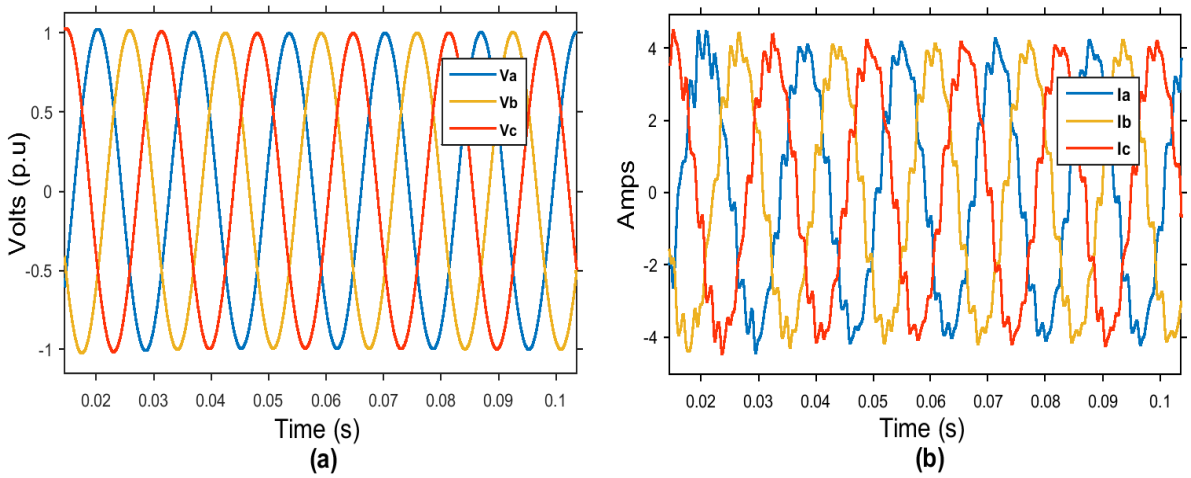

Figure 5.7 Simulation results before D-STATCOM compensation for (a) Grid voltage (b) Grid current

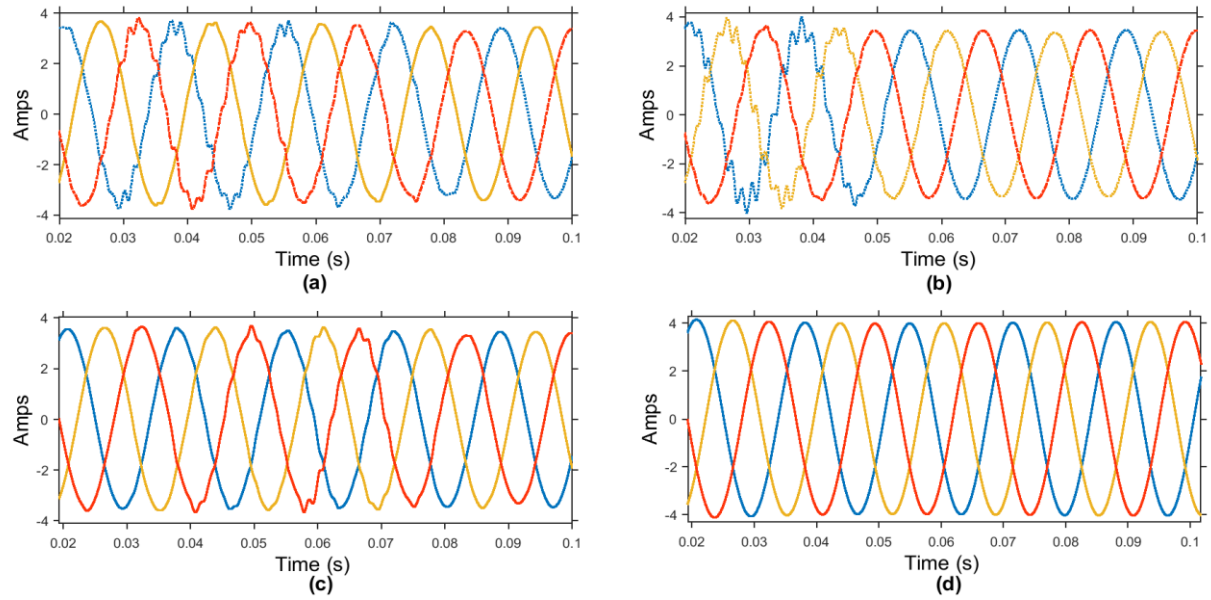

Figure 5.8 Simulation result for the grid current after compensation for (a) conventional PI controller (b) ABC algorithm (c) Jaya algorithm (d) Enhance Jaya (E-Jaya) algorithm

Figure 5.8 (a) illustrates the system's performance without the optimized D-STATCOM PI controller gain. The grid current still has some switching harmonics element after compensation; however, it considerably decreases with ABC optimization algorithm-based D-STATCOM as indicated in figure 5.8 (b). With the Jaya optimization algorithm in figure 5.8 (c), the switching harmonics were significantly mitigated. Figure 5.8 (d) depicts the grid current's performance with the E-Jaya optimization algorithm tuned PI controller; the source current became pure sinusoidal, as shown, validating the performance of the E-Jaya optimization technique.

Figures 5.9 to 5.13 present the harmonics spectral plot with the LCL filter. The THD spectrum plot using the Fast Fourier Transform (FFT) analysis of the grid current signals in MATLAB/Simulink software before and after D-STATCOM compensation. The highest current harmonics was 26% of the fundamental current, higher than the limit specified by the IEEE-519 standard obtained on the first harmonic order where the distortion content was relatively high. In the third harmonic order, the current harmonic was 12.5%, and in the fifth-order was 7%. The THD value (31.93%) has been calculated for the specified 0 to 5000Hz frequency range before D-STATCOM compensation. Figures 5.10 to 5.13 depict the optimized D-STATCOM. The THD has been reduced significantly. The first harmonics order was reduced from 26% to 1.5% with the developed E-Jaya optimization algorithm, and the THD value came to 1.01%.

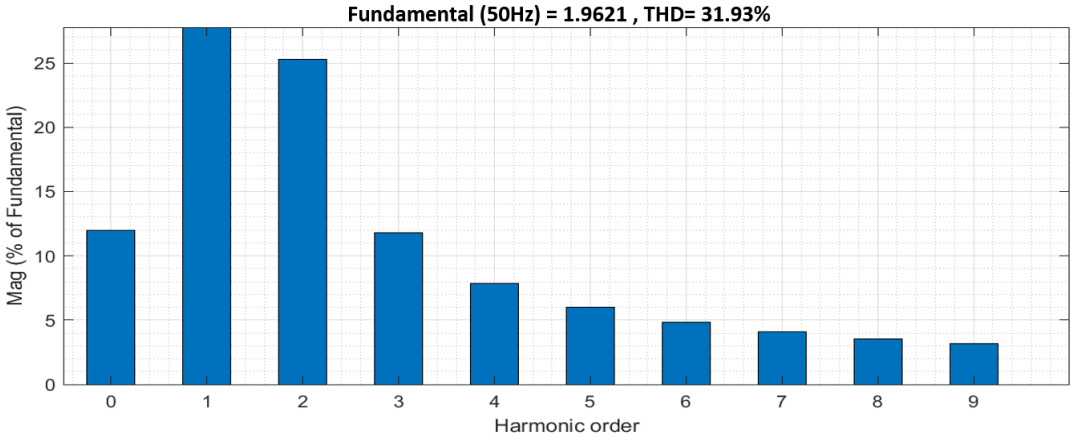

Figure 5.9 Source current spectral analysis without D-STATCOM compensation

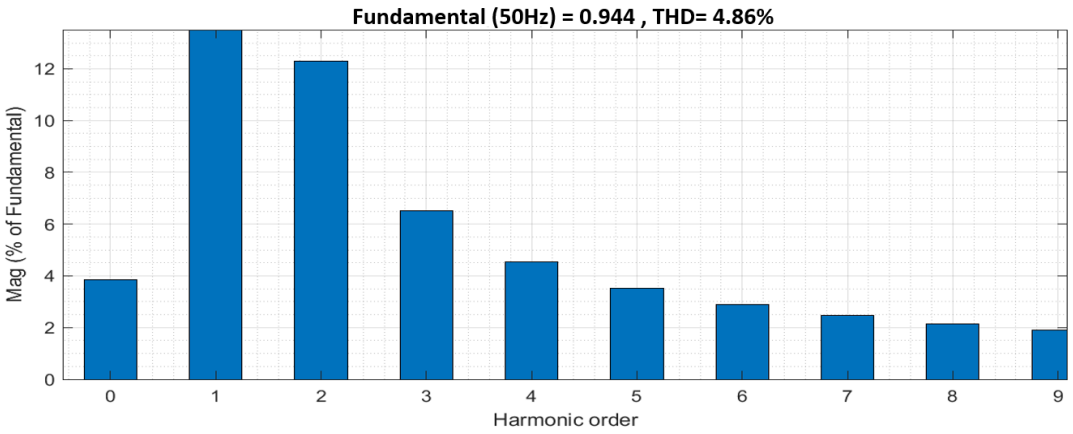

Figure 5.10 Source current spectral analysis with D-STATCOM conventional PI controller

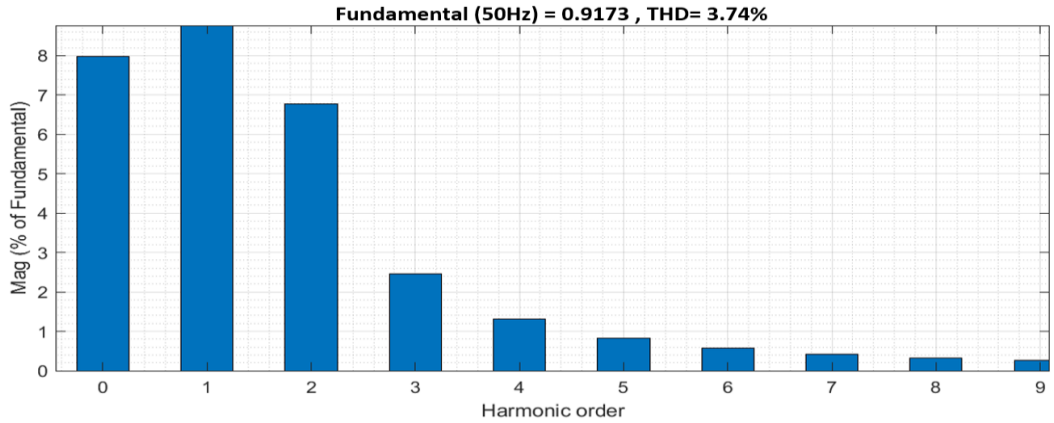

Figure 5.11 Source current spectral analysis with D-STATCOM ABC optimization algorithm

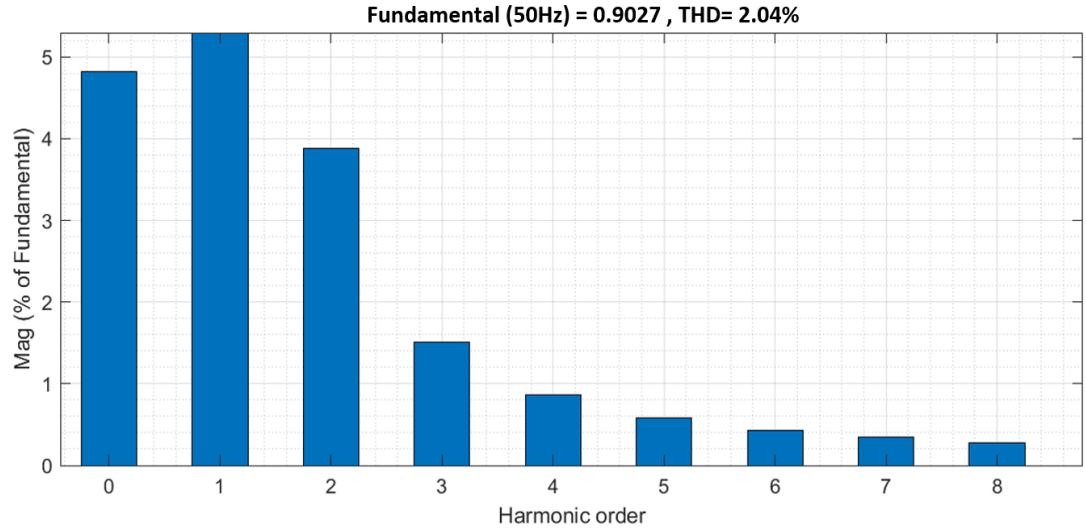

Figure 5.12 Source current spectral analysis with D-STATCOM Jaya optimization algorithm

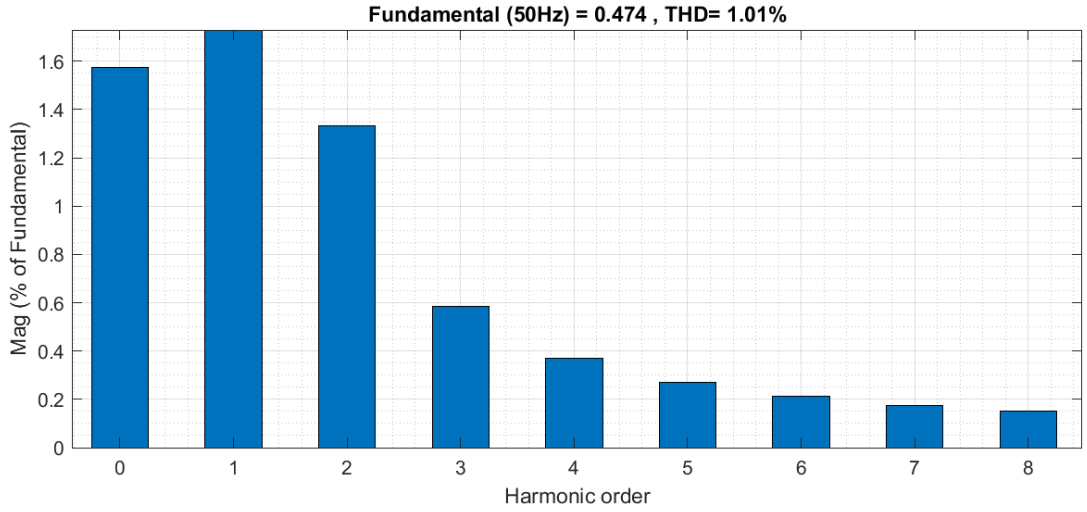

Figure 5.13 Source current spectral analysis with D-STATCOM E-Jaya optimization algorithm

5.8.3 Performance during balanced nonlinear and unbalanced linear and loads

The grid-tied PV system's performance with balanced nonlinear load, and unbalanced linear load, was simulated for this section. The model was run at 30 cycles per second with nonlinear loads. After that, the unbalanced linear load was connected to the grid. Figures 4.14 and 4.16 represent the load currents during these load switches before D-STATCOM was connected, respectively. The source currents after compensation during load change are shown in Figures. 4.15, and 4.17, respectively, for all optimized systems. Based on the results, although the ABC algorithm optimized system could minimize the load unbalancing, the required settling time after load switching is longer than the Jaya and the developed E-Jaya optimized D-STATCOM. Table 5.4 summarizes the comparative analysis of E-Jaya-based D-STACOM with ABC and Jaya optimization algorithm optimized systems.

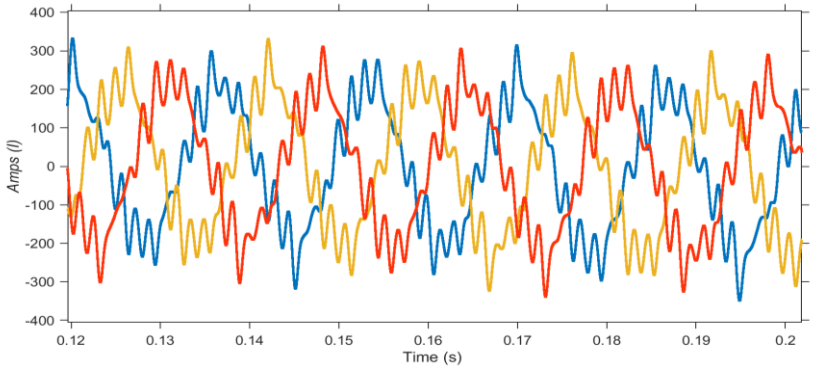

Figure 5.14 Load current during balanced nonlinear load

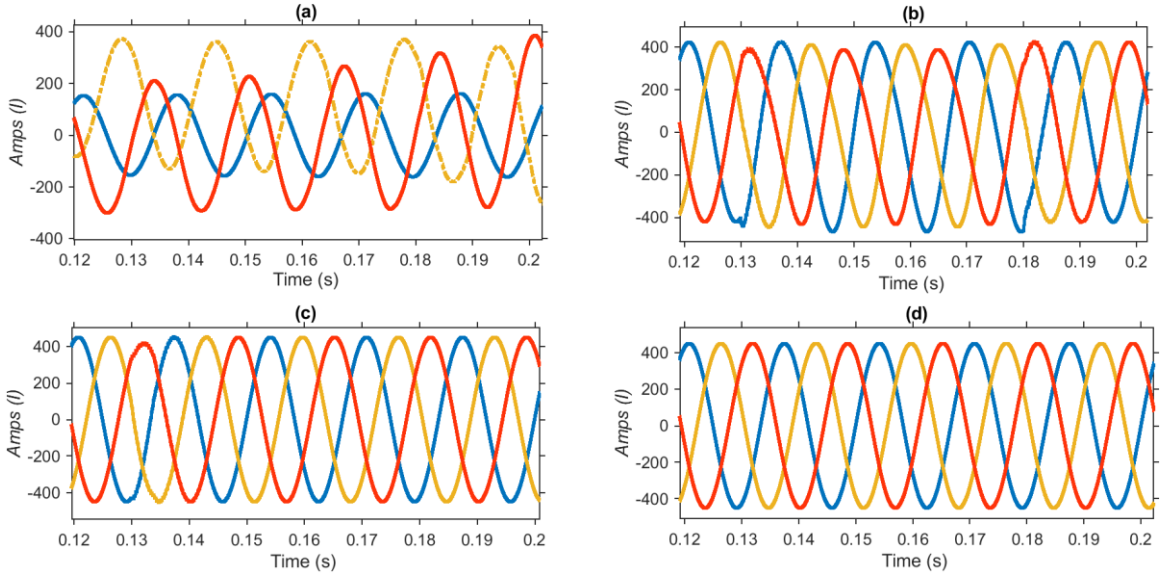

Figure 5.15 Source current with D-STATCOM compensation (a) without optimization. (b) With ABC optimization algorithm. (c) With Jaya optimization algorithm (d) With E-Jaya optimization algorithm.

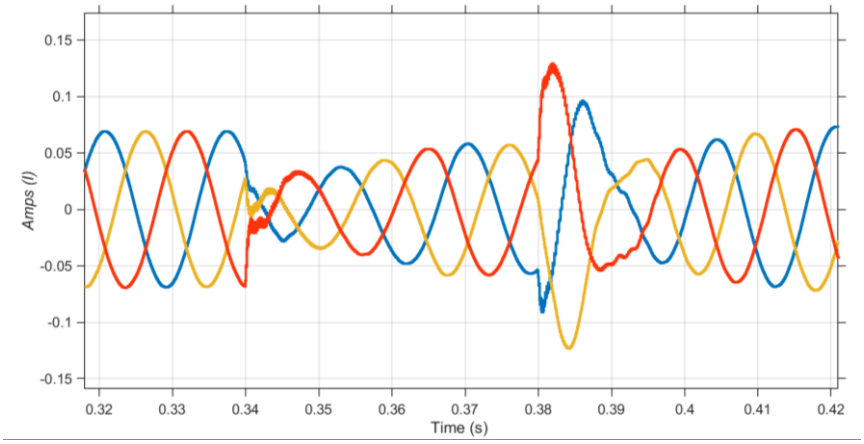

Figure 5.16 Load current during unbalanced linear load

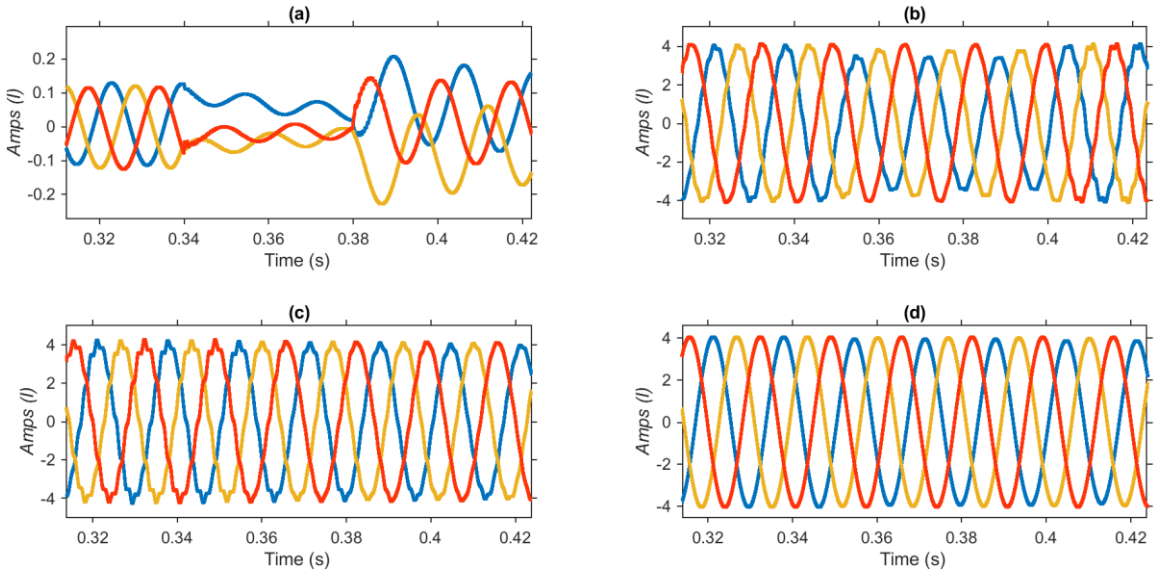

Figure 5.17 Source current with D-STATCOM compensation (a) without optimization. (b) With ABC optimization algorithm. (c) With Jaya optimization algorithm (d) With E-Jaya optimization algorithm.

The grid-tied PV system performance was analyzed with both the balanced nonlinear and unbalanced linear loads to demonstrate the compensation capacity of the developed optimized D-STATCOM for harmonics mitigation. Figure 5.16 illustrates the load current signal during the balanced nonlinear load simulation measured at PCC without the different optimized D-STATCOM connected. The D-STATCOM was connected at t = 0.1 seconds in figure 5.17, indicating that the different optimized D-STATCOM provided the necessary compensation to make the source current sinusoidal. Comparing figure 5.15 and figure 5.17 shows that E-Jaya remains unaffected by the load distorted current

like the conventional PI controlled, the ABC and Jaya optimized systems. The developed E-Jaya optimized PI controller tracks the reference efficiently when compared to ABC and Jaya algorithms. The current harmonics (THD) are reduced significantly below the IEEE required limits with the implemented E-Jaya algorithm optimized system. Figure 5.18 presents the THD bar chart for the source current with an unbalanced nonlinear load before and after optimized D-STATCOM compensation.

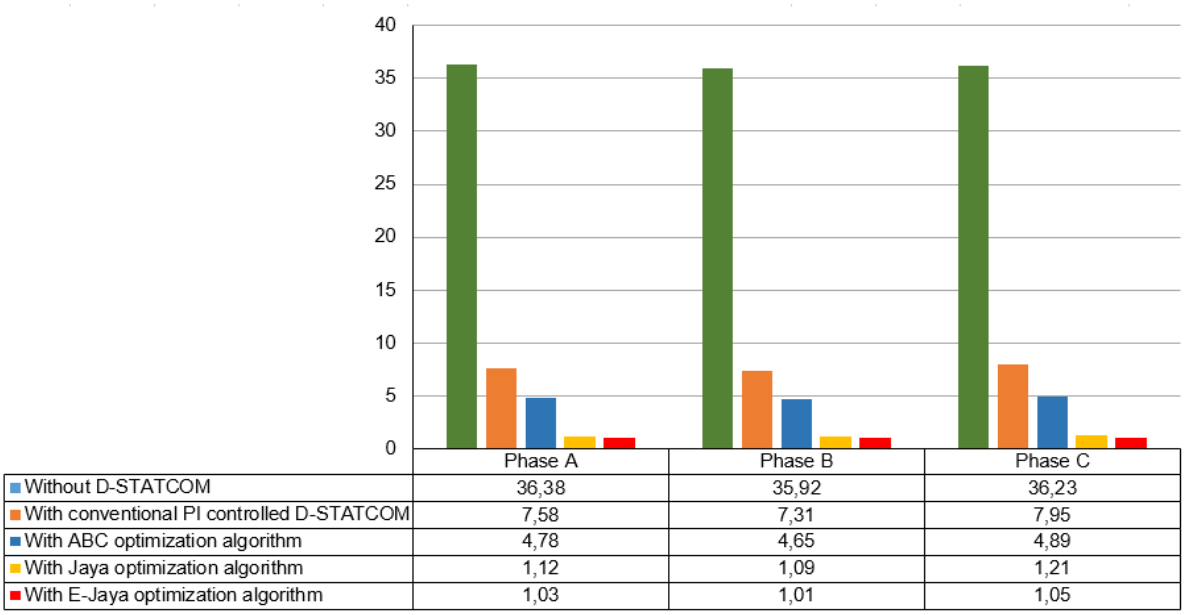

Figure 5.18 Source current total harmonic distortion pre and post-D-STATCOM connection

Table 5.4 outlines the empirical comparison of the developed E-Jaya-based D-STATCOM with the ABC and Jaya algorithm optimized systems to enhance grid-tied PV system power quality.

Table 5.4 Performance analysis of ABC, Jaya, and E-Jaya based D-STATCOM

Description	ABC	Jaya	E-Jaya
Dependence on control parameters unique to the algorithm	High	Not dependent	Not dependent
Steady-state THD (%)	2.52	1.05	1.01
Switching harmonics	High	Low	Low
Optimal solution convergence	Slow	Fast	Very Fast
Transient settling time	1.05	1	0.72
Dynamic response	Fair	Satisfactory	Very Good
Controlled reference tracking	Good	Good	Precise

CHAPTER SIX

Summary, Contributions, and Future Work

6.1. Summary

PV systems, which rely on one of the earth's natural resources, sunlight, are thought to be the most efficient alternative sources of electrical power. However, power quality is becoming a major concern as more distributed PV systems integrate into existing low voltage (LV) distribution systems. PV systems have significant benefits on the distribution system in meeting local energy demand. Still, there are a few power quality drawbacks as the PV systems are susceptible to solar irradiation variations, which poses concerns for LV distribution systems. From the existing literature reviewed in chapter two, it is established that these PV systems trigger a set of power quality issues such as harmonics and voltage quality. Besides that, conventional distribution systems, due to unbalanced loading and line configurations, are unbalanced. As a result, it is imperative to investigate PV system penetration's performance and impacts in unbalanced system circumstances. This thesis provides a comprehensive review of different custom power device applications and optimization methods in the literature, emphasizing their benefits and drawbacks while weighing their advantages and applications. The impact of different power quality problems in an unbalanced distribution system with PV system integration was explored in the first part of this thesis, including voltage rise/dip, voltage unbalances, voltage flicker emissions, and harmonic distortion. A novel optimization method was implemented to track D-STATCOM PI-controller gains to improve the FACT device's power quality compensation performance.

To investigate the impact of a grid-tied PV system on power quality, an accurate simulation model of a distribution system, PV system, and different load unit types required was analyzed, as stated in chapter three. This chapter also covered the theory behind each unit of the grid-tied PV system and their MATLAB/Simulink models. Following an investigation of the possible power quality issues, a novel compensation approach, Enhanced Jaya optimized D-STATCOM, was developed to address selected issues caused by PV penetrations on the distribution grid.

The voltage quality issues with PV penetration were analyzed in chapter four. The investigation began with the simulations of the IEEE-13 bus unbalanced distribution test system using Simulink. A defined dynamic model of a PV system was used in this study to represent a practical PV operating scenario to study the severity of voltage quality problems, and the study was carried out in two case studies. Additionally, the field-measured data used in this study were presented. The contributions of the thesis and the key conclusions taken from this study are highlighted below.

- Simulations were run for the first case study to test voltage rise and voltage unbalance in three scenarios: single PV system integration at the feeder's beginning, distributed PV penetration at multiple buses near the loads, and increased PV system capacity penetration. The grid was assumed to have 110 kW PV penetration in the first two scenarios, and this penetration was increased by 218% in the third scenario. According to the results, the voltage rise due to distributed PV integration was higher than the lumped PV penetration in the first case. The third scenario had a higher voltage rise and voltage unbalance impact due to increased PV penetration. According to the results, the PV power injected into the grid provided voltage support on the heavily loaded phases. Consequently, due to unbalanced phase loading, the voltage rise in each phase of three-phase grid-tied PV systems is different, with lightly loaded phases having higher values.

- Similarly, in the first and second scenarios, the voltage unbalance factor was within the regulated limit and lower than the third scenario. In the third scenario, the voltage unbalance increased due to the integration of distributed PV systems, which indicates the impact of the randomly distributed grid-tied PV system on the distribution network.

- In the second case study, fault analysis was used to determine the impact of PV integration in the distribution system using two types of faults (single and three-phase fault). An unbalanced fault occurrence was simulated on bus 634's Phase-A, resulting in a 25% voltage drop from the nominal voltage.

Simultaneously, the other two phases remained unaffected—the three-phase balanced fault event, causing more than an 80% voltage dip about the nominal voltage, was also stimulated. The results revealed that during fault conditions, the unbalanced voltage dip is partially mitigated by PV power and primarily compensated using a PI-controlled D-STATCOM. As compared to a PV system alone, the custom power unit effectively mitigated the voltage dip. It is observed that before the fault, there were no significant harmonics as the total harmonic deviation was 5.19%, which is within the required limit of 8% for voltage harmonics (THDv). During the faults, the measured THDv increased to 39.16%, above the required limit. The measured THDv at the PCC with the conventional D-STATCOM compensation effectively mitigated the fault impact and improved the grid THDv to 4.67%. Besides, field measurement-based investigations were conducted on the Durban University of Technology (DUT) Steve Biko campus PV site in chapter four to investigate the voltage quality issues caused by PV system penetration in a typical distribution grid. PV power generation is heavily influenced by solar irradiation and temperature, which are variable, affecting grid voltages. The impact of rapid variations in solar irradiation levels on voltage variation issues was investigated in this study. The performance analysis was conducted on the DUT grid-tied PV system, which has a 110 kW installed capacity. The ELSPEC power quality analyzer was installed at the PCC to record the field measurements. The power quality measurements at the PV inverter output level and the low voltage side of the distribution transformer for different operating days were recorded for this study. According to the results, the magnitudes of the grid voltages increased due to the PV power injection. The voltage levels were well within limits. Also investigated was the voltage flicker caused by solar irradiation variation. The voltage flickers were within the limit set by local and international standards during the measurement period.

In chapter five, to address these power quality issues, a new approach of adopting the FACT device, D-STATCOM, with the help of a novel control strategy was designed and implemented with MATLAB/Simulink simulations. Although different optimization techniques have been applied to D-STATCOM in the extant literature to track the PI controller gains' optimized value, as described in chapter two; however, those optimization algorithms are based on algorithm-

specific control parameters. If these parameters are not selected properly, the algorithms may fail to converge to optimal value or take longer to reach the optimal global value. As a result, Enhanced Jaya (E-Jaya) was developed as an optimization method for D-STATCOM. Its accuracy is independent of algorithm-specific control parameters. Through simulation with different load types connected to the grid in a typical grid scenario, the superiority of the E-Jaya optimized D-STATCOM over ABC, and Jaya optimization-based D-STATCOM was demonstrated. With the E-Jaya optimization implementation, the D-STATCOM current controller tracked the reference current better under balanced nonlinear and unbalanced linear load conditions. According to the simulation results, the THDs of the source current after compensation were significantly minimized to 1.01% from 31.93%. Therefore, it's evident that the D-STATCOM based on the E-Jaya optimization algorithm is effective for harmonic and reactive power compensation.

6.2 The Thesis Contribution

The performance of a grid-connected PV system and its related power quality issues have been analyzed, and a novel optimization approach based on D-STATCOM was implemented to mitigate the issues. This research investigates the application of optimized D-STATCOM to mitigate source voltage and source current harmonics caused by nonlinear loads through voltage control of dynamic loads. This study developed and implemented E-Jaya, a novel metaheuristic optimization algorithm to mitigate power quality issues in a grid-tied PV system using a VSC-based D-STATCOM. The following are the key contributions of this thesis:

- A comprehensive literature review of the impact and performance of grid-tied PV systems was conducted to discover a research gap in the field, leading to the implementation of a novel metaheuristic optimization algorithm.
- Various voltage quality issues due to PV system penetration on an unbalanced distribution grid were investigated using MATLAB/Simulink.
- Typical distribution system operating scenarios were modelled and simulated using the IEEE-13 bus test system with dynamic linear and nonlinear harmonic producing load models. A non-specific parameter

optimization method has been implemented to mitigate the observed power quality issues.

- Power quality issues relating to grid-tied PV systems have been investigated practically using field measurements obtained at the DUT Steve Biko campus PV power plant. Also studied was the impact of solar irradiation on voltage flicker and total demand distortion, which gives a better insight into the impact of harmonic distortion in low voltage distribution systems.
- A novel D-STATCOM control algorithm called E-Jaya was designed and implemented to compensate for power quality issues in an unbalanced grid-tied PV system. The algorithm converges faster to the optimal value than other optimization algorithms like ABC and Jaya. It has optimized PI controller gains for better performance, as observed from the results obtained through simulation.

6.3 Future Works Suggestions

Further research studies may be conducted to expand on the work outlined in this thesis. The following is a list of possible future research projects involving the penetration of renewable energy technologies into low-voltage distribution systems.

- ✓ Further investigation could be conducted using other real-time simulation software to study the D-STATCOM operation in mitigating voltage quality issues with different scenarios.

- ✓ An optimized D-STATCOM controller's performance may be investigated for reactive power compensation, voltage regulation, power factor improvement, and unbalanced load compensation in wind power plants.

- ✓ Field measurement from a PV system with higher installed capacity could be studied to understand and mitigate the harmonic resonance issues accompanied by PV systems penetration.

- ✓ In the low voltage distribution grid, energy storage systems are critical. If a STATCOM device has an energy storage system, it is referred to as an Energy Storage Enabled STATCOM (E-STATCOM). The device

performance may be investigated for voltage control applications. It is necessary to investigate the combined impact of PV and energy storage technologies' on a grid-tied PV system.

References

[1] B. Dudley, "BP statistical review of world energy," in *World Petroleum Congress*, London, 2019, pp. 1-64.

[2] (International Energy Agency, 23/09/2019). *Key World Energy Statistics: World Energy Outlook*.

[3] "Solar PV based on data from IEA Photovoltaic Power Systems Programme (PVPS), Snapshot of Global Photovoltaic Markets," 2018.

[4] (2020). *Installed renewable energy capacity trends* Available: https://www.irena.org/solar

[5] A. K. Aliyu, B. Modu, and C. W. Tan, "A review of renewable energy development in Africa: A focus in South Africa, Egypt and Nigeria," *Renewable and Sustainable Energy Reviews,* vol. 81, pp. 2502-2518, 2018.

[6] M. Karimi, H. Mokhlis, K. Naidu, S. Uddin, and A. Bakar, "Photovoltaic penetration issues and impacts in distribution network–A review," *Renewable and Sustainable Energy Reviews,* vol. 53, pp. 594-605, 2016.

[7] A. P. Kenneth and K. Folly, "Voltage rise issue with high penetration of grid connected PV," *IFAC Proceedings Volumes,* vol. 47, pp. 4959-4966, 2014.

[8] A. A. Adebiyi, A. K. Saha, I. J. Lazarus, and E. E. Ojo, "Investigation to Determine the Impacts of SPV Penetration on an Unbalanced Distribution Grid," in *2019 IEEE PES/IAS PowerAfrica*, 2019, pp. 116-120.

[9] A. A. Adebiyi, I. Lazaru, A. K. Saha, and E. E. Ojo, "High PV Penetration Impact on an Unbalanced Distribution Network," in *2019 IEEE PES/IAS PowerAfrica*, 2019, pp. 706-710.

[10] IEA, "SDG7: Data and Projections.," https://www.iea.org/reports/sdg7-data-and-projections, Paris,November 2019.

[11] A. Saberian, P. Farzan, M. F. Nejad, H. Hizam, C. Gomes, M. A. M. Radzi*, et al.*, "Role of FACTS devices in improving penetration of renewable energy," in *IEEE 7th International Power Engineering and Optimization Conference (PEOCO)*, 2013, pp. 432-437.

[12] Eskom, "Grid connection code for renewable power plants (RPPs) connected to the electricity transmission system (TS) or the distribution system (DS) in South Africa," in *Grid Code Version 2.8* vol. 2.8 ed. South Africa: National Energy Regulator of South Africa (NERSA), 2014, p. 64.

[13] U. J. Minnaar, B. Peterson, H. Mostert, J. Rens, and G. Botha, "Power quality grid code compliance for renewable power plants in South Africa," *IET Generation, Transmission & Distribution,* vol. 13, pp. 137-144, 2018.

[14] A. A. Adebiyi, I. J. Lazarus, A. K. Saha, and E. E. Ojo, "Performance analysis of 8 kW Grid-tied solar photovoltaic power plant in Durban South Africa," *International Journal of Mechanical Engineering and Technology,* vol. 10, pp. 82-95, 2019.

[15] M. H. Bollen, *Overview of power quality and power quality standards*. USA: IEEE, 2000.

[16] A. Zegaoui, M. Aillerie, P. Petit, J. Sawicki, A. Jaafar, C. Salame*, et al.*, "Comparison of two common maximum power point trackers by simulating of PV generators," *Energy Procedia,* vol. 6, pp. 678-687, 2011.

[17] K. Mertens, *Photovoltaics: fundamentals, technology, and practice*, 2nd ed.: John Wiley & Sons, 2019.

[18] A. N. A. Ali, M. H. Saied, M. Z. Mostafa, and T. M. Abdel-Moneim, "A survey of maximum PPT techniques of PV systems," in *2012 IEEE Energytech*, 2012, pp. 1-17.

[19] N. Femia, G. Petrone, G. Spagnuolo, and M. Vitelli, "Optimization of perturb and observe maximum power point tracking method," *IEEE transactions on power electronics,* vol. 20, pp. 963-973, 2005.

[20] H. Dghim, A. El-Naggar, and I. Erlich, "Harmonic distortion in low voltage grid with grid-connected photovoltaic," in *18th International Conference on Harmonics and Quality of Power (ICHQP)*, 2018, pp. 1-6.
[21] *Grid connection code for renewable power plants (RPPs) connected to the electricity transmission system (TS) or the distribution system (DS) in South Africa,* N. E. R. o. S. A. (NERSA), 2019.
[22] D. Morgan, A. Marshal, N. Williams, and W. Hove, "The Durban Solar City Framework as a case study for small scale embedded generators," in *24th Association of Municipal Electricities Utilities of Southern Africa Technical Convention 2013*, Buffalo City Metropolitan Municipality, Eastern Cape, South Africa, 2013, pp. 1-6.
[23] S. R. Wenham, M. A. Green, M. E. Watt, R. Corkish, and A. Sproul, *Applied photovoltaics*: Routledge, 2013.
[24] J. Chandrasekaran, D. Nithyaprakash, K. Ajjan, S. Maruthamuthu, D. Manoharan, and S. Kumar, "Hybrid solar cell based on blending of organic and inorganic materials—An overview," *Renewable and Sustainable Energy Reviews,* vol. 15, pp. 1228-1238, 2011.
[25] M. Drießen, D. Amiri, N. Milenkovic, B. Steinhauser, S. Lindekugel, J. Benick*, et al.*, "Solar cells with 20% efficiency and lifetime evaluation of epitaxial wafers," *Energy Procedia,* vol. 92, pp. 785-790, 2016.
[26] M. A. Green, "Commercial progress and challenges for photovoltaics," *Nature Energy,* vol. 1, p. 15015, 2016.
[27] W. Shockley, "The Theory of p-n Junctions in Semiconductors and p-n Junction Transistors," *Bell System Technical Journal,* vol. 28, pp. 435-489, 1949.
[28] P. Würfel and U. Würfel, *Physics of solar cells: from basic principles to advanced concepts*: John Wiley & Sons, 2016.
[29] A. A. Husain, W. Z. W. Hasan, S. Shafie, M. N. Hamidon, and S. S. Pandey, "A review of transparent solar photovoltaic technologies," *Renewable and Sustainable Energy Reviews,* vol. 94, pp. 779-791, 2018.
[30] S. Said, A. Massoud, M. Benammar, and S. Ahmed, "A matlab/simulink-based photovoltaic array model employing simpowersystems toolbox," *Journal of Energy and Power Engineering,* vol. 6, pp. 1-11, 2012.
[31] H. A. Aribisala, "Improving the efficiency of solar photovoltaic power system," Master dissertation, Electrical Engineering, University of Rhode Island, USA, 2013.
[32] A. Polman, M. Knight, E. C. Garnett, B. Ehrler, and W. C. Sinke, "Photovoltaic materials: Present efficiencies and future challenges," *Science,* vol. 352, p. 4424, 2016.
[33] J. Khan and M. H. Arsalan, "Solar power technologies for sustainable electricity generation–A review," *Renewable and Sustainable Energy Reviews,* vol. 55, pp. 414-425, 2016.
[34] G. Wei and S. R. Forrest, "Intermediate-band solar cells employing quantum dots embedded in an energy fence barrier," *Nano Letters,* vol. 7, pp. 218-222, 2007.
[35] R. King, D. Law, K. Edmondson, C. Fetzer, G. Kinsey, H. Yoon*, et al.*, "40% efficient metamorphic GaInP⁄ GaInAs⁄ Ge multijunction solar cells," *Applied physics letters,* vol. 90, pp. 183-516, 2007.
[36] A. Le Bris and J.-F. Guillemoles, "Hot carrier solar cells: Achievable efficiency accounting for heat losses in the absorber and through contacts," *Applied Physics Letters,* vol. 97, p. 113506, 2010.
[37] M. A. Green, K. Emery, Y. Hishikawa, W. Warta, and E. D. Dunlop, "Solar cell efficiency tables (Version 45)," *Progress in photovoltaics: research and applications,* vol. 23, pp. 1-9, 2015.
[38] B. P. Singh, S. K. Goyal, S. A. Siddiqui, and P. Kumar, "A Study and Comprehensive Overview of Inverter Topologies for Grid-Connected

Photovoltaic Systems (PVS)," in *Intelligent Computing Techniques for Smart Energy Systems*, ed: Springer, 2020, pp. 1009-1017.
[39] P. Jain, V. Agarwal, and B. P. Muni, "Hybrid phase locked loop for controlling master-slave configured centralized inverters in large solar photovoltaic power plants," *IEEE Transactions on Industry Applications,* vol. 54, pp. 3566-3574, 2018.
[40] C. A. Rojas, J. Fletcher, P. Acuna, R. P. Aguilera, and J. P. Astorga, "Model Predictive Control of a Multi-String LCL-Type Grid-Connected H-NPC PV Converter," in *2018 IEEE 27th International Symposium on Industrial Electronics (ISIE)*, 2018, pp. 252-257.
[41] C. A. Rojas, J. Fletcher, P. Acuna, R. P. Aguilera, and J. P. Astorga, "Model Predictive Control of a Multi-String LCL-Type Grid-Connected H-NPC PV Converter," in *IEEE 27th International Symposium on Industrial Electronics (ISIE)*, 2018, pp. 252-257.
[42] A. Hassan, A. Dash, and D. De, "Comparison of converter structures for residential PV system with module based maximum power point tracking," in *Technologies for Smart-City Energy Security and Power (ICSESP)*, 2018, pp. 1-6.
[43] D. Voglitsis, N. P. Papanikolaou, and A. C. Kyritsis, "Active cross-correlation anti-islanding scheme for PV module-integrated converters in the prospect of high penetration levels and weak grid conditions," *IEEE Transactions on Power Electronics,* vol. 34, pp. 2258-2274, 2018.
[44] K. Zeb, W. Uddin, M. A. Khan, Z. Ali, M. U. Ali, N. Christofides*, et al.*, "A comprehensive review on inverter topologies and control strategies for grid connected photovoltaic system," *Renewable and Sustainable Energy Reviews,* vol. 94, pp. 1120-1141, 2018.
[45] W. Omran, "Performance analysis of grid-connected photovoltaic systems.," PhD Thesis, Electrical and Computer Engineering, University of Waterloo, 2010.
[46] S. Deshpande and N. Bhasme, "A review of topologies of inverter for grid connected PV systems," in *Innovations in Power and Advanced Computing Technologies (i-PACT)*, 2017, pp. 1-6.
[47] M. Díez-Mediavilla, M. Dieste-Velasco, M. d. C. Rodríguez-Amigo, T. García-Calderón, and C. Alonso-Tristán, "Performance of grid-tied PV facilities based on real data in Spain: Central inverter versus string system," *Energy conversion and management,* vol. 86, pp. 1128-1133, 2014.
[48] L. Zhang, K. Sun, Y. W. Li, X. Lu, and J. Zhao, "A distributed power control of series-connected module-integrated inverters for PV grid-tied applications," *IEEE Transactions on Power Electronics,* vol. 33, pp. 7698-7707, 2017.
[49] D. Leuenberger and J. Biela, "PV-module-integrated AC inverters (AC modules) with subpanel MPP tracking," *IEEE Transactions on Power Electronics,* vol. 32, pp. 6105-6118, 2016.
[50] G. Masson and I. Kaizuka, "Trends 2017 in Photovoltaic Applications—Survey Report of Selected IEA Countries between 1992 and 2016," Technical Report IEA PVPS T1-32: 2017, International Energy Agency …2017.
[51] X.-F. Wang, Y. Song, and M. Irving, *Modern power systems analysis*: Springer Science & Business Media, 2010.
[52] C. Balu and D. Maratukulam, *Power system voltage stability*: McGraw Hill, 1994.
[53] B. Howe, "A New vision of PQ research for the next 10 years," in *2007 9th International Conference on Electrical Power Quality and Utilisation*, 2007, pp. 1-5.
[54] A. R. Abdullah, N. Abidullah, N. Shamsudin, N. Ahmad, and M. Jopri, "Performance Verification of Power Quality Signals Classification System," in *Applied Mechanics and Materials*, 2015, pp. 1158-1163.
[55] D. Chathurangi, U. Jayatunga, M. Rathnayake, A. Wickramasinghe, A. Agalgaonkar, and S. Perera, "Potential power quality impacts on LV distribution

networks with high penetration levels of solar PV," in *18th International Conference on Harmonics and Quality of Power (ICHQP)*, 2018, pp. 1-6.
[56] IEA, "World Energy Outlook 2018," https://www.iea.org/reports/world-energy-outlook-2018, Paris, 2018.
[57] A. Á. Téllez, G. López, I. Isaac, and J. González, "Optimal reactive power compensation in electrical distribution systems with distributed resources. Review," *Heliyon,* vol. 4, pp. 1-30, 2018.
[58] L. R. de Araujo, D. R. R. Penido, and F. de Alcântara Vieira, "A multiphase optimal power flow algorithm for unbalanced distribution systems," *International Journal of Electrical Power & Energy Systems,* vol. 53, pp. 632-642, 2013.
[59] W. Yi-Bo, W. Chun-Sheng, L. Hua, and X. Hong-Hua, "Steady-state model and power flow analysis of grid-connected photovoltaic power system," in *IEEE international conference on industrial technology*, 2008, pp. 1-6.
[60] M. Farhoodnea, A. Mohamed, H. Shareef, and H. Zayandehroodi, "Power quality impact of grid-connected photovoltaic generation system in distribution networks," in *IEEE Student Conference on Research and Development (SCOReD)*, 2012, pp. 1-6.
[61] S. Ali, N. Pearsall, and G. Putrus, "Impact of high penetration level of grid-connected photovoltaic systems on the UK low voltage distribution network," in *International Conference on Renewable Energies and Power Quality*, 2012, pp. 1-4.
[62] D. Motyka, M. Kajanová, and P. Braciník, "The Impact of Embedded Generation on Distribution Grid Operation," in *7th International Conference on Renewable Energy Research and Applications (ICRERA)*, 2018, pp. 360-364.
[63] Y. Zhou, L. Liu, and H. Li, "Autonomous control integrating fast voltage regulation and islanding detection for high penetration PV application," in *Twenty-Sixth Annual IEEE Applied Power Electronics Conference and Exposition (APEC)*, 2011, pp. 606-612.
[64] M. Chidi, O. Ipinnimo, S. Chowdhury, and S. Chowdhury, "Investigation of impact of integrating on-grid home based solar power systems on voltage rise in the utility network," in *IEEE Power and Energy Society General Meeting*, 2012, pp. 1-7.
[65] D. L. King, S. Gonzalez, G. M. Galbraith, and W. E. Boyson, "Performance model for grid-connected photovoltaic inverters," *Sandia National Laboratories SAND2007-5036,* vol. 38, pp. 655-660, 2007.
[66] C. Liu, X. Wang, J. Guo, M. Huang, and X. Wu, "Chance-constrained scheduling model of grid-connected microgrid based on probabilistic and robust optimisation," *IET Generation, Transmission & Distribution,* vol. 12, pp. 2499-2509, 2018.
[67] S. K. Firth, K. J. Lomas, and S. J. Rees, "A simple model of PV system performance and its use in fault detection," *Solar energy,* vol. 84, pp. 624-635, 2010.
[68] S. Rahman and B. H. Chowdhury, "Simulation of photovoltaic power systems and their performance prediction," *IEEE Transactions on energy conversion,* vol. 3, pp. 440-446, 1988.
[69] A. Woyte, V. Van Thong, R. Belmans, and J. Nijs, "Voltage fluctuations on distribution level introduced by photovoltaic systems," *IEEE Transactions on energy conversion,* vol. 21, pp. 202-209, 2006.
[70] A. A. A. El-Ela, R. A. El-Sehiemy, E. S. Ali, and A.-M. Kinawy, "Minimisation of voltage fluctuation resulted from renewable energy sources uncertainty in distribution systems," *IET Generation, Transmission & Distribution,* vol. 13, pp. 2339-2351, 2019.
[71] V. Acquaviva, P. Poggi, M. Muselli, and A. Louche, "Grid-connected rooftop PV systems for reducing voltage drops at the end of the feeder—a case study in Corsica Island," *Energy,* vol. 25, pp. 741-756, 2000.

[72] D. M. Riley and G. K. Venayagamoorthy, "Characterization and modeling of a grid-connected photovoltaic system using a recurrent neural network," in *The 2011 International Joint Conference on Neural Networks*, 2011, pp. 1761-1766.
[73] M. H. Bollen, "Understanding power quality problems," in *Voltage sags and Interruptions*, ed: IEEE press, 2000.
[74] J. Arrillaga, N. R. Watson, and S. Chen, *Power system quality assessment*: Chichester, New York: Wiley, 2000.
[75] W. E. Reid, "Power quality issues-standards and guidelines," *IEEE transactions on industry applications,* vol. 32, pp. 625-632, 1996.
[76] A. Kannan, V. Kumar, T. Chandrasekar, and B. J. Rabi, "A review of power quality standards, electrical software tools, issues and solutions," in *International Conference on Renewable Energy and Sustainable Energy (ICRESE)*, 2013, pp. 91-97.
[77] A. Chakrabarti and S. Halder, *Power System Analysis: Operation And Control 3rd Edition*: PHI Learning Pvt. Ltd., 2010.
[78] E. Committee, "IEEE recommended practice for monitoring electric power quality," *IEEE Std,* pp. c1-81, 2009.
[79] M. H. Bollen, *Understanding power quality problems. In Voltage sags and Interruptions.*: IEEE press, 2000.
[80] M. A. Shuvra and B. H. Chowdhury, "Distributed voltage control of active MV distribution networks in the presence of high PV penetration," in *IEEE Power & Energy Society Innovative Smart Grid Technologies Conference (ISGT)*, 2018, pp. 1-5.
[81] A. Sharma, M. Kolhe, U.-M. Nils, K. Muddineni, A. Mudgal, and S. Garud, "Voltage Rise Issues and Mitigation Techniques Due to High PV Penetration into the Distribution Network," in *International Conference on Automation and Computational Engineering (ICACE)*, 2018, pp. 72-78.
[82] N. Jenkins and J. Thornycroft, "Grid Connection of Photovoltaic Systems: Technical and Regulatory Issues," in *McEvoy's Handbook of Photovoltaics*, ed: Elsevier, 2018, pp. 847-876.
[83] X. Su, M. A. Masoum, and P. J. Wolfs, "Optimal PV inverter reactive power control and real power curtailment to improve performance of unbalanced four-wire LV distribution networks," *IEEE Transactions on Sustainable Energy,* vol. 5, pp. 967-977, 2014.
[84] S. Ghosh, S. Rahman, and M. Pipattanasomporn, "Local distribution voltage control by reactive power injection from PV inverters enhanced with active power curtailment," in *IEEE PES General Meeting| Conference & Exposition*, 2014, pp. 1-5.
[85] F. Bai, R. Yan, and T. K. Saha, "Impact of Power Fluctuations on Voltage Variations for Remote Distribution Networks with High PV Penetrations," in *IEEE Power & Energy Society General Meeting (PESGM)*, 2018, pp. 1-5.
[86] A. A. Adebiyi, I. J. Lazarus, A. K. Saha, and E. E. Ojo, "Performance analysis of grid-tied photovoltaic system under varying weather condition and load," *International Journal of Electrical & Computer Engineering (2088-8708),* vol. 11, 2021.
[87] R. C. Dugan, McGranaghan, M. F, Santoso, S., Beaty H. W, *Electrical power systems quality*: McGraw-Hill, 2010.
[88] M. Patsalides, D. Evagorou, G. Makrides, Z. Achillides, G. E. Georghiou, A. Stavrou*, et al.*, "The effect of solar irradiance on the power quality behaviour of grid connected photovoltaic systems," in *International Conference on Renewable Energy and Power Quality*, 2007, pp. 1-7.
[89] A. A. Adebiyi, E. E. Ojo, and I. E. Davidson, "Performance Evaluation of a Grid-tied PV System in the East Coast of South Africa," in *2020 IEEE PES/IAS PowerAfrica*, 2020, pp. 1-5.

[90] I. E. Commission, "Electromagnetic Compatibility (EMC)—Part 4-15: Testing and Measurement Techniques-Flickermeter-Functional and Design Specifications," IEC 61000-4-15-2010, Std.,2010.
[91] I. E. Commission, "Testing and Measurement Techniques—Power Quality Measurement Methods," IEC Standard 2003.
[92] A. Chanhome and S. Chaitusaney, "Voltage fluctuations relief by applying VAr control scheme function," in *proceedings of 13th International Conference on Electrical Engineering/Electronics, Computer, Telecommunications and Information Technology (ECTI-CON)*, 2016, pp. 1-6.
[93] R. Yan and T. K. Saha, "Investigation of voltage sensitivities to photovoltaic power fluctuations in unbalanced distribution networks," in *IEEE Power and Energy Society General Meeting*, 2012, pp. 1-7.
[94] K. W. Kow, Y. W. Wong, R. K. Rajkumar, and R. K. Rajkumar, "A review on performance of artificial intelligence and conventional method in mitigating PV grid-tied related power quality events," *Renewable and Sustainable Energy Reviews,* vol. 56, pp. 334-346, 2016.
[95] J. Marcos, L. Marroyo, E. Lorenzo, D. Alvira, and E. Izco, "Power output fluctuations in large scale PV plants: one year observations with one second resolution and a derived analytic model," *Progress in Photovoltaics: Research and Applications,* vol. 19, pp. 218-227, 2011.
[96] P. Chaudhari, P. Rane, A. Bawankar, P. Shete, K. Kalange, A. Moghe*, et al.*, "Design and implementation of statcom for reactive power compensation and voltage fluctuation mitigation in microgrid," in *IEEE International Conference on Signal Processing, Informatics, Communication and Energy Systems (SPICES)*, 2015, pp. 1-5.
[97] M. E. El-Hawary, *Electrical energy systems*: Crc Press, 2018.
[98] R. C. Dugan, M. F. McGranaghan, and H. W. Beaty, "Electrical power systems quality," *New York, NY: McGraw-Hill,| c1996,* 1996.
[99] O. Ipinnimo, S. Chowdhury, S. Chowdhury, and J. Mitra, "A review of voltage dip mitigation techniques with distributed generation in electricity networks," *Electric Power Systems Research,* vol. 103, pp. 28-36, 2013.
[100] A. Chidurala, T. Saha, and N. Mithulananthan, "Field investigation of voltage quality issues in distribution network with PV penetration," in *IEEE PES Asia-Pacific Power and Energy Engineering Conference (APPEEC)*, 2015, pp. 1-5.
[101] J. D. Mondol, Y. Yohanis, M. Smyth, and B. Norton, "Long term performance analysis of a grid connected photovoltaic system in Northern Ireland," *Energy Conversion and Management,* vol. 47, pp. 2925-2947, 2006.
[102] O. Ipinnimo, S. Chowdhury, and S. Chowdhury, "Effects of distributed generation (DG) on voltage dips in electricity networks," in *20th Southern African Universities Power Engineering Conference. Cape Town*, 2011, pp. 82-87.
[103] P. Mohammadi, H. El-Kishyky, M. Abdel-Akher, and M. Abdel-Salam, "The impacts of distributed generation on fault detection and voltage profile in power distribution networks," in *IEEE International Power Modulator and High Voltage Conference (IPMHVC)*, 2014, pp. 191-196.
[104] Y. Wang, Q. Xu, Y. Hu, and G. Chen, "Fast-transient repetitive controller based current control strategy for a cascaded DSTATCOM," in *IEEE Energy Conversion Congress and Exposition (ECCE)*, 2015, pp. 6704-6709.
[105] K. Yang and G. Chen, "Compensation current control for DSTATCOM based on repetitive control," *Dianli Xitong Zidonghua (Automation of Electric Power Systems),* vol. 37, pp. 80-85, 2013.
[106] J. Arrillaga and N. R. Watson, *Power system harmonics*: John Wiley & Sons, 2004.
[107] A. Chidurala, T. K. Saha, and N. Mithulananthan, "Harmonic impact of high penetration photovoltaic system on unbalanced distribution networks–learning

from an urban photovoltaic network," *IET Renewable Power Generation,* vol. 10, pp. 485-494, 2016.
[108] M. G. Villalva, J. R. Gazoli, and E. Ruppert Filho, "Comprehensive approach to modeling and simulation of photovoltaic arrays," *IEEE Transactions on power electronics,* vol. 24, pp. 1198-1208, 2009.
[109] A. R. Reisi, M. H. Moradi, and S. Jamasb, "Classification and comparison of maximum power point tracking techniques for photovoltaic system: A review," *Renewable and sustainable energy reviews,* vol. 19, pp. 433-443, 2013.
[110] A. Chidurala, T. Saha, and N. Mithulananthan, "Harmonic characterization of grid connected PV systems & validation with field measurements," in *IEEE Power & Energy Society General Meeting*, 2015, pp. 1-5.
[111] F. J. Ruiz-Rodriguez, J. C. Hernandez, and F. Jurado, "Harmonic modelling of PV systems for probabilistic harmonic load flow studies," *International Journal of Circuit Theory and Applications,* vol. 43, pp. 1541-1565, 2015.
[112] A. Chidurala, T. K. Saha, N. Mithulananthan, and R. C. Bansal, "Harmonic emissions in grid connected PV systems: A case study on a large scale rooftop PV site," in *IEEE PES General Meeting*| *Conference & Exposition*, 2014, pp. 1-5.
[113] Y. Li, W. Wang, B. Yuwen, S. Wei, W. Su, and Z. Lu, "Harmonic Model and Propagation in Power System: A Review," in *45th Annual Conference of the IEEE Industrial Electronics Society*, 2019, pp. 6147-6151.
[114] X. Guo, J. Zhou, R. He, X. Jia, and C. A. Rojas, "Leakage current attenuation of a three-phase cascaded inverter for transformerless grid-connected PV systems," *IEEE Transactions on Industrial Electronics,* vol. 65, pp. 676-686, 2017.
[115] X. Guo and X. Jia, "Hardware-based cascaded topology and modulation strategy with leakage current reduction for transformerless PV systems," *IEEE Transactions on Industrial Electronics,* vol. 63, pp. 7823-7832, 2016.
[116] M. Obi and R. Bass, "Trends and challenges of grid-connected photovoltaic systems–A review," *Renewable and Sustainable Energy Reviews,* vol. 58, pp. 1082-1094, 2016.
[117] D. Bernet and M. Hiller, "Grid-connected medium-voltage converters with parallel voltage-source active filters," *IET Electric Power Applications,* vol. 13, pp. 1507-1513, 2019.
[118] A. Benrabah, D. Xu, and Z. Gao, "Active disturbance rejection control of LCL-filtered grid-connected inverter using Padé approximation," *IEEE Transactions on Industry Applications,* vol. 54, pp. 6179-6189, 2018.
[119] S. Sakar, M. E. Balci, S. H. A. Aleem, and A. F. Zobaa, "Integration of large-scale PV plants in non-sinusoidal environments: Considerations on hosting capacity and harmonic distortion limits," *Renewable and Sustainable Energy Reviews,* vol. 82, pp. 176-186, 2018.
[120] A. Ghosh and G. Ledwich, *Power quality enhancement using custom power devices*: Springer science & business media, 2012.
[121] E. Fuchs and M. A. Masoum, *Power quality in power systems and electrical machines*: Academic press, 2011.
[122] M. Bajaj and A. K. Singh, "Grid integrated renewable DG systems: A review of power quality challenges and state-of-the-art mitigation techniques," *International Journal of Energy Research,* vol. 44, pp. 26-69, 2020.
[123] M. Farhadi-Kangarlu, E. Babaei, and F. Blaabjerg, "A comprehensive review of dynamic voltage restorers," *International Journal of Electrical Power & Energy Systems,* vol. 92, pp. 136-155, 2017.
[124] N. G. Hingorani, "Introducing custom power," *IEEE spectrum,* vol. 32, pp. 41-48, 1995.
[125] V. Remya, P. Parthiban, V. Ansal, and B. C. Babu, "Dynamic voltage restorer (DVR)–a review," *Journal of Green Engineering,* vol. 8, pp. 519-572, 2018.

[126] V. Cárdenas, M. A. González-García, and R. Álvarez-Salas, "A dynamic voltage restorer with the functions of voltage restoration, regulation using reactive power, and active filtering," *Electric Power Components and Systems,* vol. 43, pp. 1596-1609, 2015.
[127] H. Hafezi and R. Faranda, "Dynamic voltage conditioner: A new concept for smart low-voltage distribution systems," *IEEE Transactions on Power Electronics,* vol. 33, pp. 7582-7590, 2017.
[128] F. B. Ajaei, S. Farhangi, and R. Iravani, "Fault current interruption by the dynamic voltage restorer," *IEEE transactions on power delivery,* vol. 28, pp. 903-910, 2013.
[129] M. Nabipour, M. Razaz, S. G. Seifossadat, and S. Mortazavi, "A novel adaptive fuzzy membership function tuning algorithm for robust control of a PV-based Dynamic Voltage Restorer (DVR)," *Engineering Applications of Artificial Intelligence,* vol. 53, pp. 155-175, 2016.
[130] R. Satputaley, V. Borghate, and Y. Anusha, "A new 5-level transistor clamped H-bridge topology for DVR with repetitive controller," in *IEEE Region 10 Conference (TENCON)*, 2015, pp. 1-6.
[131] A. A. Adebiyi, I. J. Lazarus, A. K. Saha, and E. E. Ojo, "An Experimental Analysis of the Impact of a Grid-Tied Photovoltaic System on Harmonic Distortion," in *Proceedings of International Conference on Power Electronics and Renewable Energy Systems*, 2022, pp. 431-444.
[132] J. Roldán-Pérez, A. García-Cerrada, A. Rodríguez-Cabero, and J. L. Zamora-Macho, "Comprehensive Design and Analysis of a State-Feedback Controller for a Dynamic Voltage Restorer," *Energies,* vol. 11, pp. 1-26, 2018.
[133] A. M. Saeed, S. H. A. Aleem, A. M. Ibrahim, M. E. Balci, and E. E. El-Zahab, "Power conditioning using dynamic voltage restorers under different voltage sag types," *Journal of advanced research,* vol. 7, pp. 95-103, 2016.
[134] F. Shahnia, A. Ghosh, G. Ledwich, and F. Zare, "Voltage unbalance improvement in low voltage residential feeders with rooftop PVs using custom power devices," *International Journal of Electrical Power & Energy Systems,* vol. 55, pp. 362-377, 2014.
[135] A. M. Rauf and V. Khadkikar, "An enhanced voltage sag compensation scheme for dynamic voltage restorer," *IEEE transactions on industrial electronics,* vol. 62, pp. 2683-2692, 2014.
[136] L. B. G. Campanhol, S. A. O. da Silva, A. A. de Oliveira, and V. D. Bacon, "Power flow and stability analyses of a multifunctional distributed generation system integrating a photovoltaic system with unified power quality conditioner," *IEEE Transactions on Power Electronics,* vol. 34, pp. 6241-6256, 2018.
[137] R. Dharmalingam, S. S. Dash, K. Senthilnathan, A. B. Mayilvaganan, and S. Chinnamuthu, "Power quality improvement by unified power quality conditioner based on CSC topology using synchronous reference frame theory," *The Scientific World Journal,* vol. 2014, pp. 1-7, 2014.
[138] L. N. Popavath and P. Kaliannan, "Photovoltaic-STATCOM with low voltage ride through strategy and power quality enhancement in a grid integrated wind-PV system," *Electronics,* vol. 7, pp. 1-11, 2018.
[139] A. A. Adebiyi and K. Akindeji, "Investigating the effect of Static Synchronous Compensator (STATCOM) for voltage enhancement and transmission line losses mitigation," in *Proceedings of IEEE PES PowerAfrica*, 2017, pp. 462-467.
[140] H. K. Shah, P. Kapil, and M. Shah, "Simulation & analysis of distribution static compensator (D-STATCOM)," in *Proceedings of Nirma University International Conference on Engineering*, 2011, pp. 1-4.
[141] Z. Xi, "Control Strategy of STATCOM during System Faults," PhD Thesis, North Carolina State University, Raleigh, North Carolina, 2013.

[142] M. Noroozian, N. Petersson, B. Thorvaldson, A. Nilsson, and C. Taylor, "Benefits of SVC and STATCOM for electric utility application," in *IEEE PES Transmission and Distribution Conference and Exposition*, 2003, pp. 1143-1150.
[143] A. A. Adebiyi and K. Akindeji, "Investigating the effect of Static Synchronous Compensator (STATCOM) for voltage enhancement and transmission line losses mitigation," in *2017 IEEE PES PowerAfrica*, 2017, pp. 462-467.
[144] G. Gupta, W. L. Fritz, and M. Kahn, "A comprehensive review of DSTATCOM: control and compensation strategies," *International Journal of Applied Engineering Research,* vol. 12, pp. 3387-3393, 2017.
[145] B. B. Zad, J. Lobry, F. Vallee, and O. Durieux, "Improvement of on-load tap changer performance in voltage regulation of MV distribution," in *proceedings of 22nd International Conference on Electricity Distribution*, Stockholm, 2013, pp. 1-4.
[146] P. Kumar, N. Kumar, and A. Akella, "Review of D-STATCOM for stability analysis," *IOSR Journal of Electrical and Electronics Engineering,,* vol. 1, pp. 1-9, 2012.
[147] V. Murthy and A. Kumar, "Comparison of optimal DG allocation methods in radial distribution systems based on sensitivity approaches," *International Journal of Electrical Power & Energy Systems,* vol. 53, pp. 450-467, 2013.
[148] R. Sirjani and A. R. Jordehi, "Optimal placement and sizing of distribution static compensator (D-STATCOM) in electric distribution networks: A review," *Renewable and Sustainable Energy Reviews,* vol. 77, pp. 688-694, 2017.
[149] V. K. Kannan and N. Rengarajan, "Photovoltaic based distribution static compensator for power quality improvement," *International Journal of Electrical Power & Energy Systems,* vol. 42, pp. 685-692, 2012.
[150] R. K. Agarwal, I. Hussain, and B. Singh, "Implementation of LLMF control algorithm for three-phase grid-tied SPV-DSTATCOM system," *IEEE Transactions on Industrial Electronics,* vol. 64, pp. 7414-7424, 2016.
[151] M. Badoni, A. Singh, and B. Singh, "Adaptive neurofuzzy inference system least-mean-square-based control algorithm for DSTATCOM," *IEEE Transactions on industrial informatics,* vol. 12, pp. 483-492, 2016.
[152] M. Badoni, A. Singh, and B. Singh, "Real-time recurrent learning-based algorithm for control of DSTATCOM," in *Proceedings of the Annual IEEE India Conference (INDICON)*, 2015, pp. 1-6.
[153] R. Kumar, B. Singh, D. Shahani, and C. Jain, "Dual-tree complex wavelet transform-based control algorithm for power quality improvement in a distribution system," *IEEE transactions on industrial electronics,* vol. 64, pp. 764-772, 2016.
[154] T. A. Kumar and L. S. Rao, "Improvement of power quality of distribution system using ANN-LMBNN based D-STATCOM," in *Proceedings of Innovations in Power and Advanced Computing Technologies (i-PACT)*, Vellore, India, 2017, pp. 1-6.
[155] M. Moazzami, G. B. Gharehpetian, H. Shahinzadeh, and S. H. Hosseinian, "Optimal locating and sizing of DG and D-STATCOM using Modified Shuffled Frog Leaping Algorithm," in *Proceedings of 2nd Conference on Swarm Intelligence and Evolutionary Computation (CSIEC)*, Kerman, Iran, 2017, pp. 54-59.
[156] J. Shi, A. Noshadi, A. Kalam, and P. Shi, "Fuzzy logic control of DSTATCOM for improving power quality and dynamic performance," in *Proceedings of Australasian Universities Power Engineering Conference (AUPEC)*, Wollongong, NSW, Australia, 2015, pp. 1-6.
[157] S. K. Patel, S. R. Arya, R. Maurya, and B. Singh, "Interior point algorithm for optimal control of distribution static compensator under distorted supply voltage conditions," *IET Generation, Transmission & Distribution,* vol. 10, pp. 1778-1791, 2016.

[158] F. Shahnia, A. Ghosh, G. Ledwich, and F. Zare, "Voltage correction in low voltage distribution networks with rooftop PVs using custom power devices," in *37th Annual Conference of the IEEE Industrial Electronics Society (IECON 2011)*, 2011, pp. 991-996.
[159] S. A. Mohamed, N. Luo, J. González, T. Pujol, and L. Pacheco, "FACTS Family for Voltage Sag Alleviation: Performance Study and Analysis," *Renewable Energies and Power Quality Journal (RE&PQJ),* vol. 1, pp. 561-566, 2019.
[160] E. Hossain, M. R. Tür, S. Padmanaban, S. Ay, and I. Khan, "Analysis and mitigation of power quality issues in distributed generation systems using custom power devices," *IEEE Access,* vol. 6, pp. 16816-16833, 2018.
[161] P. R. Kasari, M. Paul, B. Das, and A. Chakraborti, "Analysis of D-STATCOM for power quality enhancement in distribution network," in *IEEE Region 10 Conference (TENCON 2017)*, 2017, pp. 1421-1426.
[162] S. Torabi, D. Nazarpour, and Y. Shayestehfard, "Compensation of sags and swells voltage using Dynamic Voltage Restorer (DVR) during single line to ground and three-phase faults," *International Journal on Technical and Physical Problems of Engineering (IJTPE),* vol. 4, pp. 126-132, 2012.
[163] S. Mishra and P. K. Ray, "Power quality improvement using photovoltaic fed DSTATCOM based on JAYA optimization," *IEEE Transactions on Sustainable Energy,* vol. 7, pp. 1672-1680, 2016.
[164] O. P. Mahela and A. G. Shaik, "A review of distribution static compensator," *Renewable and Sustainable Energy Reviews,* vol. 50, pp. 531-546, 2015.
[165] B. Singh, S. R. Arya, S. K. Dube, A. Chandra, and K. Al-Haddad, "Implementation of DSTATCOM using neural network based radial basis function," in *IEEE Industry Applications Society Annual Meeting*, 2013, pp. 1-8.
[166] S. R. Arya, B. Singh, A. Chandra, and K. Al-Haddad, "Learning-based anti-Hebbian algorithm for control of distribution static compensator," *IEEE Transactions on Industrial Electronics,* vol. 61, pp. 6004-6012, 2014.
[167] B. Singh and S. R. Arya, "Implementation of single-phase enhanced phase-locked loop-based control algorithm for three-phase DSTATCOM," *IEEE transactions on power delivery,* vol. 28, pp. 1516-1524, 2013.
[168] B. Singh, P. Jayaprakash, D. P. Kothari, A. Chandra, and K. Al Haddad, "Comprehensive study of DSTATCOM configurations," *IEEE Transactions on Industrial Informatics,* vol. 10, pp. 854-870, 2014.
[169] T. Zaveri, B. Bhalja, and N. Zaveri, "A novel approach of reference current generation for power quality improvement in three-phase, three-wire distribution system using DSTATCOM," *International Journal of Electrical Power & Energy Systems,* vol. 33, pp. 1702-1710, 2011.
[170] K. H. LaCommare and J. H. Eto, "Understanding the cost of power interruptions to US electricity consumers," Lawrence Berkeley National Lab.(LBNL), Berkeley, CA (United States)2004.
[171] S. Bhattacharyya, J. Myrzik, and W. Kling, "Consequences of poor power quality-an overview," in *42nd International Universities Power Engineering Conference*, 2007, pp. 651-656.
[172] R. Targosz and J. Manson, "Pan-European power quality survey," in *9th International Conference on Electrical Power Quality and Utilisation*, 2007, pp. 1-6.
[173] B. Howe, "A New vision of PQ research for the next 10 years," in *9th International Conference on Electrical Power Quality and Utilisation*, 2007, pp. 1-5.
[174] S. Sewchurran and I. E. Davidson, "Guiding principles for grid code compliance of large utility scale renewable power plant intergration onto South Africa's transmission/distribution networks," in *2016 IEEE International Conference on Renewable Energy Research and Applications (ICRERA)*, 2016, pp. 528-537.

[175] E. Buraimoh, A. A. Adebiyi, O. J. Ayamolowo, and I. E. Davidson, "South Africa Electricity Supply System: The Past, Present and The Future," in *2020 IEEE PES/IAS PowerAfrica*, 2020, pp. 1-5.
[176] A. Std, "C84. 1-2006," *For Electric Power Systems and Equipment-Voltage Ratings (60 Hz),* 2006.
[177] E. S. L. Committee, "NRS 048-2: 2003. Pretoria: Standards South Africa, 2003," vol. Electricity Suppliers Liaison Committee, ed. Johannesburg: Technology Standardization Department (TSD), Eskom, 2003, pp. 1-33.
[178] A. D. Rodriguez, F. M. Fuentes, and A. J. Matta, "Comparative analysis between voltage unbalance definitions," in *2015 Workshop on Engineering Applications-International Congress on Engineering (WEA)*, Bogota, Colombia, 2015, pp. 1-7.
[179] I. E. Commission, "IEC 61000-4-30, Electromagnetic compatibility (EMC)-Part 4-30: Testing and measurement techniques-Power quality measurement methods," ed: Edition 3.0, 2015.
[180] D. Schwanz, F. Möller, S. K. Rönnberg, J. Meyer, and M. H. Bollen, "Stochastic assessment of voltage unbalance due to single-phase-connected solar power," *IEEE Transactions on Power Delivery,* vol. 32, pp. 852-861, 2016.
[181] P. M. Ivry, "Predicting Stochastic Harmonics of Multiple Converters in a Power System (microgrid)," PhD thesis, Electrical Engineering, University of Nottingham, Nottingham, United Kingdom, 2016.
[182] K. Dartawan and A. M. Najafabadi, "Case study: Applying IEEE Std. 519-2014 for harmonic distortion analysis of a 180 MW solar farm," in *2017 IEEE Power & Energy Society General Meeting*, 2017, pp. 1-5.
[183] I.-I. E. Commission, "IEC 61800-3:2018," in *Adjustable speed electrical power drive systems - Part 3: EMC requirements and specific test methods*, ed. Frankfurt, Germany: European Committee for Standards - Electrical, 2018, p. 128.
[184] D. G. Photovoltaics and E. Storage, "IEEE Guide for Design, Operation, and Integration of Distributed Resource Island Systems with Electric Power Systems," *IEEE Std 1547.4-2011,* pp. 1-54, 2011.
[185] I. S. Association, "519-2014-IEEE Recommended Practices and Requirements for Harmonic Control in Electric Power Systems," *New York, IEEE,* 2014.
[186] ABB, "Guide to harmonics with AC drives," 2017.
[187] M. E. Ya'acob, H. Hizam, T. Khatib, and M. A. M. Radzi, "A comparative study of three types of grid connected photovoltaic systems based on actual performance," *Energy Conversion and Management,* vol. 78, pp. 8-13, 2014.
[188] F. Katiraei and J. R. Aguero, "Solar PV integration challenges," *IEEE Power and Energy Magazine,* vol. 9, pp. 62-71, 2011.
[189] A. M. Humada, M. Hojabri, S. Mekhilef, and H. M. Hamada, "Solar cell parameters extraction based on single and double-diode models: A review," *Renewable and Sustainable Energy Reviews,* vol. 56, pp. 494-509, 2016.
[190] M. B. Rhouma, A. Gastli, L. B. Brahim, F. Touati, and M. Benammar, "A simple method for extracting the parameters of the PV cell single-diode model," *Renewable Energy,* vol. 113, pp. 885-894, 2017.
[191] T. Ahmad, S. Sobhan, and M. F. Nayan, "Comparative analysis between single diode and double diode model of PV cell: concentrate different parameters effect on its efficiency," *Journal of Power and Energy Engineering,* vol. 4, pp. 31-46, 2016.
[192] H. K. Mehta, H. Warke, K. Kukadiya, and A. K. Panchal, "Accurate Expressions for Single-Diode-Model Solar Cell Parameterization," *IEEE Journal of Photovoltaics,* vol. 9, pp. 803-810, 2019.
[193] A. Dehghanzadeh, G. Farahani, and M. Maboodi, "A novel approximate explicit double-diode model of solar cells for use in simulation studies," *Renewable energy,* vol. 103, pp. 468-477, 2017.

[194] Y. Chen, Y. Sun, and Z. Meng, "An improved explicit double-diode model of solar cells: Fitness verification and parameter extraction," *Energy conversion and management,* vol. 169, pp. 345-358, 2018.
[195] M. H. Qais, H. M. Hasanien, and S. Alghuwainem, "Parameters extraction of three-diode photovoltaic model using computation and Harris Hawks optimization," *Energy,* vol. 195, p. 117040, 2020.
[196] T. Wei, F. Yu, G. Huang, and C. Xu, "A Particle-Swarm-Optimization-Based Parameter Extraction Routine for Three-Diode Lumped Parameter Model of Organic Solar Cells," *IEEE Electron Device Letters,* vol. 40, pp. 1511-1514, 2019.
[197] D. Allam, D. Yousri, and M. Eteiba, "Parameters extraction of the three diode model for the multi-crystalline solar cell/module using Moth-Flame Optimization Algorithm," *Energy Conversion and Management,* vol. 123, pp. 535-548, 2016.
[198] T. Markvart and L. Castañer, "Principles of solar cell operation," in *McEvoy's Handbook of Photovoltaics*, ed: Elsevier, 2018, pp. 3-28.
[199] V. J. Chin, Z. Salam, and K. Ishaque, "Cell modelling and model parameters estimation techniques for photovoltaic simulator application: A review," *Applied Energy,* vol. 154, pp. 500-519, 2015.
[200] A. Adebiyi, I. Lazarus, A. Saha, and E. Ojo, "Performance analysis of PV panels connected in various orientations under different climate conditions," in *Proceedings of the 5th Southern African Solar Energy Conference (SASEC 2018)*, 2018, pp. 46-51.
[201] A. R. Jordehi, "Parameter estimation of solar photovoltaic (PV) cells: A review," *Renewable and Sustainable Energy Reviews,* vol. 61, pp. 354-371, 2016.
[202] K. Ishaque, Z. Salam, and H. Taheri, "Simple, fast and accurate two-diode model for photovoltaic modules," *Solar energy materials and solar cells,* vol. 95, pp. 586-594, 2011.
[203] S. Steingrube, O. Breitenstein, K. Ramspeck, S. Glunz, A. Schenk, and P. P. Altermatt, "Explanation of commonly observed shunt currents in c-Si solar cells by means of recombination statistics beyond the Shockley-Read-Hall approximation," *Journal of Applied Physics,* vol. 110, p. 014515, 2011.
[204] O. S. Elazab, H. M. Hasanien, M. A. Elgendy, and A. M. Abdeen, "Parameters estimation of single-and multiple-diode photovoltaic model using whale optimisation algorithm," *IET Renewable Power Generation,* vol. 12, pp. 1755-1761, 2018.
[205] N. Priyadarshi, K. Yadav, V. Kumar, and M. Vardia, "An experimental study on zeta buck–boost converter for application in pv system," in *Handbook of Distributed Generation*, ed: Springer, 2017, pp. 393-406.
[206] S. Ding, W. X. Zheng, J. Sun, and J. Wang, "Second-order sliding-mode controller design and its implementation for buck converters," *IEEE Transactions on Industrial Informatics,* vol. 14, pp. 1990-2000, 2017.
[207] H. Fathabadi, "Novel high efficiency DC/DC boost converter for using in photovoltaic systems," *Solar Energy,* vol. 125, pp. 22-31, 2016.
[208] M. Salimi, "Practical implementation of the Lyapunov based nonlinear controller in DC-DC boost converter for MPPT of the PV systems," *Solar Energy,* vol. 173, pp. 246-255, 2018.
[209] S. Saravanan and N. R. Babu, "Maximum power point tracking algorithms for photovoltaic system–A review," *Renewable and Sustainable Energy Reviews,* vol. 57, pp. 192-204, 2016.
[210] C. Li, Y. Chen, D. Zhou, J. Liu, and J. Zeng, "A high-performance adaptive incremental conductance MPPT algorithm for photovoltaic systems," *Energies,* vol. 9, pp. 288-305, 2016.
[211] D. G. Holmes and T. A. Lipo, *Pulse width modulation for power converters: principles and practice* vol. 18: John Wiley & Sons, 2003.

[212] C. Jain, B. J. I. J. o. E. Singh, and S. T. i. P. Electronics, "An adjustable DC link voltage-based control of multifunctional grid interfaced solar PV system," vol. 5, pp. 651-660, 2016.
[213] W. H. Kersting, "Radial distribution test feeders," *IEEE Transactions on Power Systems,* vol. 6, pp. 975-985, 1991.
[214] S. Ouali and A. Cherkaoui, "An Improved Backward/Forward Sweep Power Flow Method Based on a New Network Information Organization for Radial Distribution Systems," *Journal of Electrical and Computer Engineering,* vol. 2020, pp. 1-12, 2020.
[215] F. Hameed, M. Al Hosani, and H. H. Zeineldin, "A modified backward/forward sweep load flow method for islanded radial microgrids," *IEEE Transactions on Smart Grid,* vol. 10, pp. 910-918, 2017.
[216] P. Kundur, N. J. Balu, and M. G. Lauby, *Power system stability and control* vol. 7: McGraw-hill New York, 1994.
[217] A. Arif, Z. Wang, J. Wang, B. Mather, H. Bashualdo, and D. Zhao, "Load modeling—A review," *IEEE Transactions on Smart Grid,* vol. 9, pp. 5986-5999, 2018.
[218] J. V. Milanovic, K. Yamashita, S. M. Villanueva, S. Ž. Djokic, and L. M. Korunović, "International industry practice on power system load modeling," *IEEE Transactions on Power Systems,* vol. 28, pp. 3038-3046, 2012.
[219] K. Rudion, A. Orths, Z. A. Styczynski, and K. Strunz, "Design of benchmark of medium voltage distribution network for investigation of DG integration," in *IEEE Power Engineering Society General Meeting*, 2006, pp. 1-6.
[220] P. Elisabet, "Three phase state estimation: Performance in changing operating conditions," Master, Electrical and Information Technology, RWTH Aschen University, Germany, 2014.
[221] Q.-N. Trinh, F. H. Choo, and P. Wang, "Control strategy to eliminate impact of voltage measurement errors on grid current performance of three-phase grid-connected inverters," *IEEE Transactions on Industrial Electronics,* vol. 64, pp. 7508-7519, 2017.
[222] Q. N. Trinh, P. Wang, Y. Tang, and F. H. Choo, "Mitigation of DC and harmonic currents generated by voltage measurement errors and grid voltage distortions in transformerless grid-connected inverters," *IEEE Transactions on Energy Conversion,* vol. 33, pp. 801-813, 2017.
[223] M. A. K. A. Biabani, S. M. Ali, and A. Jawed, "Enhancement of power quality in distribution system using D-Statcom," in *International Conference on Signal Processing, Communication, Power and Embedded System (SCOPES)*, 2016, pp. 2093-2098.
[224] S. Stanković and L. Söder, "Analytical estimation of reactive power capability of a radial distribution system," *IEEE Transactions on Power Systems,* vol. 33, pp. 6131-6141, 2018.
[225] P. Nijhawan1, R. S. Bhatia2, and D. K. Jain3, "Application of PI controller based DSTATCOM for improving the power quality in a power system network with induction furnace load," *Sonklanakarin Journal of Science and Technology,* vol. 34, pp. 195-201, 2012.
[226] J. Dannehl, C. Wessels, and F. W. Fuchs, "Limitations of voltage-oriented PI current control of grid-connected PWM rectifiers with LCL filters," *IEEE transactions on industrial electronics,* vol. 56, pp. 380-388, 2008.
[227] J. Yin, S. Duan, and B. Liu, "Stability analysis of grid-connected inverter with LCL filter adopting a digital single-loop controller with inherent damping characteristic," *IEEE Transactions on Industrial Informatics,* vol. 9, pp. 1104-1112, 2012.
[228] V. Reddy, "Improvement of power quality using custom power devices," PhD PhD, Electrical Engineering, Jawaharlal Nehru Technological University, Hyderabad, India, 2012.

[229] R. Pandey, R. N. Tripathi, and T. Hanamoto, "Comprehensive analysis of LCL filter interfaced cascaded H-bridge multilevel inverter-based DSTATCOM," *Energies,* vol. 10, pp. 346-368, 2017.
[230] B. Magoro and T. Khoza, "Grid Connection code for renewable power plants (RPPs) connected to the electricity Transmission System (TS) or the Distribution System (DS) in South Africa," *National Energy Regulator of South Africa (NERSA), Version 2.8,* vol. 2, pp. 372-378, 2012.
[231] T. Andersson and D. Nilsson, "Test and evaluation of voltage dip immunity," Master Dissertation, Department of Electrical Engineering, Chalmers University of Technology, Swedish, 2002.
[232] J. C. Smith, G. Hensley, and L. Ray, "IEEE Recommended Practice for Monitoring Electric Power Quality," *IEEE Std 1159-2019 (Revision of IEEE Std 1159-2009),* pp. 1-98, 2019.
[233] Y. Geng, K. Yang, Z. Lai, P. Zheng, H. Liu, and R. Deng, "A Novel Low Voltage Ride Through Control Method for Current Source Grid-Connected Photovoltaic Inverters," *IEEE Access,* vol. 7, pp. 51735-51748, 2019.
[234] A. Q. Al-Shetwi, M. Hannan, K. P. Jern, A. A. Alkahtani, and A. PG Abas, "Power Quality Assessment of Grid-Connected PV System in Compliance with the Recent Integration Requirements," *Electronics,* vol. 9, p. 366, 2020.
[235] L. Wang, "The fault causes of overhead lines in distribution network," in *MATEC Web of Conferences*, 2016, pp. 1-5.
[236] M. Steglich, C. Löwe, B. Bauernschmitt, C. Rehtanz, R. Böhm, and J. Franke, "A novel method to reduce the harmonic currents in the residual earth fault current during a single phase to ground fault in compensated grids," in *IEEE PES Innovative Smart Grid Technologies Europe (ISGT-Europe)*, 2019, pp. 1-5.
[237] A. T. Johns, "Electrical Engineer's Reference Book," M. A. Laughton and D. J. Warne, Eds., Sixteenth Edition ed Oxford: Newnes, 2003, pp. 1–30.
[238] S. Chattopadhyay, M. Mitra, and S. Sengupta, "Electric power quality," in *Electric power quality*, ed Dordrecht: Springer Netherlands, 2011, pp. 5-12.
[239] M. Elshahed, "Assessment of sudden voltage changes and flickering for a grid-connected photovoltaic plant," *Int. Journal of Renewable Energy Research. IJRER,* vol. 6, pp. 1-8, 2016.
[240] K.-H. Tan, F.-J. Lin, C.-Y. Tsai, and Y.-R. Chang, "A distribution static compensator using a CFNN-AMF controller for power quality improvement and DC-link voltage regulation," *Energies,* vol. 11, pp. 1-17, 2018.
[241] F. H. Gandoman, A. Ahmadi, A. M. Sharaf, P. Siano, J. Pou, B. Hredzak*, et al.*, "Review of FACTS technologies and applications for power quality in smart grids with renewable energy systems," *Renewable and sustainable energy reviews,* vol. 82, pp. 502-514, 2018.
[242] F. S. Ahmed, A. N. Hussain, and A. J. Ali, "Power quality improvement by using multiple sources of PV and battery for DSTATCOM based on coordinated design," in *Iop Conference Series Materials Science and Engineering*, 2020, pp. 1-18.
[243] S. Mishra and C. Bhende, "Bacterial foraging technique-based optimized active power filter for load compensation," *IEEE Transactions on power delivery,* vol. 22, pp. 457-465, 2006.
[244] M. Farhoodnea, A. Mohamed, H. Shareef, and H. Zayandehroodi, "Optimum D-STATCOM placement using firefly algorithm for power quality enhancement," in *IEEE 7th international power engineering and optimization conference (PEOCO)*, Langkawi, Malaysia, 2013, pp. 98-102.
[245] M. K. Joyo, Y. Raza, S. F. Ahmed, M. Billah, K. Kadir, K. Naidu*, et al.*, "Optimized Proportional-Integral-Derivative Controller for Upper Limb Rehabilitation Robot," *Electronics,* vol. 8, pp. 1-26, 2019.
[246] R. V. Rao, *Jaya: an advanced optimization algorithm and its engineering applications*: Springer, 2019.

[247] R. Vijay and C. Ravichandran, "A detailed investigation on conventional and meta-heuristic optimization algorithms for economic power scheduling problems," *International Journal of Engineering Trends and Applications,* vol. 3, pp. 40-53, 2016.
[248] S. Panda and N. P. Padhy, "Comparison of particle swarm optimization and genetic algorithm for FACTS-based controller design," *Applied soft computing,* vol. 8, pp. 1418-1427, 2008.
[249] D. Karaboga and B. Basturk, "On the performance of artificial bee colony (ABC) algorithm," *Applied soft computing,* vol. 8, pp. 687-697, 2008.
[250] D. Karaboga, "Artificial bee colony algorithm," *scholarpedia,* vol. 5, pp. 6915-6945, 2010.
[251] A. Kumar, D. Kumar, and S. Jarial, "A review on artificial bee colony algorithms and their applications to data clustering," *Cybernetics and Information Technologies,* vol. 17, pp. 3-28, 2017.
[252] S. Kumar, "Nature inspired computation methods and their application in function optimization," PhD Thesis, Electrical Engineering, Jagannath University, India, 2014.
[253] R. Rao, "Jaya: A simple and new optimization algorithm for solving constrained and unconstrained optimization problems," *International Journal of Industrial Engineering Computations,* vol. 7, pp. 19-34, 2016.
[254] C. Gong, "An enhanced Jaya algorithm with a two group Adaption," *International Journal of Computational Intelligence Systems,* vol. 10, pp. 1102-1115, 2017.